Resource

Cell Chemical Biology

A fine-tuned azobenzene for enhanced photopharmacology *in vivo*

Graphical abstract

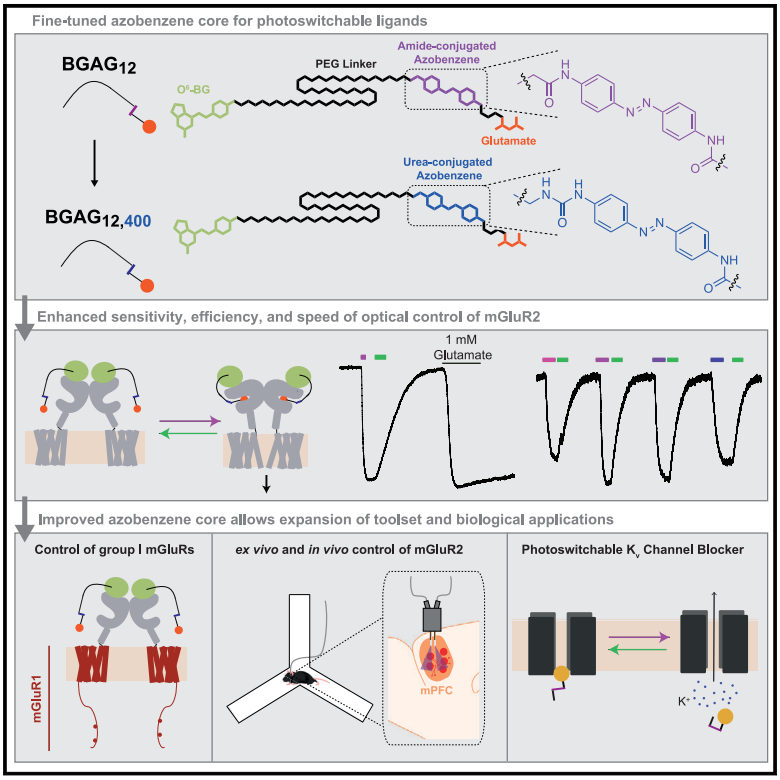

Highlights

- Azobenzene tuning for red-shift and enhanced sensitivity, efficiency and speed
- Improved photoswitches enable ultra-efficient control of GPCRs and ion channels
- Acute modulation of working memory via mGluR2 photo-activation in the mouse mPFC

Authors

Vanessa A. Gutzeit, Amanda Acosta-Ruiz, Hermany Munguba, ..., Guillaume Sandoz, Joshua Levitz, Johannes Broichhagen

Correspondence

jtl2003@med.cornell.edu (J.L.), broichhagen@fmp-berlin.de (J.B.)

In brief

Gutzeit et al. report a chemical screen that reveals an urea-conjugated azobenzene with optimal photoswitching properties. This enables the development and characterization of optimized tethered and freely diffusible photoswitchable ligands for GPCRs and ion channels, including the rapid manipulation of working memory via mGluR2 photo-activation *in vivo* in freely moving mice.

Gutzeit et al., 2021, Cell Chemical Biology *28*, 1648–1663
November 18, 2021
https://doi.org/10.1016/j.chembiol.2021.02.020

CellPress

CellPress

Cell Chemical Biology

Resource

A fine-tuned azobenzene for enhanced photopharmacology *in vivo*

Vanessa A. Gutzeit,[1,10] Amanda Acosta-Ruiz,[2,10] Hermany Munguba,[3] Stephanie Häfner,[4,5] Arnaud Landra-Willm,[4,5] Bettina Mathes,[6] Jürgen Mony,[7] Dzianis Yarotski,[6] Karl Börjesson,[7] Conor Liston,[8] Guillaume Sandoz,[4,5] Joshua Levitz,[1,2,3,11,*] and Johannes Broichhagen[6,9,*]

[1]Neuroscience Graduate Program, Weill Cornell Medicine, New York, NY 10065, USA
[2]Biochemistry, Cell and Molecular Biology Graduate Program, Weill Cornell Medicine, New York, NY 10065, USA
[3]Department of Biochemistry, Weill Cornell Medicine, New York, NY 10065, USA
[4]Université Cote d'Azur, CNRS, INSERM, iBV, Nice, France
[5]Laboratories of Excellence, Ion Channel Science and Therapeutics, Nice, France
[6]Department of Chemical Biology, Max Planck Institute for Medical Research, 69120 Heidelberg, Germany
[7]Department of Chemistry and Molecular Biology, University of Gothenburg, 41296 Gothenburg, Sweden
[8]Department of Psychiatry and Brain and Mind Research Institute, Weill Cornell Medicine, New York, NY 10065, USA
[9]Department of Chemical Biology, Leibniz-Forschungsinstitut für Molekulare Pharmakologie, 13125 Berlin, Germany
[10]These authors contributed equally
[11]Lead contact
*Correspondence: jtl2003@med.cornell.edu (J.L.), broichhagen@fmp-berlin.de (J.B.)
https://doi.org/10.1016/j.chembiol.2021.02.020

SUMMARY

Despite the power of photopharmacology for interrogating signaling proteins, many photopharmacological systems are limited by their efficiency, speed, or spectral properties. Here, we screen a library of azobenzene photoswitches and identify a urea-substituted "azobenzene-400" core that offers bistable switching between *cis* and *trans* with improved kinetics, light sensitivity, and a red-shift. We then focus on the metabotropic glutamate receptors (mGluRs), neuromodulatory receptors that are major pharmacological targets. Synthesis of "BGAG$_{12,400}$," a photoswitchable orthogonal, remotely tethered ligand (PORTL), enables highly efficient, rapid optical agonism following conjugation to SNAP-tagged mGluR2 and permits robust optical control of mGluR1 and mGluR5 signaling. We then produce fluorophore-conjugated branched PORTLs to enable dual imaging and manipulation of mGluRs and highlight their power in *ex vivo* slice and *in vivo* behavioral experiments in the mouse prefrontal cortex. Finally, we demonstrate the generalizability of our strategy by developing an improved soluble, photoswitchable pore blocker for potassium channels.

INTRODUCTION

Photopharmacology has emerged as a methodology that offers great utility for mechanistic studies of signaling molecules (i.e., enzymes, ion channels, and receptors) by allowing the function of ligands (i.e., agonists, antagonists, and allosteric modulators) to be controlled by light through the incorporation of photoswitchable moieties (Hull et al., 2018; Paoletti et al., 2019). Azobenzene-based photoswitches are the most widely used due to their efficiency, reversibility, and repeatability (Beharry and Woolley, 2011) and most photopharmacological compounds reported to date are soluble photochromic ligands (PCLs) that can be applied directly to samples to target native proteins with light dependence. However, tethered photopharmacology, where the light-sensitive ligand is covalently attached to a modified target protein, offers the highest precision since tethered ligands are not subject to diffusion, cell-type targeting can easily be achieved through genetic encoding of the target protein, and absolute subtype specificity is ensured via attachment chemistry (Leippe et al., 2017). Tethered photopharmacology has been applied to ion channels (Banghart et al., 2004; Izquierdo-Serra et al., 2016; Lemoine et al., 2013; Lester et al., 1980; Levitz et al., 2013; Lin et al., 2015; Sandoz et al., 2012; Tochitsky et al., 2012; Volgraf et al., 2006), G protein-coupled receptors (GPCRs) (Donthamsetti et al., 2017; Levitz et al., 2013), and enzymes (DuBay et al., 2018; Leippe et al., 2020; Tsai et al., 2015) via a variety of attachment chemistries. In the case of photoswitchable, orthogonal remotely tethered ligands (PORTLs) self-labeling tags, such as SNAP, CLIP, or Halo (Xue et al., 2015) are used to allow for efficient, highly orthogonal attachment.

Despite the many advantages of photopharmacology, challenges exist for engineering efficient and user-friendly systems. Photoswitchable moieties are likely to show incomplete photoconversion, insufficient light sensitivity for some applications, require UV light, and are difficult to fine-tune to produce a maximal difference between relaxed and active states of the compound. For these reasons, strategies are needed to overcome these shortcomings.

One receptor family that has been extensively targeted for photopharmacology are the metabotropic glutamate receptors (mGluRs). mGluRs are class C GPCRs that play a variety of neuromodulatory roles in the central and peripheral nervous systems and serve as drug targets for a range of disorders (Nicoletti et al., 2011). Their ubiquitous expression throughout many physiological systems (Ferraguti and Shigemoto, 2006), their rapid and spatially confined signaling (Reiner and Levitz, 2018), the existence of many receptor subtypes that exist in overlapping expression patterns (Lee et al., 2020), and the paucity of fully subtype-selective ligands together make mGluRs important targets for photopharmacology (Goudet et al., 2018). Indeed, mGluR2 was the first GPCR to be controlled via tethered photopharmacology, first via attachment to cysteines (Carroll et al., 2015; Levitz et al., 2013) and more recently via self-labeling tags as the original target of PORTLs (Berry et al., 2017; Broichhagen et al., 2015a; Levitz et al., 2017). Recently, we introduced branched PORTLs for mGluRs, which incorporate two or four azobenzene-conjugated glutamates to enhance photoswitch efficiency and enable optical control of mGluR2 in freely moving mice (Acosta-Ruiz et al., 2020). However, many engineering challenges for mGluR-tethered photopharmacology still exist, including the need for further improvements to efficiency, light sensitivity, speed, and extension to other subtypes. For example, in the aforementioned recent study (Acosta-Ruiz et al., 2020) we developed a chimera strategy to enable optical control of mGluR5 signaling via incorporation of the mGluR2 ligand binding domain into a full-length mGluR5 construct. However, due to insufficient efficiency this approach has not been amenable to mGluR1, limiting the ability to probe the distinct roles of group I mGluRs (i.e., mGluR1 versus mGluR5) via tethered photopharmacology.

In this study we sought to tackle the limitations of PORTLs for mGluRs and develop widely applicable strategies. We first design and synthesize a library of azobenzene variants and identify photoswitchable cores that maintain the critical feature of bistability (i.e., the ability to maintain the *cis* isomer in the dark following illumination) while offering subtle red-shifts, enhanced light sensitivity, and improved photoswitching properties. Based on an optimized "azobenzene-400" core, we then develop an updated family of benzylguanine-azobenzene-glutamate (BGAG) PORTLs for mGluRs. $BGAG_{12,400}$ shows dramatically improved photo-agonism of SNAP-tagged mGluR2 compared with previous PORTLs, including in response to 405 nm light. In addition, $BGAG_{12,400}$ enables high efficiency, spatiotemporally precise optical control of specific mGluR5- and mGluR1-mediated calcium signaling through a chimera approach. Branched $BGAG_{12,400}$-based PORTLs further enhance photoswitching properties and enable incorporation of Cy3 or Cy5 fluorophores for dual sensing and manipulation of mGluRs. We demonstrate improved photo-activation of SNAP-mGluR2 via $BGAG_{12,400}$-Cy5 in acute brain slices and *in vivo* in mice, where targeted mGluR2 activation in the medial prefrontal cortex produces a rapid (~1–2 min) effect on working memory. Finally, we demonstrate the generalizability of the azobenzene-400 core by developing AQ_{400}, a soluble photoswitchable potassium channel pore blocker with improved photoswitch efficiency and kinetics, including with native channels in sensory dorsal root ganglia (DRG) neurons. Together, this work shows that branching and azobenzene tuning together can enable the optimization of PORTLs and produces a family of tools with widespread applicability for the dissection of neuromodulatory signaling.

RESULTS

Probing modified azobenzene cores to enhance efficiency and sensitivity while maintaining bistability

With the simultaneous goals of exploring the chemical space of substituents to azobenzenes and improving the efficiency and spectral properties of photoswitchable ligands, we set out to screen modified azobenzene cores. In contrast to prior studies that have aimed to dramatically red-shift the absorption spectrum of azobenzenes into the blue, green, or red range (Broichhagen et al., 2015b; Kienzler et al., 2013; Mourot et al., 2011; Rullo et al., 2014; Samanta et al., 2013), we hoped to produce modest 10–20 nm red-shifts toward longer wavelengths to preserve photoswitch bistability while tweaking light sensitivity and photoswitching properties. Therefore, we aimed to install moieties in the para position on a "naked" azobenzene that displays a small negative Hammett parameter σ_p, thereby donating electrons into the π-system and inducing a small bathochromic shift. For this reason, we modified an azobenzene scaffold on its 4 position and measured the effect on its extinction coefficient and photoswitching kinetics (Figure 1A). We chose amide **1** as a reference point for comparison as all described PORTLs to date rely on this anchor point. Modifications to the azobenzene included N-methylation of **1** to obtain **2**, and lactams with ring sizes between 4 and 7 atoms (compounds **3**–**6**). In addition to the installation of a carbamate to produce compound **7**, urea scaffolds ($\sigma_p \sim -0.26$) (Hansch et al., 1991) were screened based on their alkylation pattern to produce compounds **8**–**12** (STAR Methods, scheme 1). We determined the maximal absorbance wavelengths of our library (Figures 1B and S1A) and their respective extinction coefficients in DMSO. When plotted against each other (Figure 1C), urea **8** and **11** are found in the upper right corner with the desired characteristics of a red-shifted peak and increased absorbance (Figures S1B and S1C). We assessed photoswitching kinetics of our library (385/500 nm, DMSO) and, when plotted versus peak wavelength (Figures 1D and S1D), urea **8** showed the fastest photoswitching, which is shown versus its parent molecule **1** in Figure 1E (for all values see Table 1). Compared with amide **1**, urea **8** shows a red-shift in maximal absorbance by 15 nm (375 versus 360 nm), an ~30% larger extinction coefficient (19,800 versus 15,300 M^{-1} cm^{-1}) and a 2-fold increase in *cis* switching kinetics at saturating light intensities (τ = 4.2 versus 8.4 s) (Figures S1E and S1F). As such, the simple urea moiety became our candidate for further investigations, especially because, compared with other variants with similar desirable properties (i.e., compound **11**), it is straightforward for synthesis. Importantly, compound **8** also showed bistability where the *cis* isomer was maintained in the dark following illumination (Table 1), an important parameter for many biological applications. Based on the red-shift that brings the absorbance peak closer to 400 nm, we term the urea-conjugated azobenzene core azobenzene-400 and set out to test this modification in the context of a PORTL.

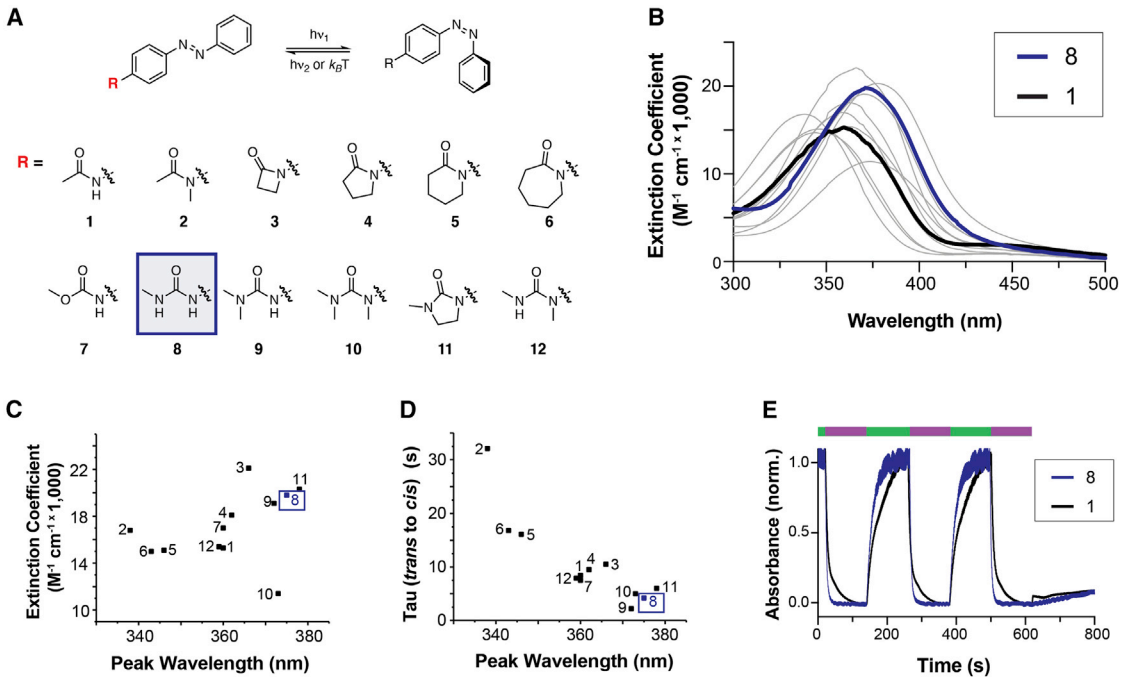

Figure 1. A screen of azobenzene variants reveals red-shifted bistable variants

(A) A screen of azobenzenes (**1**–**12**) to improve photoswitching characteristics. Azobenzenes may be switched between their *cis* and *trans* states by applying orthogonal wavelengths of light, and thermally relax into the stable *trans* state in the dark (top). Introduced substitution patterns change the electronic structure of the azobenzene and therefore alter their photophysical properties.

(B) Normalized UV-vis absorption spectra of compounds **1**–**12** in DMSO reveals hypso- or batho-chromic shifts with respect to **1**. Urea **8** (blue) red-shifts the spectra by ~14 nm.

(C) Plot of maximum extinction coefficient versus peak wavelength reveals candidates with red-shift and higher absorbance properties.

(D) Plot of *trans* to *cis* switching kinetics under 385 nm illumination versus peak wavelength reveals scaffold **8** with an optimal combination of a clear red-shift, fast switching kinetics, and a simple modification that is amenable to PORTL synthesis.

(E) Representative photoswitching trace showing the change in absorbance in response to 385 and 500 nm light for parent molecule **1** and compound **8**. All UV-vis experiments were conducted with 50 μM of sample in DMSO at room temperature.

See also Figure S1.

$BGAG_{12,400}$ enables near-complete optical control of SNAP-mGluR2

Based on the improved properties of the azobenzene-400 core, we decided to use this scaffold to synthesize a BGAG PORTL for optical control of SNAP-mGluR2 (Figure 2A). Previous studies have used $BGAG_{12}$ (Figure 2B), a BGAG variant with a 12-repeat polyethylene-glycol (PEG_{12}) linker between benzylguanine (BG) and the azobenzene core, as a benchmark for evaluating PORTL efficiency (Broichhagen et al., 2015a). As such, $BGAG_{12,400}$ was synthesized from a known precursor (Levitz et al., 2013; Broichhagen et al., 2015a) (STAR Methods, scheme 2) by reacting the free aniline with phosgene, and trapping the formed isocyanate with an excess of ethylene diamine to create a urea linkage and another free amine for further processing in one-pot. Subsequent installation of the PEG_{12} chain alongside BG was performed similarly to previous studies (Acosta-Ruiz et al., 2020), including final deprotection steps to produce $BGAG_{12,400}$ (Figure 2B). We reasoned that any observed red-shift from our library (Figure 1) should persist in BGAG molecules by creating a system with enhanced electron density, with an electron-donating urea and a neutral amide group on the 4 and 4′ positions, respectively. Indeed, UV-vis spectroscopy of $BGAG_{12}$ or $BGAG_{12,400}$ in PBS showed a red-shift of ~12 nm and an increased absorbance ($\varepsilon_{366\ nm}$ [$BGAG_{12}$] = 21,200 M^{-1} cm^{-1}; $\varepsilon_{378\ nm}$ [$BGAG_{12,400}$] = 25,800 M^{-1} cm^{-1}) (Figures 2C and 2D). Both PORTLs showed maximal *cis* occupancy following 380 nm illumination, but 405 nm illumination produced a larger *cis* occupancy for $BGAG_{12,400}$ (Figures S2A–S2C). In line with this, the photoswitching kinetics of $BGAG_{12}$ and $BGAG_{12,400}$ showed that the $BGAG_{12,400}$ system enabled faster switching in both directions in response to 380 or 500 nm light (Figures S2D–S2F). However, $BGAG_{12,400}$ showed faster relaxation under dark conditions compared with $BGAG_{12}$, although this was still on the order of minutes (τ = 77 s), making $BGAG_{12,400}$ sufficiently bistable for most biological experiments.

We next tested the ability of $BGAG_{12,400}$ to enable optical control of an mGluR in living cells. We turned to N-terminally SNAP-tagged mGluR2 (SNAP-mGluR2), which has previously been activated by the *cis* form of azobenzene-glutamate PORTLs (Figure 2A) (Acosta-Ruiz et al., 2020; Berry et al., 2017; Broichhagen et al., 2015a; Levitz et al., 2017). We decided to test $BGAG_{12,400}$ and compare it with the original $BGAG_{12}$ PORTL and its branched variant $^{2x}BGAG_{12}$. Using a previously established competition assay we found that $BGAG_{12,400}$ was able to label surface SNAP-mGluR2 with >90% efficiency in HEK293T cells (Figure S2G), in line with previous measurements of $BGAG_{12}$ (Levitz et al., 2017).

Table 1. Spectral and photophysical properties of azobenzenes 1–12

Compound	λ_{max} (nm)	ε (M^{-1} cm^{-1})	τ_{cis} (s)	τ_{trans} (s)	τ_{dark} (s)
1	360	15,300	8.4	31.7	10^6
2	338	16,800	32.1	53.1	10^5
3	366	22,100	10.5	34.5	10^6
4	362	18,100	9.5	37.7	10^6
5	343	15,000	16.8	39.4	10^2
6	346	15,100	16.1	42.0	10^6
7	360	17,000	7.5	30.6	10^6
8	375	19,800	4.2	21.1	10^3
9	372	19,100	2.2	24.4	10^3
10	373	11,400	5.0	27.6	10^2
11	378	20,300	6.0	24.8	10^3
12	359	15,400	7.9	32.4	10^3

Wavelength of maximal absorbance λ_{max}, extinction coefficient ε and *cis*/*trans*-isomerization kinetics ($\tau_{cis/trans}$) have been assessed by UV-vis spectroscopy, the latter with 385 and 500 nm of light. τ_{dark} is the time scale of the thermal relaxation following occupancy of the maximal *cis* state and illumination with 600 nm of red light to mimic dark conditions. Relaxation curves have been fitted mono-exponential or linear, dependent on their nature, to assess τ_{dark} values in orders of magnitude in seconds. Conditions were 50 μM in DMSO at room temperature.

Following labeling, we performed patch-clamp electrophysiology recordings in cells co-expressing G protein-coupled inward rectifier potassium (GIRK) channels, and found that $BGAG_{12,400}$ produced large, bistable inward photocurrents in response to 385 nm illumination that were reversed by 525 nm illumination (Figure 2E). Interestingly, following 385 nm illumination ~60 s of dark incubation did not lead to any clear relaxation to the *trans* state (Figure 2E), indicating that either the proteinaceous environment or binding of the glutamate moiety enhances the stability of the *cis* isomer in this context. Strikingly, $BGAG_{12,400}$ photocurrents were nearly as large as currents elicited by saturating (1 mM) glutamate (Figure 2F). When quantified over many cells, the photoswitch efficiency (as defined by the photocurrent amplitude compared with saturating glutamate) of $BGAG_{12,400}$ was substantially higher than that observed with $BGAG_{12}$ and comparable with $^{2x}BGAG_{12}$ (Figure 2G). Furthermore, $BGAG_{12,400}$ light responses showed faster ON kinetics compared with both $BGAG_{12}$ and $^{2x}BGAG_{12}$ (Figure 2H). The fact that $BGAG_{12,400}$ responses were faster than $^{2x}BGAG_{12}$ responses despite similar photoswitch efficiency suggests that this effect is due to the photoswitching kinetics of the modified azobenzene-400 core rather than differences in agonist efficacy. The OFF kinetics were similar across all three PORTLs and are likely limited by processes downstream of the receptor (Figure 2H). We also tested the spectral properties of $BGAG_{12,400}$ photoswitching and found that, compared with $BGAG_{12}$, there was a clear red-shift in the activation spectra (Figure 2I). Substantial photocurrents could be observed in the blue range of the visible spectrum (Figure 2J). Most importantly, 405 nm illumination produced similar $BGAG_{12,400}$ photocurrents compared with 385 nm indicating that this common laser wavelength is well suited to applications of this PORTL without the trade-off of decreased efficiency.

$BGAG_{12,400}$ enables efficient optical control of mGluR5 and mGluR1 signaling

Having successfully enhanced mGluR2 photo-activation with $BGAG_{12,400}$, we next asked if this PORTL could improve photoswitching of another mGluR system. We first turned to optical control of mGluR5 using a recently established approach based on a chimera between the mGluR2 extracellular domain (ECD) and the mGluR5 transmembrane domain (TMD) and intracellular C-terminal domain (Figure 3A) (Acosta-Ruiz et al., 2020). We co-transfected cells with the SNAP-tagged mGluR2-mGluR5 chimera and GCaMP6f to measure G_q-coupled calcium responses. Consistent with our previous study, $^{2x}BGAG_{12}$ enabled calcium responses to dim (~0.03 mW/mm^2) 385 nm light in ~50% of cells that also responded to saturating glutamate, while $BGAG_{12,400}$ produced light responses in >80% of cells (Figures 3A and 3B). $BGAG_{12,400}$ light responses were oscillatory with a similar amplitude and frequency compared with glutamate responses, demonstrating that the PORTL recapitulates the distinct signaling dynamics of mGluR5. Importantly, no light responses were observed in cells that were not labeled with $BGAG_{12,400}$ (Figure S3A).

One of the major advantages of the PORTL system is the precise spatial control enabled by light. We characterized the ability to elicit mGluR5 responses following photo-activation of small subcellular areas using targeted 405 nm laser illumination on a scanning confocal microscope. Based on the increased light sensitivity, photoswitch efficiency, and red-shifted spectra of $BGAG_{12,400}$, we hypothesized that smaller areas could be used for this PORTL to produce a calcium response compared with $^{2x}BGAG_{12}$. We imaged GCaMP6f responses while targeting 405 nm illumination to areas of 0.17, 0.87, and 13.85 μm^2. While both PORTLs produced clear calcium responses to photo-activation of the large 13.85 μm^2 area, $BGAG_{12,400}$ produce more reliable responses to smaller areas (Figures 3C and 3D). For the 0.17 μm^2 illumination, which is approximately the size of the dendritic spines where mGluR5 natively functions (Bourne and Harris, 2008; Lujan et al., 1996; Reiner and Levitz, 2018), no responses were observed with $^{2x}BGAG_{12}$, while most cells labeled with $BGAG_{12,400}$ responded with calcium oscillations (Figures 3C and 3D). Consistent with our previous finding that the size of the receptor activation area determines the probability of eliciting a calcium response but not the frequency of the response, identical calcium oscillation frequencies were observed for all three photoswitch areas (Figures 3C and S3B). Together these results demonstrate that $BGAG_{12,400}$ provides improved optical control of mGluR5 signaling, particularly for subcellular, spatiotemporally targeted control.

While mGluR5 is a widely expressed biologically important receptor on its own, it exists within the group I mGluR subfamily with mGluR1. While both receptors share a general similarity in their G protein coupling preference for G_q family proteins and are primarily found post-synaptically, they show many differences in terms of signaling dynamics, interaction partners, expression patterns, and disease roles (Lee et al., 2020; Nicoletti et al., 2011; Pin and Bettler, 2016). For example, unlike mGluR5, mGluR1 does not produce calcium oscillations in response to extended glutamate activation but rather produces slowly desensitizing responses (Kawabata et al., 1996). We have previously been unable to successfully apply the mGluR2 ECD chimera strategy to mGluR1.

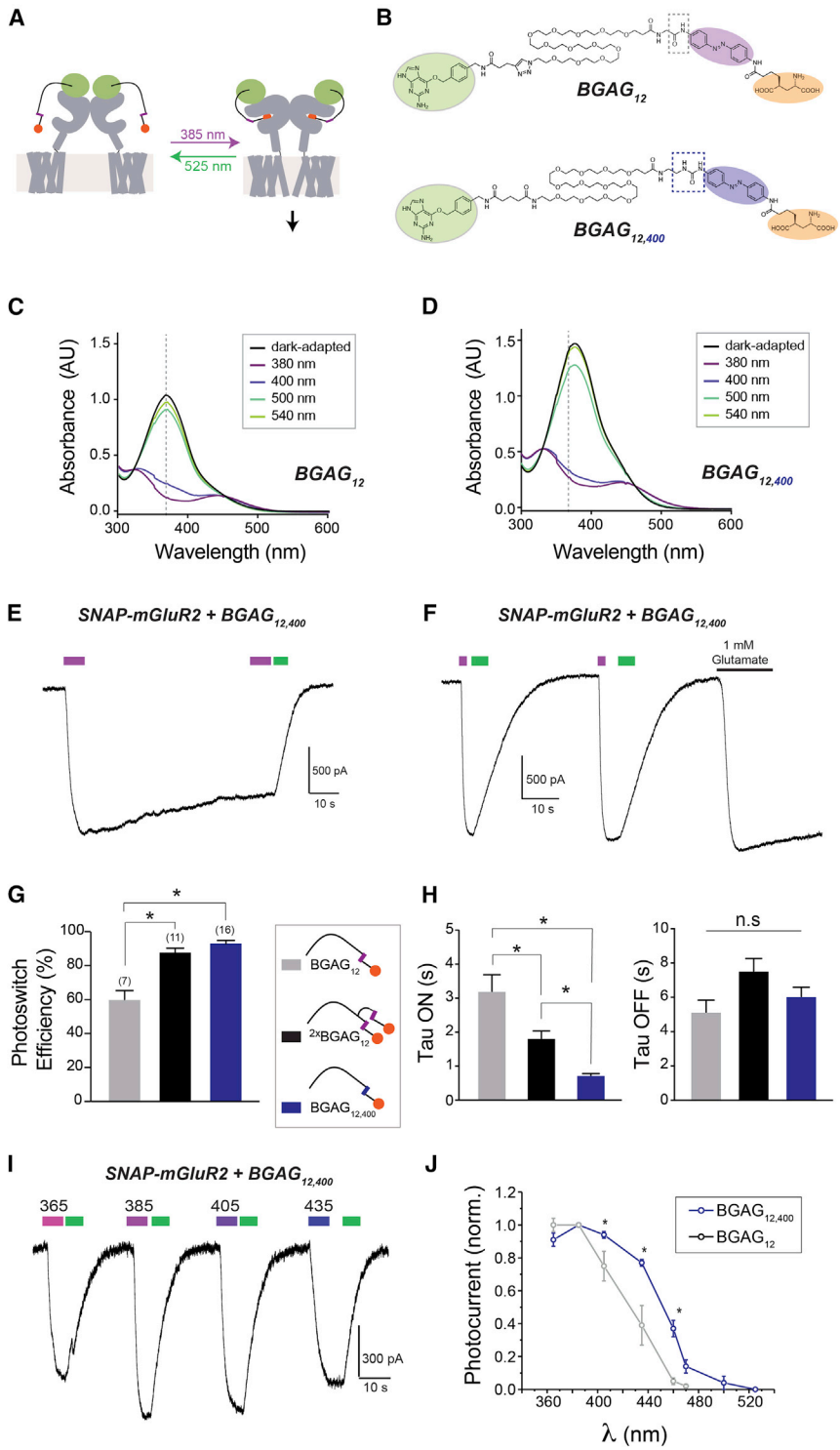

Figure 2. $BGAG_{12,400}$ enables ultra-efficient optical control of SNAP-mGluR2 with enhanced kinetics

(A) Schematic showing principle of PORTL-mediated optical control of SNAP-mGluR2. Near UV light (~385 nm) typically produces *trans* to *cis* photoconversion, which leads to agonism via the glutamate moiety (orange ball) that can be reversed by visible (>500 nm) light.

(B) Chemical structures of previously reported $BGAG_{12}$ (top), which uses a standard azobenzene core (purple), and $BGAG_{12,400}$ (bottom), which is based on the azobenzene-400 core (blue).

(C and D) UV-vis spectroscopy for $BGAG_{12}$ and $BGAG_{12,400}$ (50 μM in PBS at room temperature) following illumination with a range of wavelengths ($I = 1–2\ mW/mm^2$).

(E) Representative patch-clamp trace showing bi-stable light-induced photo-activation (385 nm light, magenta bar) and photo-deactivation (525 nm, green bar) of SNAP-mGluR2 via $BGAG_{12,400}$.

(F) Representative trace showing repeated photo-activation of SNAP-mGluR2 via $BGAG_{12,400}$ followed by application of saturating 1 mM glutamate.

(G) Summary of photoswitch efficiency (photocurrent amplitude/glutamate response) for all three PORTLs tested. *Statistical significance (unpaired t test, $p = 0.002$ for $BGAG_{12}$ versus $BGAG_{12,400}$ and $p = 0.002$ for $BGAG_{12}$ versus $^{2x}BGAG_{12}$). The number of cells tested are shown in parentheses.

(H) Summary of photoswitching kinetics following 385 nm illumination ("ON") or 525 nm illumination ("OFF"). *Statistical significance (unpaired t test, $p = 0.003$ for $BGAG_{12}$ versus $BGAG_{12,400}$ and $p = 0.0007$ for $^{2x}BGAG_{12}$ versus $^{2x}BGAG_{12,400}$).

(I and J) $BGAG_{12,400}$ produces a red-shift in photo-activation as seen in a representative trace of photocurrents in response to various wavelengths of illumination (F) and in a summary graph (G). Notably, $BGAG_{12,400}$ enables photo-activation with 405 nm light without a decrease in efficiency relative to 385 nm. In (G) all current amplitudes are normalized to the response to 385 nm light. *Statistical significance (unpaired t test between $BGAG_{12}$ and $BGAG_{12,400}$, $p = 0.05$ for 405 nm, $p = 0.04$ for 435 nm and $p = 0.009$ for 460 nm). Error bars show SEM.

See also Figure S2.

Despite maintaining the ability to respond to glutamate with large calcium transients, both $BGAG_{12}$ and $^{2x}BGAG_{12}$ produced little to no responses to 385 nm light on an SNAP-mGluR2-1 chimera (Figure S3C). We hypothesized that efficient coupling of the mGluR2 ECD and the mGluR1 TMD requires either a higher degree of photo-agonism or different PORTL photophysical properties and wondered if $BGAG_{12,400}$ could enable photo-activation. Surprisingly, $BGAG_{12,400}$ enabled robust 385 nm light-induced non-oscillatory calcium responses in ~60% of cells that also showed glutamate responses (Figure 3E). SNAP-mGluR2-1 light responses were rapid, showed comparable amplitudes (84.8% ± 1.1% versus glutamate, n = 171 cells) and a similar slow time course (~1–2 min) of desensitization to glutamate responses, and were repeatable over multiple bouts of photo-activation (Figure S3D).

Given the efficient light responses observed with SNAP-mGluR2-1 and the fact that mGluR1, similar to mGluR5, primarily

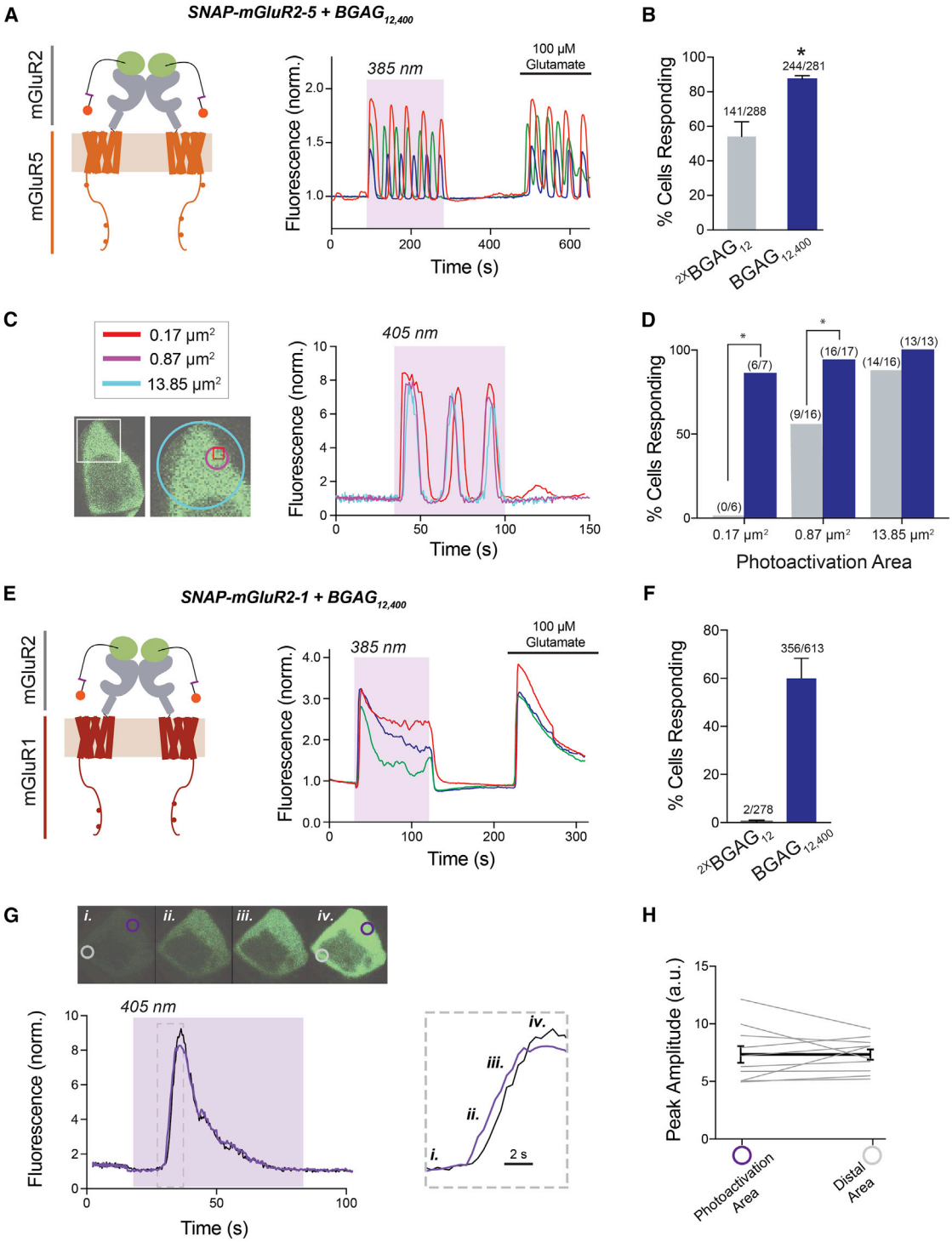

Figure 3. $BGAG_{12,400}$ enables efficient, subcellularly targeted optical control of group I mGluR signaling

(A) A chimera (left) between SNAP-tagged mGluR2 extracellular domain (gray) and the mGluR5 transmembrane and C-terminal domains (orange). Right, representative trace showing 385 nm light-induced calcium oscillations with similar amplitude and frequency compared with saturating glutamate. Each colored trace shows an individual cell.

(B) Summary bar graph showing the efficiency of photo-activation of SNAP-mGluR2-5 by $^{2x}BGAG_{12}$ and $BGAG_{12,400}$. The number of cells showing light responses divided by the total cells with glutamate responses is shown in parentheses. *Statistical significance (unpaired t test, p = 0.036).

(C and D) Photo-activation of mGluR5 signaling with spatially targeted 405 nm illumination. A representative cell (C) shows a similar oscillatory calcium response following illumination in areas of different sizes. A summary bar graph shows higher efficiency activation by $BGAG_{12,400}$ compared with $^{2x}BGAG_{12}$ at smaller areas. *Statistical significance (Pearson's chi-square test; p = 0.002 for 0.17 μm^2, p = 0.014 for 0.87 μm^2).

(legend continued on next page)

functions in spatially confined subregions of cells, we asked if this system was amenable to targeted photo-activation. We again turned to confocal microscopy and found that 405 nm photo-activation areas as small as 0.87 μm^2 produced reliable light responses in 70% of cells (n = 10 cells) (Figure 3F). We previously reported that mGluR5-induced calcium oscillations spread across HEK293 cells with limited attenuation (Acosta-Ruiz et al., 2020). Similarly, we found that cells showed a calcium transient that spread from one side of the cell to the other at ~10–20 μm/s (Figure 3G) and showed a similar amplitude both at the site of initiation and the opposite side of the cell ~15–20 μm away (Figure 3H). Together, these data demonstrate a toolset for efficient, spatiotemporally resolved optical control of characteristic mGluR5 or mGluR1 signaling via $BGAG_{12,400}$.

Branched $BGAG_{12,400}$ PORTLs further improve photoswitch efficiency and enable dual manipulation and detection

We next asked if the efficient $BGAG_{12,400}$ PORTL could be further modified to incorporate branching. We recently showed that PORTL branching can increase photoswitch efficiency, light sensitivity, and enable dual imaging and manipulation through the incorporation of fluorophores (Acosta-Ruiz et al., 2020). Our synthetic outline was designed to accommodate a branched version of $BGAG_{12,400}$, which was realized by using Fmoc-protected D-glutamate as a branching scaffold. Accordingly, PEG chain and BG end group were installed similarly to prior studies to obtain $^{2x}BGAG_{12,400}$ (Figure 4A and S4A; STAR Methods, scheme 3), which showed similar spectral properties to $BGAG_{12,400}$ (Figure S4B). To enable incorporation of a fluorescent dye for direct monitoring of PORTL-labeled cells, we aimed to install Cy3 as a red and Cy5 as a far-red fluorophore (Figure 4A). This was achieved either between the PEG chain and the azobenzene ($BGAG_{12,400}$-Cy3 and $BGAG_{12,400}$-Cy5; Figures 4A, S4C, and S4D; STAR Methods, scheme 4) or between the BG and the PEG chain ($BGAG_{12,400}$-$Cy3_{v2}$ and $BGAG_{12,400}$-$Cy5_{v2}$; Figures 4A, S4E, and S4F; STAR Methods, scheme 5). Successful fusion of the azobenzene and the respective dye can be seen by UV-vis spectroscopy (Figures S4D and S4F) and is confirmed by mass spectrometry (see supplemental information).

We tested all branched $BGAG_{12,400}$ PORTLs on SNAP-mGluR2 and observed large 385 nm light-induced photocurrents with all compounds (Figures 4B–4D). $^{2x}BGAG_{12,400}$ showed similar efficiency (Figure 4D) compared with $BGAG_{12,400}$, consistent with the interpretation that there is little room for further improvement beyond $BGAG_{12,400}$. Incorporation of Cy5 at either position produced photo-activation with the same efficiency as unbranched $BGAG_{12,400}$ (Figures 4B and 4D). This is an important improvement over $BGAG_{12}$-Cy5, where a trade-off between incorporating a fluorophore and photoswitch efficiency had to be made since only one azobenzene-glutamate is included. In addition, Cy3 incorporation into $BGAG_{12,400}$ did not prevent photo-activation, although $BGAG_{12,400}$-$Cy3_{v2}$ showed larger photocurrents than $BGAG_{12,400}$-Cy3 (Figures 4C and 4D), suggesting that there may be some interaction between the fluorophore and the azobenzene moiety. We performed fluorescent excitation scans and identified a small band around 385 nm in all compounds that can indeed be excited by 385 or 405 nm light to elicit red and far-red emission of the Cy3 and Cy5 fluorophores, respectively (Figures S4G and S4H). Due to the closer proximity of the azobenzene to the fluorophore, this crosstalk is expectedly larger for $BGAG_{12,400}$-Cy3/5 than for $BGAG_{12,400}$-$Cy3/5_{v2}$; however, this is of minimal concern as light intensities used in this plate reader are too low to ensure efficient photoswitching (Richter et al., 2015). Importantly, dye-conjugated PORTLs showed comparable sensitivity to 405 nm illumination (Figures S4I and S4J) and activation kinetics compared with $BGAG_{12,400}$ (Figure S4K). Together, these results establish optical control and detection of mGluR2 with both Cy3 and Cy5, providing a flexible toolset for a range of applications where receptor visualization is needed (see Discussion). Finally, we confirmed that fluorophore conjugation is also compatible with efficient optical control of group I mGluR signaling via SNAP-mGluR2-5 and can be combined with optical readouts (Figures S4L and S4M).

$BGAG_{12,400}$-Cy5 enables efficient *ex vivo* and *in vivo* optical control of mGluR2 in mice

Having established the efficiency of azobenzene-400 PORTLs in cultured cells, we asked if the system would also enhance studies in intact tissue and *in vivo* in rodents. Notably, a relatively limited number of *in vivo* demonstrations of tethered photopharmacology in rodents have been reported in the retina (Berry et al., 2017; Caporale et al., 2011) and, more recently, in the brain (Acosta-Ruiz et al., 2020; Davenport et al., 2020; Durand-de Cuttoli et al., 2018; Levitz et al., 2016). We first tested $BGAG_{12,400}$-Cy5 in acute slices of the medial prefrontal cortex (mPFC), a context where we have previously used branched PORTLs for interrogation of mGluR2-mediated neuromodulation (Acosta-Ruiz et al., 2020). We injected the mPFC of Grm2-Cre mice with an adeno-associated virus (AAV) encoding SNAP-mGluR2. SNAP-mGluR2 expression was Cre dependent, ensuring that expression was targeted only to mPFC cells that natively express mGluR2, which primarily includes pyramidal neurons in both layer 2/3 and layer 5 (Acosta-Ruiz et al., 2020; Lee et al., 2020). Following at least 6 weeks of expression, we locally injected either $BGAG_{12,400}$-Cy5 or $BGAG_{12}$-Cy5, a branched PORTL based on $BGAG_{12}$, into the mPFC. After 12–16 h, acute coronal slices were prepared and

(E) A chimera between SNAP-mGluR2 and mGluR1 (maroon) enables $BGAG_{12,400}$-mediated 385 nm light-induced non-oscillatory calcium responses.
(F) Summary bar graph showing the efficiency of photo-activation of SNAP-mGluR2-1 by $^{2x}BGAG_{12}$ and $BGAG_{12,400}$. The number of cells showing light responses divided by the total cells with glutamate responses is shown in parentheses.
(G and H) Photo-activation of mGluR1 signaling with spatially targeted 405 nm illumination. A representative cell (G) shows a transient calcium response following targeted illumination (purple circle) which spreads to the opposite side of the cell (measured at the gray region of interest). Representative images, top (G), show distinct time points (i, ii, iii, and iv), which are indicated in the inset zoom-in trace. Representative trace shows calcium response at the photo-activation site (purple trace) and distal site (black trace). A summary graph (H) showing calcium responses with similar amplitude at the site of photo-activation and at a distal site of the same size.
Error bars show SEM. See also Figure S3.

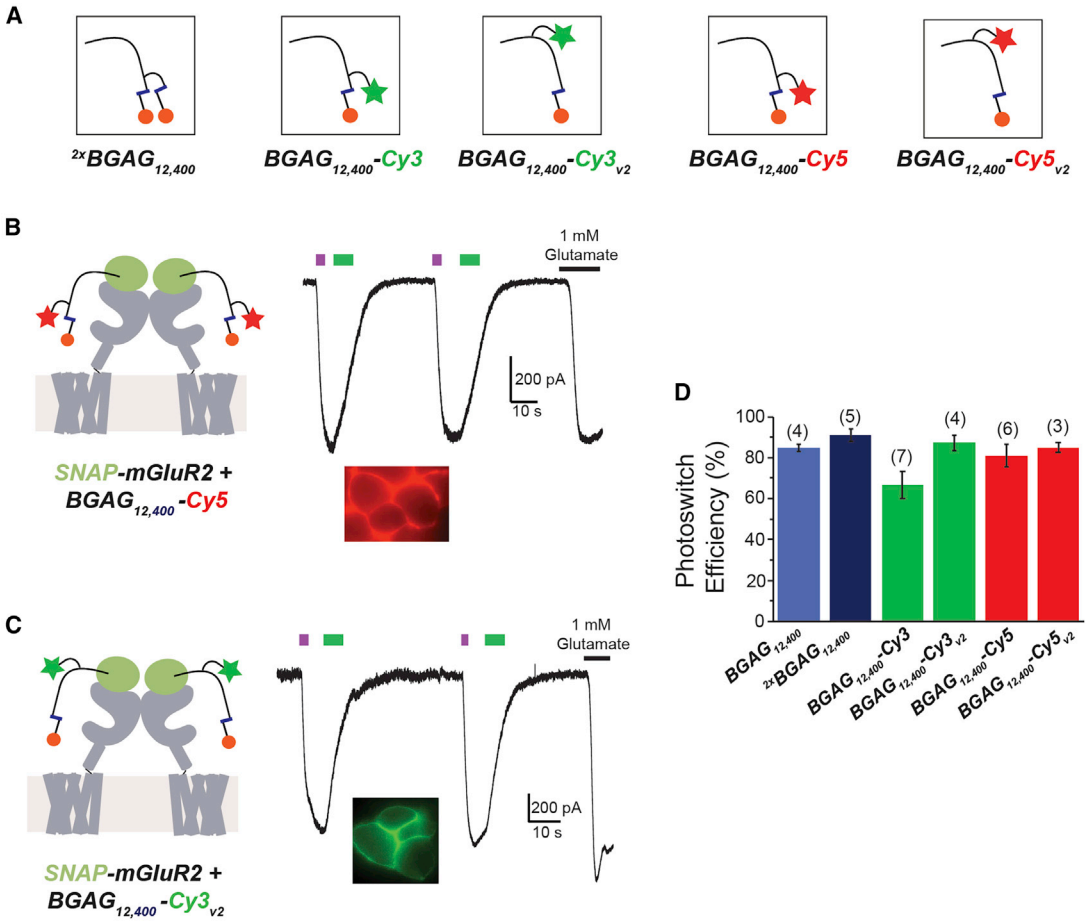

Figure 4. Branched variants of $BGAG_{12,400}$ enable incorporation of fluorophores while retaining ultra-efficient mGluR2 activation

(A) Schematic showing general design of branched azobenzene-400 PORTLs. See Figure S4 for chemical structures.

(B and C) Representative patch-clamp G protein-coupled inward rectifier potassium current traces from HEK293T cells showing efficient photo-activation of SNAP-mGluR2 by $BGAG_{12,400}$ PORTLs conjugated to Cy5 (B) or Cy3 (C). Insets show images of SNAP-mGluR2-expressing cells labeled with dye-conjugated PORTLs demonstrating clear surface fluorescence.

(D) Summary bar graph showing efficiency of photo-activation of SNAP-mGluR2 by branched $BGAG_{12,400}$ PORTLs compared with 1 mM glutamate. The number of cells tested are shown in parentheses. Error bars show SEM.

See also Figure S4.

patch-clamp recordings were made from fluorescently labeled cells (Figure 5A). The Cy5 fluorophore greatly increases the efficiency of patch-clamp experiments by serving as a molecular beacon to guide electrode placement. Fluorescence was observed in slices from mice injected with the SNAP-mGluR2 AAV (Figure 5B), but only a weak background was observed in slices from control mice that did not receive virus (Figure 5B).

As expected, 385 nm illumination resulted in a rapid hyperpolarization of neurons that was maintained in the dark and reversed by 525 nm illumination (Figure 5C). However, the amplitude of hyperpolarization was more than twice as large for $BGAG_{12,400}$-Cy5 compared with $BGAG_{12}$-Cy5, consistent with the enhanced efficiency of the azobenzene-400 PORTL (Figure 5D). Importantly, no response to light was observed in slices from mice injected with $BGAG_{12,400}$-Cy5 but not the AAV-SNAP-mGluR2 (n = 6 cells) or non-fluorescent cells from slices injected with both $BGAG_{12,400}$-Cy5 and AAV-SNAP-mGluR2 (n = 6 cells). In addition, even at a modest light intensity (~1 mW/mm^2), light-induced hyperpolarization was faster for $BGAG_{12,400}$-Cy5 with an average τ value of less than 200 ms (Figure 5E). Both PORTLs enabled re-polarization following 525 nm illumination on the 300 ms time scale (Figure 5C). Notably, this level of control in intact tissue opens up a temporal regime for the study of neuromodulation, which has not previously been available with drug perfusion or, even, uncaging where off kinetics are limited by ligand unbinding and diffusion (Reiner et al., 2015). Finally, photo-activation of SNAP-mGluR2 decreased spike firing in response to current injection (Figure 5F), consistent with reports of group II mGluR-mediated control of neuronal excitability in the prefrontal cortex (Chen et al., 2020).

We next asked if the improved properties of $BGAG_{400}$ PORTLs could be harnessed for *in vivo* studies of mGluR2. It has previously been shown that systemic treatment with mGluR2/3 agonists impairs performance in working memory assays (Aultman and Moghaddam, 2001; Schlumberger et al., 2009). However,

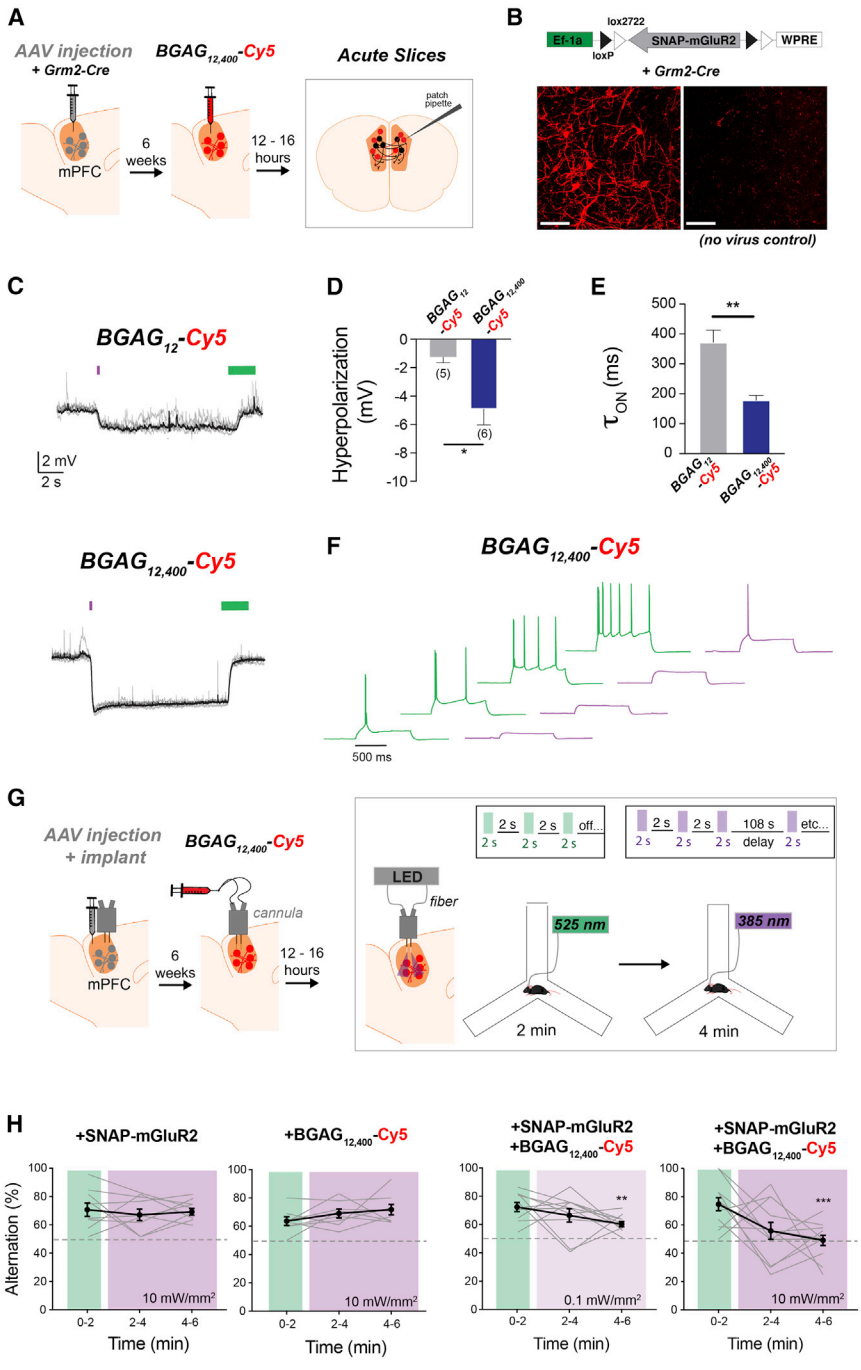

Figure 5. Rapid photo-agonism of SNAP-mGluR2 via BGAG$_{12,400}$-Cy5 *ex vivo* and *in vivo* in mouse prefrontal cortex

(A) Schematic of acute slice experiments where, 6 weeks following AAV injection, BGAG$_{12,400}$-Cy5 (or BGAG$_{12}$-Cy5) is injected into the mPFC 12–16 h before acute slice preparation and recording from fluorescent cells.

(B) Representative images of experimental and control acute slice conditions, where mice expressing SNAP-mGluR2 show robust labeling of pyramidal cells in the mPFC with BGAG$_{12,400}$-Cy5 (left) but control animals without receptor expression only show weak background fluorescence (right). Scale bars, 25 μm.

(C) Representative current-clamp traces showing light-induced hyperpolarization (385 nm, magenta bar) and re-polarization (525 nm, green bars) in slices labeled with BGAG$_{12}$-Cy5 (top) or BGAG$_{12,400}$-Cy5 (bottom).

(D and E) Summary of acute slice experiments, where BGAG$_{12,400}$-Cy5 produced a larger light-induced hyperpolarization (D) and faster on kinetics (E). *Statistical significance (unpaired two-tailed t test, p = 0.02 for amplitude and p = 0.00007 for kinetics compared with BGAG$_{12}$-Cy5).

(F) Representative spike firing in response to current injections following 525 nm (green) or 385 nm (purple) illumination in a slice labeled with BGAG$_{12,400}$-Cy5. SNAP-mGluR2 photo-activation reduced the number of spikes across different amplitude current injections ranging from 50 pA (bottom) to 200 pA (top).

(G) Schematic of *in vivo* experiments, where 6 weeks following AAV injection and implant placement, BGAG$_{12,400}$-Cy5 is infused into the mPFC 12–16 h before behavioral testing. Illumination of 515 nm is applied for the first 2 min of the Y-maze test before the receptor is activated via 385 nm illumination for the remaining 4 min.

(H) Summary of Y-maze behavioral analysis. Activation of SNAP-mGluR2 reduced alterations, but no effect is seen in mice that did not receive the SNAP-mGluR2 AAV or BGAG$_{12,400}$-Cy5. *Statistical significance (paired t test versus first 2 min of assay, p = 0.0001 for 10 mW/mm^2 and p = 0.009 for 0.1 mW/mm^2).

Error bars show SEM. See also Figure S5.

these experiments were unable to answer an important question: namely, whether mGluR2 agonists influence working memory through acute, local signaling events within the mPFC or through long-lasting effects on synaptic strength and circuit function. We have recently shown that ^{2x}BGAG$_{12}$-mediated activation of SNAP-mGluR2 in Grm2-positive cells in the mPFC mimics this effect to impair working memory performance in a Y-maze assay (Acosta-Ruiz et al., 2020). In brief, mice were observed for 5 min and those with photo-activated SNAP-mGluR2 showed impaired performance compared with control mice that either did not receive the SNAP-mGluR2 AAV or the ^{2x}BGAG$_{12}$ PORTL (Acosta-Ruiz et al., 2020). However, in these prior experiments we photo-activated SNAP-mGluR2 before placement of the mouse in the Y-maze since we were unsure of both the timing of the onset of effect and the ability of ^{2x}BGAG$_{12}$ to produce sufficiently rapid agonism following optical fiber-based illumination *in vivo*. We thus sought to take advantage of the improved efficiency and speed of the azobenzene-400 core to test if SNAP-mGluR2 photo-activation can produce rapid effects in the Y-maze assay. We injected Cre-dependent AAV-SNAP-mGluR2 into the mPFC of Grm2-Cre mice while also implanting a dual fiber optic-cannula for *in vivo* optical control (Figure 5G). Infusion of BGAG$_{12,400}$-Cy5

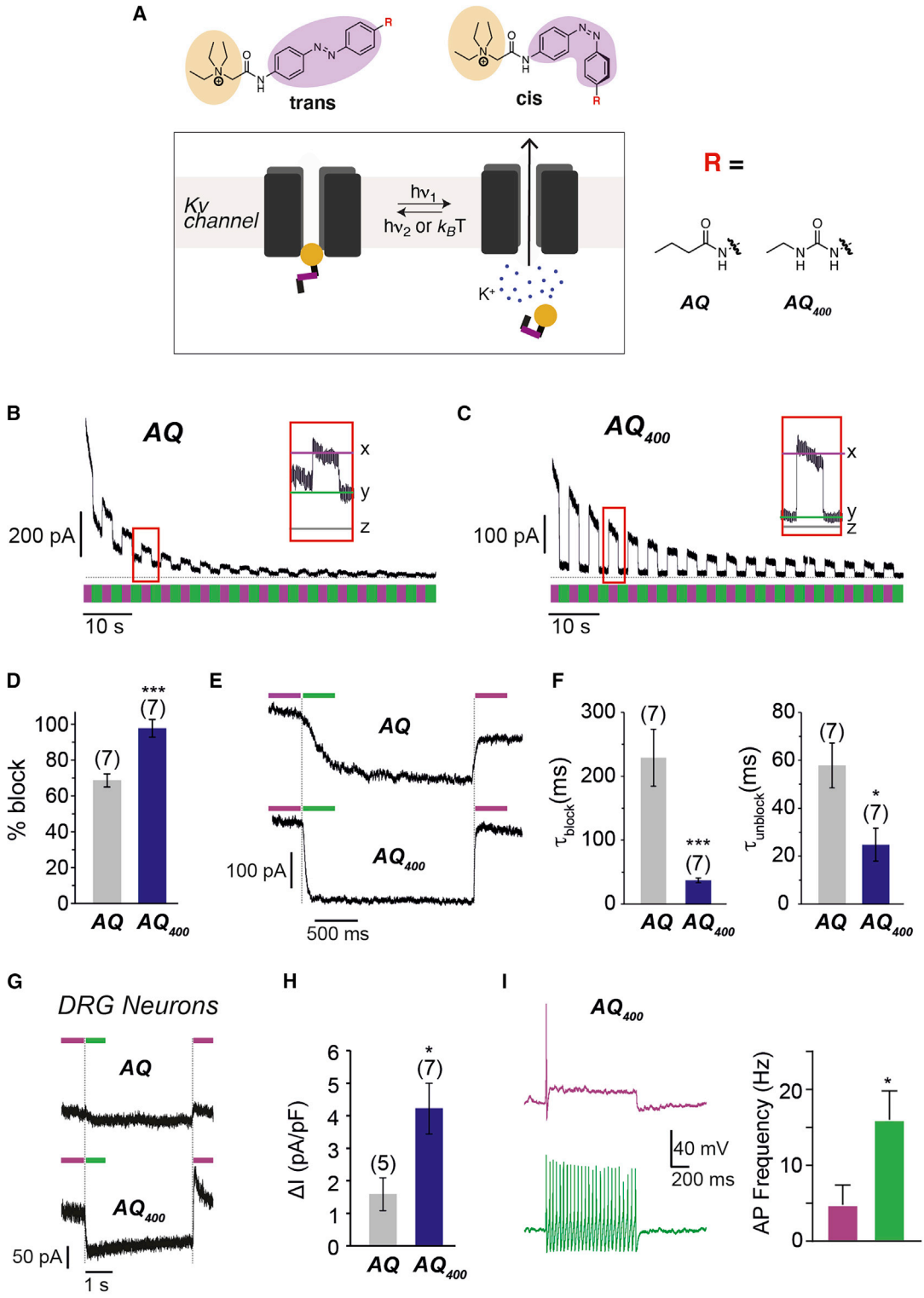

Figure 6. The azobenzene-400 core enhances efficiency of potassium channel photopharmacology

(A) Chemical structures (top) of a voltage-gated potassium channel (K_v) pore blocker bearing a quaternary ammonium (orange) and an azobenzene (purple) and schematic (bottom) showing principle of optical control of a K_v channel by AQ or AQ_{400}.

(B and C) Representative HEK293T whole-cell patch-clamp electrophysiology traces showing AQ-mediated (B) or AQ_{400}-mediated (C) photo-blocking of $K_v1.1$ by 505 nm illumination (green) and photo-unblocking by 385 nm illumination (magenta).

(D) Summary bar graph of efficiency of optical control of $K_v1.1$ for AQ versus AQ_{400}. ***Statistical significance (unpaired t test, $p < 0.001$). Error bars show SEM.

(legend continued on next page)

was performed 12–16 h before behavioral testing to label receptors (Figure S5A). To test if the rapid kinetics of SNAP-mGluR2 activation by this PORTL could produce an immediate effect on working memory performance, mice were placed in the Y-maze test and observed for 2 min before receptor activation via three 2 s pulses of 385 nm illumination at either 0.1 or 10 mW/mm^2 intensity every 2 min for 4 min (Figure 5G). Control mice received either a Cre-dependent AAV GFP virus and infusion of BGAG$_{12,400}$-Cy5, or received Cre-dependent AAV-SNAP-mGluR2 but no BGAG$_{12,400}$-Cy5 infusion. We found that photo-activation of SNAP-mGluR2 by BGAG$_{12,400}$-Cy5 at 10 mW/mm^2 led to a rapid deficit in working memory performance that was observable within 2 min and further worsened as the receptor remained active over the duration of the assay (4 min) (Figures 5H and S5B). While activation at 0.1 mW/mm^2 inhibited performance less drastically, the percent correct alternations were also reduced after 4 min of activation (Figure 5H), suggesting that this dim illumination is suitable for *in vivo* PORTL studies, especially when longer observation windows are used. Importantly, both receptor-only and PORTL-only controls showed no deficits in Y-maze performance (Figure 5H), and all groups showed a similar number of arm entries throughout the test (Figures S5C and S5D).

Together these results indicate that activation of SNAP-mGluR2 in the mPFC via the improved BGAG$_{12,400}$-Cy5 PORTL can produce rapid behavioral effects on a shorter time scale and with a lower light intensity *in vivo* than previously reported. The rapid onset and high efficiency of BGAG$_{12,400}$-Cy5 allowed us to find that targeted SNAP-mGluR2 activation in the subset of cortical neurons that natively express mGluR2 produces rapid deficits in the Y-maze. Not only does this experiment reproduce the effects seen with global treatment with mGluR2/3 agonists (Aultman and Moghaddam, 2001; Schlumberger et al., 2009), but, along with our previous finding that the behavioral deficit is reversible (Acosta-Ruiz et al., 2020), it indicates that mGluR2-mediated control of working memory proceeds through acute, local signaling events within the mPFC without the need for long-lasting effects on synaptic strength or circuit-level changes. More generally, these results demonstrate the ability of PORTL-based strategies to enable studies of the effects of GPCR activation in discrete brain regions and cell types during freely moving behaviors.

Generalizability of azobenzene-400 core: Enhanced efficiency of potassium channel photopharmacology

Having found that the azobenzene-400 core enhances the efficiency and kinetics of mGluR-targeting PORTLs across biological systems (Figures 2, 3, and 5), we asked if these improvements can be generalized to other photopharmacological tools. We turned to PCLs, which work as soluble ligands whose function can be controlled by toggling between relaxed *trans* and excited *cis* states (Broichhagen et al., 2015c). One major advantage of PCLs is that they can be used to target native proteins without the need for genetic manipulations (Hull et al., 2018; Paoletti et al., 2019). We focused on a well-established family of PCLs based on the voltage-gated potassium channel (K_v) pore blocker, tetraethyl ammonium (TEA). TEA can bind and block ion conduction either at an external binding site or at the internal entrance to the selectivity filter (Armstrong, 1971; Choi et al., 1993; Heginbotham and MacKinnon, 1992). Endowment of TEA with an azobenzene has been shown to produce a family of intracellular light-sensitive pore blockers of K_v channels that can be used in a variety of contexts, including optical control of nociception and vision restoration (Banghart et al., 2009; Fehrentz et al., 2012; Fortin et al., 2008; Laprell et al., 2017; Mourot et al., 2012; Polosukhina et al., 2012; Tochitsky et al., 2014). A simple version of this compound bearing an aliphatic tail (Banghart et al., 2009) is here referred to as AQ (azobenzene-quaternary ammonium) (Figure 6A). We synthesized both AQ and a version based on the azobenzene-400 core, termed AQ$_{400}$ (Figure 6A; STAR Methods, scheme 6) commencing with 4,4′-azodianiline, which was peptide-coupled to betaine to produce a common precursor for AQ and AQ$_{400}$. Reacting the remaining aniline with butyryl chloride or ethyl isocyanate yielded AQ and AQ$_{400}$, respectively. Both compounds produced expected absorbance spectra (Figures S6A and S6B) and, as anticipated, AQ$_{400}$ showed a red-shift of ~11 nm and an increase in absorbance in PBS ($\varepsilon_{360\ nm}$ [AQ] = 19,800 M^{-1} cm^{-1}; $\varepsilon_{371\ nm}$ [AQ$_{400}$] = 23,400 M^{-1} cm^{-1}). AQ$_{400}$ also showed enhanced photoswitching kinetics compared with AQ (Figures S6C–S6E) and accelerated thermal relaxation that was still on the minute time scale (τ = 43 s). We also recorded ^{1}H NMR spectra in the dark and under illumination of both AQs in D_2O, and found that AQ$_{400}$ outperforms AQ with higher *cis* content under 385 nm (91.9% versus 89.8%) and 405 nm (85.3% versus 75.5%) light, and higher *trans* content under 525 nm (92.8% versus 84.6%) light (Figure S6F).

We tested both PCLs delivered intracellularly via the patch pipette in HEK293T cells transfected with K_v1.1, a shaker-type K_v channel. As shown in Figures 6B and 6C, alternating illumination between 500 and 380 nm reversibly blocks and unblocks the current elicited at −20 mV, for both compounds but the efficiency of block was higher for AQ$_{400}$ than AQ (97.8% ± 5.0% versus 68.7% ± 3.6% block efficiency; Figure 6D) at 100 μM. As expected with a quaternary ammonium pore blocker (Zhou et al., 2001), AQ and AQ$_{400}$ were also capable of light-dependent block of voltage-dependent slow inactivation (Figure S6G). Since AQ is a blocker that merely needs to bind a defined pore-lining

(E and F) AQ$_{400}$ shows enhanced kinetics of K_v1.1 photo-block as observed in representative whole-cell patch-clamp traces (E) and summary bar graphs for channel blocking and unblocking (F). *Statistical significance (unpaired t test, $p < 0.001$ for τ_{Block} and $p < 0.05$ for $\tau_{Unblock}$). Data were assessed by analyzing the first ten blocking events per cell. Error bars show SEM.

(G and H) AQ$_{400}$ shows enhanced photocurrents in mouse DRG neurons compared with AQ. Whole-cell patch-clamp traces obtained at −40 mV (G) reveal a larger light-gated current (ΔI [I_{380nm}–I_{505nm}]) for AQ$_{400}$ (H). *Statistical significance (t test, $p < 0.05$). The numbers of cells tested are shown in parentheses. Error bars show SEM.

(I) Representative traces (left) of action potential (AP) firing following 25 pA current injection under illumination with 380 nm (magenta) or 505 nm (green) light in DRG neurons treated with 100 μM AQ$_{400}$. Right, summary bar graph showing reduced AP firing in 380 nm light in data from n = 6 cells. *Statistical significance (t test, $p < 0.05$). Error bars show SEM.

See also Figure S6.

site, the kinetics of block and unblock of the current may be a relatively direct reflection of the kinetics of photoconversion between *cis* and *trans* states, although unbinding from the pore may also contribute to this timing. Detailed analysis of the kinetics of the light responses demonstrate markedly accelerated block (τ_{on} = 37 ± 4 versus 229 ± 44 ms) and unblock (τ_{off} = 25 ± 7 versus 58 ± 9 ms) by AQ_{400} compared with AQ (Figures 6E and 6F).

To validate AQ_{400} as a tool to provide optical control of native potassium channels and their physiological effects, we investigated the light responses to AQ and AQ_{400} in small and medium-sized DRG neurons. We first characterized the photocurrent generated by the intracellular application of 100 μM of either compound and found that alternating illumination between 500 and 380 nm led to a rapid, reversible, and reproducible photocurrent for both compounds (Figure 6G), with a voltage-sensitivity consistent with specific blockade of potassium conductance (Figure S6H). As was observed in HEK293T cells, at −40 mV, the AQ_{400}-induced photocurrent was significantly larger (~3-fold increase) (Figure 6H). Furthermore, the blocking and unblocking kinetics observed were accelerated for AQ_{400} (τ_{Block} = 126 ± 17 versus 245 ± 52 ms and $\tau_{Unblock}$ = 26 ± 4 versus 130 ± 13 ms) (Figure S6I). These results indicate that in a native context, AQ_{400} presents similar advantages to the ones observed *in vitro.* We also tested the ability of AQ_{400} to modify action potential firing in response to current injection, where we found 380 nm light illumination substantially reduced neuronal excitability (Figure 6J) and that this reduced excitability can be maintained in the dark for extended periods due to the bistability of the photoswitch (Figure S6J).

Together these results indicate that replacement of the azobenzene core by azobenzene-400 enhances the efficiency and speed of photoswitchable pore block and indicates that the azobenzene tuning strategy reported here is broadly applicable across modes of photopharmacology.

DISCUSSION

Optical manipulation is a powerful, emerging approach for dissecting the cellular and circuit-level mechanisms of membrane signaling proteins, especially GPCRs (Abreu and Levitz, 2020; Spangler and Bruchas, 2017). Among the numerous approaches to optical manipulation that have been reported, tethered photopharmacology offers a particularly precise means of targeting specific proteins with spatial, temporal, and genetic precision. Here, we expand this toolset by fine-tuning the photoswitchable azobenzene core of a PORTL to produce optical control of signaling by mGluR2, mGluR5 and mGluR1 with the highest efficiency reported to date and straightforward application in tissue and *in vivo*. We show that the azobenzene-400 core can enable maximal *trans* to *cis* photo-activation at 385 nm with almost no drop in efficiency at 405 nm, where tissue penetration is optimal and laser lines are widely available. Critically, we show that the azobenzene-400 core is of broad use since it also enhances optical control of potassium channels via an AQ PCL. As demonstrated in DRG neurons, AQ_{400} offers a powerful means of optically controlling native potassium channels through delivery via a patch pipette, a potentially powerful strategy for spatiotemporal analysis of channel contributions to excitability, dendritic integration, or axon conduction. It is worth noting that AQ-based tethered compounds have been reported for a range of potassium channels (Banghart et al., 2004; Fortin et al., 2011; Sandoz et al., 2012), suggesting that incorporation of azobenzene-400 is likely to be able to enhance this broad family of tools. Furthermore, other existing tethered photoswitchable compounds, including those for ionotropic glutamate receptors (Volgraf et al., 2006), P2X receptor (Lemoine et al., 2013), dopamine receptors (Donthamsetti et al., 2017), $GABA_A$ receptors (Lin et al., 2015), MEK (Tsai et al., 2015), and carbonic anhydrase II (DuBay et al., 2018), should also accommodate the reported azobenzene modification and would be expected to show improved performance. In addition, photopharmacological compounds that target intracellular sites may benefit from the azobenzene-400 core to become more efficient under 405 nm of light, including recently reported photoswitchable microtubule inhibitors (Muller-Deku et al., 2020) or PHOTACs (Reynders et al., 2020).

A major question emerging from this work is: how does the urea substitution improve photoswitching of azobenzene-400 compounds? The initial decision to replace the amide linkage stemmed from the goal of red-shifting the absorption spectra of $BGAG_{12}$ (as has previously been done with modification to the azobenzene 4′-position (Broichhagen et al., 2015b; Kienzler et al., 2013; Mourot et al., 2011) and the desire to design compounds with available precursors. Notably, red-shifting azobenzene photoswitching wavelengths into the visible with long thermal half-lives has previously been obtained by using tetra *ortho*-fluoro (Bleger et al., 2012), tetra *ortho*-chloro (Rullo et al., 2014), or tetra *ortho*-methoxy azobenzenes (Samanta et al., 2013). Here, based on Hammett constants for tuning azobenzenes (Runtsch et al., 2015), we aimed to install a chemical moiety that exhibits a negative Hammett parameter (Hansch et al., 1991) in the para position to induce a subtle change (*cf.* amide: σ_p = 0.00). Importantly, our approach does not substantially alter the geometry or size of the photoswitch moiety, limiting the chance of steric issues that disrupt binding to targets. By synthesizing a small library to explore this on the azobenzene scaffold, we found N′-alkylated urea (σ_p = −0.26) to serve our needs by producing a much smaller shift than previously reported with mono- (σ_p = −0.70) and bis-alkylated amines (σ_p = −0.61), which produce larger red-shifts (~60 nm) and lack bistability (Broichhagen et al., 2014, 2015b; Kienzler et al., 2013; Mourot et al., 2011; Stawski et al., 2012). We initially determined extinction coefficients and measured photoswitching kinetics in DMSO to decide on the most promising congener before producing PORTLs (i.e., $BGAG_{400}$) and PCLs (i.e., AQ_{400}). However, the increased light absorbance and photoswitching kinetics alone likely do not explain the enhanced light-induced effects seen with these compounds. We thus assessed the percent *cis* and percent *trans* in the maximum photostationary states for AQ and AQ_{400} by ^{1}H NMR and found a higher *cis* occupancy under 385 and 405 nm and higher *trans* occupancy under 525 nm light for AQ_{400} over AQ (Figure S6F). It is reasonable to speculate that the combination of increased maximal *cis* and *trans* occupancy, increased extinction coefficient and accelerated kinetics, are able to explain the enhanced efficiency of photoswitching for both $BGAG_{12,400}$ PORTLs and the AQ_{400} PCL but further photophysical characterization is required. To further understand the enhanced switching

efficiency, we determined quantum yields (Φ) for photoswitches (Stranius and Borjesson, 2017) **1** and **8**, as well as AQ and AQ_{400} (Table S1; Figure PA1–8 in the supplemental information). In brief, $\Phi_{trans\text{-}to\text{-}cis}$ values were slightly higher for amide scaffolds, while $\Phi_{cis\text{-}to\text{-}trans}$ values were substantially higher for the urea congeners. Increased ON kinetics are, thus, likely due to the increase in extinction coefficient (i.e., light absorption), especially under low light intensities, while the enhanced OFF kinetics may be explained by enhanced $\Phi_{cis\text{-}to\text{-}trans}$.

It is worth mentioning that two previous studies used a urea-amide-conjugated azobenzene for a tethered ligand for a nicotinic acetylcholine receptor (Tochitsky et al., 2012) and a photochromic negative allosteric modulator for mGluR5 (Gomez-Santacana et al., 2017), but comparisons with a bis-amide linkage were not performed. Supporting our findings in a different photophysical system, the Raines laboratory has investigated the use of amide versus urea moieties for the development of fluorogenic dyes and found that the cross-conjugated urea on a rhodamine scaffold leads to a small 3 nm red-shift, and a substantial 3-fold increase in brightness over its amide counterpart (Lavis et al., 2006). Importantly, modification to the azobenzene core also has the potential to alter the pharmacological properties of the PORTL by introducing stabilizing or de-stabilizing interactions between the PORTL and the target protein, especially given the close proximity between the azobenzene core and the pharmacophore. Such interactions may contribute to the enhanced photoswitching seen with $BGAG_{12,400}$, including the case of the mGluR2-1 chimera where a particularly striking improvement compared with $BGAG_{12}$ or $^{2x}BGAG_{12}$ is observed, but future work will be needed to elucidate the structural basis of interactions between these photopharmacological ligands and their targets.

To date, the biggest challenges in producing useful photopharmacological tools has been the initial design of a light-sensitive pharmacophore and, in the case of tethered photopharmacology, the installation of a parent pharmacophore into a tethered context in a way that maximizes photoswitch efficiency. In the case of azobenzene-glutamate compounds, previous work has thoroughly established that 4′ substituted glutamate with a short linker to the azobenzene is well tolerated (Levitz et al., 2013), providing a scaffold for optimization. In this and other recent studies, we have produced a set of strategies for optimizing PORTL photoswitching following the identification of a photoswitchable core. This includes optimization of PORTL length (Broichhagen et al., 2015a; Levitz et al., 2017), optimization of the choice and location of self-labeling tags (Acosta-Ruiz et al., 2020), introduction of variable numbers of branches at different branch points (Acosta-Ruiz et al., 2020), and, in this study, azobenzene tuning. It is worth noting that the parent PCL to BGAG, AG_{12} shows very modest photo-agonism of mGluR2 (<20% versus 1 mM glutamate) at 0.1 mM concentration (Broichhagen et al., 2015a), but the aforementioned modifications enable PORTLs with near-complete optical control. This indicates that only modestly effective PCLs can be harnessed to produce powerful PORTLs through both an increase in local concentration and further PORTL optimization. Notably, even after many previous rounds of optimization, we find in this study that further mGluR PORTL design space is available to explore. Given the nearly unlimited chemical possibilities to introduce or remove functional groups to alter photoswitching properties, linker lengths and identity, and glutamate derivatization, we foresee further prospects for the continued enhancement of mGluR-targeting PORTL molecules. More generally, future work across membrane protein targets and pharmacological modes (i.e., antagonists and allosteric modulators) will be needed to further establish an engineering pipeline for developing PORTLs and to produce a broader toolset beyond mGluRs.

Finally, it is worth considering precisely what types of experiments can be done to harness the power of efficient PORTLs for membrane receptors. We have clustered the types of experiments that can be done into five non-mutually exclusive classes: (1) the high temporal resolution of PORTLs can be used for detailed studies of the kinetics of receptor activation and deactivation and associated downstream signaling time scales. (2) The ability to target light enables subcellular confinement of receptor activation to probe signal spreading dynamics within cells. (3) Since PORTLs use full-length receptors, incorporation of receptor variants or mutations can be used to study the role of specific residues, domains, or post-translational modifications in a physiological context without the need for genetic modifications. (4) Dye-conjugated PORTLs can enable dual control and imaging of receptor populations to understand the relationship between receptor activation and localization, including receptor mobility on the cell surface or trafficking to different intracellular compartments. (5) Targeting of activation (or antagonism) of specific receptor subtypes in intact tissue or *in vivo* to probe the role of specific receptor subpopulations in physiological processes, including behavior. Importantly, strategies are emerging for targeting native receptors with PORTLs (Donthamsetti et al., 2019; Farrants et al., 2018), which should enhance the power of such experiments while motivating further PORTL engineering. Together, the further iterative optimization and expansion of the PORTL toolset described here, combined with thoughtful application, should enable this technique to greatly contribute to our understanding of membrane protein signaling in biology.

SIGNIFICANCE

Photopharmacology describes the implementation of molecular photoswitches to endow light sensitivity to small-molecule drugs (i.e., agonists, antagonists, or allosteric modulators) to manipulate biological function. Classically, azobenzenes have served as photoswitchable scaffolds that are reversibly toggled between *trans* and *cis* states with UV and green light, respectively. To overcome the need of toxic UV light and the limitations of slow and incomplete photoconversion, we fine-tuned the structure of azobenzenes via incorporation of a urea moiety. By tethering glutamate-based versions of these modified azobenzene switches to neuromodulatory metabotropic glutamate receptors (mGluRs), we enable highly efficient, rapid control of receptor signaling with brief exposures to non-toxic light. We explore this system across the family of mGluRs and show the generalizability of this approach by expanding to photoswitchable pore blockers of voltage-gated potassium ion channels. We showcase the ability of this family of tethered photoswitchable ligands to control receptor and channel function in cultured neurons and *ex vivo* in brain slices.

Finally, we find that targeted photo-activation of mGluR2 in a subset of neurons of the medial prefrontal cortex enables acute manipulation of working memory in freely moving mice. We anticipate the engineering principles and tools reported in this study to contribute to ongoing attempts to unravel the complex interplay between molecular and systems-level neural function to enable a better understanding of the role of specific signaling proteins in health and disease.

STAR★METHODS

Detailed methods are provided in the online version of this paper and include the following:

- KEY RESOURCES TABLE
- RESOURCE AVAILABILITY
  - Lead contact
  - Materials availability
  - Data and code availability
- EXPERIMENTAL MODEL AND SUBJECT DETAILS
- METHOD DETAILS
  - Chemistry
  - Chromatography including high resolution mass spectrometry
  - NMR spectroscopy
  - Chemical synthesis
  - UV/Vis spectroscopy
  - Photostationary state measurements via NMR
  - Fluorescence spectroscopy *in vitro*
  - Quantum yield measurements
  - Molecular cloning, cell culture, and gene expression
  - HEK 293T and DRG electrophysiology
  - Calcium imaging
  - Viral expression and *in vivo* PORTL labeling
  - Acute brain slice electrophysiology
  - Y-Maze behavior
- QUANTIFICATION AND STATISTICAL ANALYSIS
  - Additional resources

SUPPLEMENTAL INFORMATION

Supplemental information can be found online at https://doi.org/10.1016/j.chembiol.2021.02.020.

ACKNOWLEDGMENTS

The authors thank Cornelia Ulrich and Sebastian Fabritz for mass spectrometry, Kai Johnsson (all MPIMR) for constant support, Corentin Charbonnier for *in vitro* measurements, and Peter Schmieder for NMR (both FMP). J.L. is supported by an R35 grant (R35 GM124731) from NIGMS and the Rohr Family Research Scholar Award. C.L. is supported by grants from NIMH, the One Mind Institute, the Rita Allen Foundation, and the Klingenstein-Simons Foundation Fund. V.A.G. is supported by an NIH F31 pre-doctoral training grant (1 F31 MH123130-01A1). G.S. is supported by the Fondation pour la Recherche Médicale (FRM DEQ20170336753), the Agence Nationale de la Recherche (ANR-17-CE18-0001 and ANR-17-ERC2-0023; ANR-11-LABX-0015-01), and S.H. is supported by Ville de Nice and UCA (Université Côte d'Azur).

AUTHOR CONTRIBUTIONS

J.L. and J.B. conceived and supervised the study. J.B. designed, and B.M., D.Y., and J.B. synthesized and characterized chemical compounds. J.L., V.A.G., A.A.-R., H.M., and C.L. designed and performed mGluR electrophysiology, imaging, and behavioral experiments. G.S., S.H., and A.L.-W. designed and performed Kv channel electrophysiology experiments. J.M. and K.B. performed quantum yield measurements. J.L. and J.B. wrote the manuscript with input from all authors.

DECLARATION OF INTERESTS

J.B. is a consultant for Vedere Bio II, Inc., and J.B. and J.L. are co-inventors on a filed provisional patent application on branched PORTLs.

Received: September 30, 2020
Revised: December 23, 2020
Accepted: February 23, 2021
Published: March 17, 2021

REFERENCES

Abreu, N., and Levitz, J. (2020). Optogenetic techniques for manipulating and sensing G protein-coupled receptor signaling. Methods Mol. Biol. *2173*, 21–51.

Acosta-Ruiz, A., Gutzeit, V.A., Skelly, M.J., Meadows, S., Lee, J., Parekh, P., Orr, A.G., Liston, C., Pleil, K.E., Broichhagen, J., et al. (2020). Branched photoswitchable tethered ligands enable ultra-efficient optical control and detection of G protein-coupled receptors in vivo. Neuron *105*, 446–463.e13.

Armstrong, C.M. (1971). Interaction of tetraethylammonium ion derivatives with the potassium channels of giant axons. J. Gen. Physiol. *58*, 413–437.

Aultman, J.M., and Moghaddam, B. (2001). Distinct contributions of glutamate and dopamine receptors to temporal aspects of rodent working memory using a clinically relevant task. Psychopharmacology (Berl) *153*, 353–364.

Banghart, M., Borges, K., Isacoff, E., Trauner, D., and Kramer, R.H. (2004). Light-activated ion channels for remote control of neuronal firing. Nat. Neurosci. *7*, 1381–1386.

Banghart, M.R., Mourot, A., Fortin, D.L., Yao, J.Z., Kramer, R.H., and Trauner, D. (2009). Photochromic blockers of voltage-gated potassium channels. Angew. Chem. Int. Ed. *48*, 9097–9101.

Banghart, M.R., and Trauner, D. (2013). A 1H NMR assay for measuring the photostationary States of photoswitchable ligands. Methods Mol. Biol. *995*, 107–120.

Beharry, A.A., and Woolley, G.A. (2011). Azobenzene photoswitches for biomolecules. Chem. Soc. Rev. *40*, 4422–4437.

Berry, M.H., Holt, A., Levitz, J., Broichhagen, J., Gaub, B.M., Visel, M., Stanley, C., Aghi, K., Kim, Y.J., Cao, K., et al. (2017). Restoration of patterned vision with an engineered photoactivatable G protein-coupled receptor. Nat. Commun. *8*, 1862.

Bleger, D., Schwarz, J., Brouwer, A.M., and Hecht, S. (2012). o-Fluoroazobenzenes as readily synthesized photoswitches offering nearly quantitative two-way isomerization with visible light. J. Am. Chem. Soc. *134*, 20597–20600.

Bourne, J.N., and Harris, K.M. (2008). Balancing structure and function at hippocampal dendritic spines. Annu. Rev. Neurosci. *31*, 47–67.

Broichhagen, J., Damijonaitis, A., Levitz, J., Sokol, K.R., Leippe, P., Konrad, D., Isacoff, E.Y., and Trauner, D. (2015a). Orthogonal optical control of a G protein-coupled receptor with a SNAP-tethered photochromic ligand. ACS Cent. Sci. *1*, 383–393.

Broichhagen, J., Frank, J.A., Johnston, N.R., Mitchell, R.K., Smid, K., Marchetti, P., Bugliani, M., Rutter, G.A., Trauner, D., and Hodson, D.J. (2015b). A red-shifted photochromic sulfonylurea for the remote control of pancreatic beta cell function. Chem. Commun. (Camb) *51*, 6018–6021.

Broichhagen, J., Frank, J.A., and Trauner, D. (2015c). A roadmap to success in photopharmacology. Acc. Chem. Res. *48*, 1947–1960.

Broichhagen, J., Schonberger, M., Cork, S.C., Frank, J.A., Marchetti, P., Bugliani, M., Shapiro, A.M., Trapp, S., Rutter, G.A., Hodson, D.J., et al. (2014). Optical control of insulin release using a photoswitchable sulfonylurea. Nat. Commun. *5*, 5116.

Caporale, N., Kolstad, K.D., Lee, T., Tochitsky, I., Dalkara, D., Trauner, D., Kramer, R., Dan, Y., Isacoff, E.Y., and Flannery, J.G. (2011). LiGluR restores visual responses in rodent models of inherited blindness. Mol. Ther. *19*, 1212–1219.

Carroll, E.C., Berlin, S., Levitz, J., Kienzler, M.A., Yuan, Z., Madsen, D., Larsen, D.S., and Isacoff, E.Y. (2015). Two-photon brightness of azobenzene photoswitches designed for glutamate receptor optogenetics. Proc. Natl. Acad. Sci. U S A *112*, E776–E785.

Chen, S., Kadakia, F., and Davidson, S. (2020). Group II metabotropic glutamate receptor expressing neurons in anterior cingulate cortex become sensitized after inflammatory and neuropathic pain. Mol. Pain *16*, 1744806920915339.

Chen, T.W., Wardill, T.J., Sun, Y., Pulver, S.R., Renninger, S.L., Baohan, A., Schreiter, E.R., Kerr, R.A., Orger, M.B., Jayaraman, V., et al. (2013). Ultrasensitive fluorescent proteins for imaging neuronal activity. Nature *499*, 295–300.

Choi, K.L., Mossman, C., Aube, J., and Yellen, G. (1993). The internal quaternary ammonium receptor site of Shaker potassium channels. Neuron *10*, 533–541.

Davenport, C.M., Rajappa, R., Katchan, L., Taylor, C.R., Tsai, M.C., Smith, C.M., de Jong, J.W., Arnold, D.B., Lammel, S., and Kramer, R.H. (2021). Relocation of an extrasynaptic $GABA_A$ receptor to inhibitory synapses freezes excitatory synaptic strength and preserves memory. Neuron *109*, 123–134.e4.

Donthamsetti, P.C., Broichhagen, J., Vyklicky, V., Stanley, C., Fu, Z., Visel, M., Levitz, J.L., Javitch, J.A., Trauner, D., and Isacoff, E.Y. (2019). Genetically targeted optical control of an endogenous G protein-coupled receptor. J. Am. Chem. Soc. *141*, 11522–11530.

Donthamsetti, P.C., Winter, N., Schonberger, M., Levitz, J., Stanley, C., Javitch, J.A., Isacoff, E.Y., and Trauner, D. (2017). Optical control of dopamine receptors using a photoswitchable tethered inverse agonist. J. Am. Chem. Soc. *139*, 18522–18535.

Dorn, M., Jurk, M., and Schmieder, P. (2012). Blue news update: BODIPY-GTP binds to the blue-light receptor YtvA while GTP does not. PLoS One *7*, e29201.

Doumazane, E., Scholler, P., Zwier, J.M., Trinquet, E., Rondard, P., and Pin, J.P. (2011). A new approach to analyze cell surface protein complexes reveals specific heterodimeric metabotropic glutamate receptors. FASEB J. *25*, 66–77.

DuBay, K.H., Iwan, K., Osorio-Planes, L., Geissler, P.L., Groll, M., Trauner, D., and Broichhagen, J. (2018). A predictive approach for the optical control of carbonic anhydrase II activity. ACS Chem. Biol. *13*, 793–800.

Durand-de Cuttoli, R., Mondoloni, S., Marti, F., Lemoine, D., Nguyen, C., Naude, J., d'Izarny-Gargas, T., Pons, S., Maskos, U., Trauner, D., et al. (2018). Manipulating midbrain dopamine neurons and reward-related behaviors with light-controllable nicotinic acetylcholine receptors. ife *7*, e37487.

Farrants, H., Gutzeit, V.A., Acosta-Ruiz, A., Trauner, D., Johnsson, K., Levitz, J., and Broichhagen, J. (2018). SNAP-tagged nanobodies enable reversible optical control of a G protein-coupled receptor via a remotely tethered photoswitchable ligand. ACS Chem. Biol. *13*, 2682–2688.

Fehrentz, T., Kuttruff, C.A., Huber, F.M., Kienzler, M.A., Mayer, P., and Trauner, D. (2012). Exploring the pharmacology and action spectra of photochromic open-channel blockers. Chembiochem *13*, 1746–1749.

Ferraguti, F., and Shigemoto, R. (2006). Metabotropic glutamate receptors. Cell Tissue Res. *326*, 483–504.

Fortin, D.L., Banghart, M.R., Dunn, T.W., Borges, K., Wagenaar, D.A., Gaudry, Q., Karakossian, M.H., Otis, T.S., Kristan, W.B., Trauner, D., et al. (2008). Photochemical control of endogenous ion channels and cellular excitability. Nat. Methods *5*, 331–338.

Fortin, D.L., Dunn, T.W., Fedorchak, A., Allen, D., Montpetit, R., Banghart, M.R., Trauner, D., Adelman, J.P., and Kramer, R.H. (2011). Optogenetic photochemical control of designer K^+ channels in mammalian neurons. J. Neurophysiol. *106*, 488–496.

Gomez-Santacana, X., Pittolo, S., Rovira, X., Lopez, M., Zussy, C., Dalton, J.A., Faucherre, A., Jopling, C., Pin, J.P., Ciruela, F., et al. (2017). Illuminating phenylazopyridines to photoswitch metabotropic glutamate receptors: from the flask to the animals. ACS Cent. Sci. *3*, 81–91.

Goudet, C., Rovira, X., and Llebaria, A. (2018). Shedding light on metabotropic glutamate receptors using optogenetics and photopharmacology. Curr. Opin. Pharmacol. *38*, 8–15.

Hansch, C., Leo, A., and Taft, R.W. (1991). A survey of Hammett substituent constants and resonance and field parameters. Chem. Rev. *91*, 165–195.

Heginbotham, L., and MacKinnon, R. (1992). The aromatic binding site for tetraethylammonium ion on potassium channels. Neuron *8*, 483–491.

Hull, K., Morstein, J., and Trauner, D. (2018). In vivo photopharmacology. Chem. Rev. *118*, 10710–10747.

Izquierdo-Serra, M., Bautista-Barrufet, A., Trapero, A., Garrido-Charles, A., Diaz-Tahoces, A., Camarero, N., Pittolo, S., Valbuena, S., Perez-Jimenez, A., Gay, M., et al. (2016). Optical control of endogenous receptors and cellular excitability using targeted covalent photoswitches. Nat. Commun. *7*, 12221.

Kawabata, S., Tsutsumi, R., Kohara, A., Yamaguchi, T., Nakanishi, S., and Okada, M. (1996). Control of calcium oscillations by phosphorylation of metabotropic glutamate receptors. Nature *383*, 89–92.

Kienzler, M.A., Reiner, A., Trautman, E., Yoo, S., Trauner, D., and Isacoff, E.Y. (2013). A red-shifted, fast-relaxing azobenzene photoswitch for visible light control of an ionotropic glutamate receptor. J. Am. Chem. Soc. *135*, 17683–17686.

Laprell, L., Tochitsky, I., Kaur, K., Manookin, M.B., Stein, M., Barber, D.M., Schon, C., Michalakis, S., Biel, M., Kramer, R.H., et al. (2017). Photopharmacological control of bipolar cells restores visual function in blind mice. J. Clin. Invest. *127*, 2598–2611.

Lavis, L.D., Chao, T.Y., and Raines, R.T. (2006). Fluorogenic label for biomolecular imaging. ACS Chem. Biol. *1*, 252–260.

Lee, J., Munguba, H., Gutzeit, V.A., Singh, D.R., Kristt, M., Dittman, J.S., and Levitz, J. (2020). Defining the homo- and heterodimerization propensities of metabotropic glutamate receptors. Cell Rep. *31*, 107605.

Leippe, P., Broichhagen, J., Cailliau, K., Mougel, A., Morel, M., Dissous, C., Trauner, D., and Vicogne, J. (2020). Transformation of receptor tyrosine kinases into glutamate receptors and photoreceptors. Angew. Chem. Int. Ed. *59*, 6720–6723.

Leippe, P., Koehler Leman, J., and Trauner, D. (2017). Specificity and speed: tethered photopharmacology. Biochemistry *56*, 5214–5220.

Lemoine, D., Habermacher, C., Martz, A., Mery, P.F., Bouquier, N., Diverchy, F., Taly, A., Rassendren, F., Specht, A., and Grutter, T. (2013). Optical control of an ion channel gate. Proc. Natl. Acad. Sci. U S A *110*, 20813–20818.

Lesage, F., Attali, B., Lazdunski, M., and Barhanin, J. (1992). Developmental expression of voltage-sensitive K^+ channels in mouse skeletal muscle and C2C12 cells. FEBS Lett. *310*, 162–166.

Lester, H.A., Krouse, M.E., Nass, M.M., Wassermann, N.H., and Erlanger, B.F. (1980). A covalently bound photoisomerizable agonist: comparison with reversibly bound agonists at electrophorus electroplaques. J. Gen. Physiol. *75*, 207–232.

Levitz, J., Broichhagen, J., Leippe, P., Konrad, D., Trauner, D., and Isacoff, E.Y. (2017). Dual optical control and mechanistic insights into photoswitchable group II and III metabotropic glutamate receptors. Proc. Natl. Acad. Sci. U S A *114*, E3546–E3554.

Levitz, J., Pantoja, C., Gaub, B., Janovjak, H., Reiner, A., Hoagland, A., Schoppik, D., Kane, B., Stawski, P., Schier, A.F., et al. (2013). Optical control of metabotropic glutamate receptors. Nat. Neurosci. *16*, 507–516.

Levitz, J., Popescu, A.T., Reiner, A., and Isacoff, E.Y. (2016). A toolkit for orthogonal and in vivo optical manipulation of ionotropic glutamate receptors. Front Mol. Neurosci. *9*, 2.

Lin, W.C., Tsai, M.C., Davenport, C.M., Smith, C.M., Veit, J., Wilson, N.M., Adesnik, H., and Kramer, R.H. (2015). A comprehensive optogenetic

pharmacology toolkit for in vivo control of GABA(A) receptors and synaptic inhibition. Neuron *88*, 879–891.

Lujan, R., Nusser, Z., Roberts, J.D., Shigemoto, R., and Somogyi, P. (1996). Perisynaptic location of metabotropic glutamate receptors mGluR1 and mGluR5 on dendrites and dendritic spines in the rat hippocampus. Eur. J. Neurosci. *8*, 1488–1500.

Mourot, A., Fehrentz, T., Le Feuvre, Y., Smith, C.M., Herold, C., Dalkara, D., Nagy, F., Trauner, D., and Kramer, R.H. (2012). Rapid optical control of nociception with an ion-channel photoswitch. Nat. Methods *9*, 396–402.

Mourot, A., Kienzler, M.A., Banghart, M.R., Fehrentz, T., Huber, F.M., Stein, M., Kramer, R.H., and Trauner, D. (2011). Tuning photochromic ion channel blockers. ACS Chem. Neurosci. *2*, 536–543.

Muller-Deku, A., Meiring, J.C.M., Loy, K., Kraus, Y., Heise, C., Bingham, R., Jansen, K.I., Qu, X., Bartolini, F., Kapitein, L.C., et al. (2020). Photoswitchable paclitaxel-based microtubule stabilisers allow optical control over the microtubule cytoskeleton. Nat. Commun. *11*, 4640.

Nicoletti, F., Bockaert, J., Collingridge, G.L., Conn, P.J., Ferraguti, F., Schoepp, D.D., Wroblewski, J.T., and Pin, J.P. (2011). Metabotropic glutamate receptors: from the workbench to the bedside. Neuropharmacology *60*, 1017–1041.

Oh, S.W., Harris, J.A., Ng, L., Winslow, B., Cain, N., Mihalas, S., Wang, Q., Lau, C., Kuan, L., Henry, A.M., et al. (2014). A mesoscale connectome of the mouse brain. Nature *508*, 207–214.

Paoletti, P., Ellis-Davies, G.C.R., and Mourot, A. (2019). Optical control of neuronal ion channels and receptors. Nat. Rev. Neurosci. *20*, 514–532.

Pin, J.P., and Bettler, B. (2016). Organization and functions of mGlu and GABAB receptor complexes. Nature *540*, 60–68.

Polosukhina, A., Litt, J., Tochitsky, I., Nemargut, J., Sychev, Y., De Kouchkovsky, I., Huang, T., Borges, K., Trauner, D., Van Gelder, R.N., et al. (2012). Photochemical restoration of visual responses in blind mice. Neuron *75*, 271–282.

Reiner, A., and Levitz, J. (2018). Glutamatergic signaling in the central nervous system: ionotropic and metabotropic receptors in concert. Neuron *98*, 1080–1098.

Reiner, A., Levitz, J., and Isacoff, E.Y. (2015). Controlling ionotropic and metabotropic glutamate receptors with light: principles and potential. Curr. Opin. Pharmacol. *20*, 135–143.

Reynders, M., Matsuura, B.S., Berouti, M., Simoneschi, D., Marzio, A., Pagano, M., and Trauner, D. (2020). PHOTACs enable optical control of protein degradation. Sci. Adv. *6*, eaay5064.

Richter, F., Scheib, U.S., Mehlhorn, J., Schubert, R., Wietek, J., Gernetzki, O., Hegemann, P., Mathes, T., and Moglich, A. (2015). Upgrading a microplate reader for photobiology and all-optical experiments. Photochem. Photobiol. Sci. *14*, 270–279.

Rullo, A., Reiner, A., Reiter, A., Trauner, D., Isacoff, E.Y., and Woolley, G.A. (2014). Long wavelength optical control of glutamate receptor ion channels using a tetra-ortho-substituted azobenzene derivative. Chem. Commun. (Camb) *50*, 14613–14615.

Runtsch, L.S., Barber, D.M., Mayer, P., Groll, M., Trauner, D., and Broichhagen, J. (2015). Azobenzene-based inhibitors of human carbonic anhydrase II. Beilstein J. Org. Chem. *11*, 1129–1135.

Samanta, S., Babalhavaeji, A., Dong, M.X., and Woolley, G.A. (2013). Photoswitching of ortho-substituted azonium ions by red light in whole blood. Angew. Chem. Int. Ed. *52*, 14127–14130.

Sandoz, G., Levitz, J., Kramer, R.H., and Isacoff, E.Y. (2012). Optical control of endogenous proteins with a photoswitchable conditional subunit reveals a role for TREK1 in GABA(B) signaling. Neuron *74*, 1005–1014.

Schindelin, J., Arganda-Carreras, I., Frise, E., Kaynig, V., Longair, M., Pietzsch, T., Preibisch, S., Rueden, C., Saalfeld, S., Schmid, B., et al. (2012). Fiji: an open-source platform for biological-image analysis. Nat. Methods *9*, 676–682.

Schlumberger, C., Schafer, D., Barberi, C., More, L., Nagel, J., Pietraszek, M., Schmidt, W.J., and Danysz, W. (2009). Effects of a metabotropic glutamate receptor group II agonist LY354740 in animal models of positive schizophrenia symptoms and cognition. Behav. Pharmacol. *20*, 56–66.

Spangler, S.M., and Bruchas, M.R. (2017). Optogenetic approaches for dissecting neuromodulation and GPCR signaling in neural circuits. Curr. Opin. Pharmacol. *32*, 56–70.

Stawski, P., Sumser, M., and Trauner, D. (2012). A photochromic agonist of AMPA receptors. Angew. Chem. Int. Ed. *51*, 5748–5751.

Stranius, K., and Borjesson, K. (2017). Determining the photoisomerization quantum yield of photoswitchable molecules in solution and in the solid state. Sci. Rep. *7*, 41145.

Tochitsky, I., Banghart, M.R., Mourot, A., Yao, J.Z., Gaub, B., Kramer, R.H., and Trauner, D. (2012). Optochemical control of genetically engineered neuronal nicotinic acetylcholine receptors. Nat. Chem. *4*, 105–111.

Tochitsky, I., Polosukhina, A., Degtyar, V.E., Gallerani, N., Smith, C.M., Friedman, A., Van Gelder, R.N., Trauner, D., Kaufer, D., and Kramer, R.H. (2014). Restoring visual function to blind mice with a photoswitch that exploits electrophysiological remodeling of retinal ganglion cells. Neuron *81*, 800–813.

Tsai, Y.H., Essig, S., James, J.R., Lang, K., and Chin, J.W. (2015). Selective, rapid and optically switchable regulation of protein function in live mammalian cells. Nat. Chem. *7*, 554–561.

Ueno, Y., Jose, J., Loudet, A., Perez-Bolivar, C., Anzenbacher, P., Jr., and Burgess, K. (2011). Encapsulated energy-transfer cassettes with extremely well resolved fluorescent outputs. J. Am. Chem. Soc. *133*, 51–55.

Vivaudou, M., Chan, K.W., Sui, J.L., Jan, L.Y., Reuveny, E., and Logothetis, D.E. (1997). Probing the G-protein regulation of GIRK1 and GIRK4, the two subunits of the KACh channel, using functional homomeric mutants. J. Biol. Chem. *272*, 31553–31560.

Volgraf, M., Gorostiza, P., Numano, R., Kramer, R.H., Isacoff, E.Y., and Trauner, D. (2006). Allosteric control of an ionotropic glutamate receptor with an optical switch. Nat. Chem. Biol. *2*, 47–52.

Xue, L., Karpenko, I.A., Hiblot, J., and Johnsson, K. (2015). Imaging and manipulating proteins in live cells through covalent labeling. Nat. Chem. Biol. *11*, 917–923.

Zhou, M., Morais-Cabral, J.H., Mann, S., and MacKinnon, R. (2001). Potassium channel receptor site for the inactivation gate and quaternary amine inhibitors. Nature *411*, 657–661.

STAR★METHODS

KEY RESOURCES TABLE

REAGENT or RESOURCE	SOURCE	IDENTIFIER
Bacterial and virus strains		
AAV9-EF1a-FLEX-SNAPmGluR2-WPRE-hGH	Acosta-Ruiz et al. 2020	N/A
AAV9-pCAG-FLEX-EGFP-WPRE	Oh et al. 2014	Addgene Cat#51502-AAV9
Chemicals, peptides, and recombinant proteins		
DIPEA	Roth	Cat#4105.1
DBU	Roth	Cat#6869.1
DMF	Roth	Cat#5921.1
DMSO	Roth	Cat#7029.1
Formic acid	Merck	Cat#5.33002.0050
TFA	Acros TCI	Cat#139721000 Cat#T0431
TSTU	Roth	Cat#2130.2
HBTU	Roth	Cat#2132.3
MeCN	VWR	Cat#83640.320
(((9*H*-Fluoren-9-yl)methoxy)carbonyl-*D*-glutamic acid	ChemCruz	Cat#sc-485525
Fmoc-Lys-Cy3	Acosta-Ruiz et al. 2020	N/A
Fmoc-Lys-Cy5	Acosta-Ruiz et al. 2020	N/A
THF	VWR	Cat#457071000
XPhos Pd G2	Aldrich	Cat#741825-1g
Cs_2CO_3	Roth	Cat#6873.2
4-iodoaniline	Aldrich	Cat#129364-25g
nitrosobenzene	Aldrich	Cat#N24609-10g
acetyl chloride	Aldrich	Cat#114189-25g
NaH, 60% in mineral oil	Aldrich	Cat#452912-100g
methyl iodide	Aldrich	Cat#67692-100mL
2-azetidinone CAS: 930-21-2	Acros	Cat#930212-1g
2-pyrrolidinone CAS: 616-45-5	TCI	Cat#616455-25g
delta-valerolactam CAS: 675-20-7	TCI	Cat#675207-25g
epsilon-caprolactam CAS: 105-60-2	TCI	Cat#105602-25g
phosgene, 15%	Aldrich	Cat#748684-100mL
methylamine hydrochloride CAS: 593-51-1	Aldrich	Cat#593511-100g
1,1-dimethylurea CAS: 598-94-7	Acros	Cat#598947-5g
1,1,3-trimethylurea CAS: 632-14-4	Alfa Aesar	Cat#632144-1g
1-methyl-2-imidaolidinone CAS: 694-32-6	Acros	Cat#694326-500mg
1,3-dimethylurea CAS: 96-31-1	TCI	Cat#96311-25g
ethylene diamine	Roth	Cat#4218.1
$FmocNHPEG_{12}COOH$	broadpharm	Cat#BP-21632
BG-COOH	Levitz et al. 2017	N/A
$BGAG_{12,400}$	this study	N/A
$^{2x}BGAG_{12,400}$	this study	N/A
$BGAG_{12,400}$-Cy3	this study	N/A
$BGAG_{12,400}$-Cy5	this study	N/A
$BGAG_{12,400}$-Cy3 v2	this study	N/A
$BGAG_{12,400}$-Cy5 v2	this study	N/A
$BGAG_{12}$-Cy5	Acosta-Ruiz et al. 2020	N/A

(*Continued on next page*)

Continued

REAGENT or RESOURCE	SOURCE	IDENTIFIER
$^{2x}BGAG_{12}$	Acosta-Ruiz et al. 2020	N/A
$BGAG_{12}$	Broichhagen et al., 2015a	N/A
4,4'-diamino azobenzene	Acros	Cat#ACRO401580250
butyryl chloride	Aldrich	Cat#236349-50g
ethyl isocyanate	Aldrich	Cat#E33300-5g
NaCl	MilliporeSigma™	Cat#S5886-1KG
HEPES	MilliporeSigma™	Cat#H4034-500G
Na+ ascorbate	MilliporeSigma™	Cat#A7631-100G
Thiourea	MilliporeSigma™	Cat#T8656-100G
Na+ pyruvate	MilliporeSigma™	Cat#P2256-100G
CaCl2.2H2O	MilliporeSigma™	Cat#C3881-500G
NMDG	MilliporeSigma™	Cat#M2004-1KG
K-Gluconate	MilliporeSigma™	Cat#PHR1130-1G
phosphocreatine-Na2	MilliporeSigma™	Cat#P7936-1G
MgATP	MilliporeSigma™	Cat#A9187-500MG
Na2- GTP	MilliporeSigma™	Cat#G8877-25MG
biocytin	MilliporeSigma™	Cat#B4261-250MG
SNAP-Surface Alexa Fluor 546	New England Biolabs	Cat#S9132S
Lipofectamine 2000	Invitrogen	Cat#11668027
Trypsin	Sigma-Aldrich	Cat# T1763
DMEM/F12	Sigma-Aldrich	Cat# 6421
DMEM	Gibco	Cat# 41965-039
FBS	Dutscher	Cat# S1900-500
Penicillin-Streptomycin	Gibco	Cat# 15140-122
Trypsin-EDTA	Gibco	Cat# 25300-054
Glutamine	Gibco	Cat# 25030-081
Dexamethasone	Sigma-Aldrich	Cat# D4902
HEPES	Gibco	Cat# 15630-080
Experimental models: cell lines		
HEK 293T Cells	American Type Culture Collection (ATCC)	Cat#CRL-3216; Cat#CR-11268
Experimental models: organisms/strains		
Mouse: STOCK Tg(Grm2-cre)MR90Gsat/Mmucd Mus musculus	Mutant Mouse Resource & Research Center	MMRRC Cat# 034611-UCD
Oligonucleotides		
Primer SNAP-mGluR2-mGluR1 Fwd1: TCTTCCACCCTGTAAAGATCCCA CACTCCTGCC	This paper	N/A
Primer SNAP-mGluR2-mGluR1 Rev1: GCTCCACTCAAGATACTCCTGAGG CAGCTCAAAG	This paper	N/A
Primer SNAP-mGluR2-mGluR1 Fwd2: GAGCTGCCTCAGGAGTATCTTGAGT GGAGCAACATC	This paper	N/A
Primer SNAP-mGluR2-mGluR1 Rev2: AGGAGTGTGGGATCTTTACAGGG TGGAAGAGCTTTG	This paper	N/A
Recombinant DNA		
SNAP-mGluR2	Doumazane et al., 2011	N/A
GIRK1-F137S	Vivaudou et al., 1997	N/A
SNAP-mGluR2-mGluR5	Acosta-Ruiz et al., 2020	N/A
SNAP-mGluR2-mGluR1	This paper	N/A

(*Continued on next page*)

Continued

REAGENT or RESOURCE	SOURCE	IDENTIFIER
CMV-GCaMP6f	Chen et al., 2013	Addgene Cat#40755
pCIKv1.1	Lesage et al., 1992	N/A
Software and algorithms		
Fiji/ImageJ, v1.8	Schindelin et al., 2012	https://imagej.nih.gov/ij/
Prism	GraphPad	https://graphpad.com
Clampex	Molecular Devices	https://www.moleculardevices.com
Clampfit	Molecular Devices	https://www.moleculardevices.com
Origin	Origin Lab Corporation	https://www.originlab.com/, RRID:SCR_002815
Microsoft Excel	Microsoft Office	https://products.office.com/en-us/excel
Doric Neuroscience Studio	Doric Lenses	http://doriclenses.com/life-sciences/software/955-doric-neuroscience-studio.html
SMART Video Tracking System	Harvard Apparatus	https://www.harvardapparatus.com/smart-video-tracking-system.html
SigmaPlot	Systat Software, inc.	https://systatsoftware.com/products/sigmaplot/
Other		
CoolLED pE4000	CoolLED	https://www.coolled.com/products/pe-4000/
Doric Combined LEDs: 4-LED Model	Doric	LEDC4_385/465/515/625

RESOURCE AVAILABILITY

Lead contact

Further information and requests for resources and reagents should be directed to and will be fulfilled by the lead contacts, Johannes Broichhagen (broichhagen@fmp-berlin.de) or Joshua Levitz (jtl2003@med.cornell.edu).

Materials availability

The availability of Compounds 1-12 and all **BGAG**s generated in this manuscript is subject to approval of use and distribution by lead contacts, Johannes Broichhagen (broichhagen@fmp-berlin.de) or Joshua Levitz (jtl2003@med.cornell.edu).

Data and code availability

The published article includes all datasets/code generated or analyzed during this study.

EXPERIMENTAL MODEL AND SUBJECT DETAILS

HEK 293T cells (authenticated by Bio-Synthesis, Inc. and tested negative for mycoplasma using a kit from Molecular Probes) were cultured in DMEM medium (Gibco) supplemented with 5% fetal bovine serum (FBS) and 1% penicillin/streptomycin (Gibco). Cells were maintained in humidified incubator with 5% CO_2 at 37 °C.

Mice were housed at the animal facilities of Université Cote d'Azur or Weill Cornell Medicine and were maintained on a 12 h light/dark cycle with constant temperature (23–24°C), humidity (45%–50%), and food and water *ad libitum*. All animal use procedures were performed in accordance with Weill Cornell Medicine Institution Animal Care & Use Committee (IACUC) guidelines under approved protocol (2017-0023) at Weill Cornell Medicine or conducted according to national and international guidelines that have been approved by the local ethical committee (CIEPAL NCE) at Université Cote d'Azur.

For DRG cultures, Dorsal Root Ganglion tissues were collected from C57BL/6J adult (>P30) female mice and treated with a mix of 2 mg/ml collagenase type II, 5 mg/ml dispase and 5 mM $CaCl_2$ for ~20 minutes twice.

For behavior experiments, male adult postnatal weeks 8-12 Grm-Cre animals from Mutant Mouse Resource & Research Center (MMRRC) under strain name STOCK Tg (Grm2-cre) MR90Gsat/Mmucd and stock number 034611-UCD were used.

METHOD DETAILS

Chemistry

Schemes for chemical synthesis including numbering are outlined in Methods Schemes 1–4. Solvents for chromatography and reactions were purchased dry over molecular sieves or in HPLC grade. Unless otherwise stated, all other reagents were used without

further purification from commercial sources. Abbreviations: Boc: *tert*-butoxycarbonyl; DIPEA: *N*,*N*-di*iso*propylethylamine; DBU: 1,8-diazabicyclo[5.4.0]undec-7-ene; DCM: dichloromethane; DMF: *N*,*N*-dimethylformamide; DMSO: dimethylsulfoxide; FA: formic acid; Fmoc: fluorenylmethyloxycarbonyl; HBTU: (2-(1*H*-benzotriazol-1-yl)-1,1,3,3-tetramethyluronium hexafluorophosphate; TFA: trifluoroacetic acid; THF: tetrahydrofuran, TSTU: *N*,*N*,*N*′,*N*′-Tetramethyl-*O*-(*N*-succinimidyl)uronium tetrafluoroborate.

Chromatography including high resolution mass spectrometry

LC-MS was performed on i) a Shimadzu MS2020 connected to a Nexera UHPLC system equipped with a Waters ACQUITY UPLC BEH C18 (1.7 μm, 50 × 2.1 mm). Buffer A: 0.1% FA in H_2O Buffer B: acetonitrile. The typical gradient was from 10% B for 0.5 min → gradient to 90% B over 4.5 min → 90% B for 0.5 min → gradient to 99% B over 0.5 min with 1 mL/min flow, or ii) an Agilent 1260 Infinity II LC System equipped with Agilent SB-C18 column (1.8 μm, 2.1 × 50 mm). Buffer A: 0.1% FA in H_2O Buffer B: 0.1% FA acetonitrile. The typical gradient was from 10% B for 0.5 min → gradient to 95% B over 5 min → 95% B for 0.5 min → gradient to 99% B over 1 min with 0.8 mL/min flow. Retention times (t_R) are given in minutes (min).

Preparative RP-HPLC was performed on a Waters e2695 system equipped with a 2998 PDA detector for product collection (at 220, 280, 370 or 460 nm) on a Supelco Ascentis® C18 HPLC Column (5 μm, 250 × 21.2 mm). Buffer A: 0.1% TFA in H_2O Buffer B: acetonitrile. The typical gradient was from 10% B for 5 min → gradient to 90% B over 45 min → 90% B for 5 min → gradient to 99% B over 5 min with 8 mL/min flow.

High resolution mass spectrometry was performed using a Bruker maXis II ETD hyphenated with a Shimadzu Nexera system. The instruments were controlled *via* Brukers otofControl 4.1 and Hystar 4.1 SR2 (4.1.31.1) software. The acquisition rate was set to 3 Hz and the following source parameters were used for positive mode electrospray ionization: End plate offset = 500 V; capillary voltage = 3800 V; nebulizer gas pressure = 45 psi; dry gas flow = 10 L/min; dry temperature = 250 °C. Transfer, quadrupole and collision cell settings are mass range dependent and were fine-adjusted with consideration of the respective analyte's molecular weight. For internal calibration sodium format clusters were used. Samples were desalted *via* fast liquid chromatography. A Supelco Titan™ C18 UHPLC Column, 1.9 μm, 80 Å pore size, 20 × 2.1 mm and a 2 min gradient from 10 to 98% aqueous MeCN with 0.1% FA (H_2O: Carl Roth GmbH + Co. KG ROTISOLV® Ultra LC-MS; MeCN: Merck KGaA LiChrosolv® Acetonitrile hypergrade for LC-MS; FA - Merck KGaA LiChropur® Formic acid 98%-100% for LC-MS) was used for separation. Sample dilution in 10% aqueous ACN (hyper grade) and injection volumes were chosen dependent of the analyte's ionization efficiency. Hence, on-column loadings resulted between 0.25–5.0 ng. Automated internal re-calibration and data analysis of the recorded spectra were performed with Bruker's DataAnalysis 4.4 SR1 software.

NMR spectroscopy

NMR spectra were recorded in deuterated solvents on a Bruker AVANCE III HD 400 equipped with a CryoProbe or on a Bruker AV-III spectrometer (600 MHz) using either a cryogenically cooled 5 mm TCI-triple resonance probe equipped with one-axis self-shielded gradients and calibrated to residual solvent peaks ($^1H/^{13}C$ in ppm): DMSO-d_6 (2.50/39.52), acetone-d_6 (2.05/29.84), $CDCl_3$ (7.26/77.0), D_2O (4.70). Multiplicities are abbreviated as follows: s = singlet, d = doublet, t = triplet, q = quartet, p = pentet, h = hexet, br = broad, m = multiplet. Coupling constants *J* are reported in Hz. Spectra are reported based on appearance, not on theoretical multiplicities derived from structural information.

Chemical synthesis

General procedure A for Buchwald-Hartwig cross coupling:

A flame-dried Schlenk flask was charged with (*E*)-1-(4-iodophenyl)-2-phenyldiazene (3) (1.0 equiv.), Pd XPhos G2 (0.1 equiv.), Cs_2CO_3 (2.4 equiv.), and the corresponding nitrogen-containing coupling partner (1.2 equiv.) dissolved in dry 1,4-dioxanes (144 equiv.) under an argon atmosphere. The reaction mixture was heated to reflux over night, before all volatiles were removed in vacuo, and the resulting residue subjected to either FCC or HPLC purification.

General procedure B for peptide coupling:

A 4 mL vial was charged with 1.0 equiv. of acid and 1.0 equiv. of amine dissolved in DMSO (1 mL / 10 mg) and 4.0 equiv. of DIPEA before 1.1 equiv. of HBTU was added in one portion (for amounts <1 mg of HBTU, stock solutions were prepared). Upon complete conversion according to LCMS (usually ~3 h), 4.0 equiv. of HOAc and 10 vol% water was added to the reaction mixture and the solution was subjected to RP-HPLC. Reaction scales were <100 nmol.

General procedure C for peptide coupling and Fmoc deprotection:

A 4 mL vial was charged with 1.0 equiv. amine dissolved in DMSO (1 mL / 10 mg) and 4.0 equiv. DIPEA. The acid (1.2 equiv.) and HBTU (1.2 equiv.) were added in one portion and the reaction mixture was allowed to stir at r.t. Upon complete conversion according to LCMS (usually ~3 h), 5 vol% of DBU was added and the reaction mixture was stirred for additional 10 minutes, before it was quenched by addition of 10 vol% HOAc and subjected to RP-HPLC. Reaction scales were <100 nmol.

General procedure D for ester saponification and Boc deprotection:

A 15 mL falcon tube was charged with protected compound and MeOH/1 M LiOH (1/1) was added and the resulting suspension was allowed to incubate for 45 min before it was quenched with glacial HOAc (5 vol% of the reaction volume under which the reaction clarified) and subjected to RP-HPLC. The freeze-dried product was put on ice and pre-cooled (4 °C) TFA was added neat. The reaction mixture was vortexed to ensure homogeneity and put back on ice for 15 min before all volatiles were removed under a gentle stream of nitrogen. The residue was taken up in DMF/water (9/1) and subjected to RP-HPLC. Reaction scales were <100 nmol.

NOTE: Azobenzene containing reaction mixtures turned deep red upon addition of TFA.

NOTE: It is feasible to cryo-freeze the ester cleaved product in liquid nitrogen with subsequent lyophilization and reuptake of the residue in neat TFA at 0 °C for quicker synthesis, however, we observed more side products which were not further characterized according to LCMS.

(E)-1-(4-Iodophenyl)-2-phenyldiazene (S3):

A round bottom flask was charged with 2.05 g (9.35 mmol, 1.0 equiv.) of 4-iodoaniline (**S1**) and 1.00 g (9.35 mmol, 1.0 equiv.) of nitrosobenzene (**S2**) dissolved in 100 mL DCM and 10 mL HOAc. The green reaction mixture was stirred for 24 h, turning to a dark brown solution, before it was quenched by addition of sat. aq. $NaHCO_3$ and extracted with DCM (3 x 200 mL). The combined organic layers were washed with water and brine, dried over $MgSO_4$, concentrated *in vacuo*, and the resulting solution subjected to FCC (DCM/hexanes = 1/5) to obtain 1.25 g (4.06 mmol) of the desired compound and an orange powder in 43% yield. Single crystals could be obtained by recrystallization from acetone.

1H NMR (400 MHz, acetone-d6): δ [ppm] = 8.00 (d, J = 8.6 Hz, 2H), 7.94 (dd, J = 7.7, 2.0 Hz, 2H), 7.73 (d, J = 8.6 Hz, 2H), 7.65–7.54 (m, 3H).

13C NMR (101 MHz, acetone-d6) δ [ppm] = 153.3, 152.9, 139.5, 132.5, 130.3, 125.3, 123.7, 98.3.

HRMS (ESI): calc. for $C_{12}H_9IN_2$ $[M+H]^+$: 308.9883, found: 308.9883.

(E)-N-(4-(Phenyldiazenyl)phenyl)acetamide (1):

A round bottom flask was charged with 200 mg (1.01 mmol, 1.0 equiv.) of 4-phenylazoaniline (**4**) dissolved in 10 mL THF and 430 μL DIPEA and cooled to 0 °C. 579 μL of AcCl was added dropwise and the reaction mixture was allowed to warm to r.t. for 1 h before it was quenched by addition of 0.6 mL MeOH and subjected to FCC ($CHCl_3$/acetone = 4/1) to obtain 200 mg (836 μmol) of the desired compound as an orange solid in 82% yield.

1H NMR (400 MHz, acetone-d6): δ [ppm] = 9.47 (s, 1H), 7.97–7.84 (m, 6H), 7.59–7.49 (m, 3H), 2.14 (d, J = 2.4 Hz, 3H).

13C NMR (101 MHz, acetone-d6) δ [ppm] = 169.3, 153.6, 149.1, 143.5, 131.6, 130.1, 124.6, 123.4, 120.0, 119.9, 24.4.

HRMS (ESI): calc. for $C_{14}H_{14}N_3O$ $[M+H]^+$: 240.1131, found: 240.1132.

$\varepsilon_{360\ nm}$ (DMSO) = 15,300 M^{-1} cm^{-1}

(E)-N-Methyl-N-(4-(phenyldiazenyl)phenyl)acetamide (2):

A Schlenk flask was charged with 20.1 mg (502 μmol, 1.2 equiv.) of NaH (60% in mineral oil) and 10 mL dry DMF and cooled to 0 °C. After 15 minutes of stirring, 100 mg (418 μmol, 1.0 equiv.) of azobenzene **1** dissolved in dry DMF was added dropwise, followed by dropwise addition of MeI (64.8 mg, 28 μL, 460 μmol 1.1 equiv.). The reaction mixture was allowed to warm to r.t. for 1 h before it was quenched by addition of aq. sat. NH_4Cl solution and subjected to RP-HPLC to obtain 102 mg (403 μmol) of the desired compound as an orange solid in 96% yield.

1H NMR (400 MHz, DMSO-d6) δ [ppm] = 7.95–7.88 (m, 4H), 7.64–7.55 (m, 5H), 3.24 (s, 3H), 1.93 (s, 3H).

13C NMR (101 MHz, DMSO-d6): δ [ppm] = 169.1, 151.9, 150.2, 146.9, 131.7, 129.5, 127.7, 123.5, 122.6, 36.7, 22.5.

HRMS (ESI): calc. for $C_{15}H_{16}N_3O$ $[M+H]^+$: 254.1288, found: 254.1288.

$\varepsilon_{338\ nm}$ (DMSO) = 16,800 M^{-1} cm^{-1}

(E)-1-(4-(Phenyldiazenyl)phenyl)azetidin-2-one (3):

Compound **3** was prepared according to general procedure A with 50.0 mg (162 μmol) of **S3**. HPLC purification. Yield: 41%; 16.3 mg.

1H NMR (400 MHz, DMSO-d6) δ [ppm] = 7.95 (d, J = 8.8 Hz, 2H), 7.87–7.85 (m, 2H), 7.59–7.53 (m, 5H), 3.73 (t, J = 4.6 Hz, 2H), 3.15 (t, J = 4.6 Hz, 2H).

13C NMR (101 MHz, DMSO-d6): δ [ppm] = 165.2, 152.0, 147.6, 141.1, 131.1, 129.4, 124.2, 122.4, 116.4, 38.4, 36.2.

HRMS (ESI): calc. for $C_{15}H_{14}N_3O$ $[M+H]^+$: 252.1131, found: 252.1132.

$\varepsilon_{366\ nm}$ (DMSO) = 22,100 M^{-1} cm^{-1}

(E)-1-(4-(Phenyldiazenyl)phenyl)pyrrolidin-2-one (4):

Compound **4** was prepared according to general procedure A with 27.3 mg (89 μmol) of **S3**. HPLC purification. Yield: 43%; 10.1 mg.

1H NMR (400 MHz, DMSO-d6): δ [ppm] = 7.95–7.86 (m, 6H), 7.61–7.55 (m, 3H), 3.92 (t, J = 7.0 Hz, 2H), 2.67 (t, J = 8.1 Hz, 2H), 2.10 (p, J = 7.6 Hz, 2H).

13C NMR (101 MHz, DMSO-d6): δ [ppm] = 174.5, 152.0, 144.6, 142.4, 131.2, 129.5, 123.3, 122.4, 119.3, 48.1, 32.5, 17.3.

HRMS (ESI): calc. for $C_{16}H_{16}N_3O$ $[M+H]^+$: 266.1288, found: 266.1287.

$\varepsilon_{362\ nm}$ (DMSO) = 18,100 M^{-1} cm^{-1}

(E)-1-(4-(Phenyldiazenyl)phenyl)piperidin-2-one (5):

Compound **5** was prepared according to general procedure A with 50.0 mg (162 μmol) of **S3**. FCC purification (gradient: 10–90% DCM in hexanes). Yield: 90%; 40.7 mg.

1H NMR (400 MHz, CDCl3) δ [ppm] = 7.96–7.90 (m, 4H), 7.54–7.43 (m, 5H), 3.71 (d, J = 6.5 Hz, 2H), 2.61 (s, 2H), 2.00–1.97 (m, 4H).

13C NMR (101 MHz, CDCl3): δ [ppm] = 170.1, 152.6, 150.6, 145.6, 131.0, 129.1, 126.4, 123.6, 122.9, 51.4, 33.0, 23.5, 21.4.

HRMS (ESI): calc. for $C_{17}H_{18}N_3O$ $[M+H]^+$: 280.1444. found: 280.1443.

$\varepsilon_{343\ nm}$ (DMSO) = 15,000 M^{-1} cm^{-1}

(E)-1-(4-(Phenyldiazenyl)phenyl)azepan-2-one (6):

Compound **6** was prepared according to general procedure A with 50.0 mg (162 μmol) of **S3**. HPLC purification. Yield: 33%, 15.7 mg.

1H NMR (400 MHz, DMSO-d6) δ [ppm] = 7.91–7.87 (m, 4H), 7.63–7.54 (m, 3H), 7.46 (d, J = 8.7 Hz, 2H), 3.84–3.82 (m, 2H), 2.67–2.64 (m, 2H), 1.78–1.70 (m, 6H).

13C NMR (101 MHz, DMSO-d6): δ [ppm] = 174.6, 151.9, 149.2, 147.2, 131.5, 129.5, 126.8, 122.9, 122.5, 51.8, 37.1, 28.9, 28.4, 23.0.

HRMS (ESI): calc. for $C_{18}H_{20}N_3O$ [M+H]+: 294.1601, found: 294.1603.

$\varepsilon_{346\ nm}$ (DMSO) = 15,100 M^{-1} cm^{-1}

Methyl (E)-(4-(phenyldiazenyl)phenyl)carbamate (7):

A round bottom flask was charged with 270 mg (1.37 mmol, 1.0 equiv.) of 4-phenylazoaniline (**S4**) dissolved in 10 mL DCM and 562 μL DIPEA (2.2 equiv.) and cooled to 0 °C. 1 mL of phosgene (1.4 M in toluene, 1.1 equiv.) was added dropwise (the reaction mixture turning deep red upon formation of the isocyanate) and was allowed to warm to r.t. for 1 h before half of the solution's volume (the other half, see compound **8**) was transferred into a round bottom flask containing 20 mL MeOH and 562 μL DIPEA. The reaction mixture was heated to 70 °C for 2 h, before all volatiles were removed *in vacuo* and the crude subjected to FCC (gradient MeOH/DCM = 0/100 → 0.5/100) to obtain 148 mg (580 μmol) of the desired compound as an orange solid in 85% yield.

1H NMR (400 MHz, DMSO-d6): δ [ppm] = 10.09 (s, 1H), 7.89–7.83 (m, 4H), 7.70–7.68 (m, 2H), 7.60–7.51 (m, 3H), 3.71 (s, 3H).

13C NMR (101 MHz, DMSO-d6): δ [ppm] = 153.9, 152.1, 147.1, 142.5, 130.9, 129.4, 123.8, 122.3, 118.2, 51.9.

HRMS (ESI): calc. for $C_{14}H_{14}N_3O_2$ $[M+H]^+$: 256.1081, found: 256.1081.

$\varepsilon_{360\ nm}$ (DMSO) = 17,000 M^{-1} cm^{-1}

(E)-1-Methyl-3-(4-(phenyldiazenyl)phenyl)urea (8):

The other half of the isocyanate containing solution from compound preparation **7** was transferred into a round bottom flask containing 100 mg (1.49 mmol, 2.2 equiv.) $MeNH_2$ x HCl suspended in 20 mL THF and 562 μL DIPEA. The reaction mixture was heated to 70 °C for 2 h, before all volatiles were removed *in vacuo* and the crude subjected to FCC (gradient MeOH/DCM = 0/100 → 2/100) to obtain 150 mg (590 μmol) of the desired compound as an orange solid in 86% yield.

1H NMR (400 MHz, DMSO-d6): δ [ppm] = 8.99 (s, 1H), 7.84–7.81 (m, 4H), 7.62 (d, J = 8.9 Hz, 2H), 7.56 (t, J = 7.4 Hz, 2H), 7.54–7.46 (m, 1H), 6.18 (q, J = 4.6 Hz, 1H), 2.67 (d, J = 4.6 Hz, 3H).

13C NMR (101 MHz, DMSO-d6): δ [ppm] = 155.4, 152.1, 146.1, 144.2, 130.6, 129.4, 123.9, 122.2, 117.5, 26.3.

HRMS (ESI): calc. for $C_{14}H_{14}N_4O$ $[M+H]^+$: 255.1240, found: 255.1240.

$\varepsilon_{375\ nm}$ (DMSO) = 19,800 M^{-1} cm^{-1}

(E)-1,1-Dimethyl-3-(4-(phenyldiazenyl)phenyl)urea (9):

Compound **9** was prepared according to general procedure A with 50.0 mg (162 μmol) of **S3**. HPLC purification. Yield: 86%; 37.5 mg.

1H NMR (400 MHz, DMSO-d6) δ [ppm] = 8.70 (s, 1H), 7.84–7.81 (m, 4H), 7.73 (d, J = 9.0 Hz, 2H), 7.59–7.51 (m, 3H), 2.96 (s, 6H).

13C NMR (101 MHz, DMSO-d6): δ [ppm] = 155.3, 152.1, 146.4, 144.4, 130.7, 129.4, 123.4, 122.2, 119.2, 36.3.

HRMS (ESI): calc. for $C_{12}H_{12}N_3$ $[M\text{-}Me_2NCO+2H]^+$: 198.1026, found: 198.1025.

$\varepsilon_{372\ nm}$ (DMSO) = 19,100 M^{-1} cm^{-1}

(E)-1,1,3-Trimethyl-3-(4-(phenyldiazenyl)phenyl)urea (10):

Compound **10** was prepared according to general procedure A with 27.8 mg (90 μmol) of **S3**. HPLC purification. Yield: 24%; 6.1 mg.

1H NMR (400 MHz, acetone-d6): δ [ppm] = 7.89–7.84 (m, 4H), 7.60–7.53 (m, 3H), 7.22 (d, J = 8.9 Hz, 2H), 3.24 (s, 3H), 2.80 (s, 6H).

13C NMR (101 MHz, acetone-d6): δ [ppm] = 161.6, 153.6, 150.5, 148.5, 131.6, 130.1, 125.0, 123.3, 121.7, 38.2, 37.7.

HRMS (ESI): calc. for $C_{16}H_{19}N_4O$ $[M+H]^+$: 283.1553, found: 283.1551.

$\varepsilon_{373\ nm}$ (DMSO) = 11,400 M^{-1} cm^{-1}

(E)-1-Methyl-3-(4-(phenyldiazenyl)phenyl)imidazolidin-2-one (11):

Compound **11** was prepared according to general procedure A with 50.0 mg (162 μmol) of **S3**. HPLC purification. Yield: 77%; 34.9 mg.

1H NMR (400 MHz, DMSO-d6) δ [ppm] = 7.90 (d, J = 9.1 Hz, 2H), 7.87–7.83 (m, 2H), 7.80 (d, J = 9.1 Hz, 2H), 7.59–7.54 (m, 3H), 3.91–3.87 (m, 2H), 3.54–3.48 (m, 2H), 2.81 (s, 3H).

13C NMR (101 MHz, DMSO-d6): δ [ppm] = 157.0, 152.1, 146.2, 143.9, 130.8, 129.4, 123.6, 122.2, 116.6, 43.2, 41.9, 30.8.

HRMS (ESI): calc. for $C_{16}H_{17}N_4O$ $[M+H]^+$: 281.1397, found: 281.1395.

$\varepsilon_{378\ nm}$ (DMSO) = 20,300 M^{-1} cm^{-1}

(E)-1-Methyl-3-(4-(phenyldiazenyl)phenyl)imidazolidin-2-one (12):

Compound **12** was prepared according to general procedure A with 50.0 mg (162 μmol) of **S3**. HPLC purification. Yield: 44%; 20.7 mg.

1H NMR (400 MHz, DMSO-d6) δ [ppm] = 7.90–7.86 (m, 4H), 7.62–7.53 (m, 3H), 7.48 (d, J = 8.8 Hz, 2H), 6.47 (q, J = 4.5 Hz, 1H), 3.24 (s, 3H), 2.62 (d, J = 4.3 Hz, 3H).

13C NMR (101 MHz, DMSO-d6): δ [ppm] = 157.0, 152.0, 148.3, 147.5, 131.2, 129.5, 125.5, 123.2, 122.4, 36.6, 27.4.

HRMS (ESI): calc. for $C_{15}H_{17}N_4NaO$ $[M+H]^+$: 291.1216, found: 291.1218.

$\varepsilon_{359\ nm}$ (DMSO) = 15,400 M^{-1} cm^{-1}

Dimethyl (2S,4S)-2-(4-((4-((E)-(4-(3-(2-aminoethyl)ureido)phenyl)diazenyl)phenyl)amino)-4-oxo-butyl)-4-((tert-butoxycarbonyl)amino)pentanedioate (S6):

A flame-dried 250 mL Schlenk flask under an argon atmosphere was charged with 500 mg (0.87 mmol, 1.0 equiv.) of dimethyl (2*S*,4*S*)-2-(4-((4-((*E*)-(4-aminophenyl)diazenyl)phenyl)amino)-4-oxobutyl)-4-((*tert*-butoxycarbonyl)amino)pentanedioate (**S5**) (Broichhagen et al., 2015a), before addition of 100 mL dry THF and 317 μL DIPEA (1.82 mmol, 2.1 equiv.). The reaction mixture was vigorously stirred and cooled to 0 °C in an ice-bath and 680 μL of phosgene (1.4 M in toluene; 0.95 mmol, 1.1 equiv.) was added dropwise.

The yellow solution turned red upon stirring for 15 min and was transferred into an addition funnel to be added dropwise to a solution of ethylene diamine (1.0 mL, 900 mg, 15 mmol, 17.2 equiv.) in 100 mL dry THF at 0 °C. Upon complete addition, the ice bath was removed and the reaction mixture was allowed to stir for 5 min before it was quenched by addition of glacial HOAc (2.0 mL). The reaction mixture was concentrated *in vacuo* not exceeding 30 °C and 2 mL of DMF were added. The crude was subjected to RP-HPLC to obtain 350 mg (0.46 mmol) of the desired compound (TFA salt) as a deep red powder in 53% yield.

1H NMR (400 MHz, DMSO-d6): δ [ppm] = 10.20 (s, 1H), 9.27 (s, 1H), 7.94–7.70 (m, 9H), 7.63 (d, J = 9.0 Hz, 2H), 7.25 (d, J = 8.2 Hz, 1H), 6.64 (t, J = 5.8 Hz, 1H), 4.01 (td, J = 8.7, 5.7 Hz, 1H), 3.61 (s, 6H), 3.35 (q, J = 6.0 Hz, 2H), 2.92 (q, J = 5.9 Hz, 2H), 2.45 (t, J = 6.2 Hz, 1H), 2.40–2.30 (m, 2H), 1.95–1.79 (m, 2H), 1.64–1.48 (m, 4H), 1.37 (s, 9H).

HRMS (ESI): calc. for $C_{31}H_{44}N_7O_8$ $[M+H]^+$: 642.3246, found: 642.3248.

(2S,4S)-2-(4-((4-((E)-(4-(3-(1-Amino-39-oxo-3,6,9,12,15,18,21,24,27,30,33,36-dodecaoxa-40-azadotetracontan-42-yl)ureido)phenyl)diazenyl)phenyl)amino)-4-oxobutyl)-4-((tert-butoxycarbonyl)amino)pentanedioic acid (S7):

S7 was prepared according to general procedure C.

Acid: $FmocPEG_{12}COOH$; amine **S6**.

HRMS (ESI): calc. for $C_{56}H_{94}N_8O_{21}$ $[M+2H]^{2+}$: 607.3261, found: 607.3260.

(2S,4S)-2-(4-((4-((E)-(4-(3-(1-(4-(((2-Amino-9H-purin-6-yl)oxy)methyl)phenyl)-3,7,47-trioxo-11,14,17,20,23,26,29,32,35,38,41,44-dodecaoxa-2,8,48-triazapentacontan-50-yl)ureido)-phenyl)diazenyl)phenyl)amino)-4-oxobutyl)-4-((tert-butoxycarbonyl)amino)pentanedioic acid (S8)

S8 was prepared according to general procedure B.

Acid: **BG-COOH**; amine **S7**.

HRMS (ESI): calc. for $C_{76}H_{116}N_{14}O_{24}$ $[M+2H]^{2+}$: 804.4138, found: 804.4134.

(2S,4S)-2-(4-((4-((E)-(4-(3-(1-(4-(((2-Amino-9H-purin-6-yl)oxy)methyl)phenyl)-3,7,47-trioxo-11,14,17,20,23,26,29,32,35,38,41,44-dodecaoxa-2,8,48-triazapentacontan-50-yl)ureido)-phenyl)-diazenyl)phenyl)amino)-4-oxobutyl)-4-((tert-butoxycarbonyl)amino)pentanedioic acid ($BGAG_{12,400}$):

$BGAG_{12,400}$ was prepared according to general procedure D from compound **S8**.

HRMS (ESI): calc. for $C_{74}H_{112}N_{14}O_{24}$ $[M+2H]^{2+}$: 790.3981, found: 790.3980; ester cleaved intermediate.

HRMS (ESI): calc. for $C_{69}H_{105}N_{14}O_{22}$ $[M+3H]^{3+}$: 493.9170, found: 493.9178, **$BGAG_{12,400}$**.

Tetramethyl 4,4'-(((((1E,1'E)-((((S)-7-amino-6,10-dioxo-2,5,11,14-tetraazapentadecanedioyl)-bis-(azanediyl))bis(4,1-phenylene))bis(diazene-2,1-diyl))bis(4,1-phenylene))bis(azanediyl))bis(4-oxobutane-4,1-diyl))(2S,2'S,4S,4'S)-bis(2-((tert-butoxycarbonyl)amino)pentanedioate) (S10):

S10 was prepared according to general procedure C, with 3.0 equiv of HBTU and 3.0 equiv. of **S6**.

Acid: **S9**

HRMS (ESI): calc. for $C_{82}H_{103}N_{15}O_{20}$ $[M+2H]^{2+}$: 808.8746, found: 808.8733; Fmoc protected intermediate.

HRMS (ESI): calc. for $C_{62}H_{85}N_{15}O_{16}$ $[M–Boc+2H]^{2+}$: 647.8144, found: 647.8135; **S10**.

Tetramethyl 4,4'-(((((1E,1'E)-((((S)-7-(1-amino-3,6,9,12,15,18,21,24,27,30,33,36-dodecaoxa-nona-triacontan-39-amido)-6,10-dioxo-2,5,11,14-tetraazapentadecanedioyl)bis-(azanediyl))bis(4,1-phenylene))bis(diazene-2,1-diyl))bis(4,1-phenylene))bis(azanediyl))-bis(4-oxobutane-4,1-diyl))(2S,2'S,4S,4'S)-bis(2-((tert-butoxycarbonyl)amino)-pentanedioate) (S11):

S11 was prepared according to general procedure C at 50 °C.

Acid: $FmocPEG_{12}COOH$; amine **S10**.

HRMS (ESI): calc. for $C_{109}H_{156}N_{16}O_{33}$ $[M+2H]^{2+}$: 1109.0520, found: 1109.0513; Fmoc protected intermediate.

HRMS (ESI): calc. for $C_{94}H_{146}N_{16}O_{31}$ $[M+2H]^{2+}$: 998.0180, found: 998.0150; **S10**. Compound S12:

Tetramethyl 4,4'-(((((1E,1'E)-((((S)-7-(1-(4-(((2-amino-9H-purin-6-yl)oxy)methyl)phenyl)-3,7-dioxo-11,14,17,20,23,26,29,32,35,38,41,44-dodecaoxa-2,8-diazaheptatetracontan-47-amido)-6,10-dioxo-2,5,11,14-tetraazapentadecanedioyl)bis(azanediyl))bis(4,1-phenylene))bis(diazene-2,1-diyl))bis(4,1-phenylene))bis(azanediyl))bis(4-oxobutane-4,1-diyl))(2S,2'S,4S,4'S)-bis(2-((tert-butoxycarbonyl)amino)pentanedioate) (S12):

S12 was prepared according to general procedure B.

Acid: **BG-COOH**; amine **S11**.

HRMS (ESI): calc. for $C_{112}H_{164}N_{22}O_{34}$ $[M+2H]^{2+}$: 1181.0900, found: 1181.0876.

(2S,2'S,4S,4'S)-4,4'-(((((1E,1'E)-((((S)-7-(1-(4-(((2-Amino-9H-purin-6-yl)oxy)methyl)phenyl)-3,7-dioxo-11,14,17,20,23,26,29,32,35,38,41,44-dodecaoxa-2,8-diazaheptatetracontan-47-amido)-6,10-dioxo-2,5,11,14-tetraazapentadecanedioyl)bis(azanediyl))bis(4,1-phenylene))bis(diazene-2,1-diyl))bis(4,1-phenylene))bis(azanediyl))bis(4-oxobutane-4,1-diyl))bis(2-aminopentanedioic acid) ($^{2x}BGAG_{12,400}$):

$^{2x}BGAG_{12,400}$ was prepared according to general procedure D from compound **S12**.

HRMS (ESI): calc. for $C_{108}H_{156}N_{22}O_{34}$ $[M+2H]^{2+}$: 1153.0587, found: 1153.0575; ester cleaved intermediate.

HRMS (ESI): calc. for $C_{98}H_{142}N_{22}O_{30}$ $[M+4H]^{4+}$: 527.0067, found: 527.0063; **$^{2x}BGAG_{12,400}$**.

1-(6-(((S)-5-((((9H-Fluoren-9-yl)methoxy)carbonyl)amino)-5-carboxypentyl)amino)-6-oxohexyl)-3,3-dimethyl-2-((E)-3-((Z)-1,3,3-trimethylindolin-2-ylidene)prop-1-en-1-yl)-3H-indol-1-ium (S13):

Compound **S13** was prepared as reported previously(Acosta-Ruiz et al., 2020). A round bottom flask was charged with 50.0 mg (109 μmol, 1.0 equiv.) of 1-(5-carboxypentyl)-3,3-dimethyl-2-((*E*)-3-((*Z*)-1,3,3-trimethylindolin-2-ylidene)prop-1-en-1-yl)-3*H*-indol-

1-ium (Ueno et al., 2011) which was dissolved in 2.1 mL DMSO and 72 μL DIPEA. TSTU (32.9 mg, 109 μmol, 1.0 equiv.) was added in one portion and the mixture was incubated for 30 min before 53.1 mg (131 μmol, 1.2 equiv.) of Fmoc-Lys-OH hydrochloride (Aldrich, #17290) was added in one portion. The reaction mixture was incubated for another hour before it was quenched by addition of 72 μL HOAc and subjected to RP-HPLC to obtain 49.0 mg (60.0 μmol) of the desired product as a red powder after lyophilization in 56% yield.

HRMS (ESI): calc. for $C_{51}H_{59}N_4O_5$ $[M]^+$: 807.4480, found: 807.4488.

1-(6-(((S)-5-((((9H-Fluoren-9-yl)methoxy)carbonyl)amino)-5-carboxypentyl)amino)-6-oxohexyl)-3,3-dimethyl-2-((1E,3E)-5-((Z)-1,3,3-trimethylindolin-2-ylidene)penta-1,3-dien-1-yl)-3H-indol-1-ium (S14):

Compound **S14** was prepared as reported previously(Acosta-Ruiz et al., 2020). A round bottom flask was charged with 35.0 mg (72.4 μmol, 1.0 equiv.) of 1-(5-carboxypentyl)-3,3-dimethyl-2-((1*E*,3*E*)-5-((*Z*)-1,3,3-trimethylindolin-2-ylidene)penta-1,3-dien-1-yl)-3*H*-indol-1-ium (Ueno et al., 2011) which was dissolved in 1.5 mL DMSO and 50 μL DIPEA. TSTU (21.8 mg, 72.4 μmol, 1.0 equiv.) was added in one portion and the mixture was incubated for 30 min before 32.0 mg (86.8 μmol, 1.2 equiv.) of Fmoc-Lys-OH hydrochloride (Aldrich, #17290) was added in one portion. The reaction mixture was incubated for another hour before it was quenched by addition of 50 μL HOAc and subjected to RP-HPLC to obtain 26 mg (32.2 μmol) of the desired product as a blue powder after lyophilization in 45% yield.

HRMS (ESI): calc. for $C_{53}H_{61}N_4O_5$ $[M]^+$: 833.4636, found: 833.4639.

1-(6-(((S)-5-Amino-6-((2-(3-(4-((E)-(4-((5S,7S)-7-((tert-butoxycarbonyl)amino)-8-methoxy-5-(methoxycarbonyl)-8-oxooctanamido)phenyl)diazenyl)phenyl)ureido)ethyl)amino)-6-oxohexyl)-amino)-6-oxohexyl)-3,3-dimethyl-2-((E)-3-((Z)-1,3,3-trimethylindolin-2-ylidene)prop-1-en-1-yl)-3H-indol-1-ium (S15):

S15 was prepared according to general procedure C.

Acid: **S13**; amine **S6**.

HRMS (ESI): calc. for $C_{84}H_{103}N_{11}O_{12}$ $[M+H–Boc]^{2+}$: 665.8548, found: 665.8544; Fmoc protected intermediate.

HRMS (ESI): calc. for $C_{67}H_{91}N_{11}O_{10}$ $[M+H]^{2+}$: 604.8470, found: 604.8466; **S15**.

1-((S)-1-Amino-41-((2-(3-(4-((E)-(4-((5S,7S)-7-((tert-butoxycarbonyl)amino)-8-methoxy-5-(methoxycarbonyl)-8-oxooctanamido)phenyl)diazenyl)phenyl)ureido)ethyl)carbamoyl)-39,47-dioxo-3,6,9,12,15,18,21,24,27,30,33,36-dodecaoxa-40,46-diazadopentacontan-52-yl)-3,3-dimethyl-2-((E)-3-((Z)-1,3,3-trimethylindolin-2-ylidene)prop-1-en-1-yl)-3H-indol-1-ium (S17):

S17 was prepared according to general procedure C.

Acid: FmocNHPEG$_{12}$COOH; amine **S15**.

HRMS (ESI): calc. for $C_{109}H_{154}N_{12}O_{25}$ $[M+H]^{2+}$: 1016.0584, found: 1016.0581; Fmoc protected intermediate.

HRMS (ESI): calc. for $C_{94}H_{144}N_{12}O_{23}$ $[M+H]^{2+}$: 905.0244, found: 905.0243.

1-((S)-1-(4-(((2-Amino-9H-purin-6-yl)oxy)methyl)phenyl)-49-((2-(3-(4-((E)-(4-((5S,7S)-7-((tert-butoxycarbonyl)amino)-8-methoxy-5-(methoxycarbonyl)-8-oxooctanamido)phenyl)diazenyl)-phenyl)ureido)ethyl)carbamoyl)-3,7,47,55-tetraoxo-11,14,17,20,23,26,29,32,35,38,41,44-dodecaoxa-2,8,48,54-tetraazahexacontan-60-yl)-3,3-dimethyl-2-((E)-3-((Z)-1,3,3-trimethylindolin-2-ylidene)prop-1-en-1-yl)-3H-indol-1-ium (S19):

S19 was prepared according to general procedure B.

Acid: **BG-COOH**; amine **S17**.

HRMS (ESI): calc. for $C_{112}H_{163}N_{18}O_{26}$ $[M+2H]^{3+}$: 725.7333, found: 725.7329.

1-((S)-49-((2-(3-(4-((E)-(4-((5S,7S)-7-Amino-5,7-dicarboxyheptanamido)phenyl)diazenyl)phenyl)-ureido)ethyl) carbamoyl)-1-(4-(((2-amino-9H-purin-6-yl)oxy)methyl)phenyl)-3,7,47,55-tetraoxo-11,14,17,20,23,26,29,32,35,38,41,44-dodecaoxa-2,8,48,54-tetraazahexacontan-60-yl)-3,3-dimethyl-2-((E)-3-((Z)-1,3,3-trimethylindolin-2-ylidene)prop-1-en-1-yl)-3H-indol-1-ium (BGAG$_{12,400}$-Cy3):

BGAG$_{12,400}$-Cy3 was prepared according to general procedure D from compound **S19**.

HRMS (ESI): calc. for $C_{110}H_{159}N_{18}O_{26}$ $[M+H]^{2+}$: 1074.0807, found: 1074.0810; ester cleaved intermediate.

HRMS (ESI): calc. for $C_{105}H_{150}N_{18}O_{24}$ $[M+2H]^{3+}$: 683.0388, found: 683.0385; **BGAG$_{12,400}$-Cy3**.

1-(6-(((S)-5-Amino-6-((2-(3-(4-((E)-(4-((5S,7S)-7-((tert-butoxycarbonyl)amino)-8-methoxy-5-(methoxycarbonyl)-8-oxooctanamido)phenyl)diazenyl)phenyl)ureido)ethyl)amino)-6-oxohexyl)-amino)-6-oxohexyl)-3,3-dimethyl-2-((1E,3E)-5-((Z)-1,3,3-trimethylindolin-2-ylidene)penta-1,3-dien-1-yl)-3H-indol-1-ium (S16):

S16 was prepared according to general procedure C.

Acid: **S14**; amine **S6**.

HRMS (ESI): calc. for $C_{84}H_{103}N_{11}O_{12}$ $[M+H]^{2+}$: 728.8888, found: 728.8878; Fmoc protected intermediate.

HRMS (ESI): calc. for $C_{69}H_{93}N_{11}O_{10}$ $[M+H]^{2+}$: 617.8548, found: 617.8548; **S16**.

1-((S)-1-Amino-41-((2-(3-(4-((E)-(4-((5S,7S)-7-((tert-butoxycarbonyl)amino)-8-methoxy-5-(methoxycarbonyl)-8-oxooctanamido)phenyl)diazenyl)phenyl)ureido)ethyl)carbamoyl)-39,47-dioxo-3,6,9,12,15,18,21,24,27,30,33,36-dodecaoxa-40,46-diazadopentacontan-52-yl)-3,3-dimethyl-2-((1E,3E)-5-((Z)-1,3,3-trimethylindolin-2-ylidene)penta-1,3-dien-1-yl)-3H-indol-1-ium (S18):

S18 was prepared according to general procedure C.

Acid: FmocNHPEG$_{12}$COOH; amine **S16**.

HRMS (ESI): calc. for $C_{111}H_{156}N_{12}O_{25}$ $[M+H]^{2+}$: 1029.0663, found: 1029.0645; Fmoc protected intermediate.

HRMS (ESI): calc. for $C_{96}H_{146}N_{12}O_{23}$ $[M+H]^{2+}$: 918.0322, found: 918.0317; **S18**.

1-((S)-1-(4-(((2-Amino-9H-purin-6-yl)oxy)methyl)phenyl)-49-((2-(3-(4-((E)-(4-((5S,7S)-7-((tert-butoxycarbonyl)amino)-8-methoxy-5-(methoxycarbonyl)-8-oxooctanamido)-phenyl)diazenyl)-phenyl)ureido)ethyl)carbamoyl)-3,7,47,55-tetraoxo-11,14,17,20,23,26,29,32,35,38,41,44-dodecaoxa-2,8,48,54-tetraazahexacontan-60-yl)-3,3-dimethyl-2-((1E,3E)-5-((Z)-1,3,3-trimethylindolin-2-ylidene)penta-1,3-dien-1-yl)-3H-indol-1-ium (S20):

S20 was prepared according to general procedure B.

Acid: **BG-COOH**; amine **S18**.

HRMS (ESI): calc. for $C_{114}H_{165}N_{18}O_{26}$ $[M+2H]^{3+}$: 734.4052, found: 734.4050.

1-((S)-49-((2-(3-(4-((E)-(4-((5S,7S)-7-Amino-5,7-dicarboxyheptanamido)phenyl)diazenyl)phenyl)-ureido)ethyl) carbamoyl)-1-(4-(((2-amino-9H-purin-6-yl)oxy)methyl)phenyl)-3,7,47,55-tetraoxo-11,14,17,20,23,26,29,32,35,38,41,44-dodecaoxa-2,8,48,54-tetraazahexacontan-60-yl)-3,3-dimethyl-2-((1E,3E)-5-((Z)-1,3,3-trimethylindolin-2-ylidene)penta-1,3-dien-1-yl)-3H-indol-1-ium (BGAG$_{12,400}$-Cy5):

BGAG$_{12,400}$-Cy5 was prepared according to general procedure D from compound **S20**.

HRMS (ESI): calc. for $C_{112}H_{161}N_{18}O_{26}$ $[M+2H]^{3+}$: 725.0615, found: 725.0613; ester cleaved intermediate.

HRMS (ESI): calc. for $C_{107}H_{152}N_{18}O_{24}$ $[M+2H]^{3+}$: 691.3747, found: 691.3755; **BGAG$_{12,400}$-Cy5**.

1-((S)-47-Amino-1-((4-((E)-(4-((5S,7S)-7-((tert-butoxycarbonyl)amino)-8-methoxy-5-(methoxycarbonyl)-8-oxooctanamido)phenyl)diazenyl)phenyl)amino)-1,6,46,53-tetraoxo-9,12,15,18,21,24,27,30,33,36,39,42-dodecaoxa-2,5,45,52-tetraazaoctapentacontan-58-yl)-3,3-dimethyl-2-((E)-3-((Z)-1,3,3-trimethylindolin-2-ylidene)prop-1-en-1-yl)-3H-indol-1-ium (S21):

S21 was prepared according to general procedure C.

Acid: **S13**; amine **S7**.

HRMS (ESI): calc. for $C_{94}H_{144}N_{12}O_{23}$ $[M+H]^{2+}$: 905.0244, found: 905.0422.

1-((S)-47-(5-((4-(((2-Amino-9H-purin-6-yl)oxy)methyl)benzyl)amino)-5-oxopentanamido)-1-((4-((E)-(4-((5S,7S)-7-((tert-butoxycarbonyl)amino)-8-methoxy-5-(methoxycarbonyl)-8-oxooctanamido)phenyl)diazenyl)phenyl)amino)-1,6,46,53-tetraoxo-9,12,15,18,21,24,27,30,33,36,39,42-dodecaoxa-2,5,45,52-tetraazaoctapentacontan-58-yl)-3,3-dimethyl-2-((E)-3-((Z)-1,3,3-trimethylindolin-2-ylidene)prop-1-en-1-yl)-3H-indol-1-ium (S23):

S23 was prepared according to general procedure B.

Acid: **BG-COOH**; amine **S21**.

HRMS (ESI): calc. for $C_{112}H_{163}N_{18}O_{26}$ $[M+2H]^{3+}$: 725.7333, found: 725.7326.

1-((S)-1-((4-((E)-(4-((5S,7S)-7-Amino-5,7-dicarboxyheptanamido)phenyl)diazenyl)phenyl)amino)-47-(5-((4-(((2-amino-9H-purin-6-yl)oxy)methyl)benzyl)amino)-5-oxopentanamido)-1,6,46,53-tetraoxo-9,12,15,18,21,24,27,30,33,36,39,42-dodecaoxa-2,5,45,52-tetraazaoctapentacontan-58-yl)-3,3-dimethyl-2-((E)-3-((Z)-1,3,3-trimethylindolin-2-ylidene)prop-1-en-1-yl)-3H-indol-1-ium (BGAG$_{12,400}$–Cy3 v2):

BGAG$_{12,400}$–Cy3 was prepared according to general procedure D from compound **S23**.

HRMS (ESI): calc. for $C_{110}H_{159}N_{18}O_{26}$ $[M+2H]^{3+}$: 716.3896, found: 716.3895; ester cleaved intermediate.

HRMS (ESI): calc. for $C_{105}H_{151}N_{18}O_{24}$ $[M+2H]^{3+}$: 683.0388, found: 683.0385; **BGAG$_{12,400}$–Cy3**.

1-((S)-47-Amino-1-((4-((E)-(4-((5S,7S)-7-((tert-butoxycarbonyl)amino)-8-methoxy-5-(methoxycarbonyl)-8-oxooctanamido)phenyl)diazenyl)phenyl)amino)-1,6,46,53-tetraoxo-9,12,15,18,21,24,27,30,33,36,39,42-dodecaoxa-2,5,45,52-tetraazaoctapentacontan-58-yl)-3,3-dimethyl-2-((1E,3E)-5-((Z)-1,3,3-trimethylindolin-2-ylidene)penta-1,3-dien-1-yl)-3H-indol-1-ium (S22):

S22 was prepared according to general procedure C.

Acid: **S14**; amine **S7**.

HRMS (ESI): calc. for $C_{96}H_{146}N_{12}O_{23}$ $[M+H]^{2+}$: 918.0322, found: 918.0320.

1-((S)-47-(5-((4-(((2-Amino-9H-purin-6-yl)oxy)methyl)benzyl)amino)-5-oxopentanamido)-1-((4-((E)-(4-((5S,7S)-7-((tert-butoxycarbonyl)amino)-8-methoxy-5-(methoxycarbonyl)-8-oxooctan-amido)phenyl)diazenyl)phenyl)amino)-1,6,46,53-tetraoxo-9,12,15,18,21,24,27,30,33,36,39,42-dodecaoxa-2,5,45,52-tetraazaoctapentacontan-58-yl)-3,3-dimethyl-2-((1E,3E)-5-((Z)-1,3,3-trimethylindolin-2-ylidene)penta-1,3-dien-1-yl)-3H-indol-1-ium (S24):

S24 was prepared according to general procedure B.

Acid: **BG-COOH**; amine **S22**.

HRMS (ESI): calc. for $C_{114}H_{165}N_{18}O_{26}$ $[M+2H]^{3+}$: 734.4052, found: 734.4047.

1-((S)-1-((4-((E)-(4-((5S,7S)-7-Amino-5,7-dicarboxyheptanamido)phenyl)diazenyl)phenyl)amino)-47-(5-((4-(((2-amino-9H-purin-6-yl)oxy)methyl)benzyl)amino)-5-oxopentanamido)-1,6,46,53-tetraoxo-9,12,15,18,21,24,27,30,33,36,39,42-dodecaoxa-2,5,45,52-tetraazaoctapentacontan-58-yl)-3,3-dimethyl-2-((1E,3E)-5-((Z)-1,3,3-trimethylindolin-2-ylidene)penta-1,3-dien-1-yl)-3H-indol-1-ium (BGAG$_{12,400}$–Cy5 v2):

BGAG$_{12,400}$–Cy5 v2 was prepared according to general procedure D from compound **S24**.

HRMS (ESI): calc. for $C_{112}H_{161}N_{18}O_{26}$ $[M+2H]^{3+}$: 725.0615, found: 725.0613; ester cleaved intermediate.

HRMS (ESI): calc. for $C_{107}H_{153}N_{18}O_{24}$ $[M+2H]^{3+}$: 691.7106, found: 691.7099; **BGAG$_{12,400}$–Cy5 v2**.

(E)-2-((4-((4-Aminophenyl)diazenyl)phenyl)amino)-N,N,N-triethyl-2-oxoethan-1-aminium (x TFA) (S26):

A round bottom flask was charged with 240 mg (1.13 mmol, 1.1 equiv.) of 4,4'-diamino azobenzene (**S25**), 200 mg (1.02 mmol, 1.0 equiv.) *N*-(carboxymethyl)-*N*,*N*-diethylethanaminium chloride (Banghart et al., 2009) dissolved in 4 mL DMSO and 500 μL DIPEA. To the vigorously stirred solution, 425 mg (1.13 mmol, 1.1 equiv.) HBTU was added in one portion and the reaction mixture was stirred at r.t. o.n. before it was quenched by addition of 500 μL HOAc and 500 μL H_2O and subjected to RP-HPLC purification to obtain 145 mg (0.31 mmol) of the desired product in 30% yield. The final compound was soluble up to 20 mg/mL in D_2O.

1H NMR (400 MHz, D2O): δ [ppm] = 7.74 (d, J = 8.8 Hz, 2H), 7.69 (d, J = 9.0 Hz, 2H), 7.57–7.38 (m, 2H), 7.25 (d, J = 8.9 Hz, 2H), 4.02 (s, 2H), 3.50 (q, J = 7.2 Hz, 6H), 1.26 (t, J = 7.2 Hz, 9H).

13C NMR (101 MHz, D2O): δ [ppm] = 162.91 (q, J = 35.3 Hz), 162.64, 148.78, 147.99, 139.33, 138.78, 125.13, 123.10, 121.64, 121.61, 116.32 (q, J = 291.9 Hz), 56.41, 54.64, 6.93.

HRMS (ESI): calc. for $C_{20}H_{28}N_5O$ $[M]^+$: 354.2288, found: 354.2288.

(E)-2-((4-((4-Butyramidophenyl)diazenyl)phenyl)amino)-N,N,N-triethyl-2-oxoethan-1-aminium (x TFA) (AQ):

A flame-dried 250 mL Schlenk flask under an argon atmosphere was charged with 50 mg (107 μmol, 1.0 equiv.) of **S26**, before addition of 10 mL dry THF and 37 μL DIPEA (214 μmol, 2.0 equiv.). The reaction mixture was vigorously stirred and cooled to 0 °C in an ice-bath and 16.7 μL of butyryl chloride (161 μmol, 1.5 equiv.) was added. Upon addition, the ice bath was removed and the reaction mixture was allowed to stir for 45 min while warming to r.t., before it was quenched by addition of glacial HOAc (0.1 mL). The reaction mixture was concentrated *in vacuo* and subjected to RP-HPLC to obtain 30.3 mg (57.2 μmol) of the desired compound (TFA salt) as a highly hygroscopic, orange powder in 53% yield. The final compound was soluble up to 10 mg/mL in D_2O.

1H NMR (400 MHz, D2O): δ [ppm] = 7.88–7.64 (m, 4H), 7.60–7.54 (m, 4H), 4.07 (s, 2H), 3.57 (q, J = 7.2 Hz, 6H), 2.32 (t, J = 7.4 Hz, 2H), 1.64 (q, J = 7.4 Hz, 2H), 1.33 (t, J = 7.2 Hz, 9H), 0.93 (t, J = 7.4 Hz, 3H).

13C NMR (101 MHz, D2O): δ [ppm] = 175.8, 162.5, 149.1, 148.4, 140.3, 138.8, 123.6, 123.5, 121.5, 121.2, 56.4, 54.7, 38.5, 18.9, 12.8, 7.0.

HRMS (ESI): calc. for $C_{24}H_{34}N_5O_2$ $[M]^+$: 424.2707, found: 424.2704.

$\varepsilon_{360\ nm}$ (PBS) = 19,800 M^{-1} cm^{-1}

(E)-N,N,N-Triethyl-2-((4-((4-(3-ethylureido)phenyl)diazenyl)phenyl)amino)-2-oxoethan-1-aminium chloride (x TFA) (AQ_{400}):

A microwave vial was charged with 50 mg (107 μmol, 1.0 equiv.) of **S26**, before addition of 5 mL dry THF and 37 μL DIPEA (214 μmol, 2.0 equiv.) and 350 μL (4.42 mmol, 41 equiv.) ethyl isocyanate. The reaction mixture was vigorously stirred at 80 °C under microwave irradiation for 5 h, before it was quenched by addition of glacial HOAc (0.1 mL). The reaction mixture was concentrated *in vacuo* and subjected to RP-HPLC to obtain 30.0 mg (56.5 μmol) of the desired compound (TFA salt) as a hygroscopic, orange powder in 53% yield. The final compound was soluble up to 10 mg/mL in D_2O.

1H NMR (400 MHz, D2O): δ [ppm] = 7.90–7.64 (m, 4H), 7.58 (d, J = 8.9 Hz, 2H), 7.43 (d, J = 9.0 Hz, 2H), 4.06 (s, 2H), 3.57 (q, J = 7.2 Hz, 6H), 3.18 (q, J = 7.3 Hz, 2H), 1.34 (t, J = 7.2 Hz, 9H), 1.11 (t, J = 7.2 Hz, 3H).

13C NMR (101 MHz, D2O): δ [ppm] = 161.9, 157.3, 151.1, 147.6, 142.3, 138.5, 123.8, 123.3, 121.5, 119.5, 56.4, 54.7, 34.8, 14.3, 7.0.

HRMS (ESI): calc. for $C_{23}H_{33}N_6O_2$ $[M]^+$: 425.2660, found: 425.2659.

$\varepsilon_{371\ nm}$ (PBS) = 23,400 M^{-1} cm^{-1}

UV/Vis spectroscopy

UV/Vis spectroscopy was performed on either: i) a JASCO V-770 UV/Vis/NIR Spectrophotometer (PbS-version) with a PAC-743 Peltierthermo 6/8 sample switching unit and a Julabo F-250 cooling system, using a Hellma quartz glass cuvettes (10 mm pathlength) and light for switching was delivered by a TILL Polychrome V coupled to a fiber optic (light intensities~ 1–2 mW/cm^2); or ii) a NanoDrop 2000c using a Hellma quartz glass cuvettes (10 mm pathlength) and light for switching was delivered by a CoolLED pE-4000 (intensities used: $I_{385\ nm}$ = 0.459 mW/mm^2; $I_{405\ nm}$ = 0.798 mW/mm^2; $P_{500\ nm}$ = 8.20 mW/mm^2; $P_{525\ nm}$ = 4.95 mW/mm^2). Full spectra were acquired either in the dark or under appropriate illumination, and kinetic traces were recorded at one wavelength under annotated illumination. Results were exported and plotted in GraphPad Prism 8 and kinetic traces were fitted monoexponentially using IgorPro or GraphPad Prism 8 and plotted in GraphPad Prism 8. For the determination of extinction coefficients, see supplemental information.

Photostationary state measurements via NMR

Photostationary state measurements were made via ^1H nuclear magnetic resonance (NMR) based on previous studies(Banghart and Trauner, 2013). AQ and AQ_{400} were dissolved in deuterated PBS (obtained by lyophilization of 5 mL PBS and reconstitution with 5 mL D_2O) at a concentration of 100 μM and transferred to an NMR tube. Prior to measurement, the NMR tube was warmed with a heat gun to approx. 80 °C and allowed to cool to r.t. in the dark (~3 min) to ensure a 100% *trans* population. A custom-build fibre optic cable with an etched end surface (Dorn et al., 2012) was coupled to a CoolLED pE-4000 (powers used: $P_{385\ nm}$ = 101 mW; $P_{405\ nm}$ = 188 mW; $P_{500\ nm}$ = 58 mW; $P_{525\ nm}$ = 35 mW), inserted into the photoswitch solution and the tube was carefully lowered into the magnet. ^1H NMR spectra were acquired on a Bruker AV-III spectrometer (600 MHz) using either a cryogenically cooled 5 mm TCI-triple resonance probe equipped with one-axis self-shielded gradients. 90° pulses were determined for every sample, while delay time was set

to d1 = 18 seconds with a total of 16 scans. Spectra were phase and baseline corrected, and integrated aromatic peaks served to calculate the photostationary state of AQ and AQ_{400} in the dark, and under illumination of 385, 405, 500 or 525 nm.

Fluorescence spectroscopy *in vitro*

For measurements of fluorophore conjugated PORTLs (Figure S4) Compounds were dissolved in activity buffer (containing in mM: NaCl 50, HEPES 50, pH = 7.3, 0.1% BSA) to a final concentration of 200 nM and were transferred into Greiner black flat bottom 96 well plates and excitation and emission profiles were recorded on a TECAN INFINITE M PLEX plate reader. Experiments were run in quadruplicate. Data normalization, integration and plotting was performed in GraphPad Prism 8.

Quantum yield measurements

Quantum yields were acquired according to a published procedure (Stranius and Borjesson, 2017) on a Lambda 950 spectrophotometer (PerkinElmer), which is outlined in the supplemental information.

Molecular cloning, cell culture, and gene expression

Experiments were performed using previously described N-terminally SNAP- or CLIP-tagged rat or human mGluR(Doumazane et al., 2011) or mGluR chimeras(Acosta-Ruiz et al., 2020) and GIRK1-F137S(Vivaudou et al., 1997). The chimeric SNAP-mGluR2-mGluR1 construct was made via Gibson assembly using the extracellular domain of SNAP-tagged rat mGluR2 (K23 to E559) and rat mGluR1 transmembrane domain and C-terminal domain (Y585 to STOP).

HEK 293T cells were plated at low density on poly-L-lysine coated coverslips (18 mm) and transfected the following day using Lipofectamine 2000 (Thermo Fisher). 24-48 hrs after transfection, cells were used for electrophysiology or imaging experiments. As previously described (25), for SNAP-mGluR2 electrophysiology experiments each coverslip received SNAP-mGluR2, GIRK1-F137S and tdTomato as a transfection marker. For calcium imaging experiments, each coverslip received the receptor of interest plus GCaMP6f(Chen et al., 2013). For potassium channel experiments, cells were co-transfected with $K_v1.1$(Lesage et al., 1992) and eYFP using the calcium phosphate method with a total amount 3.6 μg of DNA and a ratio of 5:1.

For DRG cultures, Dorsal Root Ganglion tissues were collected from female mice and treated with a mix of 2 mg/ml collagenase type II, 5 mg/ml Dispase and 5 mM $CaCl_2$ for ~ 20 minutes twice. Neurons were dissociated by triturating through needles of 21G and 26G then seeded on poly-lysine and laminin coated coverslips. The NeuroBasal A-based culture medium contained 1x B27, 2 mM L-glutamine, 100 ng/ml NGF, 10 ng/ml NT3, 2 ng/ml GDNF, 10 ng/ml BDNF, 30 ng/ml Retinoic acid and a mix Penitrem A/Streptomycin.

HEK 293T and DRG electrophysiology

Whole cell patch clamp recordings from HEK 293T cells expressing SNAP-mGluR2 were performed as previously described (Acosta-Ruiz et al., 2020). Briefly, voltage clamp recordings at -60 mV were performed in a high potassium (120 mM) solution to enable large inward currents upon receptor activation. Cells were incubated with 1-10 μM of PORTL for 45-60 min at 37 °C in the appropriate extracellular recording solution. Labeling efficiency was determined as previously described[25]. Illumination was applied to the entire field of view using a CoolLED pE-4000 through a 40× objective. Light intensity in the sample plane was 1-2 mW/mm^2. pClamp software was used for data acquisition, control of illumination and data analysis.

Whole cell patch clamp recordings from HEK 293T cells expressing $K_v1.1$ were performed using glass pipettes of resistance between 3 and 6 MΩ filled with intracellular solution containing (in mM): 155 KCl, 5 EGTA, 3 $MgCl_2$, 10 HEPES, pH 7.3. The extracellular bath solution contained (in mM): 150 NaCl, 5 KCl, 2 $CaCl_2$ and 10 HEPES. Cells were voltage clamped using a MultiClamp700B (Molecular Devices) amplifier in the whole cell mode. The holding potential was set to -80 mV and stepped to -20 mV to elucidate K^+ currents. Illumination was controlled using a Lambda DG4 high speed wavelength switcher (Sutter) with 380 nm and 500 nm filters through a 40× objective. Light intensity in the sample plane was 10-20 mW/mm^2. pClamp software was used for data acquisition, control of illumination and data analysis.

Whole cell patch clamp recordings from small-diameter (<25 μm) DRG neurons were performed in extracellular solution containing (in mM): 140 NaCl, 5 KCl, 1 $MgCl_2$, 2 $CaCl_2$, 10 HEPES, 10 glucose, pH 7.4 with NaOH. Glass pipettes were pulled with a resistance < 5 MΩ and filled with intracellular solution containing (in mM): 155 KCl, 5 EGTA, 3 $MgCl_2$, 10 HEPES, pH 7.3 with KOH. Neurons were patch clamped using an Axopatch 200B (Molecular Devices) amplifier in the whole cell mode. Series resistance (< 10 MΩ) was not compensated. Signals were filtered at 10 kHz and digitized at 20 kHz. After establishing whole-cell access, membrane capacitance was determined with amplifier circuitry. The amplifier was then switched to current-clamp mode to measure resting membrane potential (Vrest). Neurons were excluded from analysis if the Vrest was higher than -40 mV. To test neuronal excitability, neurons were held at Vrest and injected with 1 s depolarizing 25 pA currents in steps.

Calcium imaging

HEK 293T cells were imaged with a 20x objection on an inverted microscope (Olympus IX-73) at room temperature in extracellular solution containing (in mM): 135 NaCl, 5.4 KCl, 10 HEPES, 2 $CaCl_2$, 1 $MgCl_2$, pH = 7.4 with continuous perfusion. Calcium indicator GCaMP6f was excited using a 488 nm laser at 0.5 Hz with a 100 ms exposure time. For photoactivation, a 500 ms flash of 385 nm light from a CoolLED pE-4000 or of UV light from a CoolLED pE-300 ultra was applied just after each frame. Time lapse movies were recorded with an scMOS camera (Hamamatsu ORCA-Flash4v3.0). Experiments using spatial light targeting were done on a Zeiss LSM880 scanning confocal microscope using ZEN Black software with a 63x objective, a 488 nm laser for imaging and a 405 nm

laser for photoactivation. Photoactivation was performed by scanning a 405 nm laser at 100% power in a defined region for 40 iterations between each imaging frame. Image analysis was performed using ZEN (Zeiss) and ImageJ (Fiji) (Schindelin et al., 2012) and calculations of oscillation frequency and Ca^{2+} wave velocity were performed as previously described (Acosta-Ruiz et al., 2020).

Viral expression and *in vivo* PORTL labeling

Experiments were conducted as previously described (Acosta-Ruiz et al., 2020). Briefly, male Grm2-Cre heterozygous mice were injected at p60 in the mPFC (AP + 1.85, ML +/- 0.35, DV -2.2, -1.8) with 500-1,000 nL per hemisphere of either AAV9-EF1a-FLEX-SNAP-mGluR2-WPRE-hGH or AAV9-CAG-FLEX-GFP (Oh et al., 2014) using a Kopf stereotaxic and World Precision Instruments microinjection syringe pump with a 10 μL syringe and 33g blunt needle. All imaging and slice experiments were performed at least 6 weeks after viral injection.

For behavioral experiments, custom Dual opto-fluid cannulas with interchangeable injectors (Doric Lenses) were implanted to target bilateral mPFC (cannula: AP +1.85, ML +/-0.35, DV -1.5, fiberoptic: AP +1.85, ML +/-0.35, DV -1.8) and adhered to the scull using C & B Metabond (Parkell). Prior to behavioral tests, both experimental and control mice were anesthetized using isoflurane and dual opto-cannula plugs were replaced with 100 μm inner diameter micro-injectors. 10 μM $BGAG_{12,400}$-Cy5 was infused through micro-injectors at 100 nl per minute for a total of 1000 nL per hemisphere using polyethylene tubing connected to a Harvard Apparatus (Harvard Biosciences, Inc.) 11 Elite dual syringe infusion pump and 10 μl Hamilton Company syringes. Micro-injectors were then replaced with optical fibers with 200 μm diameter and 0.22 numerical aperture (NA).

Acute brain slice electrophysiology

Slice preparation was performed as previously described (Acosta-Ruiz et al., 2020), with the following modifications. Briefly, 12–16 hours following microinfusions of 10 μM $BGAG_{12}$-Cy5 or $BGAG_{12,400}$-Cy5 in the medial prefrontal cortex (mPFC), mice were deeply anesthetized with isoflurane and perfused with ice-cold NMDG-HEPES aCFS (in mM): 93 NMDG, 2.5 KCl, 1.2 NaH_2PO_4, 30 $NaHCO_3$, 20 HEPES, 25 Glucose, 5 sodium ascorbate, 2 thiourea, 3 sodium pyruvate, 10 $MgSO_4$, 0.5 $CaCl_2$. 300 μm coronal slices of the mPFC were collected in the same solution and kept for 30 min at 34 °C, followed by at least 45 minutes at room temperature in a modified HEPES aCSF containing (in mM): 92 NaCl, 2.5 KCl, 1.2 NaH_2PO_4, 30 $NaHCO_3$, 20 HEPES, 25 Glucose, 5 sodium ascorbate, 2 thiourea, 3 sodium pyruvate, 2 $MgSO_4$, 2 $CaCl_2$. Solutions were pH-corrected to 7.4, 300-310 mOsm and were continuously bubbled with 95% O_2/5% CO_2

Recordings were performed at 29-31 °C in a standard oxygenated aCSF containing (in mM): 124 NaCl, 2.5 KCl, 1.2 NaH_2PO_4, 24 $NaHCO_3$, 5 HEPES, 12.5 Glucose, 1.3 $MgSO_4$, 2.5 $CaCl_2$. Whole-cell patch-clamp recordings were performed on a computer-controlled amplifier (MultiClamp 700B Axon Instruments, Foster City, CA) and acquired with an Axoscope 1550B (Axon Instruments) at a sampling rate of 10 kHz in current clamp and 500 Hz for current-evoked firing. For current clamp experiments, pipettes of 3-7 MΩ resistance were filled with a solution containing (in mM): 130 K-Gluconate, 4 KCl, 10 HEPES, 0.3 EGTA, 10 Na_2-phosphocreatine, 4 Mg-ATP, 0.3 Na_2-GTP, 13.4 Biocytin, pH 7.35, 280-290 mOsm.

For both visualizing of Cy5 fluorescence and photoswitching, we used a CoolLED pE-400 coupled to the microscope and filtered through an Olympus U-MF2 filter cube with a 635 BrightLine Beamsplitter and 692/40 emission filter. Light intensity for photoswitching at the sample was 1-2 mW/mm^2 and light stimulation protocols were automated using pClamp. All data was analyzed in Clampfit and Prism (Graphpad Software, Inc.).

Y-Maze behavior

All behavior was performed 6 to 10 weeks after virus injection and 12 to 16 hours after $BGAG_{12,400}$-Cy5 injection. Experiments were conducted as previously described (Acosta-Ruiz et al., 2020). Briefly, dual fiberoptic cannulas were connected to a dual fiberoptic patchcord (200 μm diameter per cord, Doric) to a fiberoptic rotary joint (Doric) and then attached to a mono fiberoptic patch chord (400 μm, Doric) connected to a 4 Channel LED Driver (LEDD_4) and a 12V Fan Power Adaptor (FPA). The LED unit was manipulated via Doric Neuroscience studio software (DORIC STUDIO V5.3.3.6). During light stimulation, 3 2-second pulses of 385 nm or 515 nm light were delivered in triplicate with a 2-second interval, followed by a delay interval of 108 seconds and repeated continuously until the paradigm was completed. The light stimulation protocol was immediately started when mice entered the maze. Mice received 2 minutes of 515 nm light followed by 4 minutes of 385 nm light. Mice were tracked using SMART software (Harvard Apparatus) and the number of spontaneous alterations were counted for 6 minutes.

QUANTIFICATION AND STATISTICAL ANALYSIS

Statistical analysis was performed using Microsoft Excel, SigmaPlot (Systat Software Inc.), GraphPad (GraphPad Software Inc.) for all *in vitro* experiments, HEK293T and rodent physiology and behavior. Individual statistical methods are indicated in the figure legends. Statistical significance is indicated in the text and figure legends as $*p < 0.05$, $**p < 0.01$ and $***p < 0.001$. No additional methods beyond the statistical tests stated in the text and figured legends were used to determine whether the data met assumptions of the statistical approach.

Additional resources

Synthetic schemes

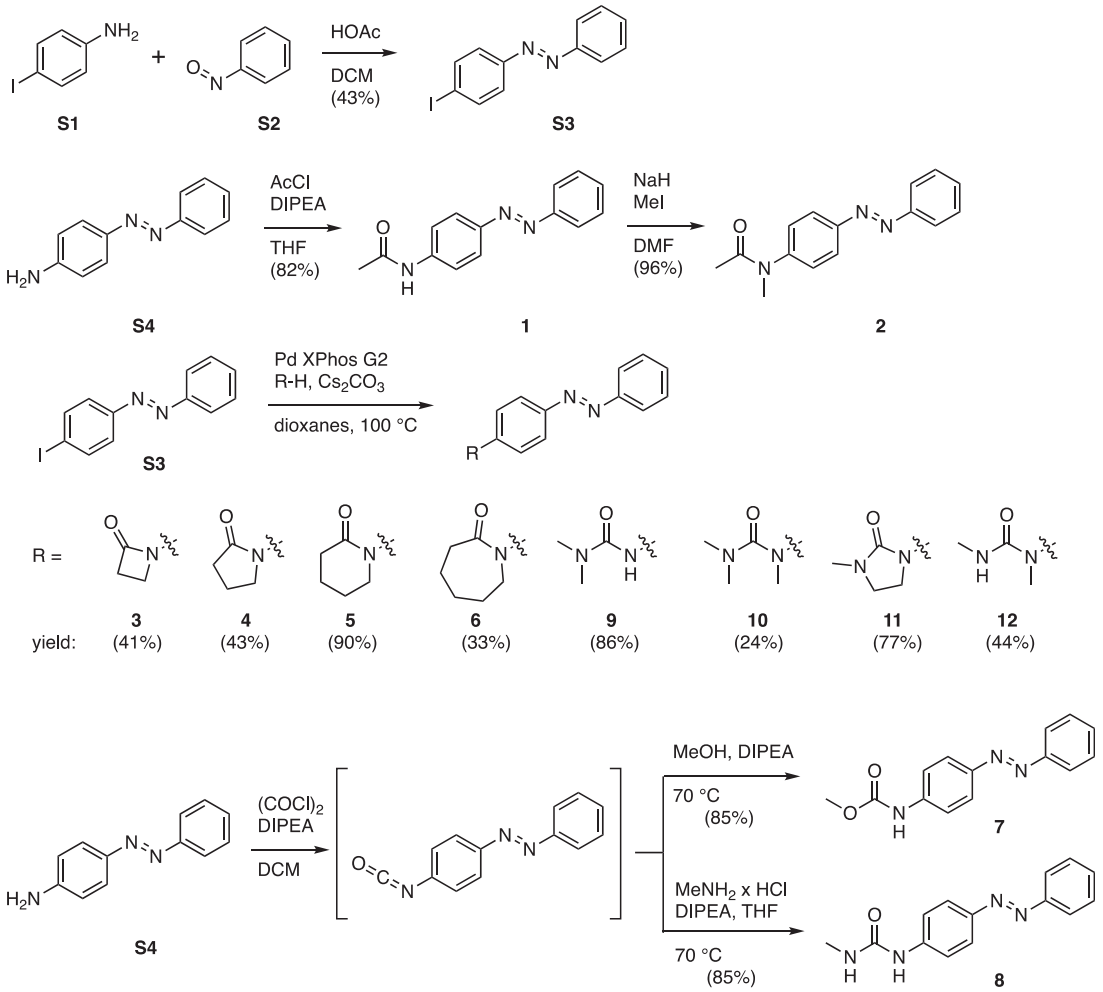

Methods Scheme 1: Synthesis of an azobenzene library.

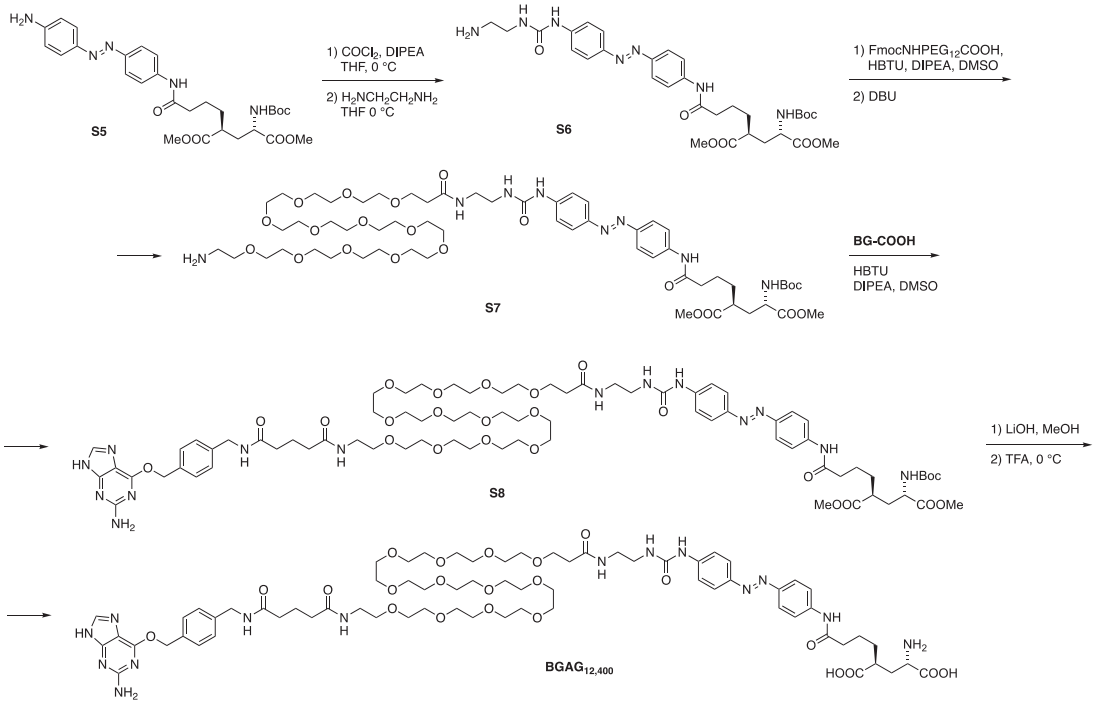

Methods Scheme 2: Synthesis of $BGAG_{12,400}$.

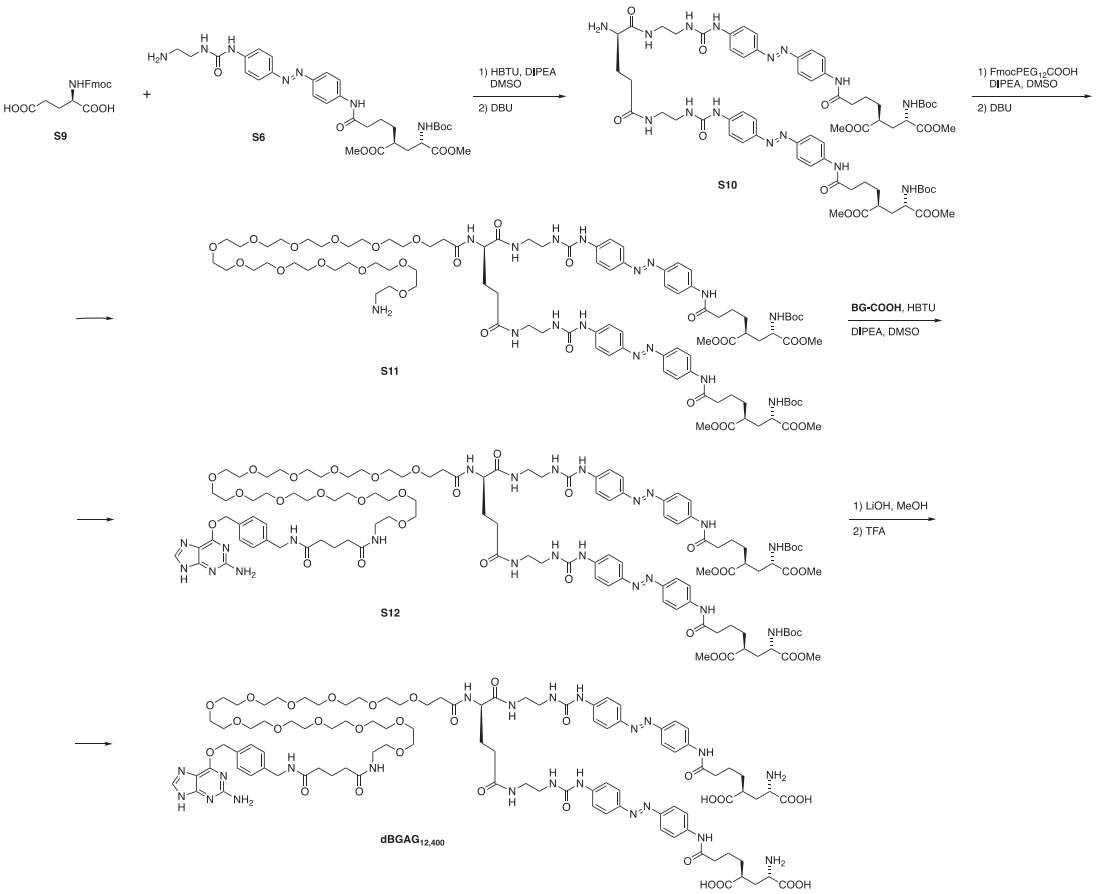

Methods Scheme 3: Synthesis of $^{2x}BGAG_{12,400}$.

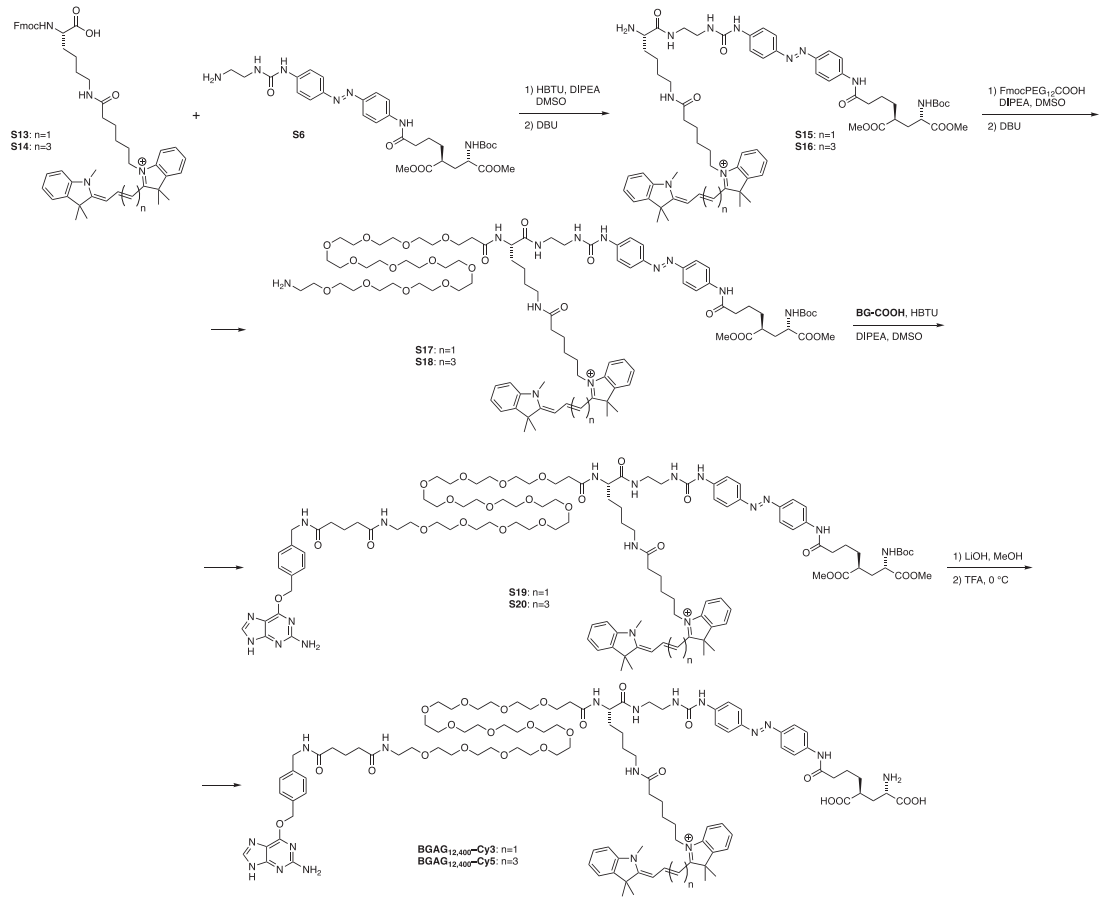

Methods Scheme 4: Synthesis of $BGAG_{12,400}$-Cy3 and $BGAG_{12,400}$-Cy5.

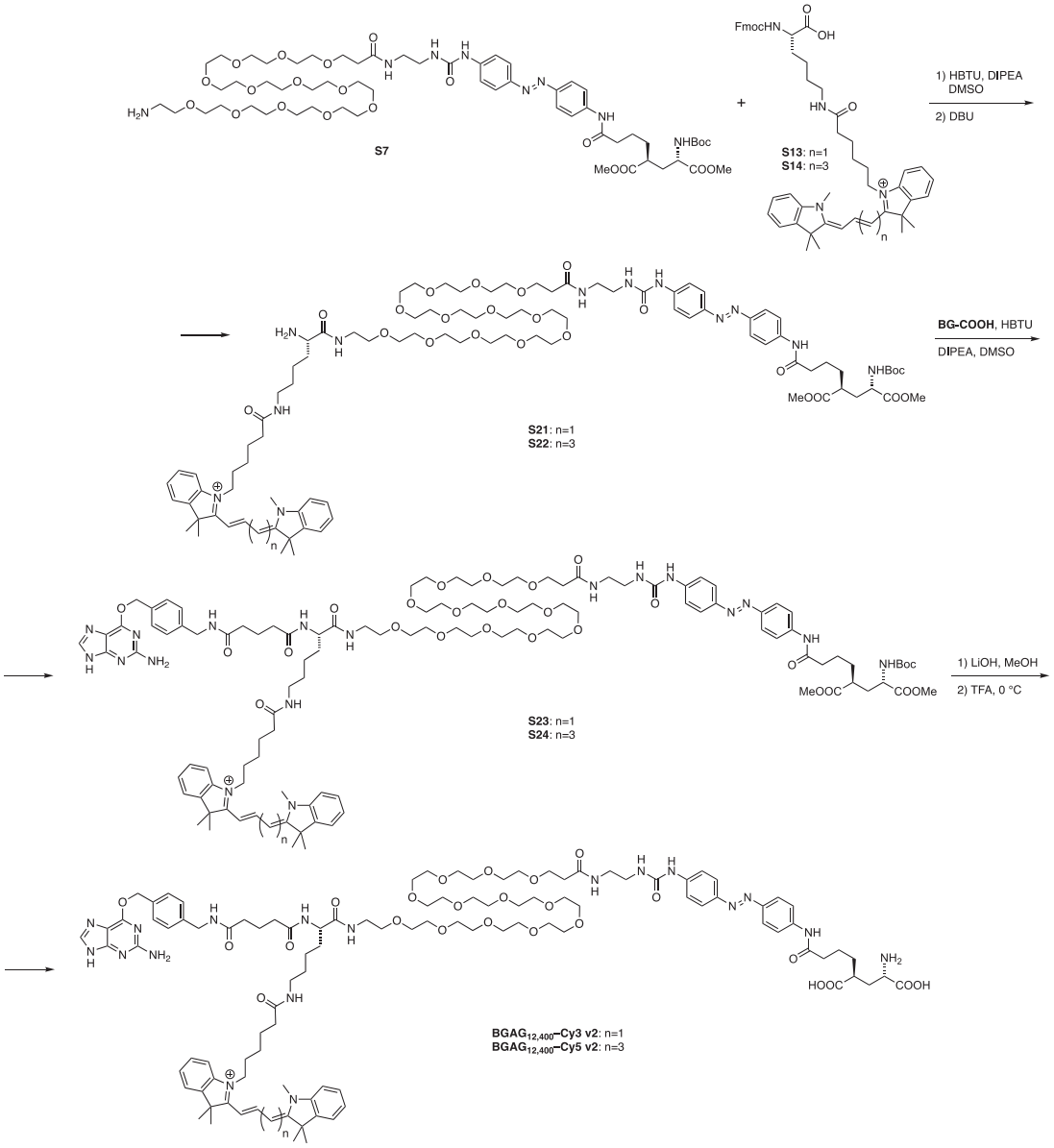

Methods Scheme 5: Synthesis of $BGAG_{12,400}$-$Cy3_{v2}$ and $BGAG_{12,400}$-$Cy5_{v2}$.

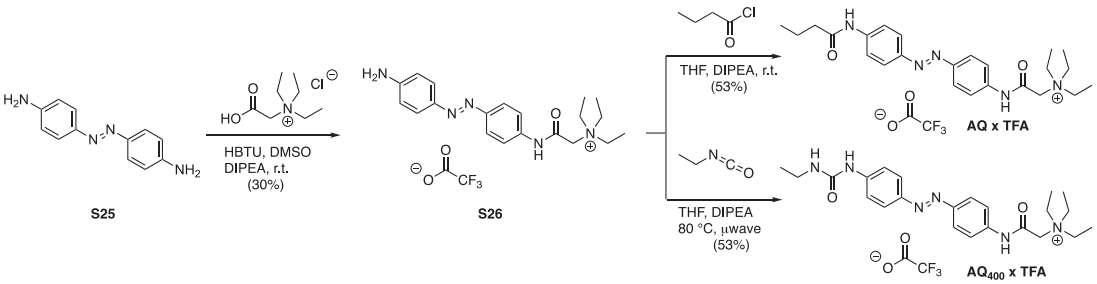

Methods Scheme 6: Synthesis of AQ and AQ_{400}.

Cell Chemical Biology, Volume *28*

Supplemental information

A fine-tuned azobenzene

for enhanced photopharmacology *in vivo*

Vanessa A. Gutzeit, Amanda Acosta-Ruiz, Hermany Munguba, Stephanie Häfner, Arnaud Landra-Willm, Bettina Mathes, Jürgen Mony, Dzianis Yarotski, Karl Börjesson, Conor Liston, Guillaume Sandoz, Joshua Levitz, and Johannes Broichhagen

Supplementary Information for:

A fine-tuned azobenzene for enhanced photopharmacology *in vivo*

Vanessa A. Gutzeit[1#], Amanda Acosta-Ruiz[2#], Hermany Munguba[3], Stephanie Häfner[4,5], Arnaud Landra-Willm[4,5], Bettina Mathes[6], Jürgen Mony[7], Dzianis Yarotski[6], Karl Börjesson[7], Conor Liston[8], Guillaume Sandoz[4,5], Joshua Levitz[1,2,3*%], Johannes Broichhagen[6,9*]

[1] Neuroscience Graduate Program, Weill Cornell Medicine, New York, NY 10065, USA.

[2] Biochemistry, Cell and Molecular Biology Graduate Program, Weill Cornell Medicine, New York, NY 10065, USA.

[3] Department of Biochemistry, Weill Cornell Medicine, New York, NY 10065, USA.

[4] Université Cote d'Azur, CNRS, INSERM, iBV, France.

[5] Laboratories of Excellence, Ion Channel Science and Therapeutics Nice, France.

[6] Department of Chemical Biology, Max Planck Institute for Medical Research, Jahnstr. 29, 69120 Heidelberg, Germany.

[7] Department of Chemistry and Molecular Biology, University of Gothenburg, Kemigården 4, 412 96 Gothenburg, Sweden

[8] Department of Psychiatry and Brain and Mind Research Institute, Weill Cornell Medicine, New York, NY 10065, USA.

[9] Department of Chemical Biology, Leibniz-Forschungsinstitut für Molekulare Pharmakologie, Robert-Rössle-Str. 10, 13125 Berlin, Germany.

[#] These authors contributed equally

* To whom correspondence should be addressed: broichhagen@fmp-berlin.de or jtl2003@med.cornell.edu

1. *Supplementary Figures:*

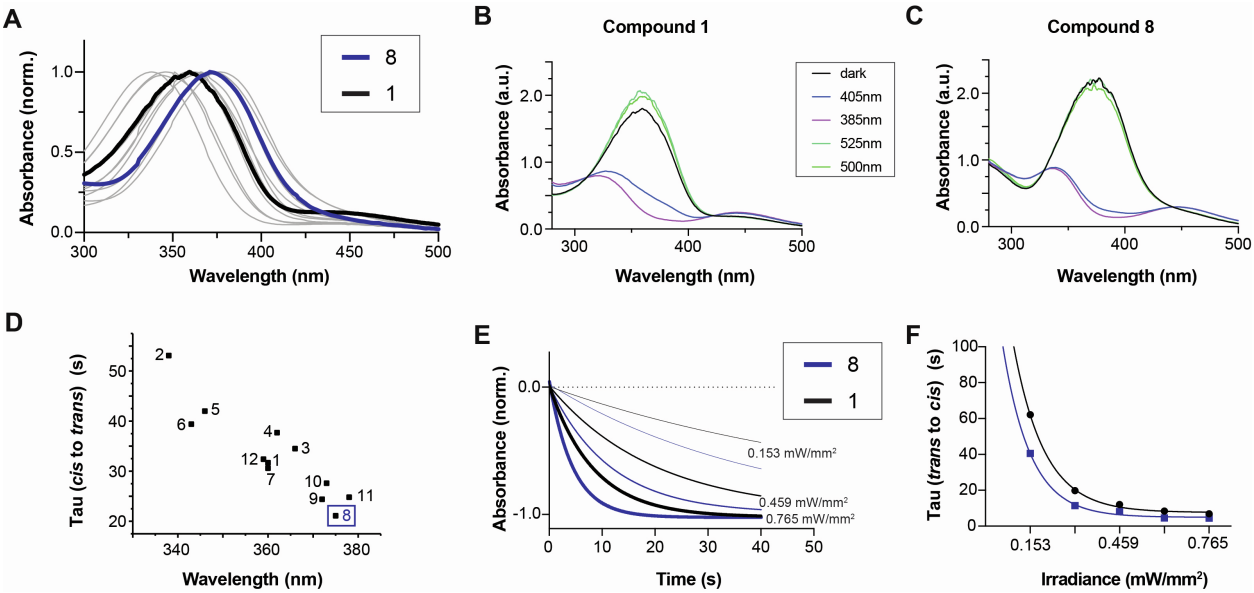

Figure S1. Photophysical Characterization of Azobenzene Test Compounds, Related to Figure 1.

(A) Normalized UV/Vis Absorbance spectra for all compounds at 50 μM in DMSO at room temperature. The shift between compound 8 (blue) and compound 1 (black) is highlighted.

(B-C) UV/Vis absorption spectra of Compound 1 and Compound 8 in the dark and under illumination with different wavelengths of light showing clear UV photoconversion which is enhanced at 405 nm for Compound 8.

(D) Summary of *cis* to *trans* photoswitching kinetics for all compounds in response to 500 nm illumination under identical conditions (50 μM, DMSO, RT).

(E-F) Kinetics of *trans* to *cis* photoswitching for compound 1 and 8 in response to different light intensities at 385 nm recorded at 360 nm.

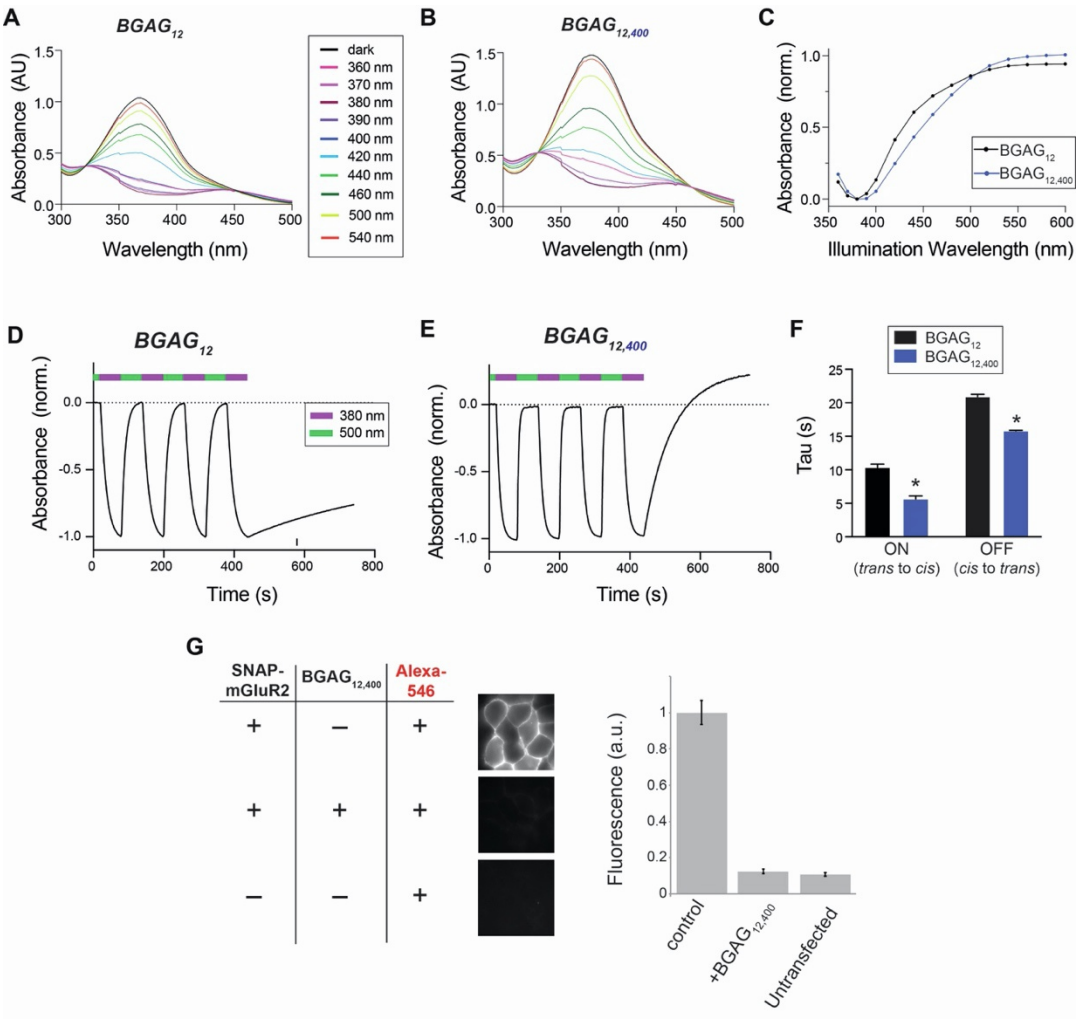

Figure S2. Further Characterization of BGAG$_{12,400}$, Related to Figure 2.

(A-B) UV/Vis absorbance spectra for BGAG12 (A) and BGAG12,400 (B) in the dark and in response to a wide range of illumination wavelengths. All measurements are taken at 50 μM in PBS at room temperature.

(C) Summary of absorbance at the *trans* peak for BGAG$_{12}$ (366 nm) and BGAG$_{12,400}$ (378 nm) in response to different wavelengths of light. Note that both PORTLs show maximal cis occupancy around 380-390 nm but a clear red-shift is observed for BGAG$_{12,400}$.

(D-E) *in vitro* photoswitching of BGAG$_{12}$ and BGAG$_{12,400}$ in response to 385 and 500 nm as assessed by measuring absorbance at the *trans* peak (I = 1-2 mW/mm^2).

(F) Summary of photoswitching kinetics for BGAG12 and BGAG12,400 obtained from single exponential fits to multiple bouts of illumination with 385 nm (ON; *trans* to *cis*) or 500 nm illumination (OFF; *cis* to *trans*). * indicates statistical significance (unpaired t-test; p=0.0005 for ON, p=0.0002 for OFF).

(G) 10 μM BGAG$_{12,400}$ is able to nearly completely label SNAP-mGluR2 and prevent subsequent labeling by 3 μM BG-Alexa-546.

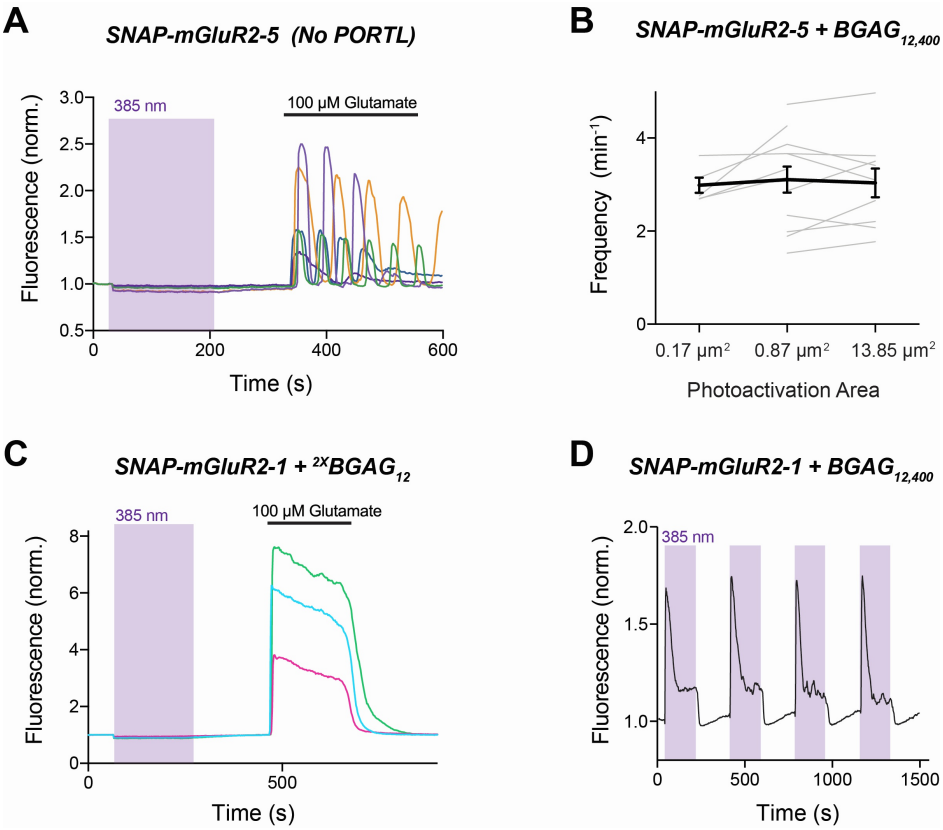

Figure S3. Further Characterization of Optical Control of Group I mGluR Signaling, Related to Figure 3.

(A) Representative calcium imaging trace showing no 385 nm light response in cells expressing SNAP-mGluR2-5 in the absence of a PORTL.

(B) Summary graph showing the calcium oscillation frequency in response to photoactivation of subcellular areas of different sizes. Gray lines represent values for individual cells while the thicker black line shows the average across all cells.

(C) Representative calcium imaging trace showing no 385 nm light response in cells expressing SNAP-mGluR2-1 following labeling with $^{2x}BGAG_{12}$.

(D) Representative trace showing repeatable 385 nm light responses in a cell expressing SNAP-mGluR2-1 and labeled with $BGAG_{12,400}$.

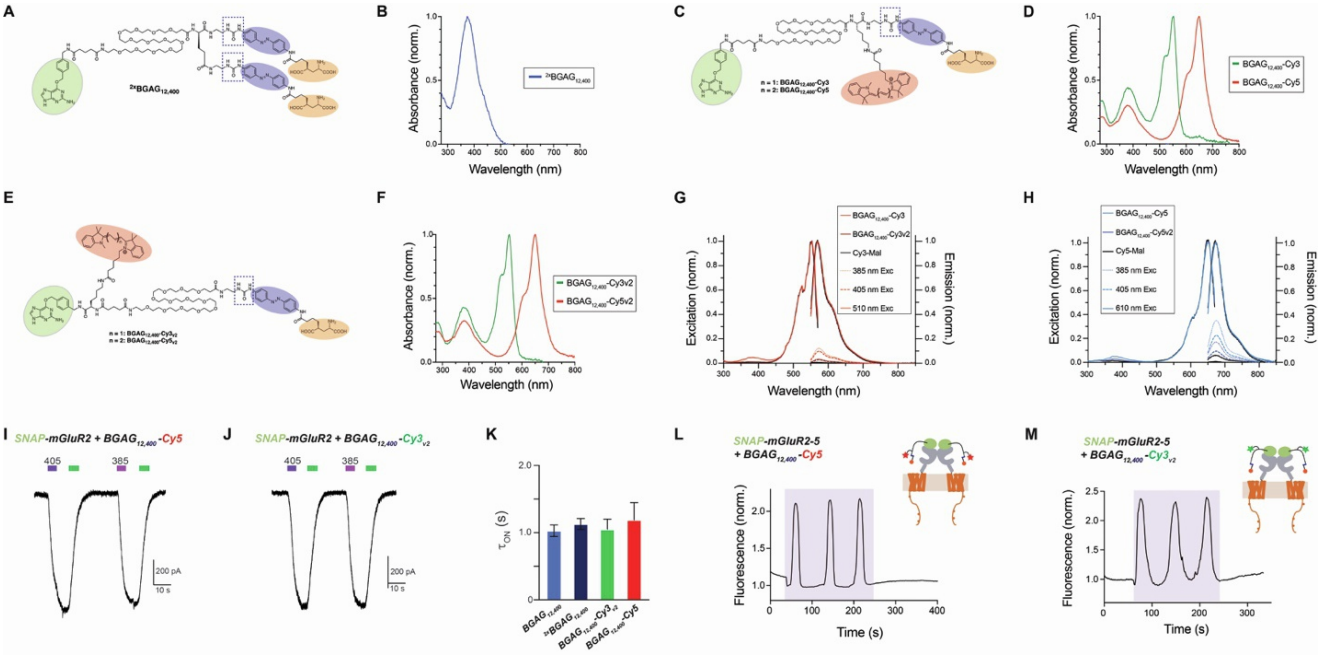

Figure S4: Further Characterization of Branched $BGAG_{12,400}$ PORTLs, Related to Figure 4.

(A-F) Chemical structures (A, C, E) and UV/Vis absorption spectra (B, D, F) for branched $BGAG_{12,400}$ PORTLs. All samples were 20 μM in PBS at room temperature.

(G) Fluorescence excitation and emission spectra of 200 nM $BGAG_{12,400}$-Cy3 and $BGAG_{12,400}$-Cy3v2 in activity buffer (50 mM NaCl, 50 mM HEPES, pH=7.3, 0.1% BSA). Emission was recorded after excitation with different wavelengths of light at 385, 405 and 510 nm.

(H) Fluorescence excitation and emission spectra of 200 nM $BGAG_{12,400}$-Cy5 and $BGAG_{12,400}$-Cy5v2 in activity buffer (50 mM NaCl, 50 mM HEPES, pH=7.3, 0.1% BSA). Emission was recorded after excitation with different wavelengths of light at 385, 405 and 610 nm.

(I-J) Representative patch clamp GIRK current traces showing similar photocurrents in response to 405 nm or 385 nm illumination for SNAP-mGluR2 conjugated to either $BGAG_{12,400}$-Cy5 (I) or $BGAG_{12,400}$-$Cy3_{v2}$ (J).

(K) Comparison of ON kinetics of SNAP-mGluR2 photo-activation by branched $BGAG_{12,400}$ variants and $BGAG_{12,400}$.

(L-M) Representative calcium imaging traces showing 385 nm induced calcium oscillations in cells expressing SNAP-mGluR2-5 and labeled with either $BGAG_{12,400}$-Cy5 (L) or $BGAG_{12,400}$-$Cy3_{v2}$ (M).

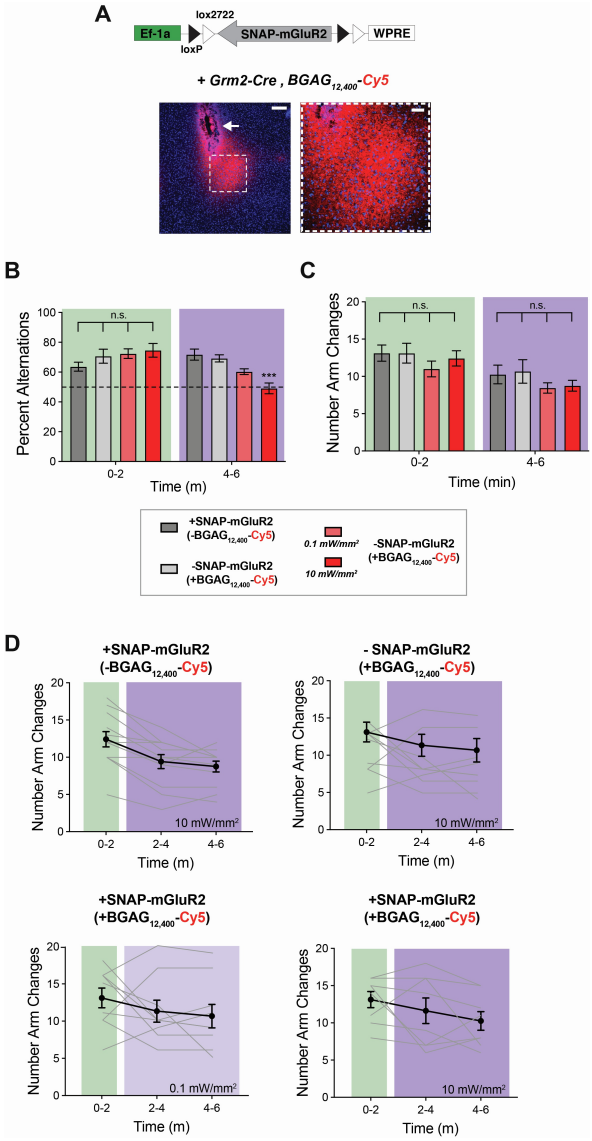

Figure S5. Further Analysis of Optical Behavioral Modulation with $BGAG_{12,400}$-Cy5, Related to Figure 5.

(A) Representative images showing AAV-mediated expression of SNAP-mGluR2 in Grm2-positive cells in the mPFC labeled with 10 µM $BGAG_{12,400}$-Cy5. Arrow indicates needle track from injection (scale bars: left=250 µm, right =50 µm).

(B) Percent alternations in the Y-maze were decreased for experimental mice during the 4 minutes they received 10 mW/mm^2 385 nm light, but not during the baseline 2 minutes. *** indicates statistical significance (1-way ANOVA, treatment F (3, 35) = 11.72, p = 0.00001; Tukey's MC test: 10 mW Exp vs. -BGAG Ctrl p = 0.0002; 10 mW Exp vs. –SNAP-mGluR2 Ctrl p = 0.000001).

(C) Control data showing that SNAP-mGluR2 photoactivation with $BGAG_{12,400}$-Cy5 does not alter the total number of arm entries in the Y maze during the 2 min baseline or after 4 min of activation compared to controls.
(D) Summary of Y-maze control behavioral analysis, where all groups show a similar number of arm entries over time.

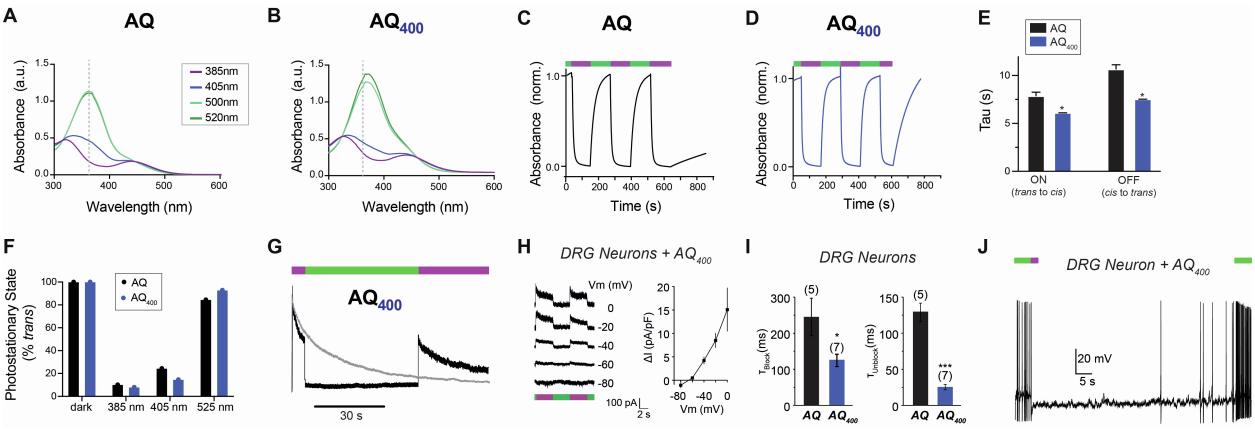

Figure S6. Further characterization of AQ_{400}, Related to Figure 6.

(A-B) UV/Vis absorption spectra of 50 µM AQ_{12} (A) and $AQ_{12,400}$ (B) in the dark and under illumination with different wavelengths of light in PBS at room temperature.

(C-D) *in vitro* photoswitching of AQ and AQ_{400} in response to 385 and 500 nm as assessed by measuring absorbance at the *trans* peak (I = 1-2 mW/mm^2).

(E) Summary of photoswitching kinetics for AQ and AQ_{400} obtained from single exponential fits to multiple bouts of illumination with 385 nm (ON; *trans* to *cis*) or 500 nm illumination (OFF; *cis* to *trans*). * indicates statistical significance (unpaired t-test; p=0.01 for ON, p=0.006 for OFF).

(F) Photostationary states assessed by ^1H NMR for AQ and AQ_{400} under different wavelengths of light by integrating the aromatic protons (powers used: $P_{385\ nm}$ = 101 mW; $P_{405\ nm}$ = 188 mW; $P_{500\ nm}$ = 58 mW; $P_{525\ nm}$ = 35 mW).

(G) Representative trace from a HEK 293 cell showing that 505 nm (green) induced pore-block by AQ_{400} slows inactivation of Kv1.1 based on the maintained current level before and after 505 nm illumination. A representative trace of a cell without a photoswitchable blocker in the pipette solution shows the normal slow inactivation of Kv1.1

(H) Left, representative whole-cell current recordings from DRG neurons in the presence of AQ_{400} (100 µM). Alternating illumination at 505 nm (green) and 385 nm (magenta) reversibly blocks and unblocks outward current elicited at different holding potentials. Right, current-voltage relationship of the relative photocurrent induced by alternating illumination (I_{385nm} - I_{505nm}) for different holding potentials in DRGs.

(I) AQ_{400} shows enhanced kinetics of photo-block in DRG neurons. * indicates statistical significance (unpaired t-test, $p<0.05$ for τ_{Block} and $p<0.001$ for $\tau_{Unblock}$). Data was assessed by analyzing the first ten blocking events per cell.

(J) Representative current clamp trace from a DRG neuron showing that 385 nm-induced receptor unblock leads to decreased firing which is stable in the dark for an extended ~60 s period.

2. *Methods S1: Chemical Synthesis, Related to STAR methods.*

2.1. General

Solvents for chromatography and reactions were purchased dry over molecular sieves or in HPLC grade. Unless otherwise stated, all other reagents were used without further purification from commercial sources. FmocNHPEG$_{12}$COOH was obtained from broadpharm (BP-21623).

LC-MS was performed on i) a Shimadzu MS2020 connected to a Nexera UHPLC system equipped with a Waters ACQUITY UPLC BEH C18 (1.7 µm, 50 × 2.1 mm). Buffer A: 0.1% FA in H_2O Buffer B: acetonitrile. The typical gradient was from 10% B for 0.5 min → gradient to 90% B over 4.5 min → 90% B for 0.5 min → gradient to 99% B over 0.5 min with 1 mL/min flow, or ii) an Agilent 1260 Infinity II LC System equipped with Agilent SB-C18 column (1.8 µm, 2.1 × 50 mm). Buffer A: 0.1% FA in H_2O Buffer B: 0.1% FA acetonitrile. The typical gradient was from 10% B for 0.5 min → gradient to 95% B over 5 min → 95% B for 0.5 min → gradient to 99% B over 1 min with 0.8 mL/min flow. Retention times (tR) are given in minutes (min).

High resolution mass spectrometry was performed using a Bruker maXis II ETD hyphenated with a Shimadzu Nexera system. The instruments were controlled *via* Brukers otofControl 4.1 and Hystar 4.1 SR2 (4.1.31.1) software. The acquisition rate was set to 3 Hz and the following source parameters were used for positive mode electrospray ionization: End plate offset = 500 V; capillary voltage = 3800 V; nebulizer gas pressure = 45 psi; dry gas flow = 10 L/min; dry temperature = 250 °C. Transfer, quadrupole and collision cell settings are mass range dependent and were fine-adjusted with consideration of the respective analyte's molecular weight. For internal calibration sodium format clusters were used. Samples were desalted *via* fast liquid chromatography. A Supelco Titan^{TM} C18 UHPLC Column, 1.9 µm, 80 Å pore size, 20 × 2.1 mm and a 2 min gradient from 10 to 98% aqueous MeCN with 0.1% FA (H_2O: Carl Roth GmbH + Co. KG ROTISOLV® Ultra LC-MS; MeCN: Merck KGaA LiChrosolv® Acetonitrile hypergrade for LC-MS; FA - Merck KGaA LiChropur® Formic acid 98%-100% for LC-MS) was used for separation. Sample dilution in 10% aqueous ACN (hyper grade) and injection volumes were chosen dependent of the analyte's ionization efficiency. Hence, on-column loadings resulted between 0.25–5.0 ng. Automated internal re-calibration and data analysis of the recorded spectra were performed with Bruker's DataAnalysis 4.4 SR1 software.

NMR spectra were recorded in deuterated solvents on a Bruker AVANCE III HD 400 equipped with a CryoProbe or on a Bruker AV-III spectrometer (600 MHz) using either a cryogenically cooled 5 mm TCI-triple resonance probe equipped with one-axis self-shielded gradients and calibrated to residual solvent peaks ($^{1}H/^{13}C$ in ppm): DMSO-d_6 (2.50/39.52), acetone-d_6 (2.05/29.84), $CDCl_3$ (7.26/77.0), D_2O (4.70). Multiplicities are abbreviated as follows: s = singlet, d = doublet, t = triplet, q = quartet, p = pentet, h =

hexet, br = broad, m = multiplet. Coupling constants *J* are reported in Hz. Spectra are reported based on appearance, not on theoretical multiplicities derived from structural information.

Preparative RP-HPLC was performed on a Waters e2695 system equipped with a 2998 PDA detector for product collection (at 220, 280, 370 or 460 nm) on a Supelco Ascentis® C18 HPLC Column (5 µm, 250 × 21.2 mm). Buffer A: 0.1% TFA in H_2O Buffer B: acetonitrile. The typical gradient was from 10% B for 5 min → gradient to 90% B over 45 min → 90% B for 5 min → gradient to 99% B over 5 min with 8 mL/min flow.

Compounds **S5**, and **BG-COOH** were previously described (Broichhagen et al., 2015; Levitz et al., 2017).

2.2. Abbreviations

Boc: *tert*-butoxycarbonyl; DIPEA: *N*,*N*-di*iso*propylethylamine; DBU: 1,8-diazabicyclo[5.4.0]undec-7-ene; DCM: dichloromethane; DMF: *N*,*N*-dimethylformamide; DMSO: dimethylsulfoxide; FA: formic acid; Fmoc: fluorenylmethyloxycarbonyl; HBTU: (2-(1*H*-benzotriazol-1-yl)-1,1,3,3-tetramethyluronium hexafluorophosphate; TFA: trifluoroacetic acid; THF: tetrahydrofuran, TSTU: *N*,*N*,*N*′,*N*′-Tetramethyl-*O*-(*N*-succinimidyl)uronium tetrafluoroborate.

2.3. General procedure A for Buchwald-Hartwig cross coupling

A flame-dried Schlenk flask was charged with (*E*)-1-(4-iodophenyl)-2-phenyldiazene (**3**) (1.0 equiv.), Pd XPhos G2 (0.1 equiv.), Cs_2CO_3 (2.4 equiv.), and the corresponding nitrogen-containing coupling partner (1.2 equiv.) dissolved in dry 1,4-dioxanes (144 equiv.) under an argon atmosphere. The reaction mixture was heated to reflux over night, before all volatiles were removed *in vacuo*, and the resulting residue subjected to either FCC or HPLC purification.

2.4. General procedure B for peptide coupling

A 4 mL vial was charged with 1.0 equiv. of acid and 1.0 equiv. of amine dissolved in DMSO (1 mL / 10 mg) and 4.0 equiv. of DIPEA before 1.1 equiv. of HBTU was added in one portion (for amounts <1 mg of HBTU, stock solutions were prepared). Upon complete conversion according to LCMS (usually ~3 h), 4.0 equiv. of HOAc and 10 vol% water was added to the reaction mixture and the solution was subjected to RP-HPLC. Reaction scales were <100 nmol.

2.5. General procedure C for peptide coupling and Fmoc deprotection

A 4 mL vial was charged with 1.0 equiv. amine dissolved in DMSO (1 mL / 10 mg) and 4.0 equiv. DIPEA. The acid (1.2 equiv.) and HBTU (1.2 equiv.) were added in one portion and the reaction mixture was allowed to stir at r.t. Upon complete conversion according to LCMS (usually ~3 h), 5 vol% of DBU was

added and the reaction mixture was stirred for additional 10 minutes, before it was quenched by addition of 10 vol% HOAc and subjected to RP-HPLC. Reaction scales were <100 nmol.

2.6. General procedure D for ester saponification and Boc deprotection

A 15 mL falcon tube was charged with protected compound and MeOH/1 M LiOH (1/1) was added and the resulting suspension was allowed to incubate for 45 min before it was quenched with glacial HOAc (5 vol% of the reaction volume under which the reaction clarified) and subjected to RP-HPLC. The freeze-dried product was put on ice and pre-cooled (4 °C) TFA was added neat. The reaction mixture was vortexed to ensure homogeneity and put back on ice for 15 min before all volatiles were removed under a gentle stream of nitrogen. The residue was taken up in DMF/water (9/1) and subjected to RP-HPLC. Reaction scales were <100 nmol.

NOTE: Azobenzene containing reaction mixtures turned deep red upon addition of TFA.

NOTE: It is feasible to cryo-freeze the ester cleaved product in liquid nitrogen with subsequent lyophilization and reuptake of the residue in neat TFA at 0 °C for quicker synthesis, however, we observed more side products which were not further characterized according to LCMS.

2.7. Determination of extinction coefficients by weighing

Compounds **1-12** were weighed using an ultrafine balance (m > 1 mg) into 1.5 mL Eppendorf tubes and 100 µL dry DMSO was added using an Eppendorf pipette to achieve a working solution according to equation (1):

$$c_{stock} = n / V = m / (M*V) \quad (1)$$

Stock solutions were further diluted to 1/100 or 1/200 in DMSO (dilution factor f = 100 or 200) and absorbance was assessed using a NanoDrop (2 µL; d = 0.1 mm) or a TECAN Spark platereader (100 µL; d = 0.56 mm). Extinction coefficients were calculated according to Lambert-Beer's law (2) using maximal absorbance value at wavelength X:

$$\varepsilon = (A_{X\ nm} * f) / (c_{stock}*d) \quad (2)$$

Solutions were capped and parafilm wrapped for storage and future use.

All measurements were performed in triplicates from three independent prepared samples.

2.8. Determination of extinction coefficients by NMR

AQ, AQ_{400}, $BGAG_{12}$ and $BGAG_{12,400}$ were dissolved in deuterated PBS (lyophilizing 5 mL of PBS and reuptake in 5 mL D_2O) with 2,2,2-trifluoroethanol (analytical standard for NMR, Aldrich, #91683) serving as an internal standard for NMR spectroscopy to determine concentrations by signal integration (relaxation delay = 18 s). Samples were transferred to a NMR tube and capped, and heated to 60 °C with subsequent

cooling in the dark to ensure all-trans before recording spectra. NMR samples were then diluted in PBS and measured on a JASCO V-550 and maximal absorbance values were used to calculate extinction coefficients with determined concentrations according to Lambert-Beer (3):

$$\varepsilon = (A_{X\ nm}) / (c_{NMR}*d) \quad (3)$$

The spectra were using Hellma quartz glass cuvettes (10 mm pathlength).

2.9. Determination of concentrations

Mole numbers for reactions were determined by dissolving the parent compound in a volume (V) ~ 10 mg/mL in DMSO and diluting into DMSO or PBS (dilution factor; f = 20 or 50) before measuring absorbance A at a NanoDrop (d = 0.1 mm). Calculations were performed according to equation 4:

$$n = c*V = A*f*V / \varepsilon*d \quad (4)$$

Extinction coefficients used for fluorophores:

ε (Cy3 @ 545 nm) = 150,000 M^{-1} cm^{-1}

ε (Cy5 @ 645 nm) = 250,000 M^{-1} cm^{-1}

2.10. Compound S3

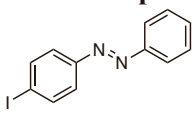

(E)-1-(4-Iodophenyl)-2-phenyldiazene

A round bottom flask was charged with 2.05 g (9.35 mmol, 1.0 equiv.) of 4-iodoaniline (**S1**) and 1.00 g (9.35 mmol, 1.0 equiv.) of nitrosobenzene (**S2**) dissolved in 100 mL DCM and 10 mL HOAc. The green reaction mixture was stirred for 24 h, turning to a dark brown solution, before it was quenched by addition of sat. aq. $NaHCO_3$ and extracted with DCM (3 x 200 mL). The combined organic layers were washed with water and brine, dried over $MgSO_4$, concentrated *in vacuo*, and the resulting solution subjected to FCC (DCM/hexanes = 1/5) to obtain 1.25 g (4.06 mmol) of the desired compound and an orange powder in 43% yield. Single crystals could be obtained by recrystallization from acetone.

^{1}H NMR (400 MHz, acetone-d_6): δ [ppm] = 8.00 (d, J = 8.6 Hz, 2H), 7.94 (dd, J = 7.7, 2.0 Hz, 2H), 7.73 (d, J = 8.6 Hz, 2H), 7.65–7.54 (m, 3H).

^{13}C NMR (101 MHz, acetone-d_6) δ [ppm] = 153.3, 152.9, 139.5, 132.5, 130.3, 125.3, 123.7, 98.3.

HRMS (ESI): calc. for $C_{12}H_9IN_2$ $[M+H]^+$: 308.9883, found: 308.9883.

2.11. Compound 1

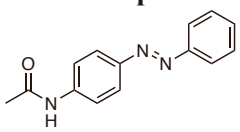

(*E*)-*N*-(4-(Phenyldiazenyl)phenyl)acetamide

A round bottom flask was charged with 200 mg (1.01 mmol, 1.0 equiv.) of 4-phenylazoaniline (**4**) dissolved in 10 mL THF and 430 µL DIPEA and cooled to 0 °C. 579 µL of AcCl was added dropwise and the reaction mixture was allowed to warm to r.t. for 1 h before it was quenched by addition of 0.6 mL MeOH and subjected to FCC ($CHCl_3$/acetone = 4/1) to obtain 200 mg (836 µmol) of the desired compound as an orange solid in 82% yield.

^{1}H NMR (400 MHz, acetone-d_6): δ [ppm] = 9.47 (s, 1H), 7.97–7.84 (m, 6H), 7.59–7.49 (m, 3H), 2.14 (d, J = 2.4 Hz, 3H).

^{13}C NMR (101 MHz, acetone-d_6) δ [ppm] = 169.3, 153.6, 149.1, 143.5, 131.6, 130.1, 124.6, 123.4, 120.0, 119.9, 24.4.

HRMS (ESI): calc. for $C_{14}H_{14}N_3O$ $[M+H]^+$: 240.1131, found: 240.1132.

$\varepsilon_{360\ nm}$ (DMSO) = 15,300 M^{-1} cm^{-1}

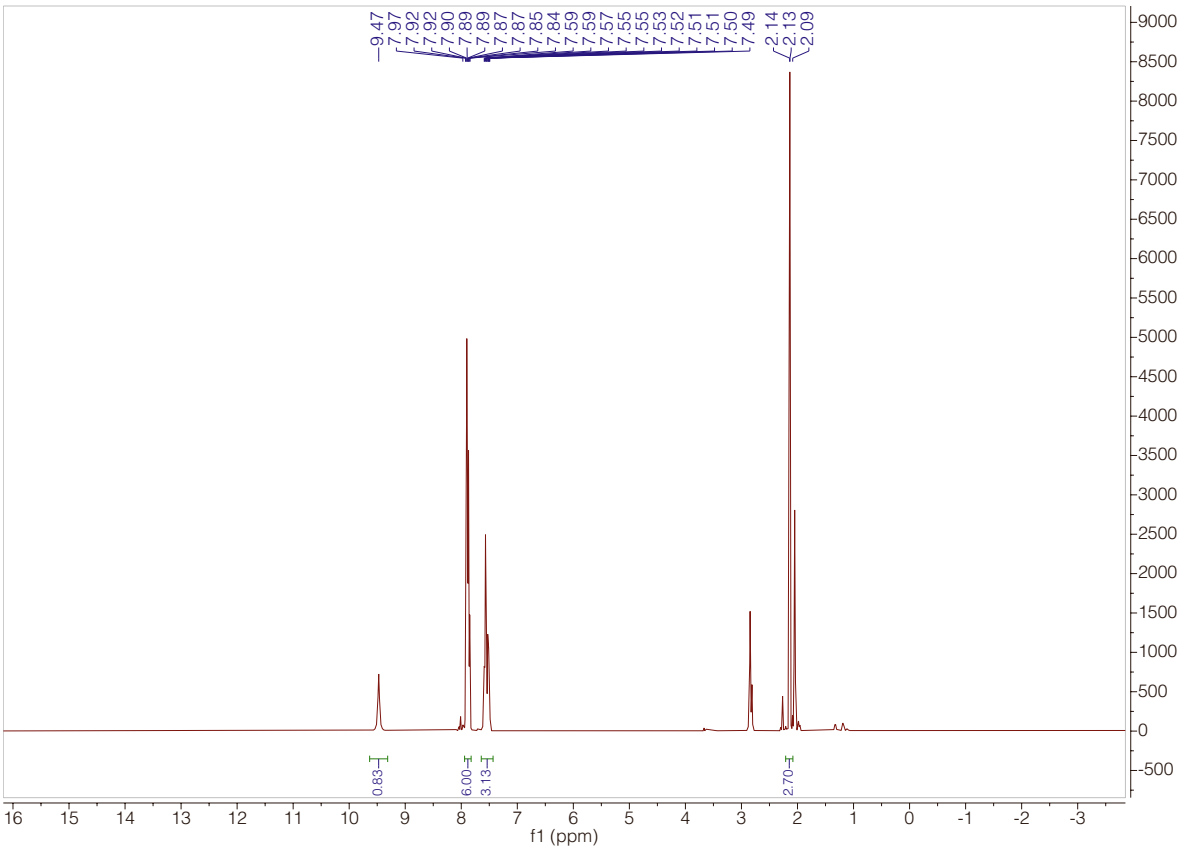
9.47
7.97
7.92
7.92
7.90
7.89
7.89
7.87
7.87
7.85
7.84
7.59
7.59
7.57
7.55
7.55
7.53
7.52
7.51
7.51
7.50
7.49
2.14
2.13
2.09
0.83
6.00
3.13
2.70
f1 (ppm)

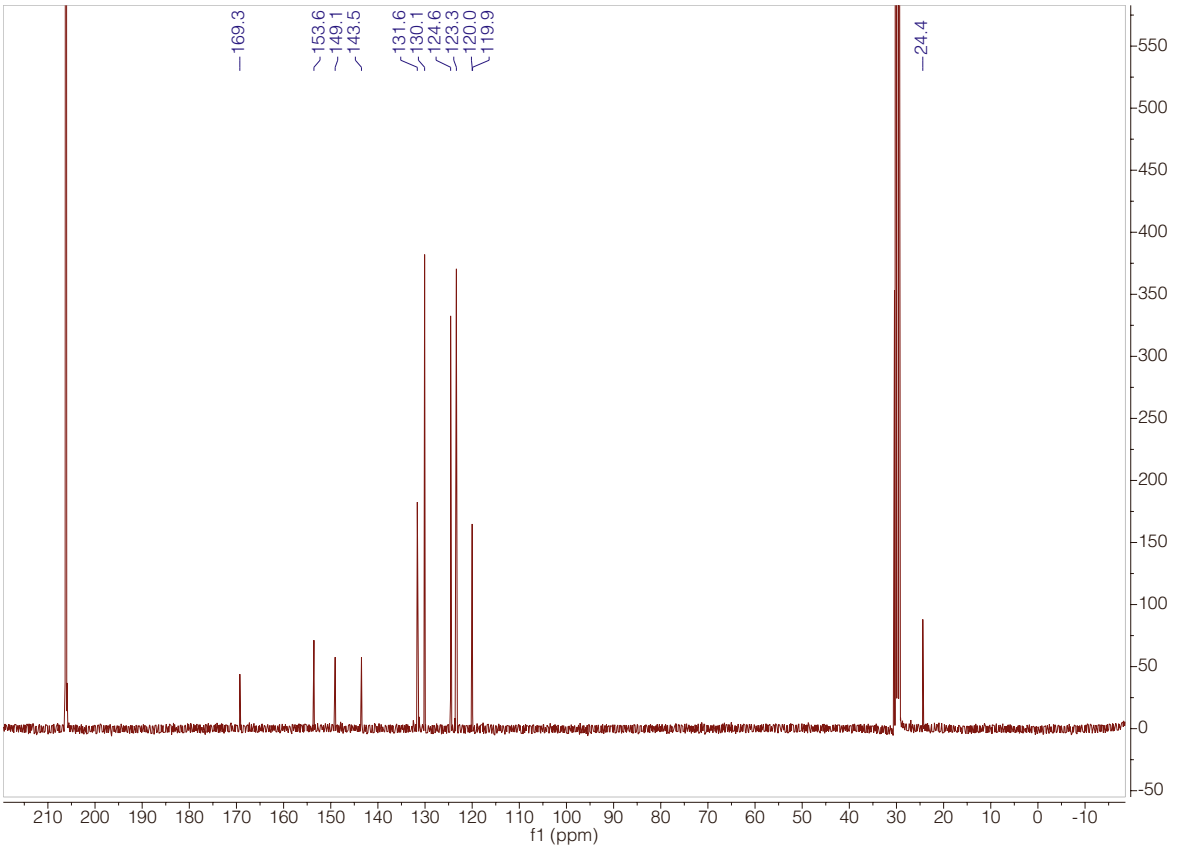
169.3
153.6
149.1
143.5
131.6
130.1
124.6
123.3
120.0
119.9
24.4
f1 (ppm)

2.12. Compound 2

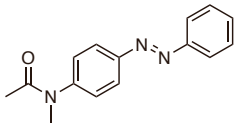

(*E*)-*N*-Methyl-*N*-(4-(phenyldiazenyl)phenyl)acetamide

A Schlenk flask was charged with 20.1 mg (502 µmol, 1.2 equiv.) of NaH (60% in mineral oil) and 10 mL dry DMF and cooled to 0 °C. After 15 minutes of stirring, 100 mg (418 µmol, 1.0 equiv.) of azobenzene **1** dissolved in dry DMF was added dropwise, followed by dropwise addition of MeI (64.8 mg, 28 µL, 460 µmol 1.1 equiv.). The reaction mixture was allowed to warm to r.t. for 1 h before it was quenched by addition of aq. sat. NH_4Cl solution and subjected to RP-HPLC to obtain 102 mg (403 µmol) of the desired compound as an orange solid in 96% yield.

^{1}H NMR (400 MHz, DMSO-d_6) δ [ppm] = 7.95–7.88 (m, 4H), 7.64–7.55 (m, 5H), 3.24 (s, 3H), 1.93 (s, 3H).

^{13}C NMR (101 MHz, DMSO-d_6): δ [ppm] = 169.1, 151.9, 150.2, 146.9, 131.7, 129.5, 127.7, 123.5, 122.6, 36.7, 22.5.

HRMS (ESI): calc. for $C_{15}H_{16}N_3O$ $[M+H]^+$: 254.1288, found: 254.1288.

$\varepsilon_{338\ nm}$ (DMSO) = 16,800 M^{-1} cm^{-1}

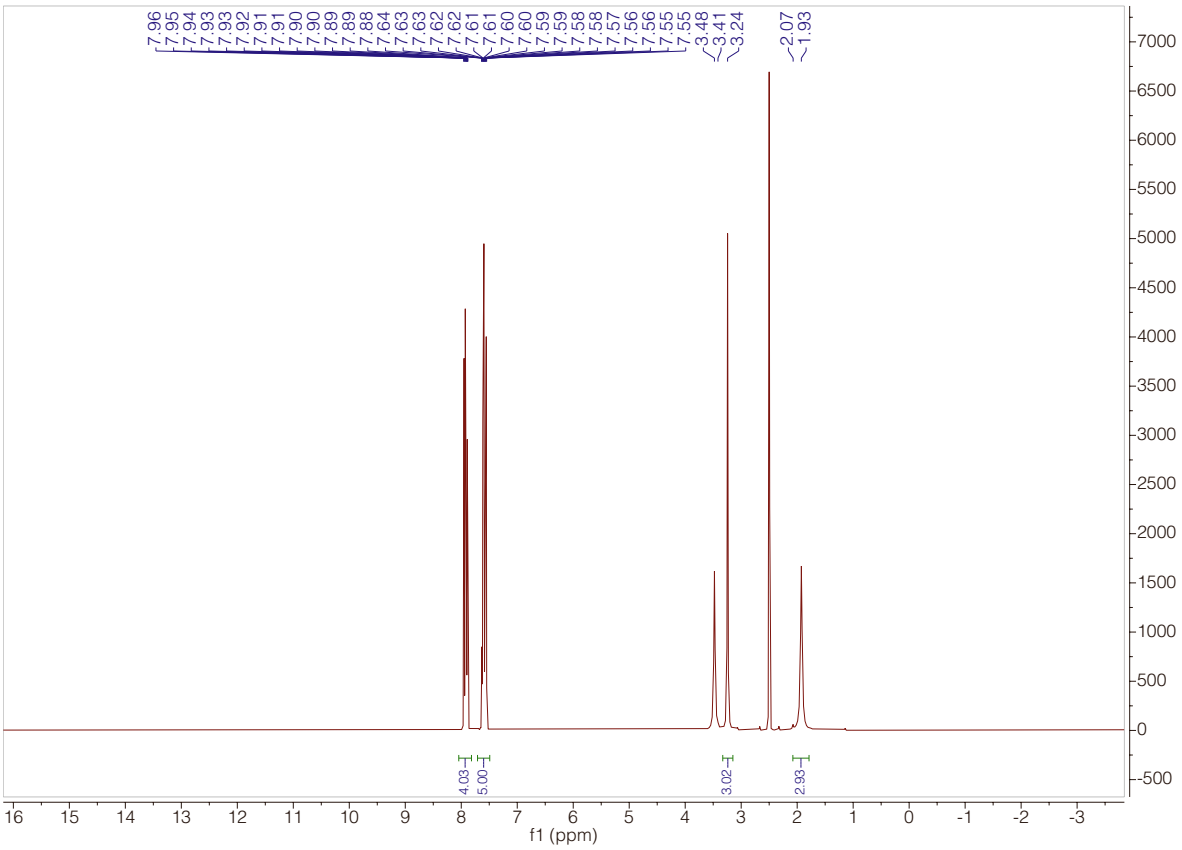
7.96
7.95
7.94
7.93
7.93
7.92
7.91
7.91
7.90
7.90
7.89
7.89
7.88
7.64
7.63
7.63
7.62
7.62
7.61
7.61
7.60
7.60
7.59
7.59
7.58
7.58
7.57
7.56
7.56
7.55
7.55
3.48
3.41
3.24
2.07
1.93
4.03
5.00
3.02
2.93
f1 (ppm)

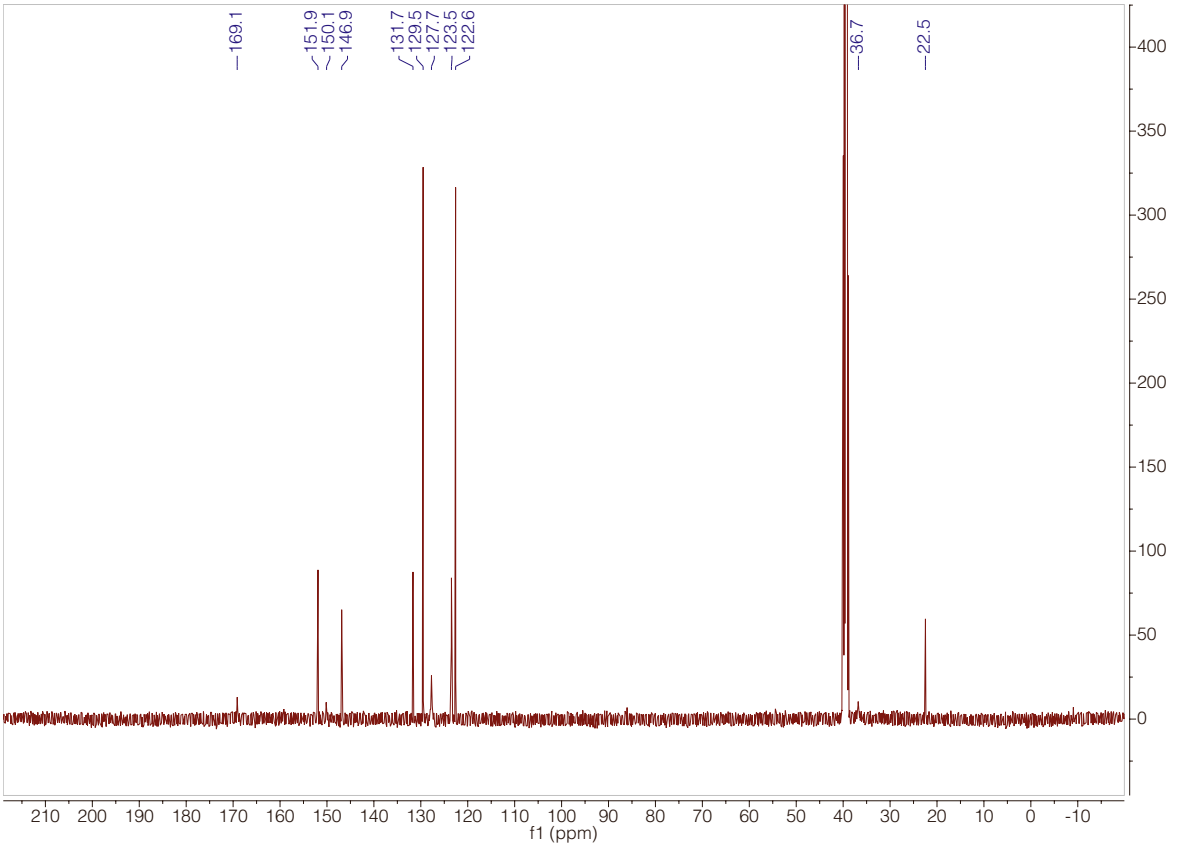
169.1
151.9
150.1
146.9
131.7
129.5
127.7
123.5
122.6
36.7
22.5
f1 (ppm)

2.13. Compound 3

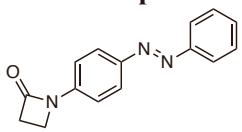

(*E*)-1-(4-(Phenyldiazenyl)phenyl)azetidin-2-one

Compound **3** was prepared according to general procedure A with 50.0 mg (162 μmol) of **S3**. HPLC purification. Yield: 41%; 16.3 mg.

^{1}H NMR (400 MHz, DMSO-d_6) δ [ppm] = 7.95 (d, J = 8.8 Hz, 2H), 7.87–7.85 (m, 2H), 7.59–7.53 (m, 5H), 3.73 (t, J = 4.6 Hz, 2H), 3.15 (t, J = 4.6 Hz, 2H).

^{13}C NMR (101 MHz, DMSO-d_6): δ [ppm] = 165.2, 152.0, 147.6, 141.1, 131.1, 129.4, 124.2, 122.4, 116.4, 38.4, 36.2.

HRMS (ESI): calc. for $C_{15}H_{14}N_3O$ $[M+H]^+$: 252.1131, found: 252.1132.

$\varepsilon_{366\ nm}$ (DMSO) = 22,100 M^{-1} cm^{-1}

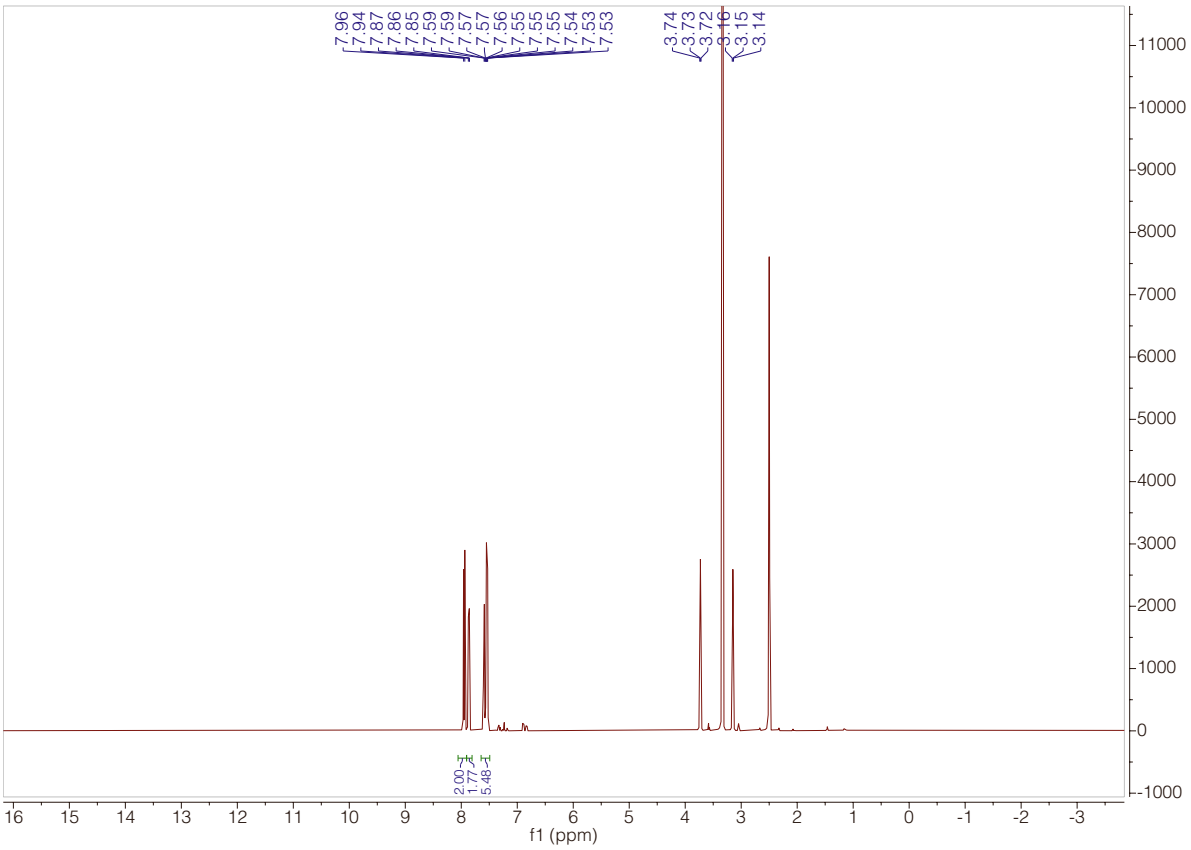
7.96
7.94
7.87
7.86
7.85
7.59
7.59
7.57
7.57
7.56
7.55
7.55
7.54
7.53
7.53
3.74
3.73
3.72
3.16
3.15
3.14
2.00
1.77
5.48
f1 (ppm)

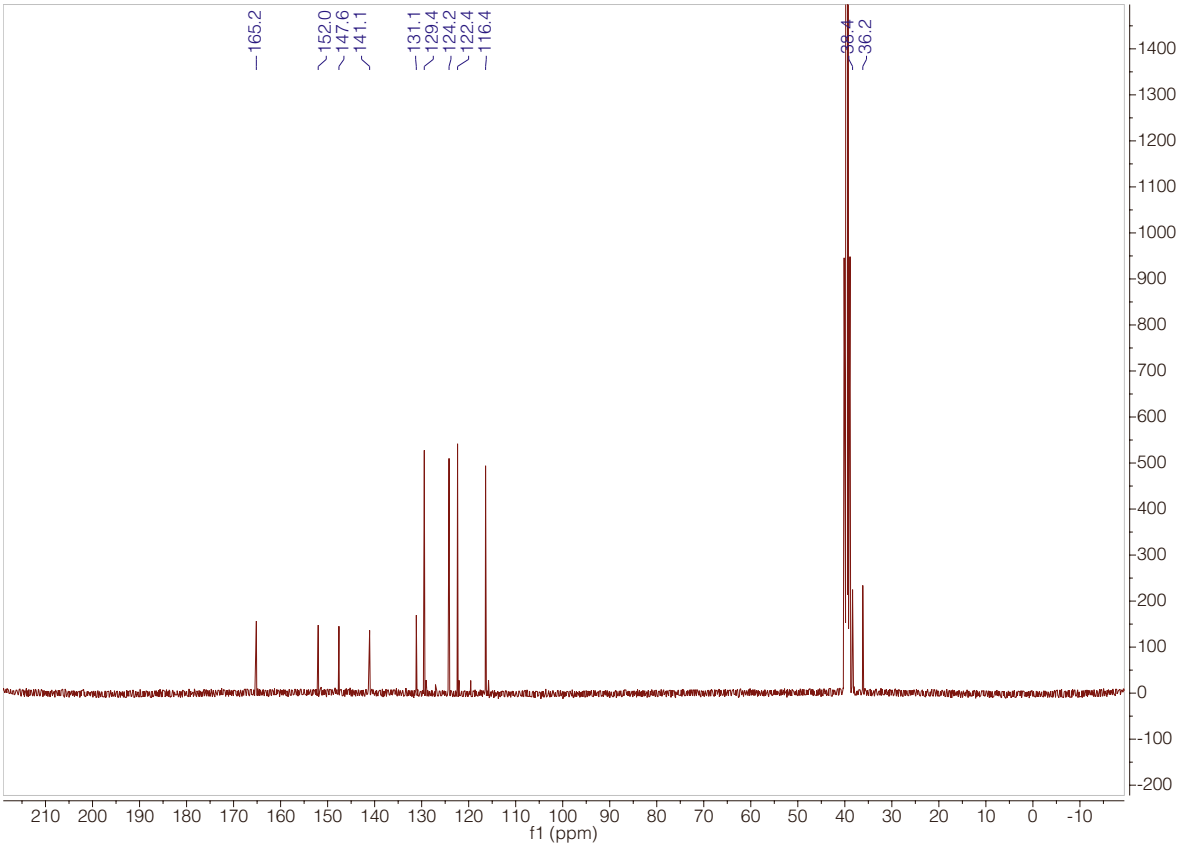
165.2
152.0
147.6
141.1
131.1
129.4
124.2
122.4
116.4
38.4
36.2
f1 (ppm)

2.14. Compound 4

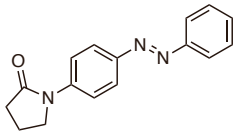

(*E*)-1-(4-(Phenyldiazenyl)phenyl)pyrrolidin-2-one

Compound **4** was prepared according to general procedure A with 27.3 mg (89 μmol) of **S3**. HPLC purification. Yield: 43%; 10.1 mg.

^{1}H NMR (400 MHz, DMSO-d_6): δ [ppm] = 7.95–7.86 (m, 6H), 7.61–7.55 (m, 3H), 3.92 (t, J = 7.0 Hz, 2H), 2.67 (t, J = 8.1 Hz, 2H), 2.10 (p, J = 7.6 Hz, 2H).

^{13}C NMR (101 MHz, DMSO-d_6): δ [ppm] = 174.5, 152.0, 144.6, 142.4, 131.2, 129.5, 123.3, 122.4, 119.3, 48.1, 32.5, 17.3.

HRMS (ESI): calc. for $C_{16}H_{16}N_3O$ $[M+H]^+$: 266.1288, found: 266.1287.

$\varepsilon_{362\ nm}$ (DMSO) = 18,100 M^{-1} cm^{-1}

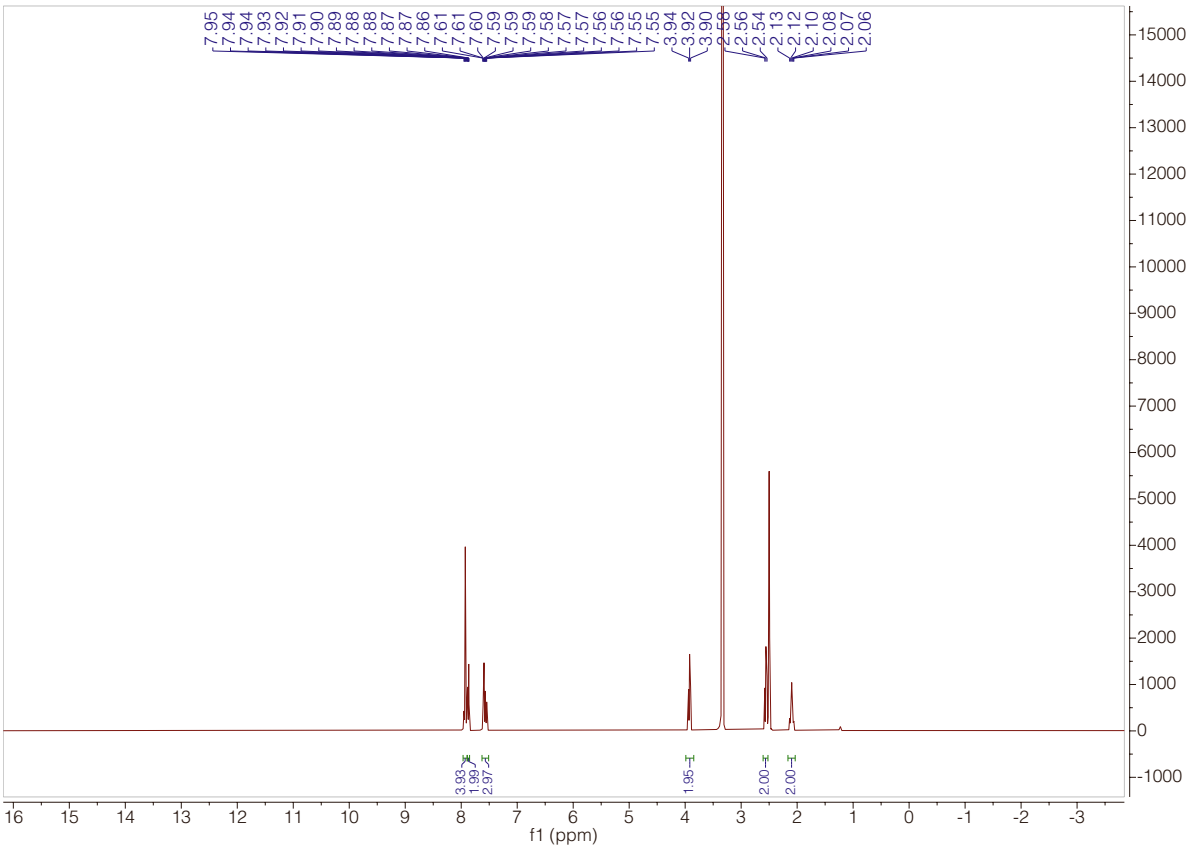
7.95
7.94
7.94
7.93
7.92
7.91
7.90
7.89
7.88
7.88
7.87
7.87
7.86
7.61
7.61
7.60
7.59
7.59
7.59
7.58
7.57
7.57
7.56
7.56
7.55
7.55
3.94
3.92
3.90
2.58
2.56
2.54
2.13
2.12
2.10
2.08
2.07
2.06
3.93
1.99
2.97
1.95
2.00
2.00
f1 (ppm)

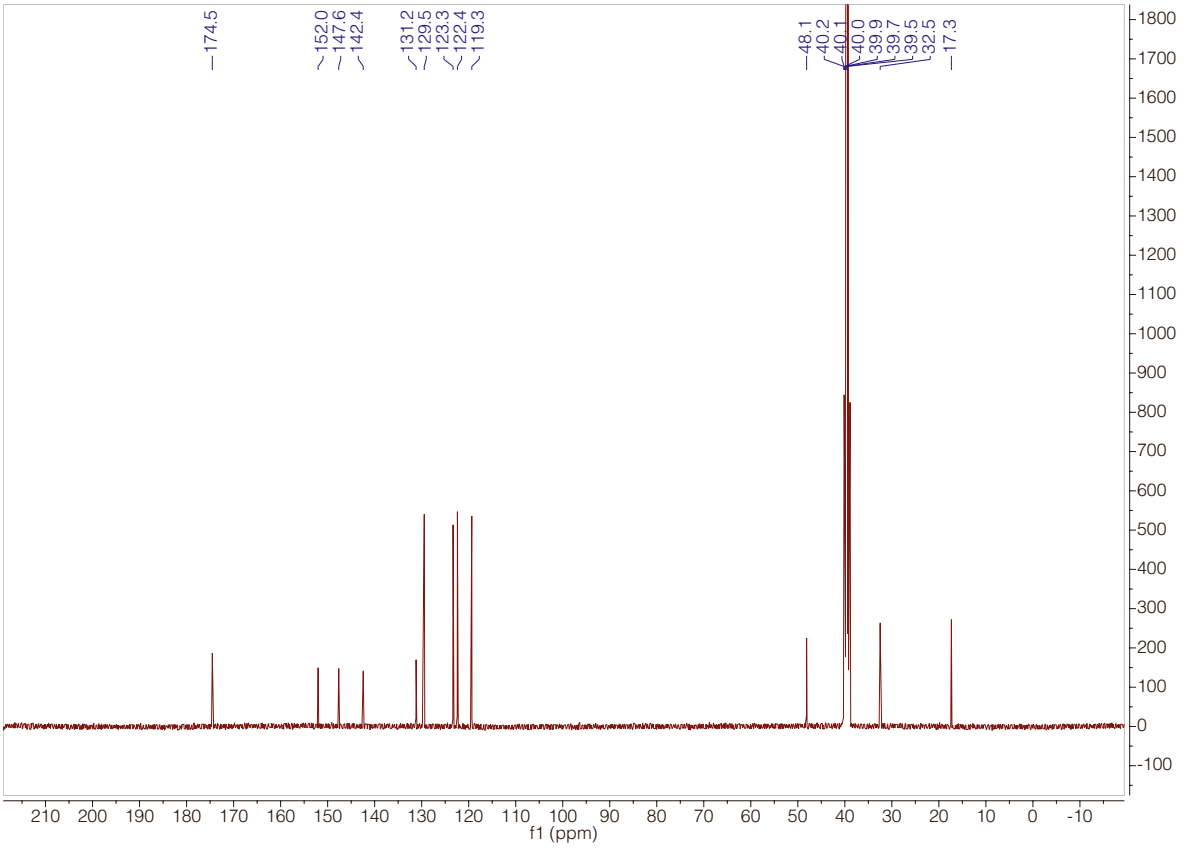
174.5
152.0
147.6
142.4
131.2
129.5
123.3
122.4
119.3
48.1
40.2
40.1
40.0
39.9
39.7
39.5
32.5
17.3
f1 (ppm)

2.15. Compound 5

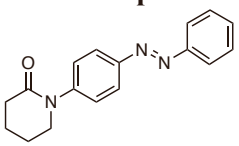

(*E*)-1-(4-(Phenyldiazenyl)phenyl)piperidin-2-one

Compound **5** was prepared according to general procedure A with 50.0 mg (162 μmol) of **S3**. FCC purification (gradient: 10–90% DCM in hexanes). Yield: 90%; 40.7 mg.

^{1}H NMR (400 MHz, $CDCl_3$) δ [ppm] = 7.96–7.90 (m, 4H), 7.54–7.43 (m, 5H), 3.71 (d, J = 6.5 Hz, 2H), 2.61 (s, 2H), 2.00–1.97 (m, 4H).

^{13}C NMR (101 MHz, $CDCl_3$): δ [ppm] = 170.1, 152.6, 150.6, 145.6, 131.0, 129.1, 126.4, 123.6, 122.9, 51.4, 33.0, 23.5, 21.4.

HRMS (ESI): calc. for $C_{17}H_{18}N_3O$ $[M+H]^+$: 280.1444. found: 280.1443.

$\varepsilon_{343\ nm}$ (DMSO) = 15,000 M^{-1} cm^{-1}

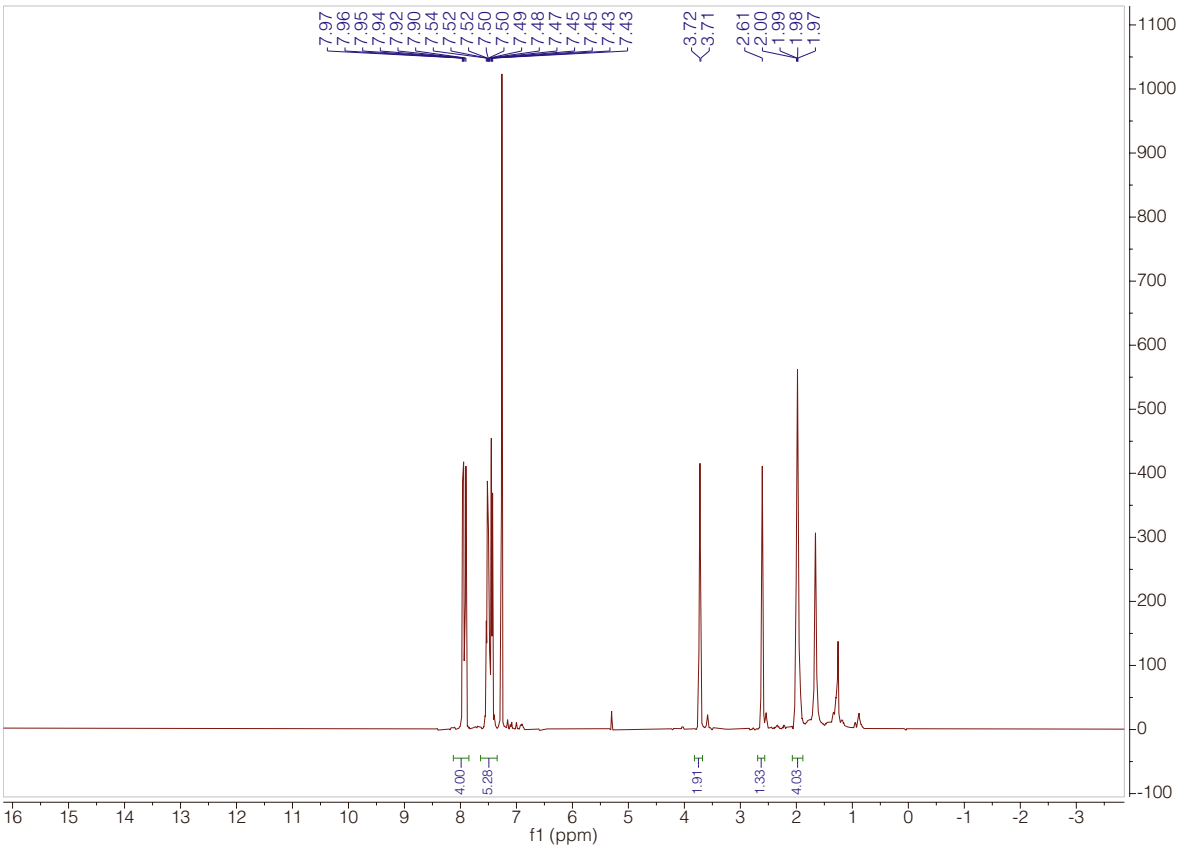
7.97
7.96
7.95
7.94
7.92
7.90
7.54
7.52
7.52
7.50
7.50
7.49
7.48
7.47
7.45
7.45
7.43
7.43
3.72
3.71
2.61
2.00
1.99
1.98
1.97
4.00
5.28
1.91
1.33
4.03
f1 (ppm)

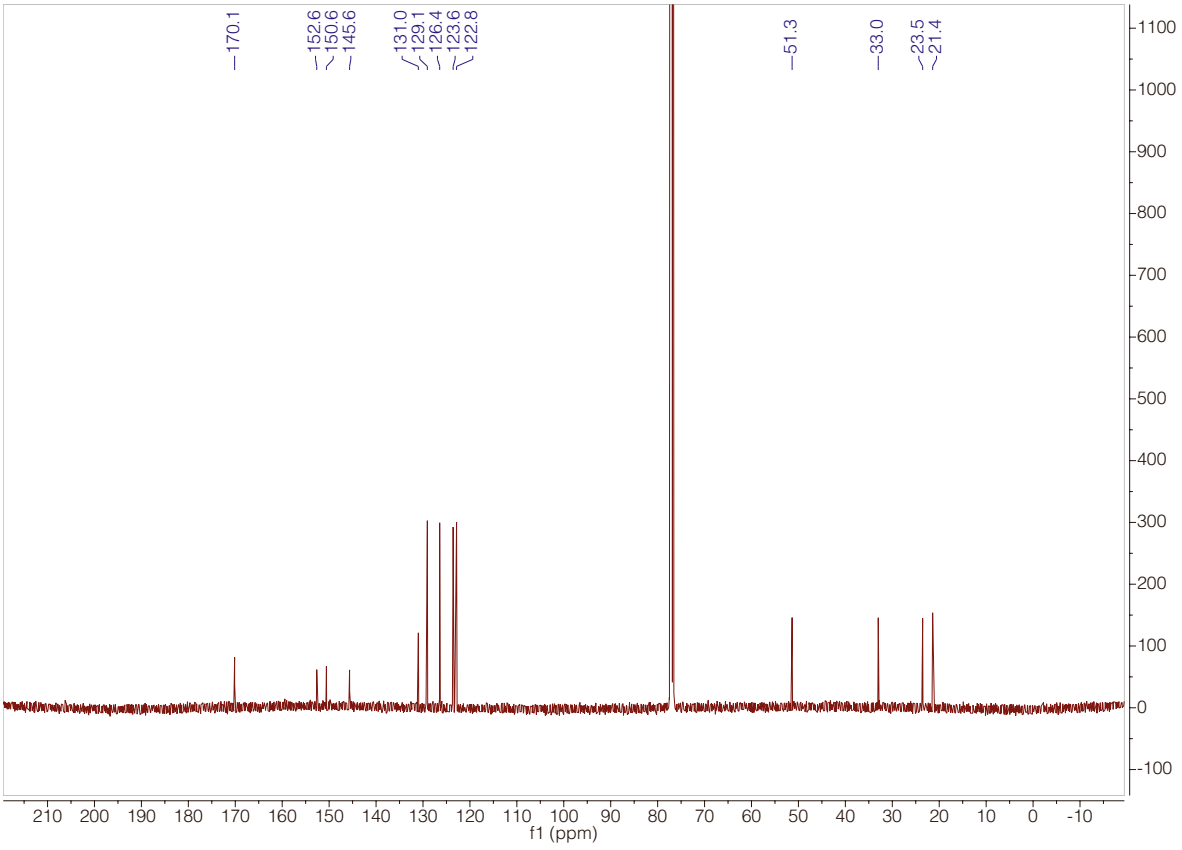
170.1
152.6
150.6
145.6
131.0
129.1
126.4
123.6
122.8
51.3
33.0
23.5
21.4
f1 (ppm)

2.16. Compound 6

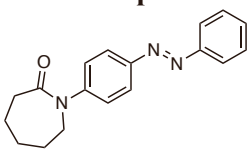

(*E*)-1-(4-(Phenyldiazenyl)phenyl)azepan-2-one

Compound **6** was prepared according to general procedure A with 50.0 mg (162 μmol) of **S3**. HPLC purification. Yield: 33%, 15.7 mg.

^{1}H NMR (400 MHz, DMSO-d_6) δ [ppm] = 7.91–7.87 (m, 4H), 7.63–7.54 (m, 3H), 7.46 (d, J = 8.7 Hz, 2H), 3.84–3.82 (m, 2H), 2.67–2.64 (m, 2H), 1.78–1.70 (m, 6H).

^{13}C NMR (101 MHz, DMSO-d_6): δ [ppm] = 174.6, 151.9, 149.2, 147.2, 131.5, 129.5, 126.8, 122.9, 122.5, 51.8, 37.1, 28.9, 28.4, 23.0.

HRMS (ESI): calc. for $C_{18}H_{20}N_3O$ [M+H]+: 294.1601, found: 294.1603.

$\varepsilon_{346\ nm}$ (DMSO) = 15,100 M^{-1} cm^{-1}

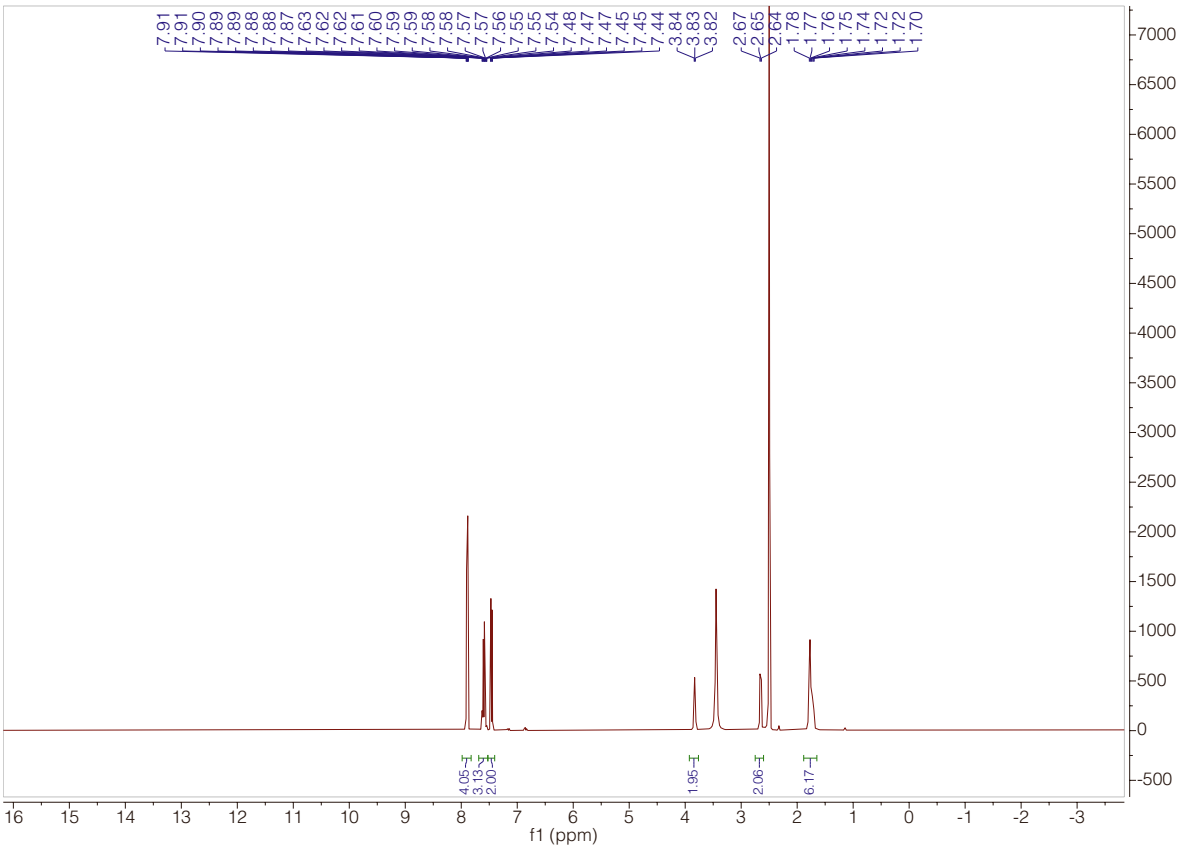
7.91
7.91
7.90
7.89
7.89
7.88
7.88
7.87
7.63
7.62
7.62
7.61
7.60
7.59
7.59
7.58
7.58
7.57
7.57
7.56
7.55
7.55
7.54
7.48
7.47
7.47
7.45
7.45
7.44
3.84
3.83
3.82
2.67
2.65
2.64
1.78
1.77
1.76
1.75
1.74
1.72
1.70
4.05
3.13
2.00
1.95
2.06
6.17
f1 (ppm)

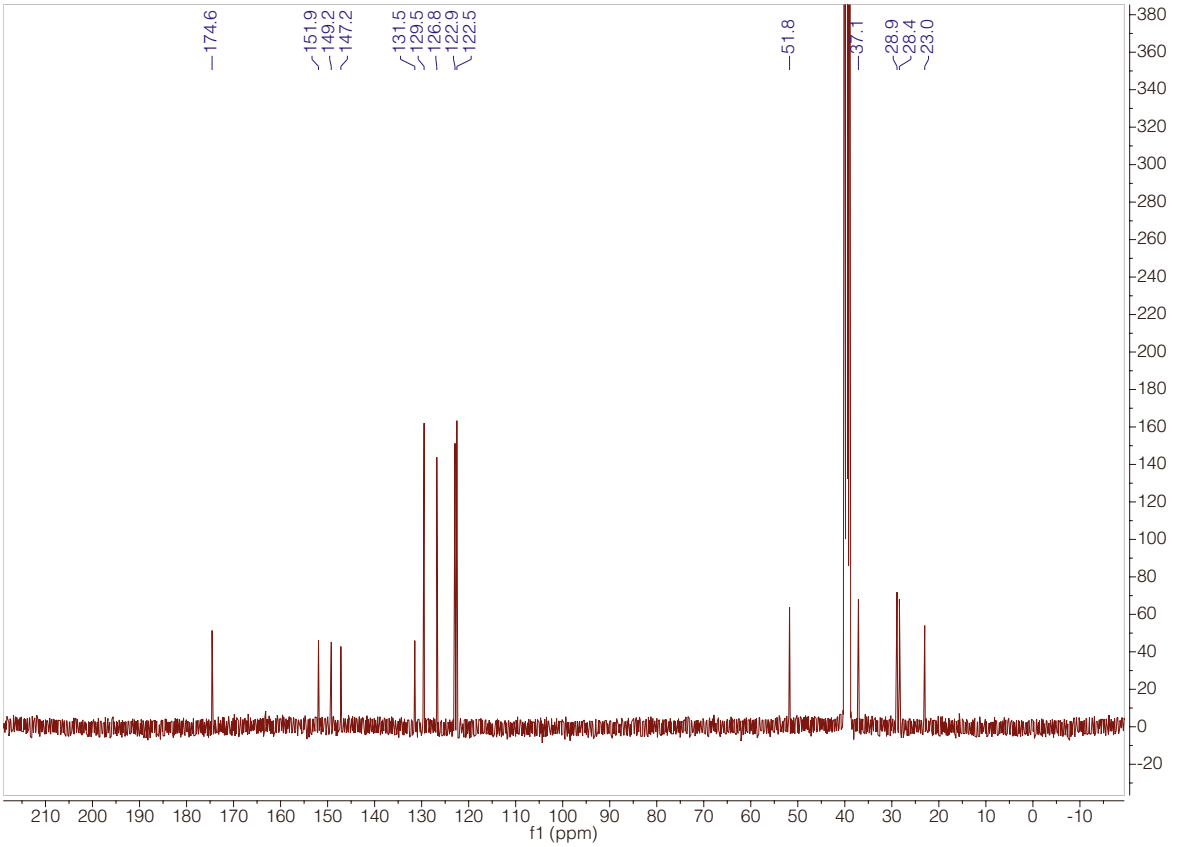
174.6
151.9
149.2
147.2
131.5
129.5
126.8
122.9
122.5
51.8
37.1
28.9
28.4
23.0
f1 (ppm)

2.17. Compound 7

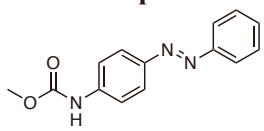

Methyl (*E*)-(4-(phenyldiazenyl)phenyl)carbamate

A round bottom flask was charged with 270 mg (1.37 mmol, 1.0 equiv.) of 4-phenylazoaniline (**S4**) dissolved in 10 mL DCM and 562 µL DIPEA (2.2 equiv.) and cooled to 0 °C. 1 mL of $COCl_2$ (1.4 M in toluene, 1.1 equiv.) was added dropwise (the reaction mixture turning deep red upon formation of the isocyanate) and was allowed to warm to r.t. for 1 h before half of the solution's volume (the other half, see compound **8**) was transferred into a round bottom flask containing 20 mL MeOH and 562 µL DIPEA. The reaction mixture was heated to 70 °C for 2 h, before all volatiles were removed *in vacuo* and the crude subjected to FCC (gradient MeOH/DCM = 0/100 → 0.5/100) to obtain 148 mg (580 µmol) of the desired compound as an orange solid in 85% yield.

^{1}H NMR (400 MHz, DMSO-d_6): δ [ppm] = 10.09 (s, 1H), 7.89–7.83 (m, 4H), 7.70–7.68 (m, 2H), 7.60–7.51 (m, 3H), 3.71 (s, 3H).

^{13}C NMR (101 MHz, DMSO-d_6): δ [ppm] = 153.9, 152.1, 147.1, 142.5, 130.9, 129.4, 123.8, 122.3, 118.2, 51.9.

HRMS (ESI): calc. for $C_{14}H_{14}N_3O_2$ $[M+H]^+$: 256.1081, found: 256.1081.

$\varepsilon_{360\ nm}$ (DMSO) = 17,000 M^{-1} cm^{-1}

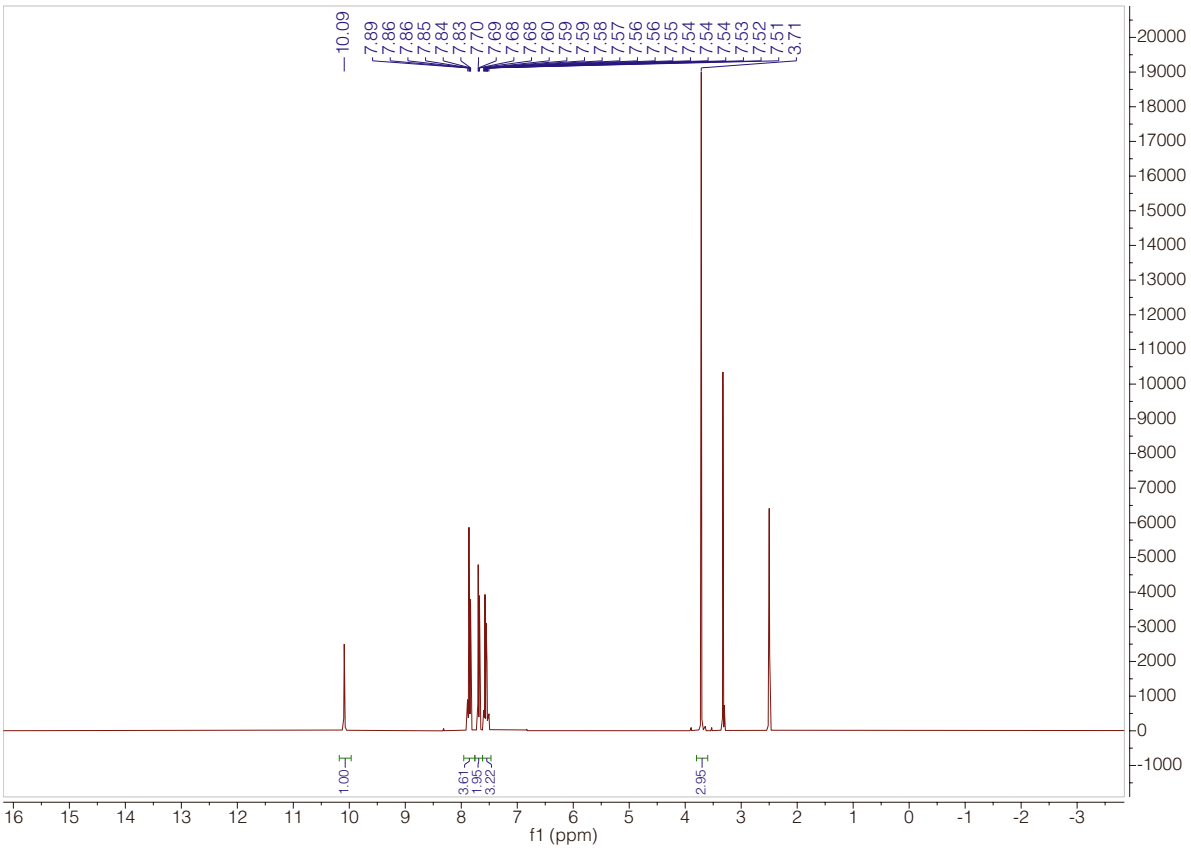
10.09
7.89
7.86
7.86
7.85
7.84
7.83
7.70
7.69
7.68
7.68
7.60
7.59
7.59
7.58
7.57
7.56
7.56
7.55
7.54
7.54
7.54
7.53
7.52
7.51
3.71
1.00
3.61
1.95
3.22
2.95
f1 (ppm)

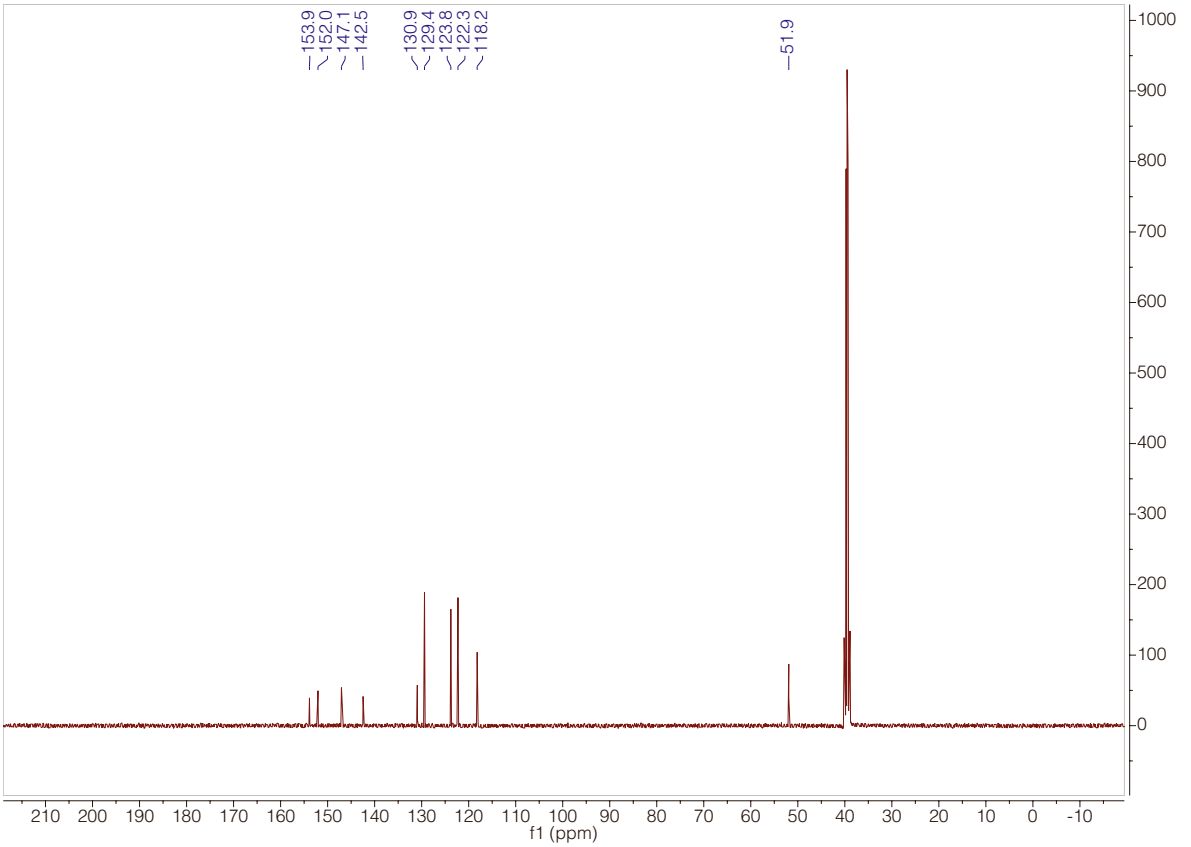
153.9
152.0
147.1
142.5
130.9
129.4
123.8
122.3
118.2
51.9
f1 (ppm)

2.18. Compound 8

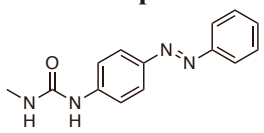

(*E*)-1-Methyl-3-(4-(phenyldiazenyl)phenyl)urea

The other half of the isocyanate containing solution from compound preparation **7** was transferred into a round bottom flask containing 100 mg (1.49 mmol, 2.2 equiv.) $MeNH_2$ x HCl suspended in 20 mL THF and 562 µL DIPEA. The reaction mixture was heated to 70 °C for 2 h, before all volatiles were removed *in vacuo* and the crude subjected to FCC (gradient MeOH/DCM = 0/100 → 2/100) to obtain 150 mg (590 µmol) of the desired compound as an orange solid in 86% yield.

^{1}H NMR (400 MHz, DMSO-d_6): δ [ppm] = 8.99 (s, 1H), 7.84–7.81 (m, 4H), 7.62 (d, J = 8.9 Hz, 2H), 7.56 (t, J = 7.4 Hz, 2H), 7.54–7.46 (m, 1H), 6.18 (q, J = 4.6 Hz, 1H), 2.67 (d, J = 4.6 Hz, 3H).

^{13}C NMR (101 MHz, DMSO-d_6): δ [ppm] = 155.4, 152.1, 146.1, 144.2, 130.6, 129.4, 123.9, 122.2, 117.5, 26.3.

HRMS (ESI): calc. for $C_{14}H_{14}N_4O$ $[M+H]^+$: 255.1240, found: 255.1240.

$\varepsilon_{375\ nm}$ (DMSO) = 19,800 M^{-1} cm^{-1}

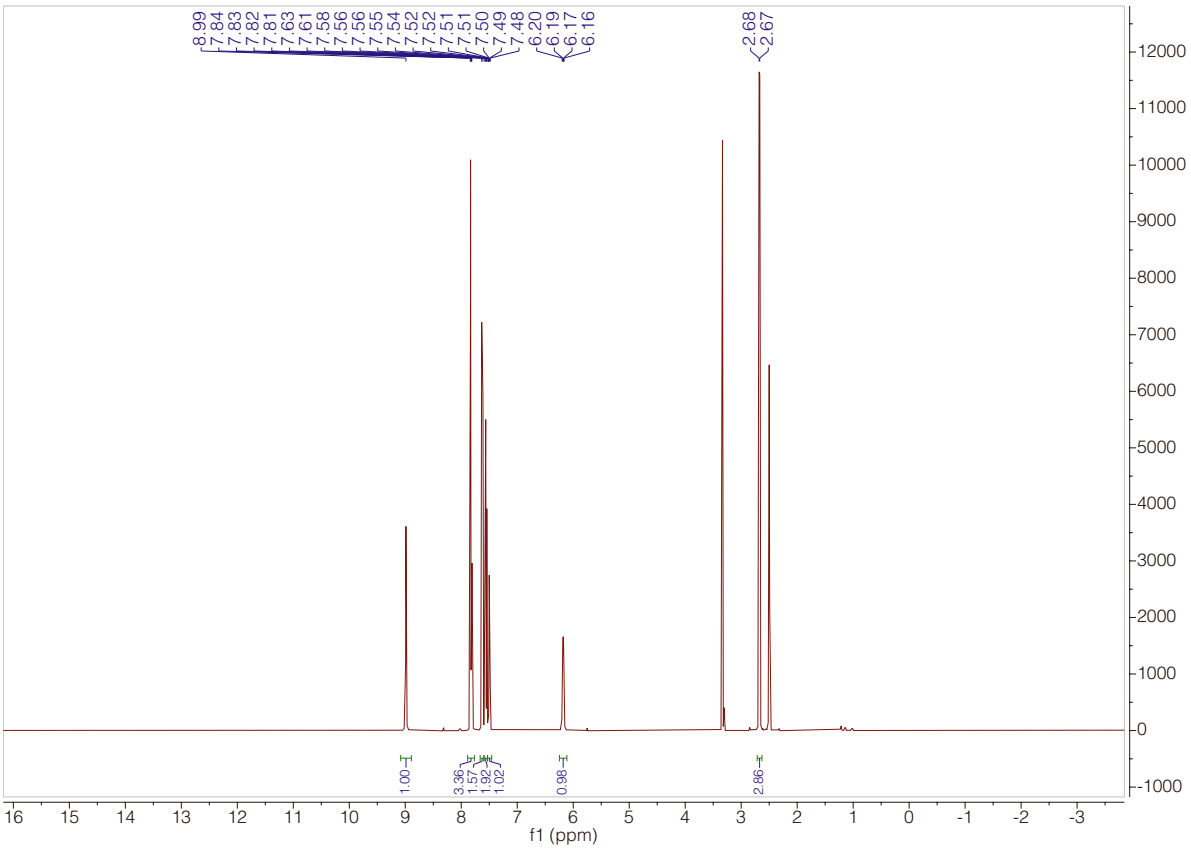
8.99
7.84
7.83
7.82
7.81
7.63
7.61
7.58
7.56
7.56
7.55
7.54
7.52
7.52
7.51
7.51
7.50
7.49
7.48
6.20
6.19
6.17
6.16
2.68
2.67
1.00
3.36
1.57
1.92
1.02
0.98
2.86
f1 (ppm)

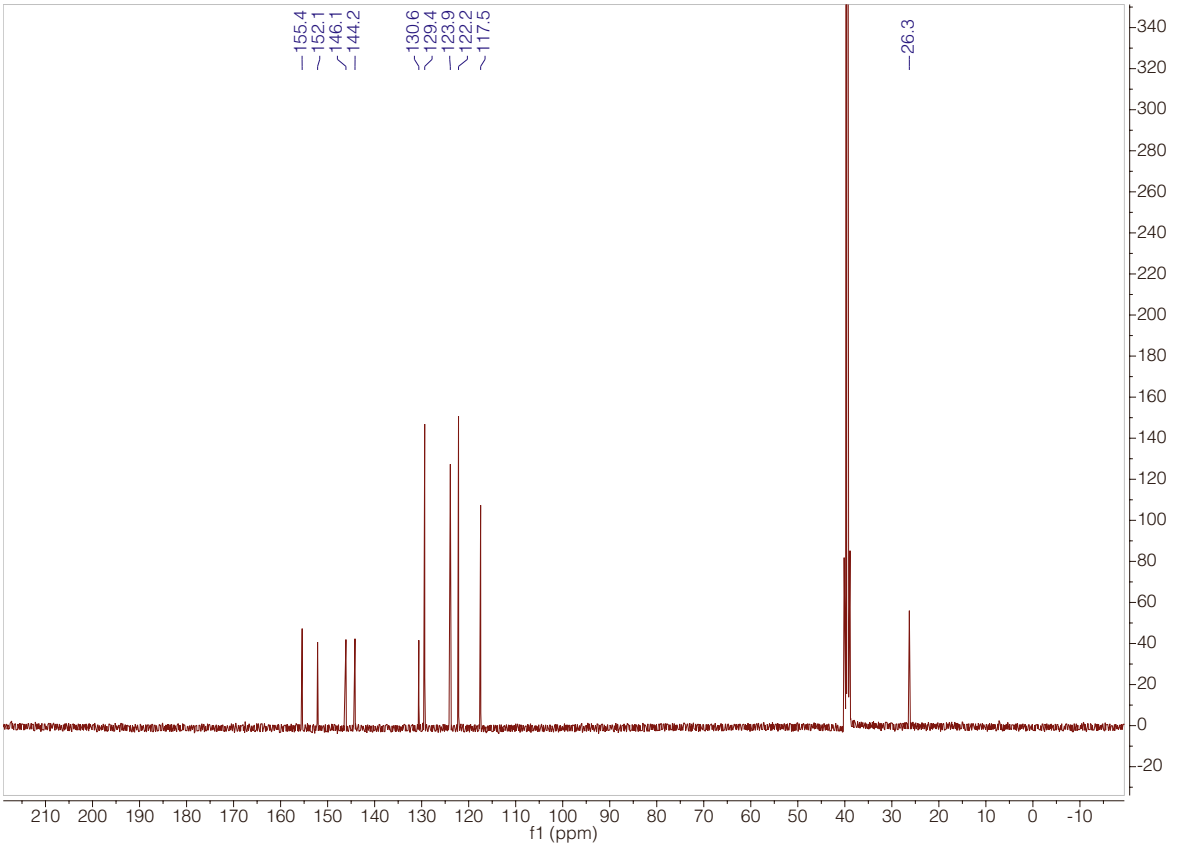
155.4
152.1
146.1
144.2
130.6
129.4
123.9
122.2
117.5
26.3
f1 (ppm)

2.19. Compound 9

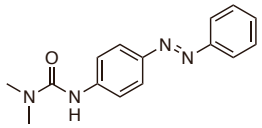

(*E*)-1,1-Dimethyl-3-(4-(phenyldiazenyl)phenyl)urea

Compound **9** was prepared according to general procedure A with 50.0 mg (162 μmol) of **S3**. HPLC purification. Yield: 86%; 37.5 mg.

^{1}H NMR (400 MHz, DMSO-d_6) δ [ppm] = 8.70 (s, 1H), 7.84–7.81 (m, 4H), 7.73 (d, J = 9.0 Hz, 2H), 7.59–7.51 (m, 3H), 2.96 (s, 6H).

^{13}C NMR (101 MHz, DMSO-d_6): δ [ppm] = 155.3, 152.1, 146.4, 144.4, 130.7, 129.4, 123.4, 122.2, 119.2, 36.3.

HRMS (ESI): calc. for $C_{12}H_{12}N_3$ [M-Me_2NCO+2H]$^+$: 198.1026, found: 198.1025.

$\varepsilon_{372\ nm}$ (DMSO) = 19,100 M^{-1} cm^{-1}

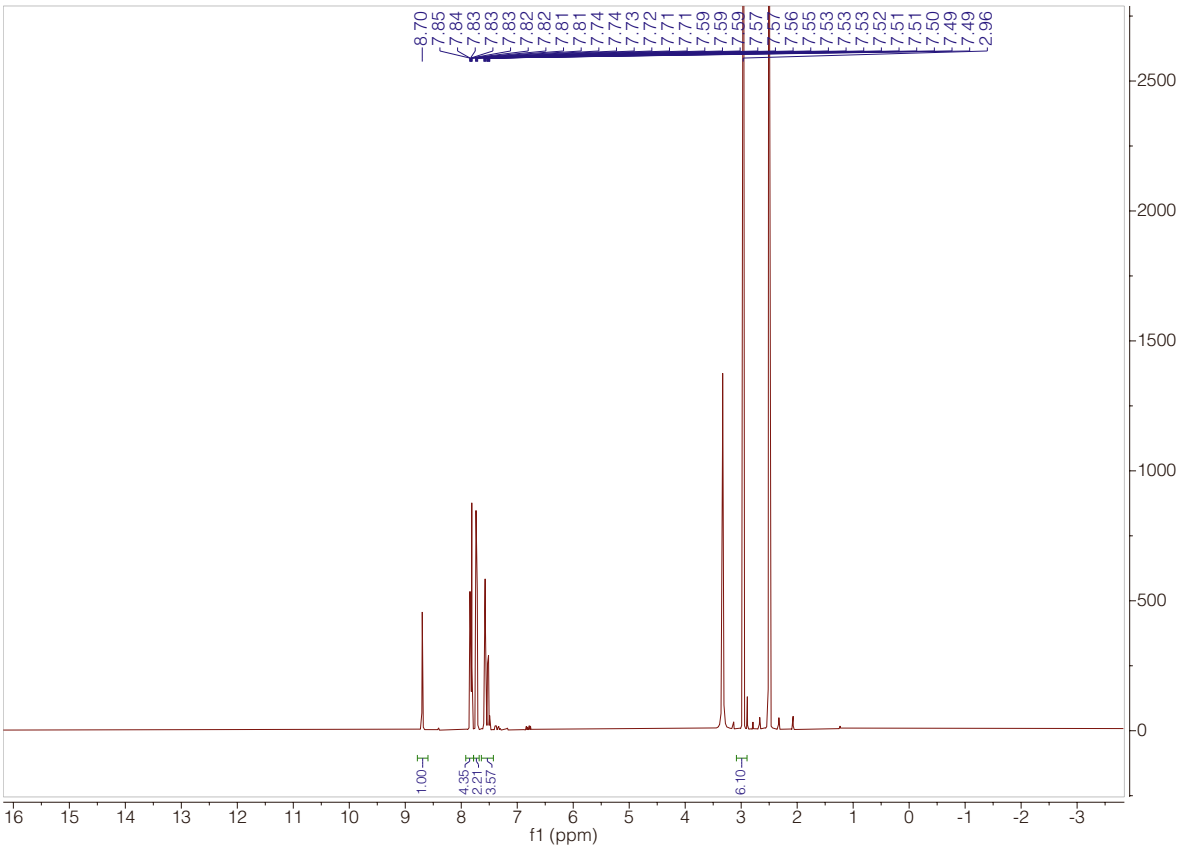
8.70
7.85
7.84
7.83
7.83
7.83
7.82
7.82
7.81
7.81
7.74
7.74
7.73
7.72
7.71
7.71
7.59
7.59
7.59
7.57
7.57
7.56
7.55
7.53
7.53
7.52
7.51
7.51
7.50
7.49
7.49
2.96
1.00
4.35
2.21
3.57
6.10
f1 (ppm)

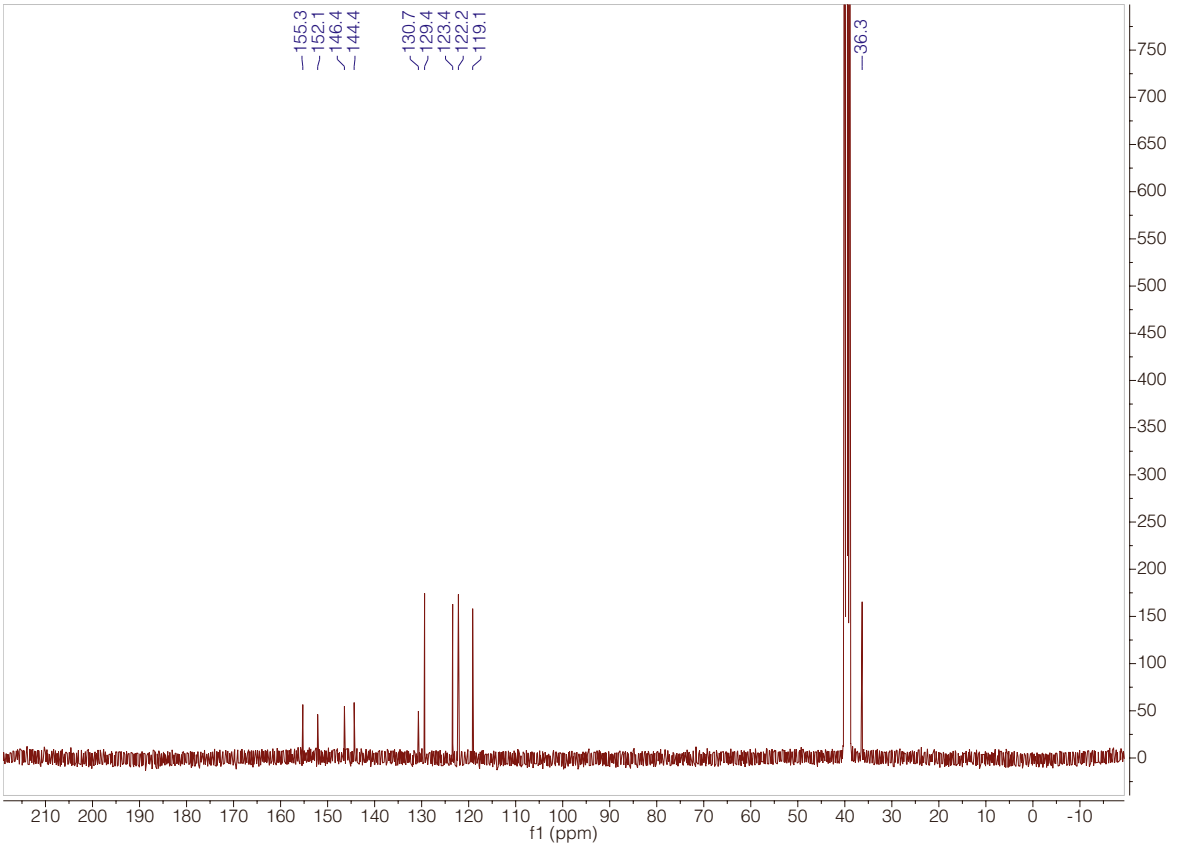
155.3
152.1
146.4
144.4
130.7
129.4
123.4
122.2
119.1
36.3
f1 (ppm)

2.20. Compound 10

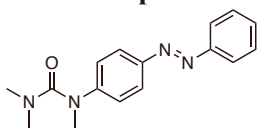

(*E*)-1,1,3-Trimethyl-3-(4-(phenyldiazenyl)phenyl)urea

Compound **10** was prepared according to general procedure A with 27.8 mg (90 μmol) of **S3**. HPLC purification. Yield: 24%; 6.1 mg.

^{1}H NMR (400 MHz, acetone-d_6): δ [ppm] = 7.89–7.84 (m, 4H), 7.60–7.53 (m, 3H), 7.22 (d, J = 8.9 Hz, 2H), 3.24 (s, 3H), 2.80 (s, 6H).

^{13}C NMR (101 MHz, acetone-d_6): δ [ppm] = 161.6, 153.6, 150.5, 148.5, 131.6, 130.1, 125.0, 123.3, 121.7, 38.2, 37.7.

HRMS (ESI): calc. for $C_{16}H_{19}N_4O$ $[M+H]^+$: 283.1553, found: 283.1551.

$\varepsilon_{373\ nm}$ (DMSO) = 11,400 M^{-1} cm^{-1}

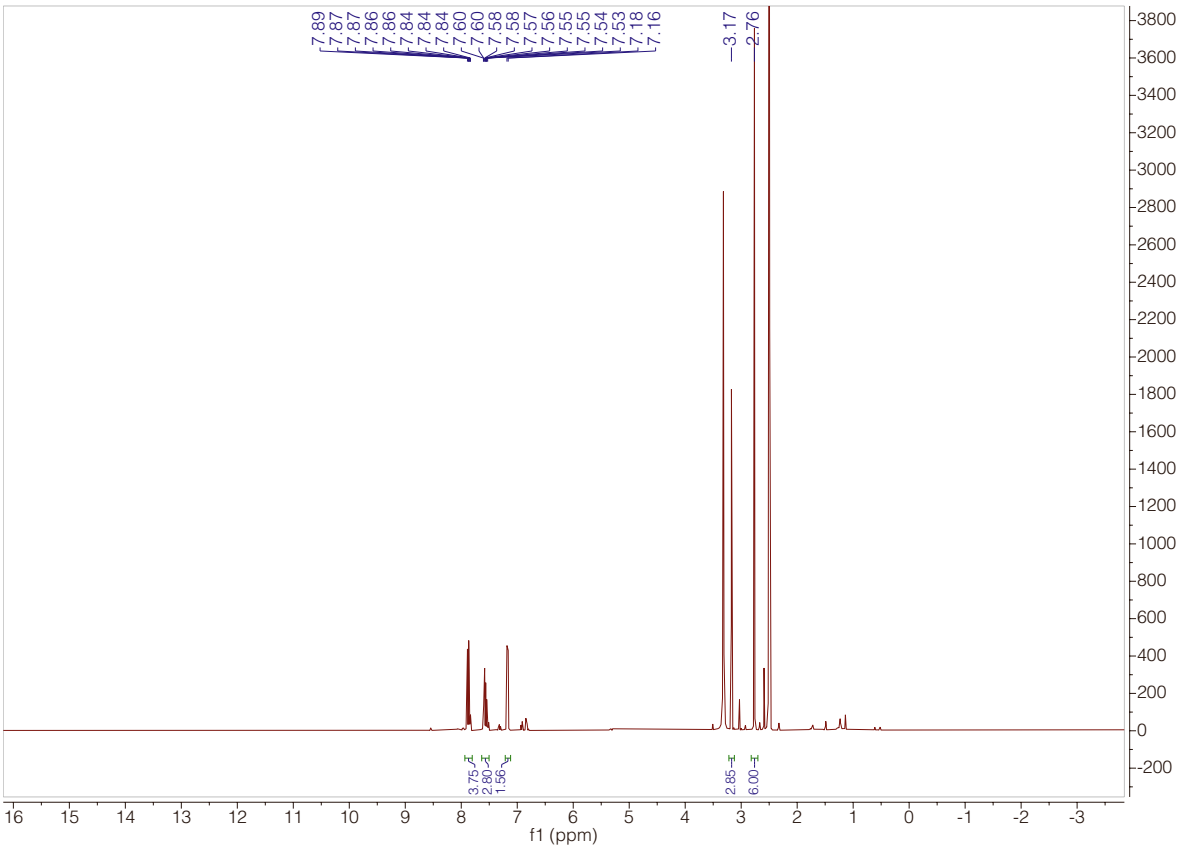
7.89
7.87
7.87
7.86
7.86
7.84
7.84
7.84
7.60
7.60
7.58
7.58
7.57
7.56
7.55
7.55
7.54
7.53
7.18
7.16
3.17
2.76
3.75
2.80
1.56
2.85
6.00
f1 (ppm)

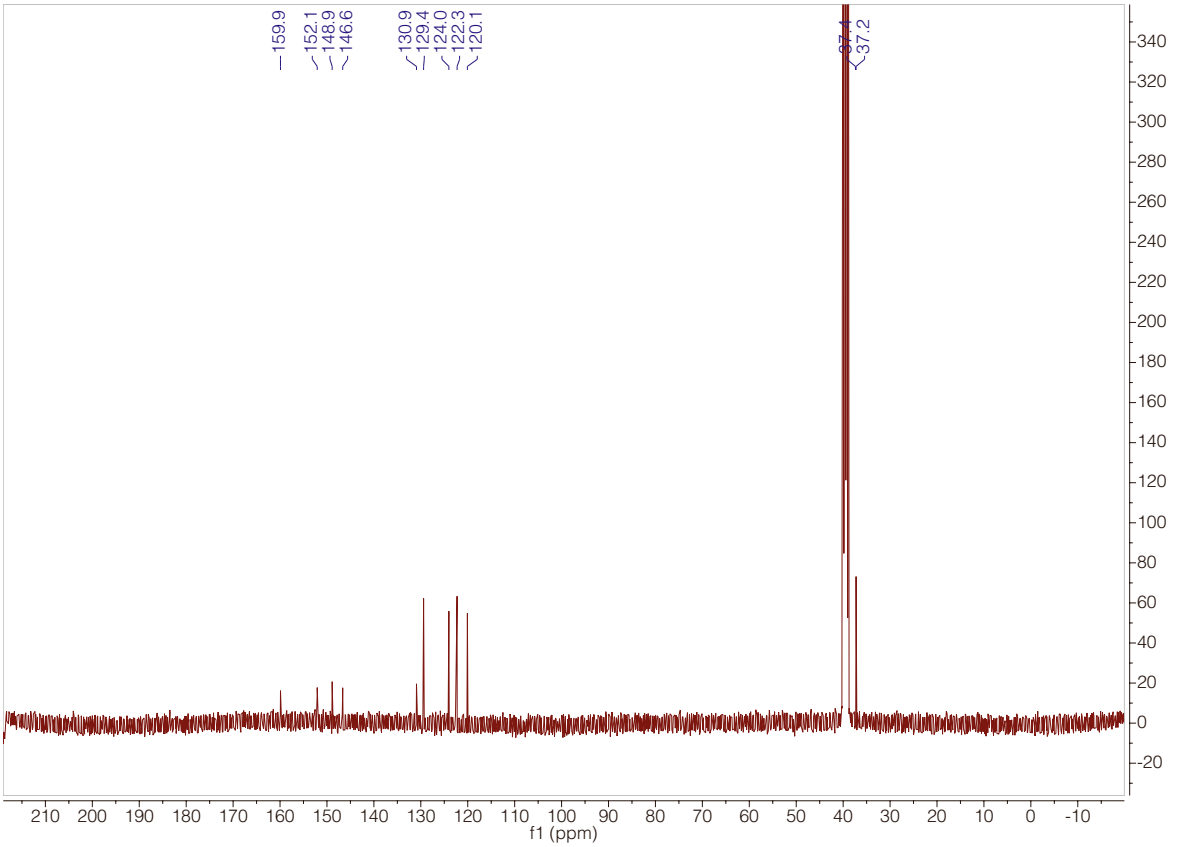
159.9
152.1
148.9
146.6
130.9
129.4
124.0
122.3
120.1
37.4
37.2
f1 (ppm)

2.21. Compound 11

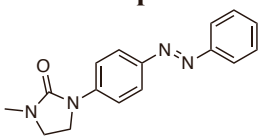

(*E*)-1-Methyl-3-(4-(phenyldiazenyl)phenyl)imidazolidin-2-one

Compound **11** was prepared according to general procedure A with 50.0 mg (162 μmol) of **S3**. HPLC purification. Yield: 77%; 34.9 mg.

^{1}H NMR (400 MHz, DMSO-d_6) δ [ppm] = 7.90 (d, J = 9.1 Hz, 2H), 7.87–7.83 (m, 2H), 7.80 (d, J = 9.1 Hz, 2H), 7.59–7.54 (m, 3H), 3.91–3.87 (m, 2H), 3.54–3.48 (m, 2H), 2.81 (s, 3H).

^{13}C NMR (101 MHz, DMSO-d_6): δ [ppm] = 157.0, 152.1, 146.2, 143.9, 130.8, 129.4, 123.6, 122.2, 116.6, 43.2, 41.9, 30.8.

HRMS (ESI): calc. for $C_{16}H_{17}N_4O$ $[M+H]^+$: 281.1397, found: 281.1395.

$\varepsilon_{378\ nm}$ (DMSO) = 20,300 M^{-1} cm^{-1}

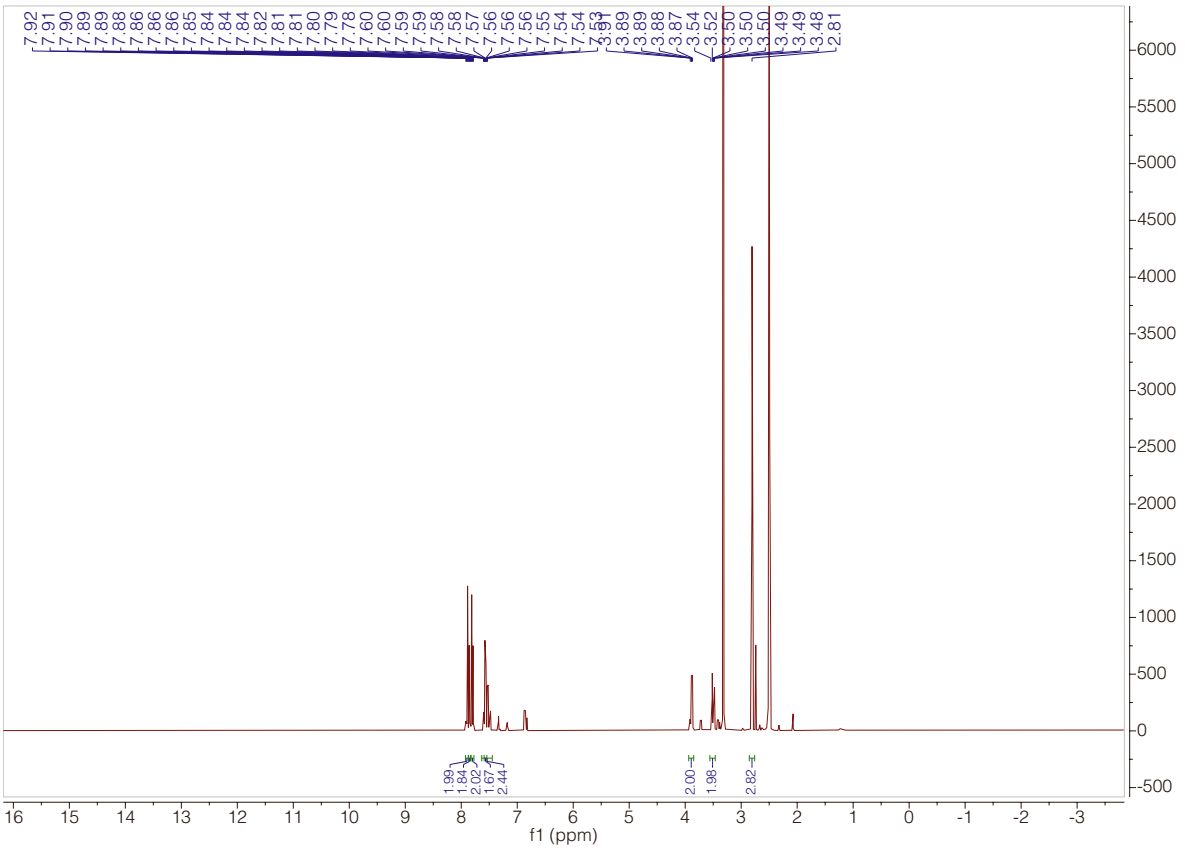
7.92
7.91
7.90
7.89
7.89
7.88
7.86
7.86
7.86
7.85
7.84
7.84
7.84
7.82
7.81
7.81
7.80
7.79
7.78
7.60
7.60
7.59
7.59
7.58
7.58
7.57
7.56
7.56
7.56
7.55
7.54
7.54
7.53
3.91
3.89
3.89
3.88
3.87
3.54
3.52
3.50
3.50
3.50
3.49
3.49
3.48
2.81
1.99
1.84
2.02
1.67
2.44
2.00
1.98
2.82
f1 (ppm)

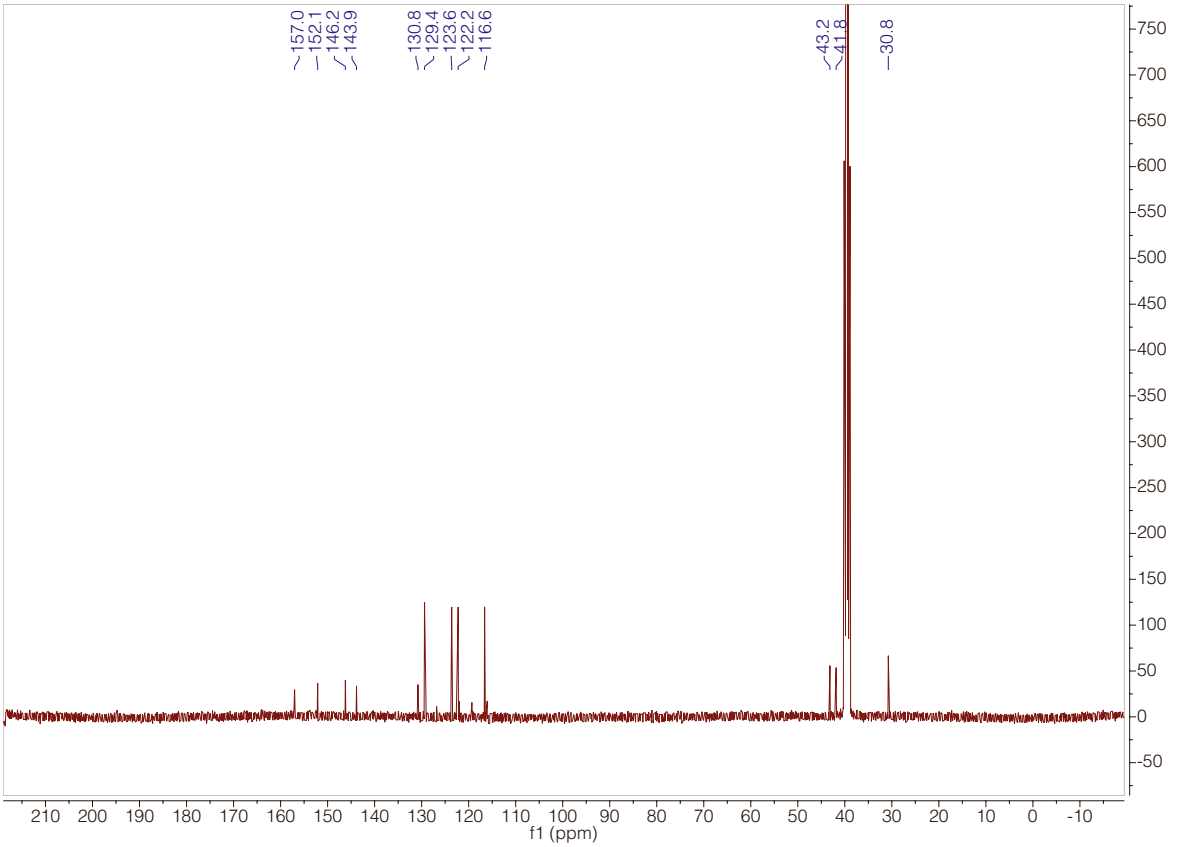
157.0
152.1
146.2
143.9
130.8
129.4
123.6
122.2
116.6
43.2
41.8
30.8
f1 (ppm)

2.22. Compound 12

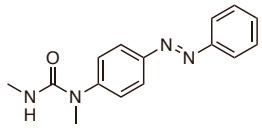

(*E*)-1-Methyl-3-(4-(phenyldiazenyl)phenyl)imidazolidin-2-one

Compound **12** was prepared according to general procedure A with 50.0 mg (162 µmol) of **S3**. HPLC purification. Yield: 44%; 20.7 mg.

^{1}H NMR (400 MHz, DMSO-d_6) δ [ppm] = 7.90–7.86 (m, 4H), 7.62–7.53 (m, 3H), 7.48 (d, J = 8.8 Hz, 2H), 6.47 (q, J = 4.5 Hz, 1H), 3.24 (s, 3H), 2.62 (d, J = 4.3 Hz, 3H).

^{13}C NMR (101 MHz, DMSO-d_6): δ [ppm] = 157.0, 152.0, 148.3, 147.5, 131.2, 129.5, 125.5, 123.2, 122.4, 36.6, 27.4.

HRMS (ESI): calc. for $C_{15}H_{17}N_4NaO$ $[M+H]^+$: 291.1216, found: 291.1218.

$\varepsilon_{359\ nm}$ (DMSO) = 15,400 M^{-1} cm^{-1}

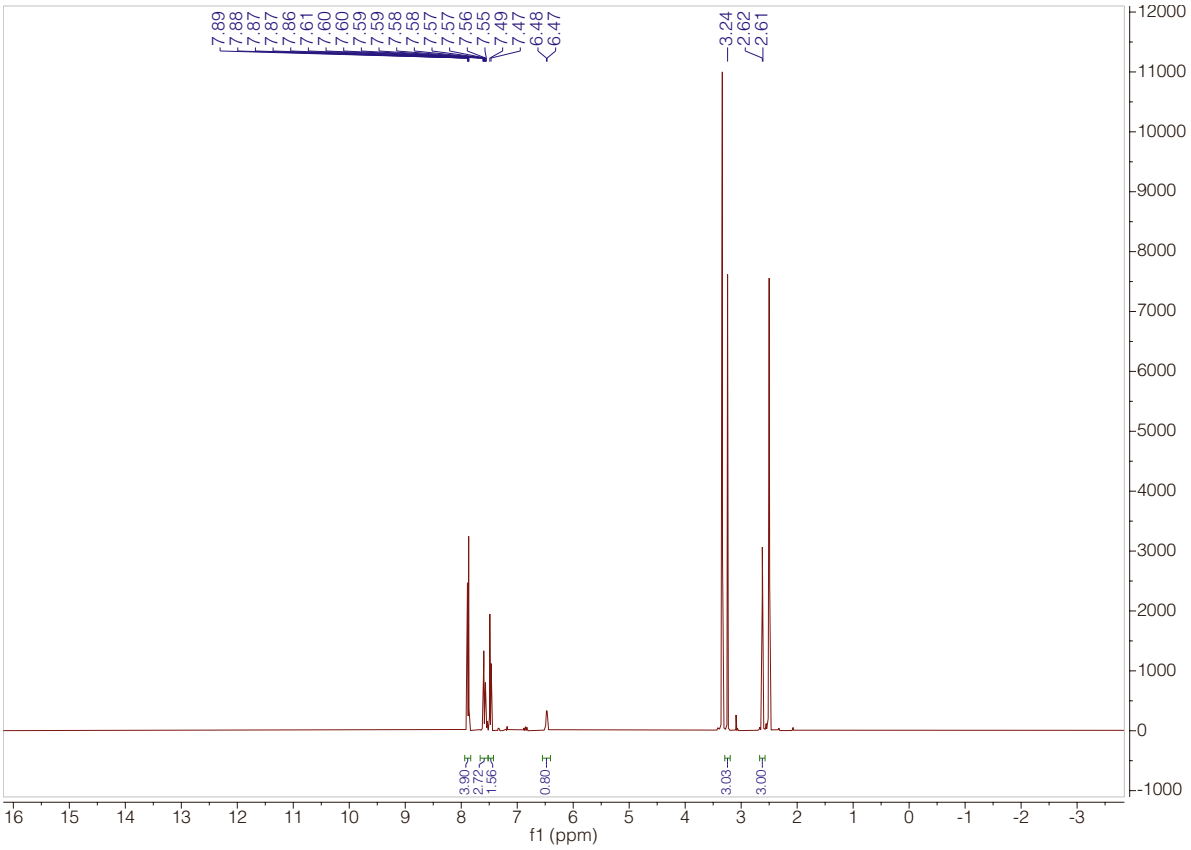
7.89
7.88
7.87
7.87
7.86
7.61
7.60
7.60
7.59
7.59
7.58
7.58
7.57
7.57
7.56
7.55
7.49
7.47
6.48
6.47
3.24
2.62
2.61
3.90
2.72
1.56
0.80
3.03
3.00
f1 (ppm)

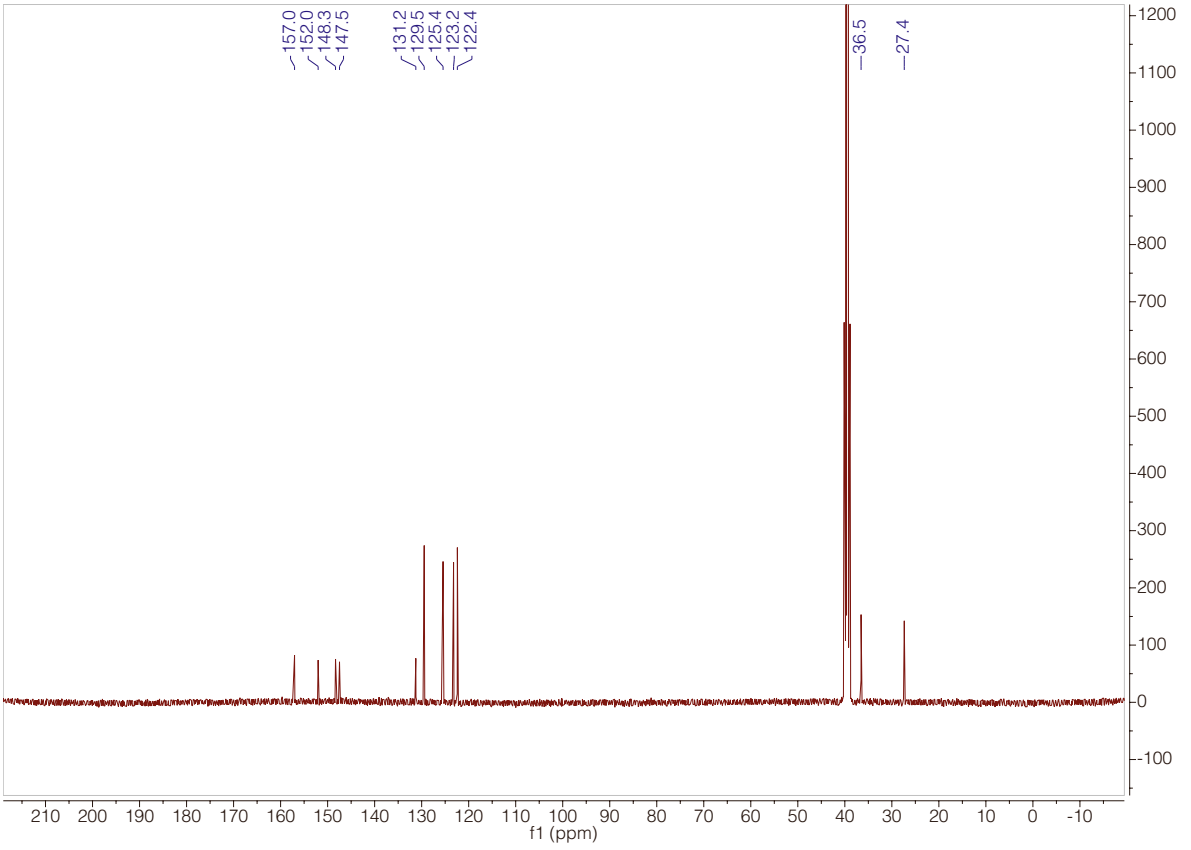
157.0
152.0
148.3
147.5
131.2
129.5
125.4
123.2
122.4
36.5
27.4
f1 (ppm)

2.23. Compound S6

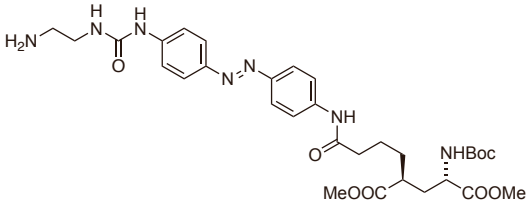

Dimethyl (2*S*,4*S*)-2-(4-((4-((*E*)-(4-(3-(2-aminoethyl)ureido)phenyl)diazenyl)phenyl)amino)-4-oxobutyl)-4-((*tert*-butoxycarbonyl)amino)pentanedioate

A flame-dried 250 mL Schlenk flask under an argon atmosphere was charged with 500 mg (0.87 mmol, 1.0 equiv.) of dimethyl (2*S*,4*S*)-2-(4-((4-((*E*)-(4-aminophenyl)diazenyl)phenyl)amino)-4-oxobutyl)-4-((*tert*-butoxycarbonyl)amino)pentanedioate (**S5**), before addition of 100 mL dry THF and 317 µL DIPEA (1.82 mmol, 2.1 equiv.). The reaction mixture was vigorously stirred and cooled to 0 °C in an ice-bath and 680 µL of $COCl_2$ (1.4 M in toluene; 0.95 mmol, 1.1 equiv.) was added dropwise. The yellow solution turned red upon stirring for 15 min and was transferred into an addition funnel to be added dropwise to a solution of ethylene diamine (1.0 mL, 900 mg, 15 mmol, 17.2 equiv.) in 100 mL dry THF at 0 °C. Upon complete addition, the ice bath was removed and the reaction mixture was allowed to stir for 5 min before it was quenched by addition of glacial HOAc (2.0 mL). The reaction mixture was concentrated *in vacuo* not exceeding 30 °C and 2 mL of DMF were added. The crude was subjected to RP-HPLC to obtain 350 mg (0.46 mmol) of the desired compound (TFA salt) as a deep red powder in 53% yield.

^{1}H NMR (400 MHz, DMSO-d_6): δ [ppm] = 10.20 (s, 1H), 9.27 (s, 1H), 7.94–7.70 (m, 9H), 7.63 (d, J = 9.0 Hz, 2H), 7.25 (d, J = 8.2 Hz, 1H), 6.64 (t, J = 5.8 Hz, 1H), 4.01 (td, J = 8.7, 5.7 Hz, 1H), 3.61 (s, 6H), 3.35 (q, J = 6.0 Hz, 2H), 2.92 (q, J = 5.9 Hz, 2H), 2.45 (t, J = 6.2 Hz, 1H), 2.40–2.30 (m, 2H), 1.95–1.79 (m, 2H), 1.64–1.48 (m, 4H), 1.37 (s, 9H).

HRMS (ESI): calc. for $C_{31}H_{44}N_7O_8$ $[M+H]^+$: 642.3246, found: 642.3248.

2.24. Compound S7

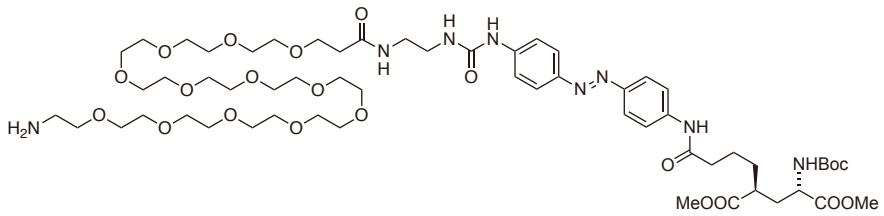

(2*S*,4*S*)-2-(4-((4-((*E*)-(4-(3-(1-Amino-39-oxo-3,6,9,12,15,18,21,24,27,30,33,36-dodecaoxa-40-azadotetracontan-42-yl)ureido)phenyl)diazenyl)phenyl)amino)-4-oxobutyl)-4-((*tert*-butoxycarbonyl)amino)pentanedioic acid

S7 was prepared according to general procedure C.

Acid: FmocPEG$_{12}$COOH; amine **S6**.

HRMS (ESI): calc. for $C_{56}H_{94}N_8O_{21}$ $[M+2H]^{2+}$: 607.3261, found: 607.3260.

2.25. Compound S8

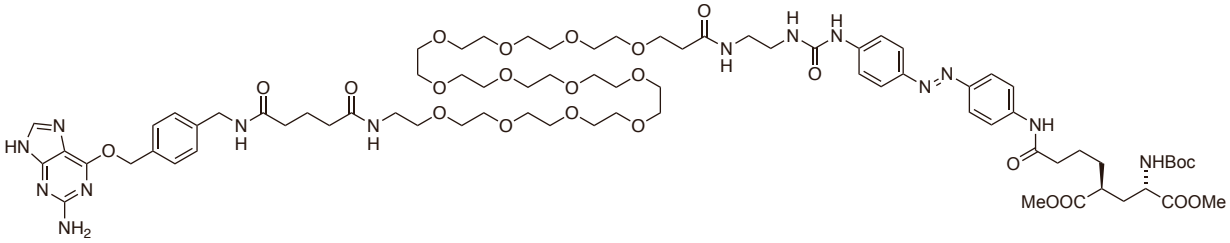

(2*S*,4*S*)-2-(4-((4-((*E*)-(4-(3-(1-(4-(((2-Amino-9*H*-purin-6-yl)oxy)methyl)phenyl)-3,7,47-trioxo-11,14,17,20,23,26,29,32,35,38,41,44-dodecaoxa-2,8,48-triazapentacontan-50-yl)ureido)-phenyl)diazenyl)phenyl)amino)-4-oxobutyl)-4-((*tert*-butoxycarbonyl)amino)pentanedioic acid

S8 was prepared according to general procedure B.

Acid: **BG-COOH**; amine **S7**.

HRMS (ESI): calc. for $C_{76}H_{116}N_{14}O_{24}$ $[M+2H]^{2+}$: 804.4138, found: 804.4134.

2.26. $BGAG_{12,400}$

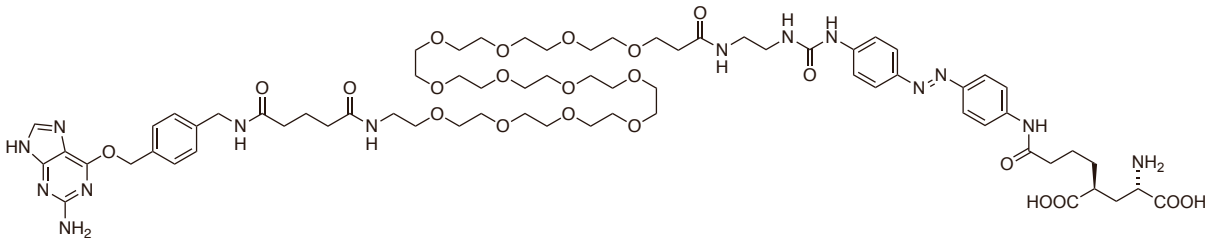

(2*S*,4*S*)-2-(4-((4-((*E*)-(4-(3-(1-(4-(((2-Amino-9*H*-purin-6-yl)oxy)methyl)phenyl)-3,7,47-trioxo-11,14,17,20,23,26,29,32,35,38,41,44-dodecaoxa-2,8,48-triazapentacontan-50-yl)ureido)-phenyl)-diazenyl)phenyl)amino)-4-oxobutyl)-4-((*tert*-butoxycarbonyl)amino)pentanedioic acid

$BGAG_{12,400}$ was prepared according to general procedure D from compound **S8**.

HRMS (ESI): calc. for $C_{74}H_{112}N_{14}O_{24}$ $[M+2H]^{2+}$: 790.3981, found: 790.3980; ester cleaved intermediate.

HRMS (ESI): calc. for $C_{69}H_{105}N_{14}O_{22}$ $[M+3H]^{3+}$: 493.9170, found: 493.9178, **$BGAG_{12,400}$**.

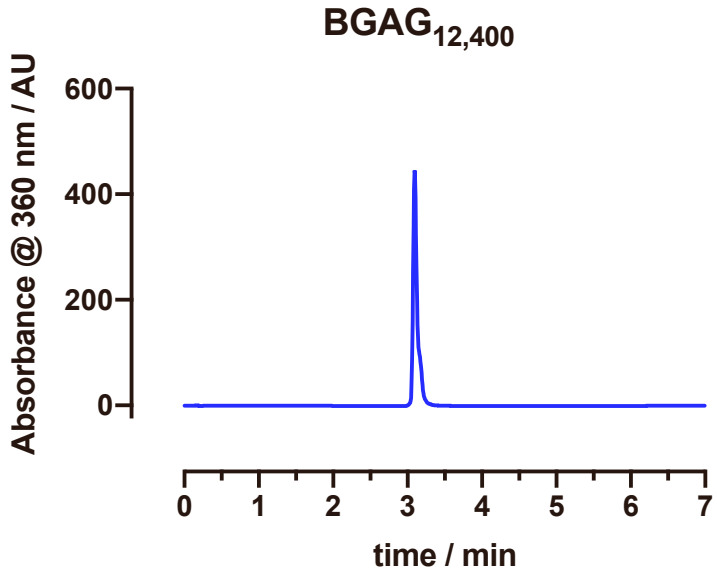

2.27. Compound S10

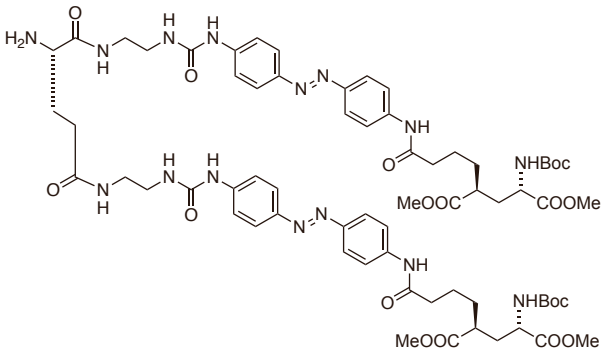

Tetramethyl 4,4'-(((((1*E*,1'*E*)-((((*S*)-7-amino-6,10-dioxo-2,5,11,14-tetraazapentadecanedioyl)-bis-(azanediyl))bis(4,1-phenylene))bis(diazene-2,1-diyl))bis(4,1-phenylene))bis(azanediyl))bis(4-oxobutane-4,1-diyl))(2*S*,2'*S*,4*S*,4'*S*)-bis(2-((*tert*-butoxycarbonyl)amino)pentanedioate)

S10 was prepared according to general procedure C, with 3.0 equiv of HBTU and 3.0 equiv. of **S6**.

Acid: **S9**

HRMS (ESI): calc. for $C_{82}H_{103}N_{15}O_{20}$ $[M+2H]^{2+}$: 808.8746, found: 808.8733; Fmoc protected intermediate.

HRMS (ESI): calc. for $C_{62}H_{85}N_{15}O_{16}$ $[M–Boc+2H]^{2+}$: 647.8144, found: 647.8135; **S10**.

2.28. Compound S11

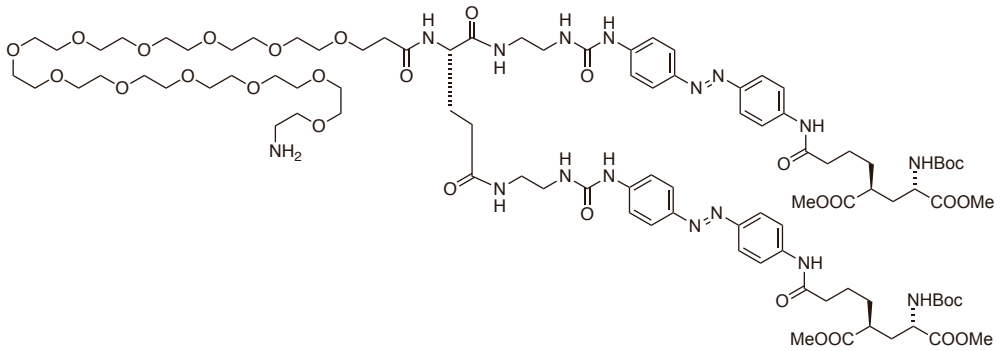

Tetramethyl 4,4'-(((((1*E*,1'*E*)-((((*S*)-7-(1-amino-3,6,9,12,15,18,21,24,27,30,33,36-dodecaoxa-nonatriacontan-39-amido)-6,10-dioxo-2,5,11,14-tetraazapentadecanedioyl)bis-(azanediyl))bis(4,1-phenylene))bis(diazene-2,1-diyl))bis(4,1-phenylene))bis(azanediyl))-bis(4-oxobutane-4,1-diyl))(2*S*,2'*S*,4*S*,4'*S*)-bis(2-((*tert*-butoxycarbonyl)amino)-pentanedioate)

S11 was prepared according to general procedure C at 50 °C.

Acid: FmocPEG$_{12}$COOH; amine **S10**.

HRMS (ESI): calc. for $C_{109}H_{156}N_{16}O_{33}$ $[M+2H]^{2+}$: 1109.0520, found: 1109.0513; Fmoc protected intermediate.

HRMS (ESI): calc. for $C_{94}H_{146}N_{16}O_{31}$ $[M+2H]^{2+}$: 998.0180, found: 998.0150; **S10**.

2.29. Compound S12

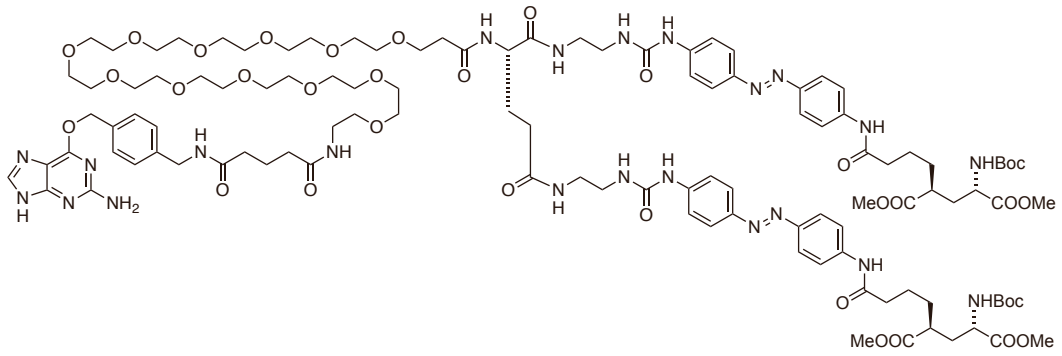

Tetramethyl 4,4'-(((((1*E*,1'*E*)-((((*S*)-7-(1-(4-(((2-amino-9*H*-purin-6-yl)oxy)methyl)phenyl)-3,7-dioxo-11,14,17,20,23,26,29,32,35,38,41,44-dodecaoxa-2,8-diazaheptatetracontan-47-amido)-6,10-dioxo-2,5,11,14-tetraazapentadecanedioyl)bis(azanediyl))bis(4,1-phenylene))bis(diazene-2,1-diyl))bis(4,1-phenylene))bis(azanediyl))bis(4-oxobutane-4,1-diyl))(2*S*,2'*S*,4*S*,4'*S*)-bis(2-((*tert*-butoxycarbonyl)amino)pentanedioate)

S12 was prepared according to general procedure B.

Acid: **BG-COOH**; amine **S11**.

HRMS (ESI): calc. for $C_{112}H_{164}N_{22}O_{34}$ $[M+2H]^{2+}$: 1181.0900, found: 1181.0876.

2.30. ^{2x}BGAG$_{12,400}$

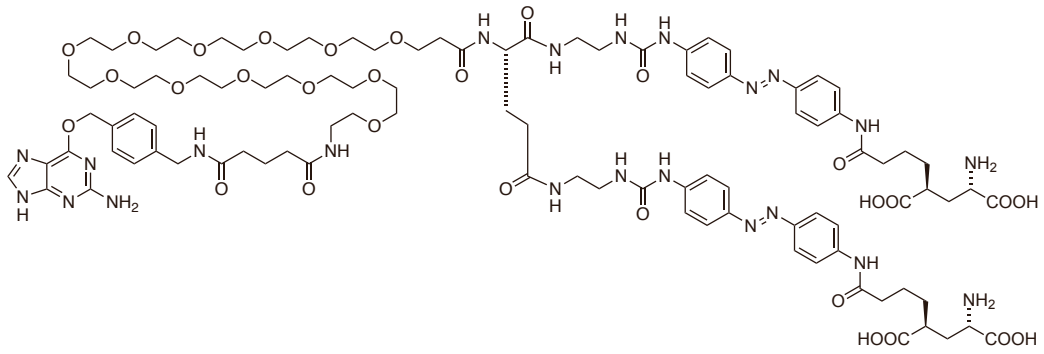

(2*S*,2'*S*,4*S*,4'*S*)-4,4'-(((((1*E*,1'*E*)-((((*S*)-7-(1-(4-(((2-Amino-9*H*-purin-6-yl)oxy)methyl)phenyl)-3,7-dioxo-11,14,17,20,23,26,29,32,35,38,41,44-dodecaoxa-2,8-diazaheptatetracontan-47-amido)-6,10-dioxo-2,5,11,14-tetraazapentadecanedioyl)bis(azanediyl))bis(4,1-phenylene))bis(diazene-2,1-diyl))bis(4,1-phenylene))bis(azanediyl))bis(4-oxobutane-4,1-diyl))bis(2-aminopentanedioic acid)

^{2x}**BGAG$_{12,400}$** was prepared according to general procedure D from compound **S12**.

HRMS (ESI): calc. for $C_{108}H_{156}N_{22}O_{34}$ $[M+2H]^{2+}$: 1153.0587, found: 1153.0575; ester cleaved intermediate.

HRMS (ESI): calc. for $C_{98}H_{142}N_{22}O_{30}$ $[M+4H]^{4+}$: 527.0067, found: 527.0063; ^{2x}**BGAG$_{12,400}$**.

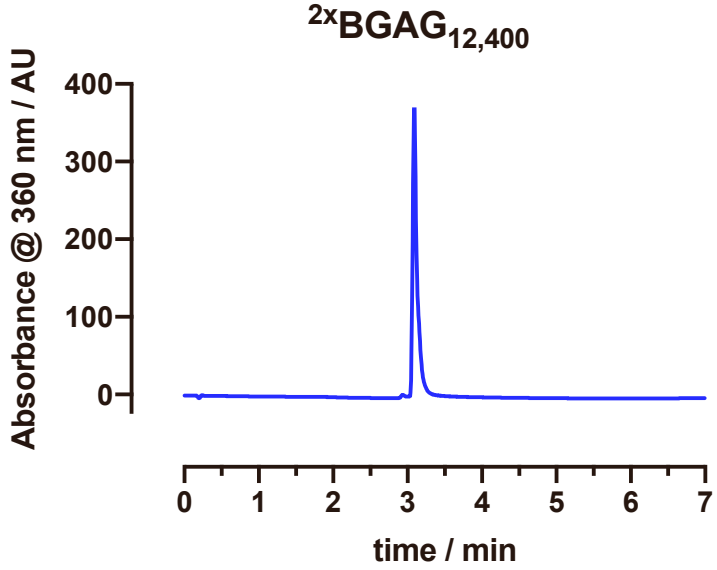

2.31. Compound S13

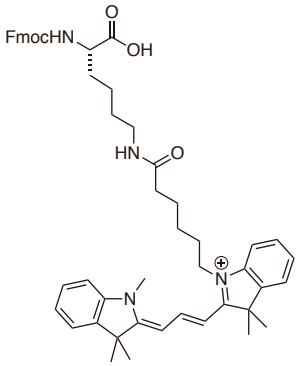

1-(6-(((*S*)-5-((((9*H*-Fluoren-9-yl)methoxy)carbonyl)amino)-5-carboxypentyl)amino)-6-oxohexyl)-3,3-dimethyl-2-((*E*)-3-((*Z*)-1,3,3-trimethylindolin-2-ylidene)prop-1-en-1-yl)-3*H*-indol-1-ium

A round bottom flask was charged with 50.0 mg (109 μmol, 1.0 equiv.) of 1-(5-carboxypentyl)-3,3-dimethyl-2-((*E*)-3-((*Z*)-1,3,3-trimethylindolin-2-ylidene)prop-1-en-1-yl)-3*H*-indol-1-ium(Ueno et al., 2011) which was dissolved in 2.1 mL DMSO and 72 μL DIPEA. TSTU (32.9 mg, 109 μmol, 1.0 equiv.) was added in one portion and the mixture was incubated for 30 min before 53.1 mg (131 μmol, 1.2 equiv.) of Fmoc-Lys-OH hydrochloride (Aldrich, #17290) was added in one portion. The reaction mixture was incubated for another hour before it was quenched by addition of 72 μL HOAc and subjected to RP-HPLC to obtain 49.0 mg (60.0 μmol) of the desired product as a red powder after lyophilization in 56% yield.

HRMS (ESI): calc. for $C_{51}H_{59}N_4O_5$ $[M]^+$: 807.4480, found: 807.4488.

2.32. Compound S14

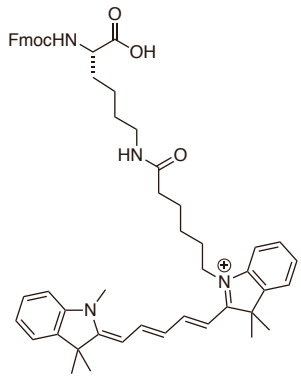

1-(6-(((*S*)-5-((((9*H*-Fluoren-9-yl)methoxy)carbonyl)amino)-5-carboxypentyl)amino)-6-oxohexyl)-3,3-dimethyl-2-((1*E*,3*E*)-5-((*Z*)-1,3,3-trimethylindolin-2-ylidene)penta-1,3-dien-1-yl)-3*H*-indol-1-ium

Compound **S14** was prepared as reported previously(Acosta-Ruiz et al., 2020). A round bottom flask was charged with 35.0 mg (72.4 μmol, 1.0 equiv.) of 1-(5-carboxypentyl)-3,3-dimethyl-2-((1*E*,3*E*)-5-((*Z*)-1,3,3-trimethylindolin-2-ylidene)penta-1,3-dien-1-yl)-3*H*-indol-1-ium(Ueno et al., 2011) which was dissolved in 1.5 mL DMSO and 50 μL DIPEA. TSTU (21.8 mg, 72.4 μmol, 1.0 equiv.) was added in one portion and the mixture was incubated for 30 min before 32.0 mg (86.8 μmol, 1.2 equiv.) of Fmoc-Lys-OH hydrochloride (Aldrich, #17290) was added in one portion. The reaction mixture was incubated for another hour before it was quenched by addition of 50 μL HOAc and subjected to RP-HPLC to obtain 26 mg (32.2 μmol) of the desired product as a blue powder after lyophilization in 45% yield.

HRMS (ESI): calc. for $C_{53}H_{61}N_4O_5$ $[M]^+$: 833.4636, found: 833.4639.

2.33. Compound S15

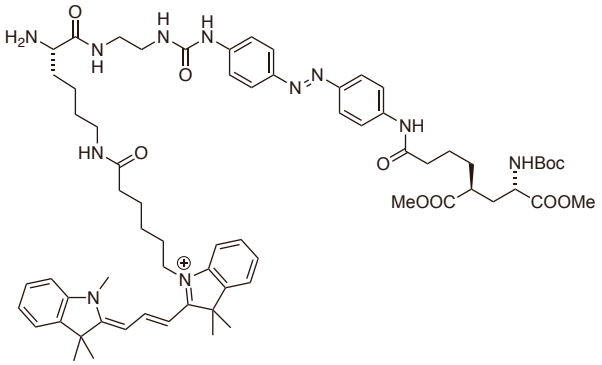

1-(6-(((*S*)-5-Amino-6-((2-(3-(4-((*E*)-(4-((5*S*,7*S*)-7-((*tert*-butoxycarbonyl)amino)-8-methoxy-5-(methoxycarbonyl)-8-oxooctanamido)phenyl)diazenyl)phenyl)ureido)ethyl)amino)-6-oxohexyl)-amino)-6-oxohexyl)-3,3-dimethyl-2-((*E*)-3-((*Z*)-1,3,3-trimethylindolin-2-ylidene)prop-1-en-1-yl)-3*H*-indol-1-ium

S15 was prepared according to general procedure C.

Acid: **S13**; amine **S6**.

HRMS (ESI): calc. for $C_{84}H_{103}N_{11}O_{12}$ $[M+H–Boc]^{2+}$: 665.8548, found: 665.8544; Fmoc protected intermediate.

HRMS (ESI): calc. for $C_{67}H_{91}N_{11}O_{10}$ $[M+H]^{2+}$: 604.8470, found: 604.8466; **27**.

2.34. Compound S17

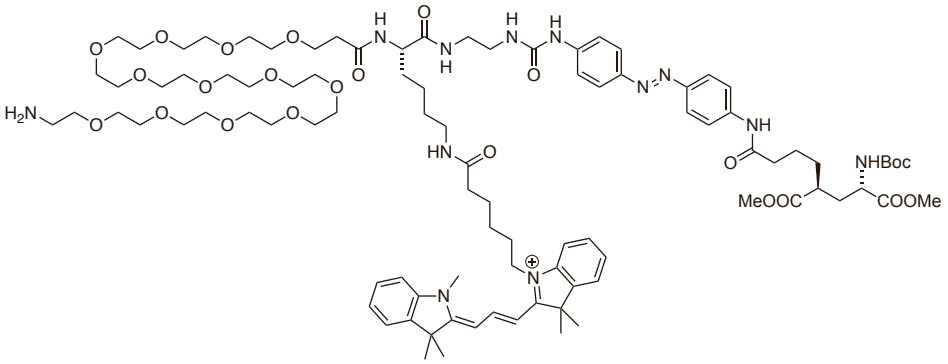

1-((*S*)-1-Amino-41-((2-(3-(4-((*E*)-(4-((5*S*,7*S*)-7-((*tert*-butoxycarbonyl)amino)-8-methoxy-5-(methoxycarbonyl)-8-oxooctanamido)phenyl)diazenyl)phenyl)ureido)ethyl)carbamoyl)-39,47-dioxo-3,6,9,12,15,18,21,24,27,30,33,36-dodecaoxa-40,46-diazadopentacontan-52-yl)-3,3-dimethyl-2-((*E*)-3-((*Z*)-1,3,3-trimethylindolin-2-ylidene)prop-1-en-1-yl)-3*H*-indol-1-ium

S17 was prepared according to general procedure C.

Acid: FmocNHPEG$_{12}$COOH; amine **S15**.

HRMS (ESI): calc. for $C_{109}H_{154}N_{12}O_{25}$ $[M+H]^{2+}$: 1016.0584, found: 1016.0581; Fmoc protected intermediate.

HRMS (ESI): calc. for $C_{94}H_{144}N_{12}O_{23}$ $[M+H]^{2+}$: 905.0244, found: 905.0243.

2.35. Compound S19

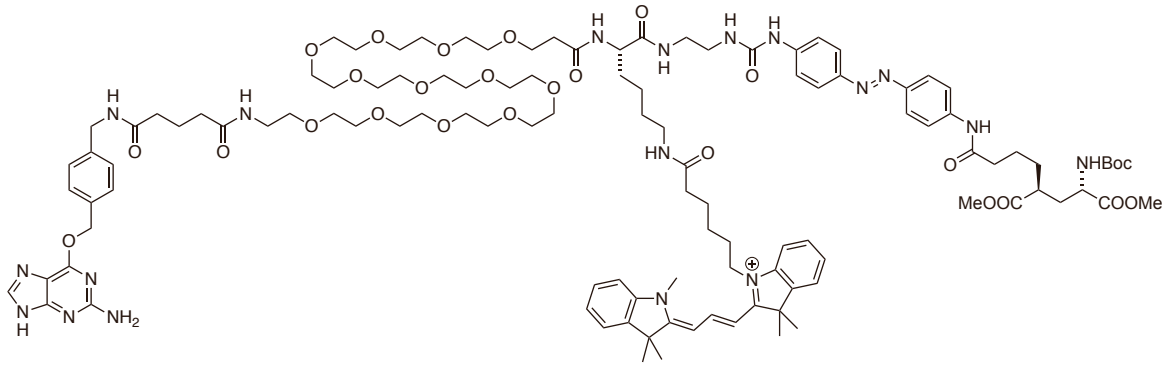

1-((*S*)-1-(4-(((2-Amino-9*H*-purin-6-yl)oxy)methyl)phenyl)-49-((2-(3-(4-((*E*)-(4-((5*S*,7*S*)-7-((*tert*-butoxycarbonyl)amino)-8-methoxy-5-(methoxycarbonyl)-8-oxooctanamido)phenyl)diazenyl)-phenyl)ureido)ethyl)carbamoyl)-3,7,47,55-tetraoxo-11,14,17,20,23,26,29,32,35,38,41,44-dodecaoxa-2,8,48,54-tetraazahexacontan-60-yl)-3,3-dimethyl-2-((*E*)-3-((*Z*)-1,3,3-trimethylindolin-2-ylidene)prop-1-en-1-yl)-3*H*-indol-1-ium

S19 was prepared according to general procedure B.

Acid: **BG-COOH**; amine **S17**.

HRMS (ESI): calc. for $C_{112}H_{163}N_{18}O_{26}$ $[M+2H]^{3+}$: 725.7333, found: 725.7329.

2.36. $BGAG_{12,400}$-Cy3

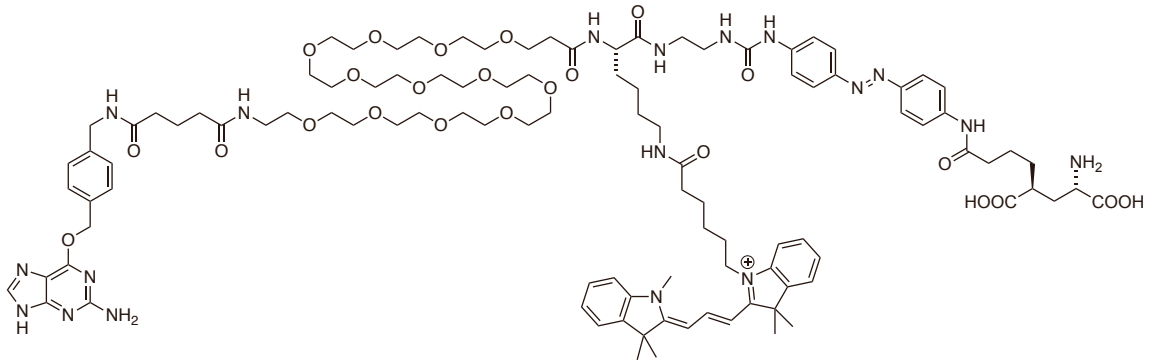

1-((*S*)-49-((2-(3-(4-((*E*)-(4-((5*S*,7*S*)-7-Amino-5,7-dicarboxyheptanamido)phenyl)diazenyl)phenyl)-ureido)ethyl)carbamoyl)-1-(4-(((2-amino-9*H*-purin-6-yl)oxy)methyl)phenyl)-3,7,47,55-tetraoxo-11,14,17,20,23,26,29,32,35,38,41,44-dodecaoxa-2,8,48,54-tetraazahexacontan-60-yl)-3,3-dimethyl-2-((*E*)-3-((*Z*)-1,3,3-trimethylindolin-2-ylidene)prop-1-en-1-yl)-3*H*-indol-1-ium

$BGAG_{12,400}$-Cy3 was prepared according to general procedure D from compound **S19**.

HRMS (ESI): calc. for $C_{110}H_{159}N_{18}O_{26}$ $[M+H]^{2+}$: 1074.0807, found: 1074.0810; ester cleaved intermediate.

HRMS (ESI): calc. for $C_{105}H_{150}N_{18}O_{24}$ $[M+2H]^{3+}$: 683.0388, found: 683.0385; **$BGAG_{12,400}$-Cy3**.

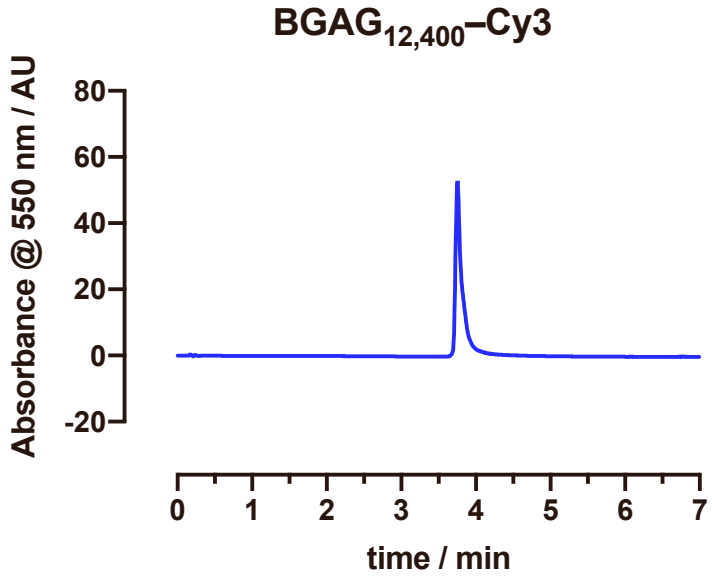

2.37. Compound S16

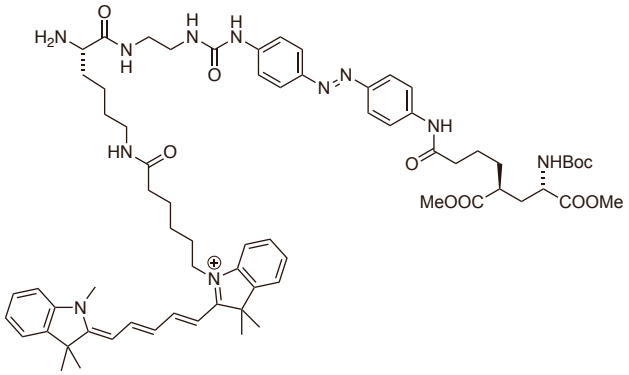

1-(6-(((*S*)-5-Amino-6-((2-(3-(4-((*E*)-(4-((5*S*,7*S*)-7-((*tert*-butoxycarbonyl)amino)-8-methoxy-5-(methoxycarbonyl)-8-oxooctanamido)phenyl)diazenyl)phenyl)ureido)ethyl)amino)-6-oxohexyl)-amino)-6-oxohexyl)-3,3-dimethyl-2-((1*E*,3*E*)-5-((*Z*)-1,3,3-trimethylindolin-2-ylidene)penta-1,3-dien-1-yl)-3*H*-indol-1-ium

S16 was prepared according to general procedure C.

Acid: **S14**; amine **S6**.

HRMS (ESI): calc. for $C_{84}H_{103}N_{11}O_{12}$ $[M+H]^{2+}$: 728.8888, found: 728.8878; Fmoc protected intermediate.

HRMS (ESI): calc. for $C_{69}H_{93}N_{11}O_{10}$ $[M+H]^{2+}$: 617.8548, found: 617.8548; **S16**.

2.38. Compound S18

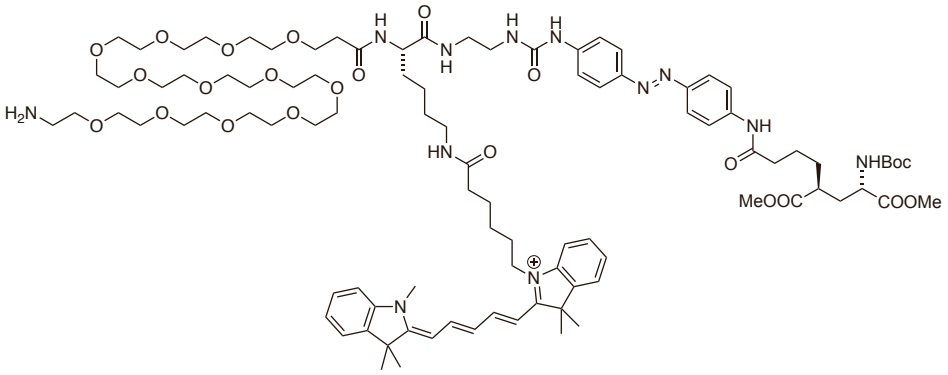

1-((*S*)-1-Amino-41-((2-(3-(4-((*E*)-(4-((5*S*,7*S*)-7-((*tert*-butoxycarbonyl)amino)-8-methoxy-5-(methoxycarbonyl)-8-oxooctanamido)phenyl)diazenyl)phenyl)ureido)ethyl)carbamoyl)-39,47-dioxo-3,6,9,12,15,18,21,24,27,30,33,36-dodecaoxa-40,46-diazadopentacontan-52-yl)-3,3-dimethyl-2-((1*E*,3*E*)-5-((*Z*)-1,3,3-trimethylindolin-2-ylidene)penta-1,3-dien-1-yl)-3*H*-indol-1-ium

S18 was prepared according to general procedure C.

Acid: FmocNHPEG$_{12}$COOH; amine **S16**.

HRMS (ESI): calc. for $C_{111}H_{156}N_{12}O_{25}$ $[M+H]^{2+}$: 1029.0663, found: 1029.0645; Fmoc protected intermediate.

HRMS (ESI): calc. for $C_{96}H_{146}N_{12}O_{23}$ $[M+H]^{2+}$: 918.0322, found: 918.0317; **S18**.

2.39. Compound S20

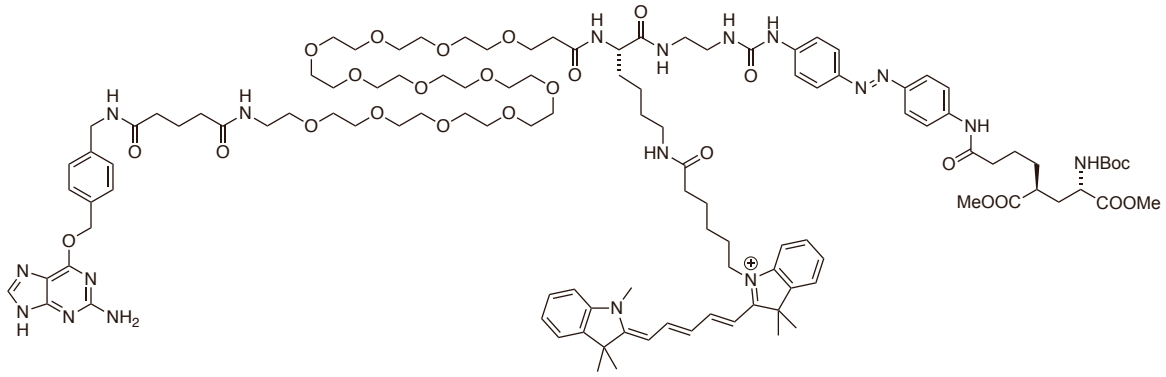

1-((*S*)-1-(4-(((2-Amino-9*H*-purin-6-yl)oxy)methyl)phenyl)-49-((2-(3-(4-((*E*)-(4-((5*S*,7*S*)-7-((*tert*-butoxycarbonyl)amino)-8-methoxy-5-(methoxycarbonyl)-8-oxooctanamido)-phenyl)diazenyl)-phenyl)ureido)ethyl)carbamoyl)-3,7,47,55-tetraoxo-11,14,17,20,23,26,29, 32,35,38,41,44-dodecaoxa-2,8,48,54-tetraazahexacontan-60-yl)-3,3-dimethyl-2-((1*E*,3*E*)-5-((*Z*)-1,3,3-trimethylindolin-2-ylidene)penta-1,3-dien-1-yl)-3*H*-indol-1-ium

S20 was prepared according to general procedure B.

Acid: **BG-COOH**; amine **S18**.

HRMS (ESI): calc. for $C_{114}H_{165}N_{18}O_{26}$ $[M+2H]^{3+}$: 734.4052, found: 734.4050.

2.40. $BGAG_{12,400}$-Cy5

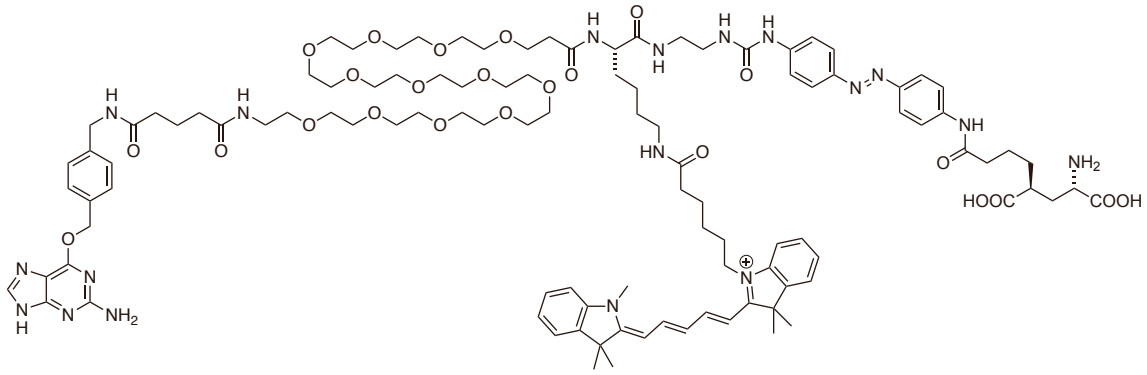

1-((*S*)-49-((2-(3-(4-((*E*)-(4-((5*S*,7*S*)-7-Amino-5,7-dicarboxyheptanamido)phenyl)diazenyl)phenyl)-ureido)ethyl)carbamoyl)-1-(4-(((2-amino-9*H*-purin-6-yl)oxy)methyl)phenyl)-3,7,47,55-tetraoxo-11,14,17,20,23,26,29,32,35,38,41,44-dodecaoxa-2,8,48,54-tetraazahexacontan-60-yl)-3,3-dimethyl-2-((1*E*,3*E*)-5-((*Z*)-1,3,3-trimethylindolin-2-ylidene)penta-1,3-dien-1-yl)-3*H*-indol-1-ium

$BGAG_{12,400}$-Cy5 was prepared according to general procedure D from compound **S20**.

HRMS (ESI): calc. for $C_{112}H_{161}N_{18}O_{26}$ $[M+2H]^{3+}$: 725.0615, found: 725.0613; ester cleaved intermediate.

HRMS (ESI): calc. for $C_{107}H_{152}N_{18}O_{24}$ $[M+2H]^{3+}$: 691.3747, found: 691.3755; **$BGAG_{12,400}$-Cy5**.

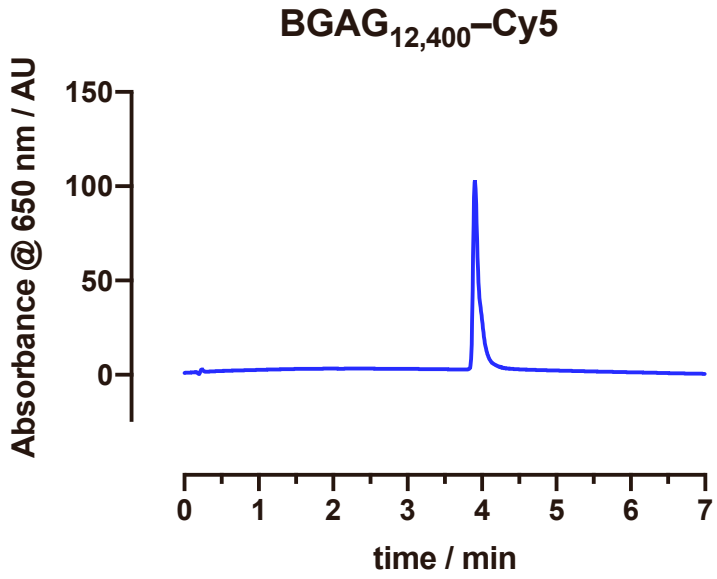

2.41. Compound S21

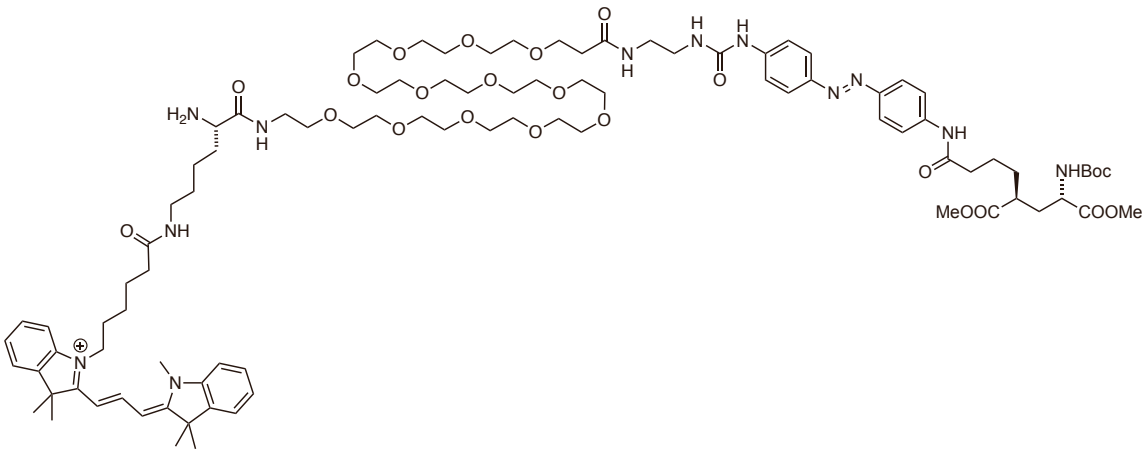

1-((*S*)-47-Amino-1-((4-((*E*)-(4-((5*S*,7*S*)-7-((*tert*-butoxycarbonyl)amino)-8-methoxy-5-(methoxycarbonyl)-8-oxooctanamido)phenyl)diazenyl)phenyl)amino)-1,6,46,53-tetraoxo-9,12,15,18,21,24,27,30,33,36,39,42-dodecaoxa-2,5,45,52-tetraazaoctapentacontan-58-yl)-3,3-dimethyl-2-((*E*)-3-((*Z*)-1,3,3-trimethylindolin-2-ylidene)prop-1-en-1-yl)-3*H*-indol-1-ium

S21 was prepared according to general procedure C.

Acid: **S13**; amine **S7**.

HRMS (ESI): calc. for $C_{94}H_{144}N_{12}O_{23}$ $[M+H]^{2+}$: 905.0244, found: 905.0422.

2.42. Compound S23

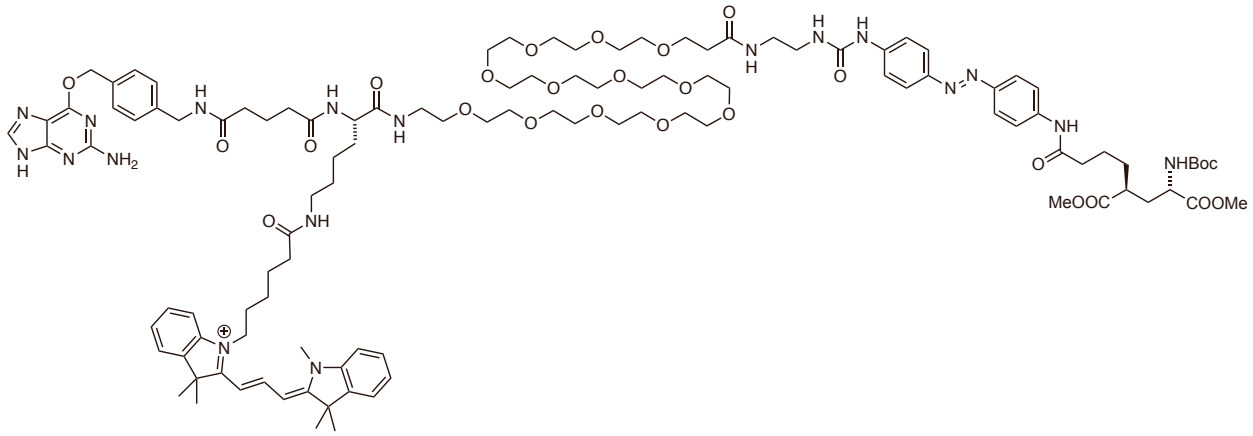

1-((*S*)-47-(5-((4-(((2-Amino-9*H*-purin-6-yl)oxy)methyl)benzyl)amino)-5-oxopentanamido)-1-((4-((*E*)-(4-((5*S*,7*S*)-7-((*tert*-butoxycarbonyl)amino)-8-methoxy-5-(methoxycarbonyl)-8-oxooctanamido)phenyl)diazenyl)phenyl)amino)-1,6,46,53-tetraoxo-9,12,15,18,21,24,27,30,33,36,39,42-dodecaoxa-2,5,45,52-tetraazaoctapentacontan-58-yl)-3,3-dimethyl-2-((*E*)-3-((*Z*)-1,3,3-trimethylindolin-2-ylidene)prop-1-en-1-yl)-3*H*-indol-1-ium

S23 was prepared according to general procedure B.

Acid: **BG-COOH**; amine **S21**.

HRMS (ESI): calc. for $C_{112}H_{163}N_{18}O_{26}$ $[M+2H]^{3+}$: 725.7333, found: 725.7326.

2.43. $BGAG_{12,400}$–Cy3 v2

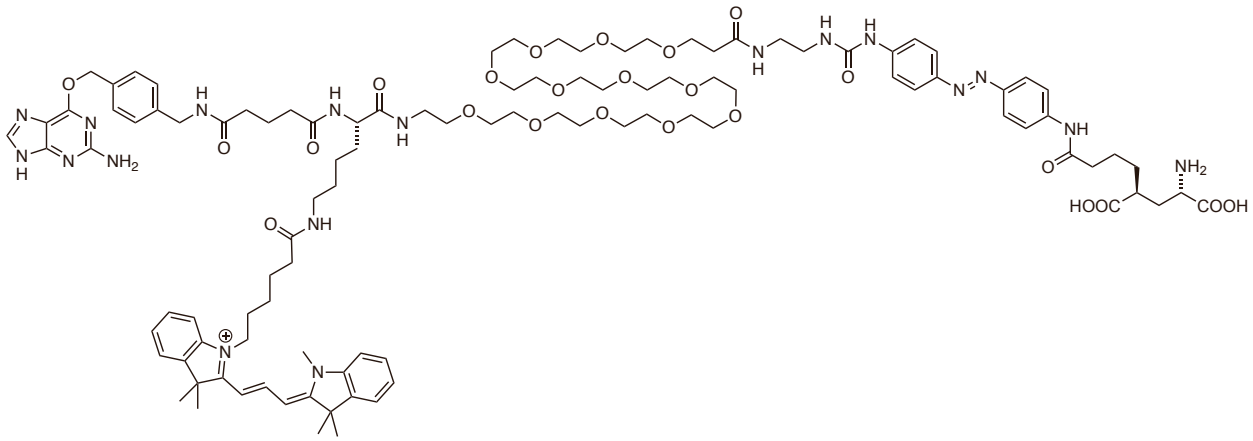

1-((*S*)-1-((4-((*E*)-(4-((5*S*,7*S*)-7-Amino-5,7-dicarboxyheptanamido)phenyl)diazenyl)phenyl)amino)-47-(5-((4-(((2-amino-9*H*-purin-6-yl)oxy)methyl)benzyl)amino)-5-oxopentanamido)-1,6,46,53-tetraoxo-9,12,15,18,21,24,27,30,33,36,39,42-dodecaoxa-2,5,45,52-tetraazaoctapentacontan-58-yl)-3,3-dimethyl-2-((*E*)-3-((*Z*)-1,3,3-trimethylindolin-2-ylidene)prop-1-en-1-yl)-3*H*-indol-1-ium

$BGAG_{12,400}$–Cy3 was prepared according to general procedure D from compound **S23**.

HRMS (ESI): calc. for $C_{110}H_{159}N_{18}O_{26}$ $[M+2H]^{3+}$: 716.3896, found: 716.3895; ester cleaved intermediate.

HRMS (ESI): calc. for $C_{105}H_{151}N_{18}O_{24}$ $[M+2H]^{3+}$: 683.0388, found: 683.0385; **$BGAG_{12,400}$–Cy3**.

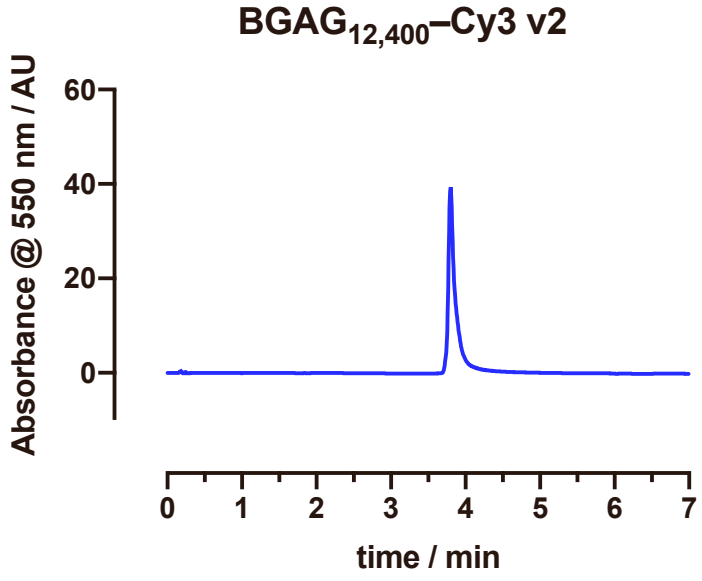

2.44. Compound S22

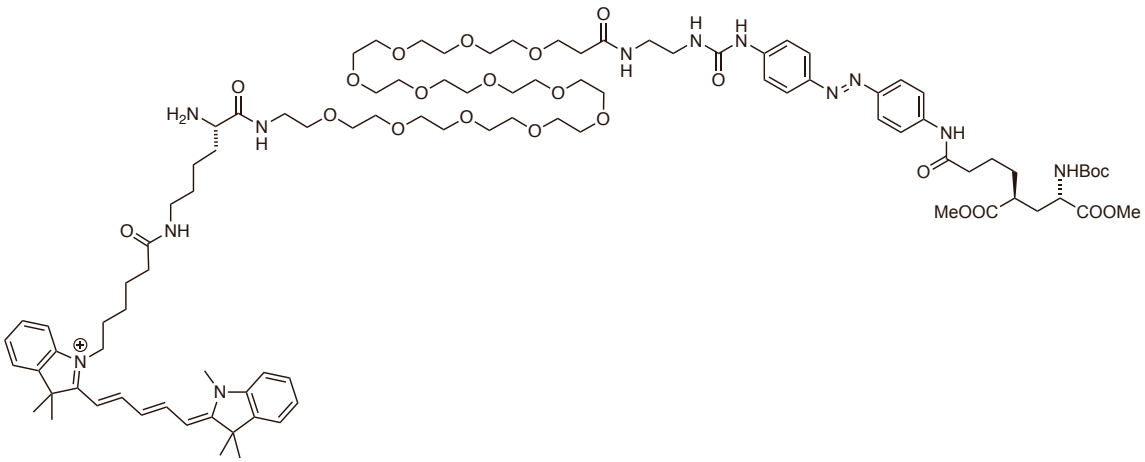

1-((*S*)-47-Amino-1-((4-((*E*)-(4-((5*S*,7*S*)-7-((*tert*-butoxycarbonyl)amino)-8-methoxy-5-(methoxycarbonyl)-8-oxooctanamido)phenyl)diazenyl)phenyl)amino)-1,6,46,53-tetraoxo-9,12,15,18,21,24,27,30,33,36,39,42-dodecaoxa-2,5,45,52-tetraazaoctapentacontan-58-yl)-3,3-dimethyl-2-((1*E*,3*E*)-5-((*Z*)-1,3,3-trimethylindolin-2-ylidene)penta-1,3-dien-1-yl)-3*H*-indol-1-ium

S22 was prepared according to general procedure C.

Acid: **S14**; amine **S7**.

HRMS (ESI): calc. for $C_{96}H_{146}N_{12}O_{23}$ $[M+H]^{2+}$: 918.0322, found: 918.0320.

2.45. Compound S24

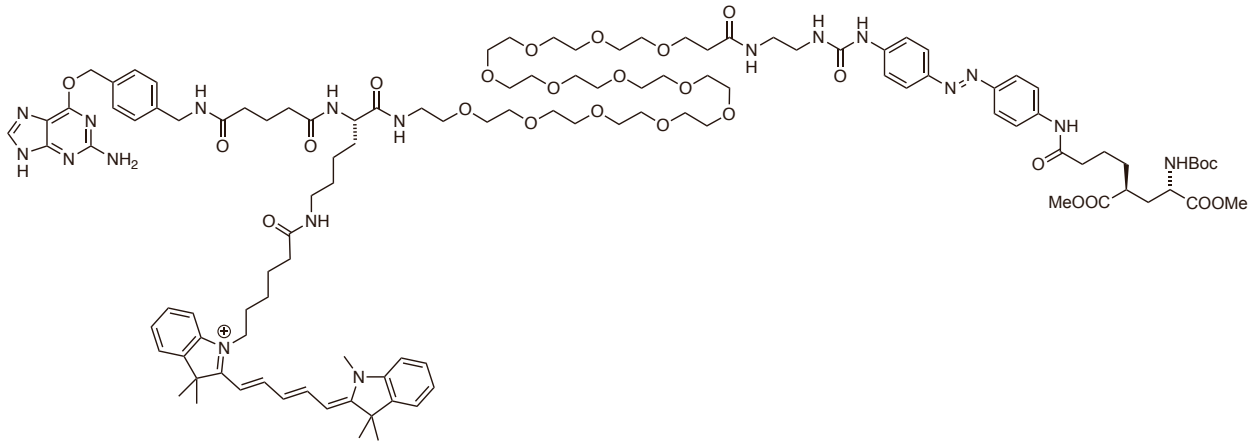

1-((*S*)-47-(5-((4-(((2-Amino-9*H*-purin-6-yl)oxy)methyl)benzyl)amino)-5-oxopentanamido)-1-((4-((*E*)-(4-((5*S*,7*S*)-7-((*tert*-butoxycarbonyl)amino)-8-methoxy-5-(methoxycarbonyl)-8-oxooctanamido)phenyl)diazenyl)phenyl)amino)-1,6,46,53-tetraoxo-9,12,15,18,21,24,27,30,33,36,39,42-dodecaoxa-2,5,45,52-tetraazaoctapentacontan-58-yl)-3,3-dimethyl-2-((1*E*,3*E*)-5-((*Z*)-1,3,3-trimethylindolin-2-ylidene)penta-1,3-dien-1-yl)-3*H*-indol-1-ium

S24 was prepared according to general procedure B.

Acid: **BG-COOH**; amine **S22**.

HRMS (ESI): calc. for $C_{114}H_{165}N_{18}O_{26}$ $[M+2H]^{3+}$: 734.4052, found: 734.4047.

2.46. $BGAG_{12,400}$–Cy5 v2

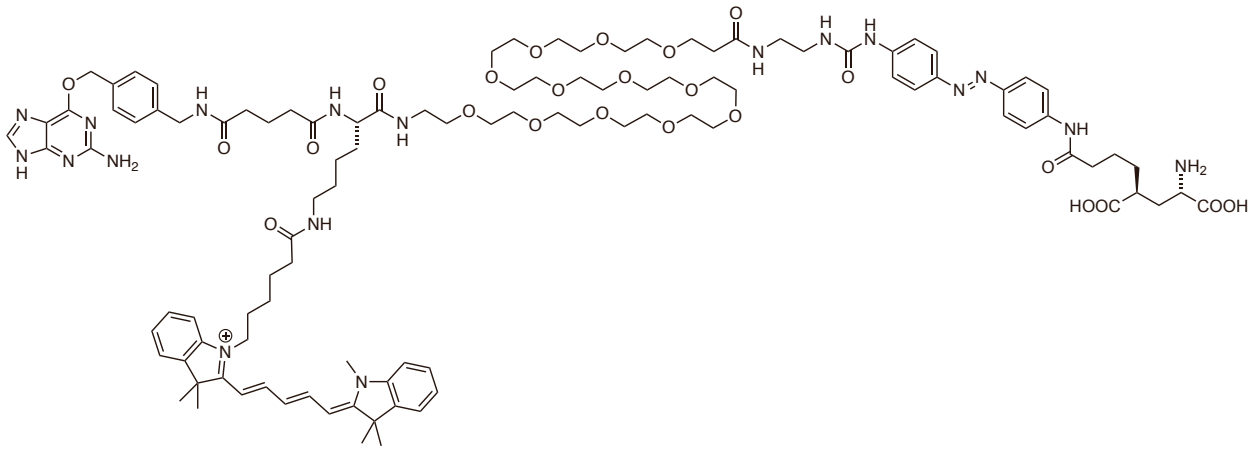

1-((*S*)-1-((4-((*E*)-(4-((5*S*,7*S*)-7-Amino-5,7-dicarboxyheptanamido)phenyl)diazenyl)phenyl)amino)-47-(5-((4-(((2-amino-9*H*-purin-6-yl)oxy)methyl)benzyl)amino)-5-oxopentanamido)-1,6,46,53-tetraoxo-9,12,15,18,21,24,27,30,33,36,39,42-dodecaoxa-2,5,45,52-tetraazaoctapentacontan-58-yl)-3,3-dimethyl-2-((1*E*,3*E*)-5-((*Z*)-1,3,3-trimethylindolin-2-ylidene)penta-1,3-dien-1-yl)-3*H*-indol-1-ium

$BGAG_{12,400}$–Cy5 v2 was prepared according to general procedure D from compound **S24**.

HRMS (ESI): calc. for $C_{112}H_{161}N_{18}O_{26}$ $[M+2H]^{3+}$: 725.0615, found: 725.0613; ester cleaved intermediate.

HRMS (ESI): calc. for $C_{107}H_{153}N_{18}O_{24}$ $[M+2H]^{3+}$: 691.7106, found: 691.7099; **$BGAG_{12,400}$–Cy5 v2**.

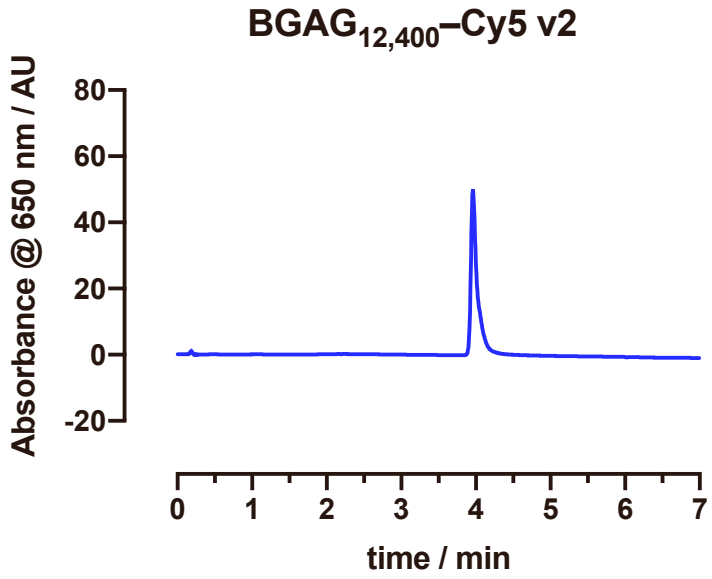

2.47. Compound S26

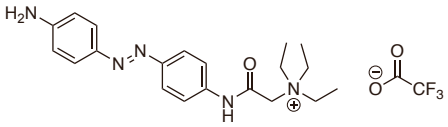

(*E*)-2-((4-((4-Aminophenyl)diazenyl)phenyl)amino)-*N*,*N*,*N*-triethyl-2-oxoethan-1-aminium (x TFA)

A round bottom flask was charged with 240 mg (1.13 mmol, 1.1 equiv.) of 4,4'-diamino azobenzene (**S25**), 200 mg (1.02 mmol, 1.0 equiv.) *N*-(carboxymethyl)-*N*,*N*-diethylethanaminium chloride(Banghart et al., 2009) dissolved in 4 mL DMSO and 500 µL DIPEA. To the vigorously stirred solution, 425 mg (1.13 mmol, 1.1 equiv.) HBTU was added in one portion and the reaction mixture was stirred at r.t. o.n. before it was quenched by addition of 500 µL HOAc and 500 µL H_2O and subjected to RP-HPLC purification to obtain 145 mg (0.31 mmol) of the desired product in 30% yield. The final compound was soluble up to 20 mg/mL in D_2O.

^{1}H NMR (400 MHz, D_2O): δ [ppm] = 7.74 (d, J = 8.8 Hz, 2H), 7.69 (d, J = 9.0 Hz, 2H), 7.57–7.38 (m, 2H), 7.25 (d, J = 8.9 Hz, 2H), 4.02 (s, 2H), 3.50 (q, J = 7.2 Hz, 6H), 1.26 (t, J = 7.2 Hz, 9H).

^{13}C NMR (101 MHz, D_2O): δ [ppm] = 162.91 (q, J = 35.3 Hz), 162.64, 148.78, 147.99, 139.33, 138.78, 125.13, 123.10, 121.64, 121.61, 116.32 (q, J = 291.9 Hz), 56.41, 54.64, 6.93.

HRMS (ESI): calc. for $C_{20}H_{28}N_5O$ $[M]^+$: 354.2288, found: 354.2288.

2.48. AQ

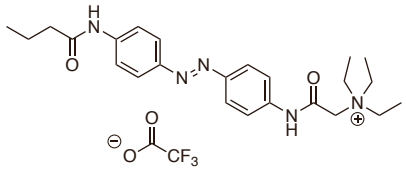

(*E*)-2-((4-((4-Butyramidophenyl)diazenyl)phenyl)amino)-*N*,*N*,*N*-triethyl-2-oxoethan-1-aminium (x TFA)

A flame-dried 250 mL Schlenk flask under an argon atmosphere was charged with 50 mg (107 µmol, 1.0 equiv.) of **S26**, before addition of 10 mL dry THF and 37 µL DIPEA (214 µmol, 2.0 equiv.). The reaction mixture was vigorously stirred and cooled to 0 °C in an ice-bath and 16.7 µL of butyryl chloride (161 µmol, 1.5 equiv.) was added. Upon addition, the ice bath was removed and the reaction mixture was allowed to stir for 45 min while warming to r.t., before it was quenched by addition of glacial HOAc (0.1 mL). The reaction mixture was concentrated *in vacuo* and subjected to RP-HPLC to obtain 30.3 mg (57.2 µmol) of the desired compound (TFA salt) as a highly hygroscopic, orange powder in 53% yield. The final compound was soluble up to 10 mg/mL in D_2O.

^{1}H NMR (400 MHz, D_2O): δ [ppm] = 7.88–7.64 (m, 4H), 7.60–7.54 (m, 4H), 4.07 (s, 2H), 3.57 (q, J = 7.2 Hz, 6H), 2.32 (t, J = 7.4 Hz, 2H), 1.64 (q, J = 7.4 Hz, 2H), 1.33 (t, J = 7.2 Hz, 9H), 0.93 (t, J = 7.4 Hz, 3H).

^{13}C NMR (101 MHz, D_2O): δ [ppm] = 175.8, 162.5, 149.1, 148.4, 140.3, 138.8, 123.6, 123.5, 121.5, 121.2, 56.4, 54.7, 38.5, 18.9, 12.8, 7.0.

HRMS (ESI): calc. for $C_{24}H_{34}N_5O_2$ $[M]^+$: 424.2707, found: 424.2704.

$\varepsilon_{360\ nm}$ (PBS) = 19,800 M^{-1} cm^{-1}

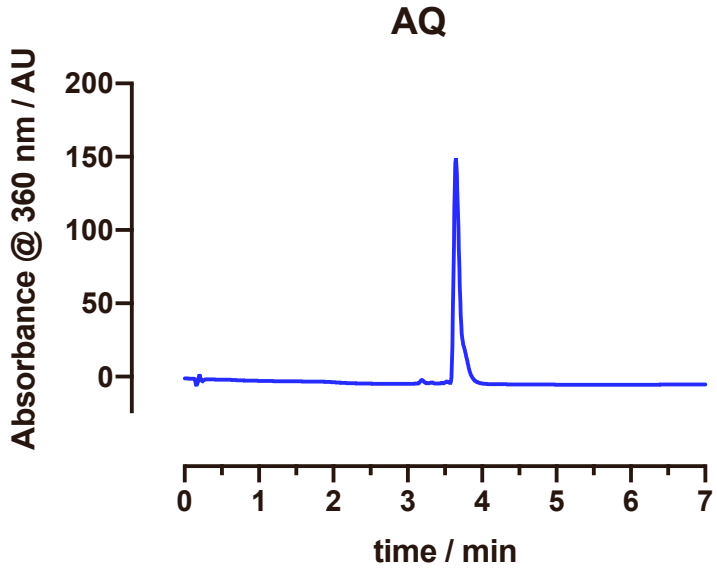

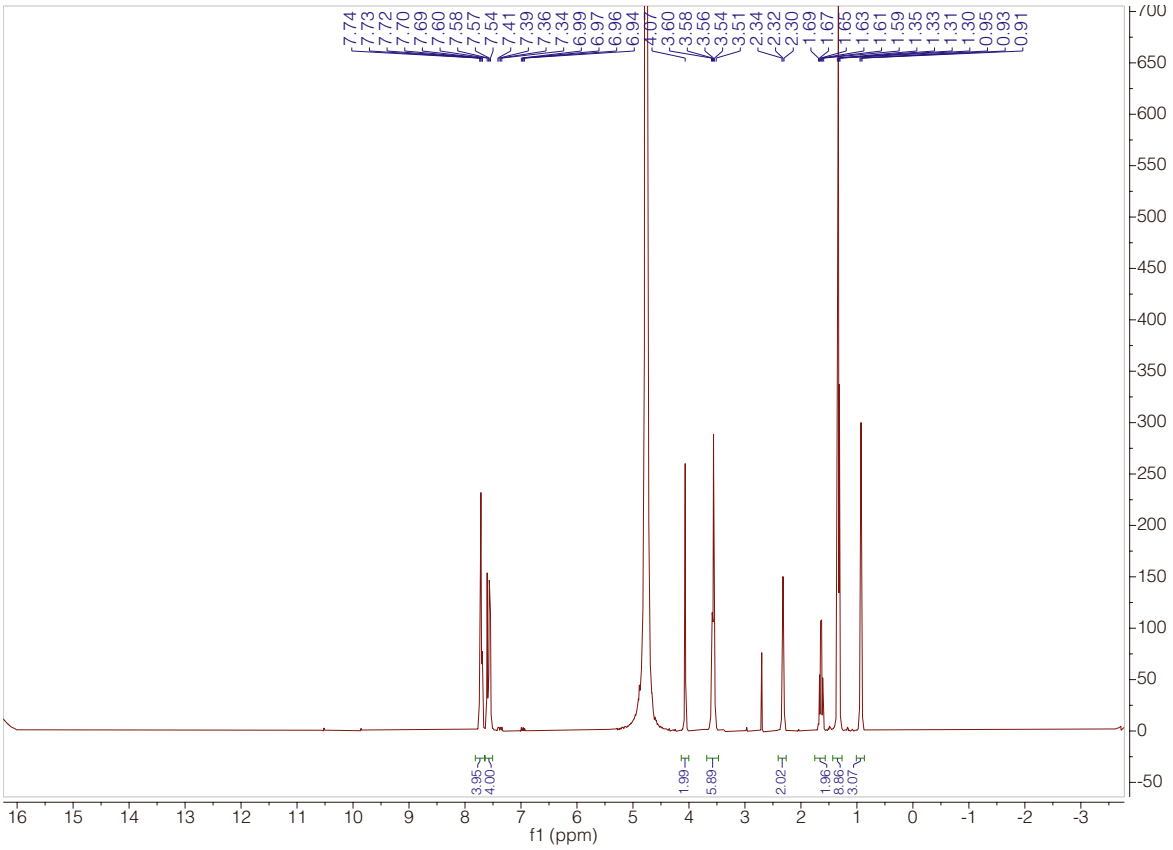
7.74
7.73
7.72
7.70
7.69
7.60
7.58
7.57
7.54
7.41
7.39
7.36
7.34
6.99
6.97
6.96
6.94
4.07
3.60
3.58
3.56
3.54
3.51
2.34
2.32
2.30
1.69
1.67
1.65
1.63
1.61
1.59
1.35
1.33
1.31
1.30
0.95
0.93
0.91
3.95
4.00
1.99
5.89
2.02
1.96
8.86
3.07
f1 (ppm)

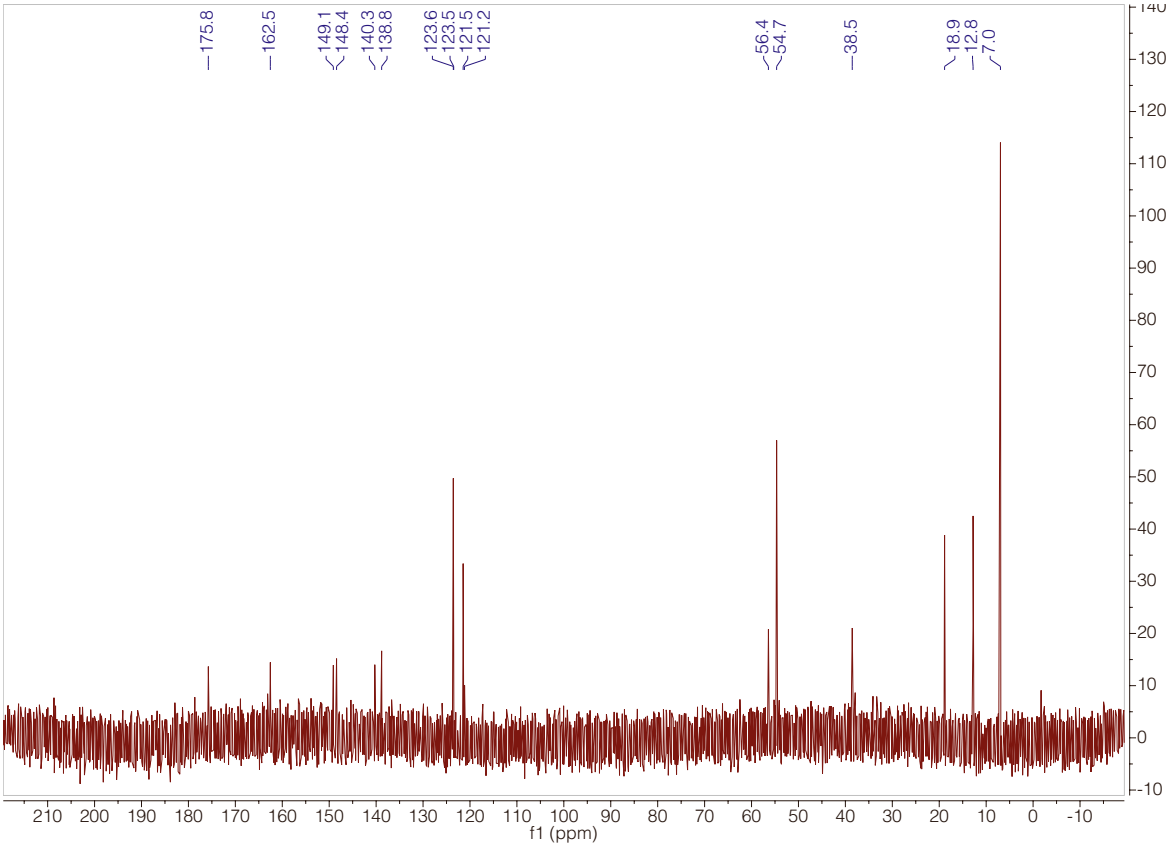
175.8
162.5
149.1
148.4
140.3
138.8
123.6
123.5
121.5
121.2
56.4
54.7
38.5
18.9
12.8
7.0
f1 (ppm)

2.49. AQ_{400}

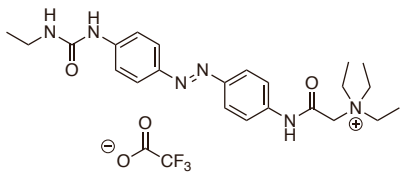

(*E*)-*N*,*N*,*N*-Triethyl-2-((4-((4-(3-ethylureido)phenyl)diazenyl)phenyl)amino)-2-oxoethan-1-aminium chloride (x TFA)

A microwave vial was charged with 50 mg (107 µmol, 1.0 equiv.) of **S26**, before addition of 5 mL dry THF and 37 µL DIPEA (214 µmol, 2.0 equiv.) and 350 µL (4.42 mmol, 41 equiv.) ethyl isocyanate. The reaction mixture was vigorously stirred at 80 °C under microwave irradiation for 5 h, before it was quenched by addition of glacial HOAc (0.1 mL). The reaction mixture was concentrated *in vacuo* and subjected to RP-HPLC to obtain 30.0 mg (56.5 µmol) of the desired compound (TFA salt) as an hygroscopic, orange powder in 53% yield. The final compound was soluble up to 10 mg/mL in D_2O.

^{1}H NMR (400 MHz, D_2O): δ [ppm] = 7.90–7.64 (m, 4H), 7.58 (d, J = 8.9 Hz, 2H), 7.43 (d, J = 9.0 Hz, 2H), 4.06 (s, 2H), 3.57 (q, J = 7.2 Hz, 6H), 3.18 (q, J = 7.3 Hz, 2H), 1.34 (t, J = 7.2 Hz, 9H), 1.11 (t, J = 7.2 Hz, 3H).

^{13}C NMR (101 MHz, D_2O): δ [ppm] = 161.9, 157.3, 151.1, 147.6, 142.3, 138.5, 123.8, 123.3, 121.5, 119.5, 56.4, 54.7, 34.8, 14.3, 7.0.

HRMS (ESI): calc. for $C_{23}H_{33}N_6O_2$ $[M]^+$: 425.2660, found: 425.2659.

$\varepsilon_{371\ nm}$ (PBS) = 23,400 M^{-1} cm^{-1}

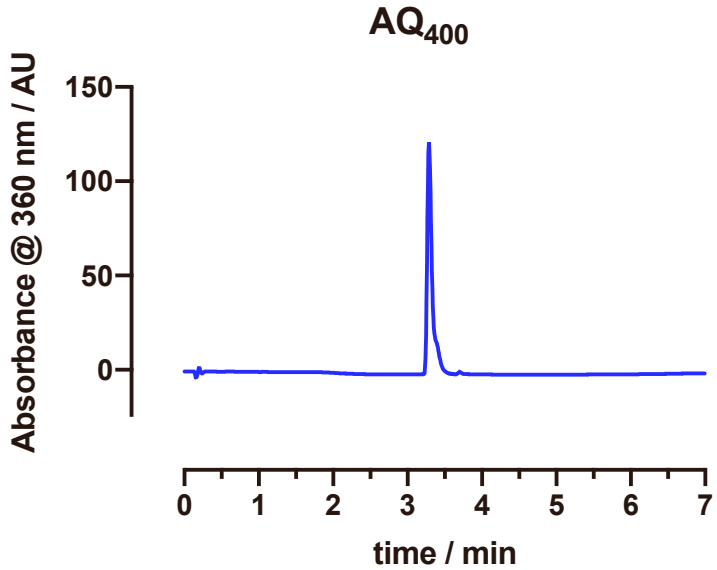

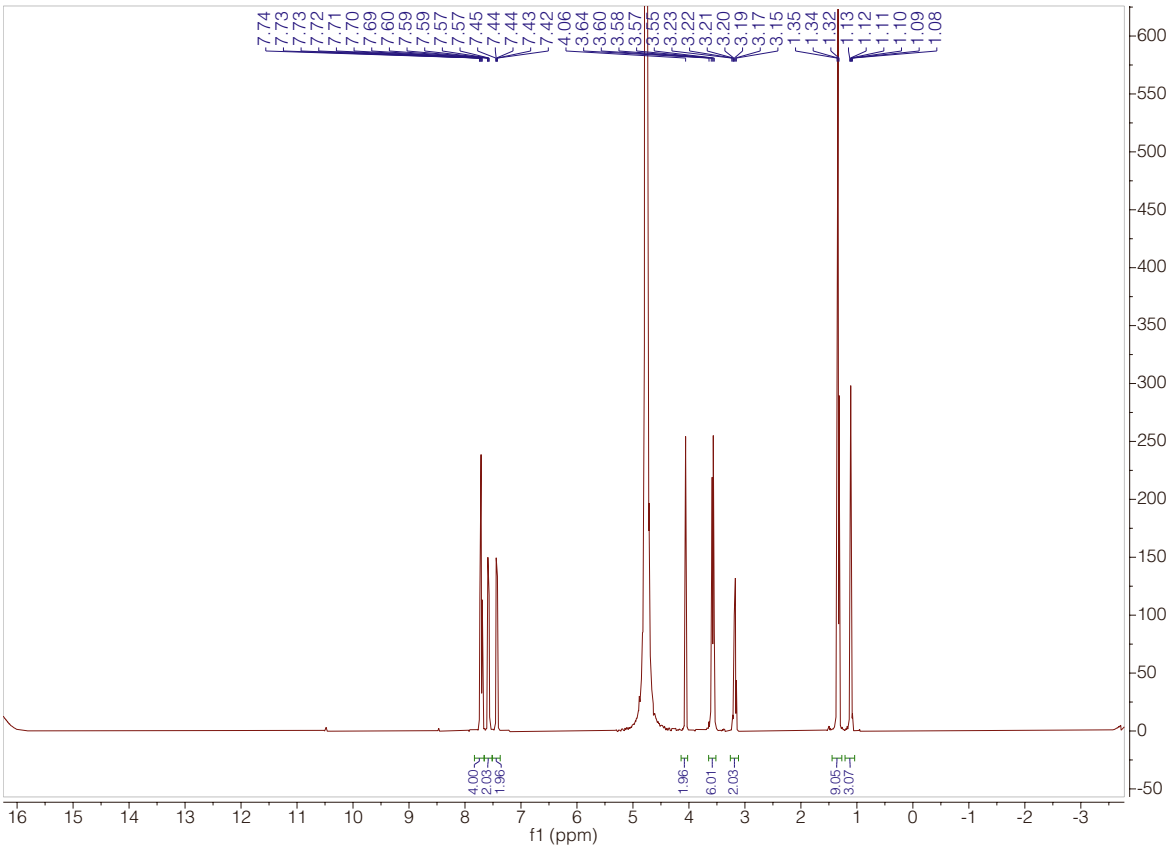
7.74
7.73
7.73
7.72
7.71
7.70
7.69
7.60
7.59
7.59
7.57
7.57
7.45
7.44
7.44
7.43
7.42
4.06
3.64
3.60
3.58
3.57
3.55
3.23
3.22
3.21
3.20
3.19
3.17
3.15
1.35
1.34
1.32
1.13
1.12
1.11
1.10
1.09
1.08
4.00
2.03
1.96
1.96
6.01
2.03
9.05
3.07
f1 (ppm)

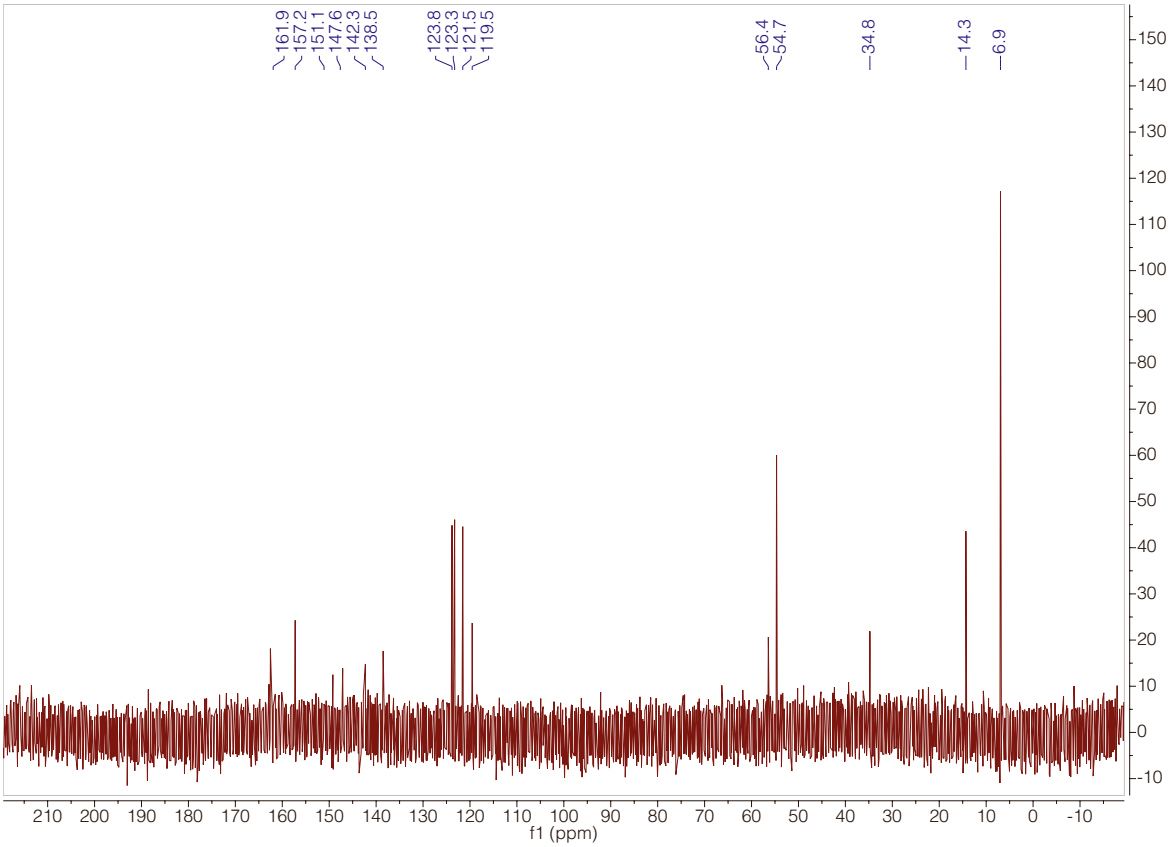
161.9
157.2
151.1
147.6
142.3
138.5
123.8
123.3
121.5
119.5
56.4
54.7
34.8
14.3
6.9
f1 (ppm)

3. *Photochemical actinometry*

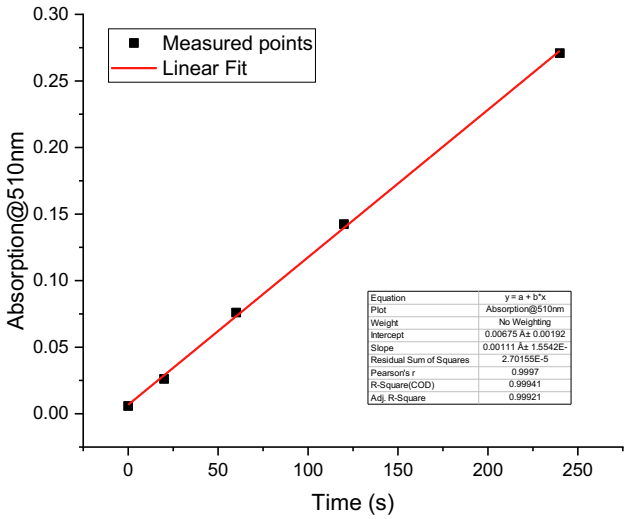

Figure PA1, Related to Figure 1 and 6. Absorbance of the tris-phenanthroline iron (II) complex as a function of irradiation time of potassium ferrioxalate (black squares). The red line shows a linear fit, which is used to calculate the photon flux.

The ferrioxalate method was used to calculate the photonflux using the protocol described in (Stranius and Borjesson, 2017). In short, a 2 ml (V_1) solution of ferrioxalate (30 mM in 0.2 N H_2SO_4) was irradiated (using a laser diode with a centre wavelength of 399 nm) under stirring. 0.5 ml (V_2) of the irradiated volume together with buffer (1.2 M NaOAc + 0.72 N H_2SO_4, 1 ml), and phenanthroline (6 mM, 2 ml) was diluted to 25 ml (V_3) and left to react for 1 h, where after the absorbance of the tris-phenanthroline complex was recorded at 510 nm (ε_{510nm}=11,100 M^{-1} cm^{-1}). The photonflux was then calculated using:

$$I = slope \cdot \frac{V_1 \cdot V_3}{V_2 \cdot \varepsilon_{510nm} \cdot l \cdot \phi} \qquad (5)$$

Where the linear fit in Figure PA1 was used to get the slope, l is the pathlength of the cuvette, and ϕ is the photochemical quantum yield of the process (~1.14@399nm). Using equation 5 the photonflux was determined to $8.8 \cdot 10^{-9}$ Einstein/s.

4. *Photoisomerization quantum yield measurements*

The rate of a photoisomerization event from species A to B can be described with (Stranius and Borjesson, 2017)

$$\frac{d[A]}{dt} = -\frac{\phi_A \cdot I \cdot \beta_A(t)}{N_A \cdot V} + \frac{\phi_B \cdot I \cdot \beta_B(t)}{N_A \cdot V} + k_{t,B\to A}[B] \qquad (6)$$

Where N_A is Avogadro's number, k_t is the rate constant for spontaneous back conversion, and V the volume of the sample (in dm^3). β describes the fraction of light absorbed by each species:

$$\beta_A(t) = \frac{[A]\cdot\varepsilon_A}{[A]\cdot\varepsilon_A + [B]\cdot\varepsilon_B}\left(1 - 10^{-Abs(t)}\right) \qquad (7)$$

Where Abs is the absorbance of the sample at the wavelength of irradiation, and ε is the molar absorptivity of each specie. Equation 6 was used to fit experimental data using the ϕ for both the forward and backward reactions as fitting parameters.

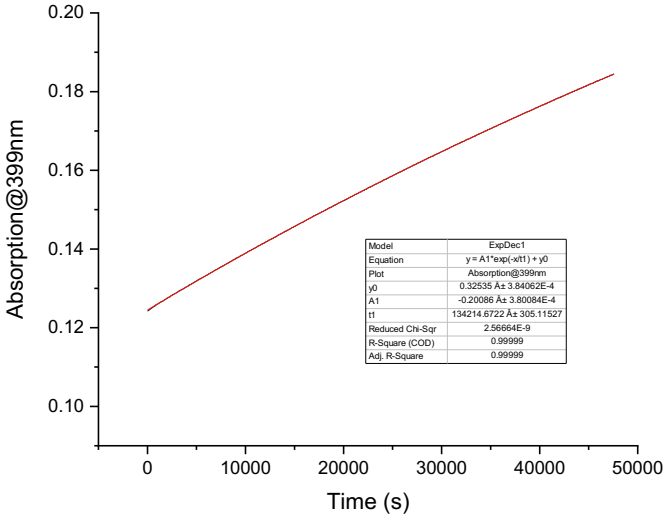

Figure PA2, Related to Figure 1. Absorption of a mixture of *cis* and *trans* of compound **1** as a function of time. The black line shows the raw data and the red line show a fit to an exponential decay function, giving the rate constant of the thermal backconversion.

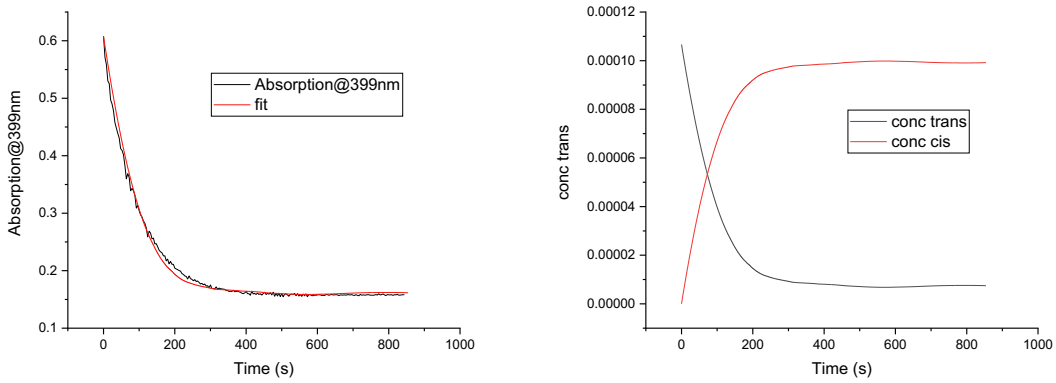

Figure PA3 Left, Related to Figure 1. Absorption of a mixture of *cis* and *trans* of compound **1** as a function of time when simultaneously irradiating the solution and a fit to equation 6, giving the quantum yield of photoisomerization. Right: Concentration of the *trans* and *cis* isomers of compound **1** during the photoisomerization event.

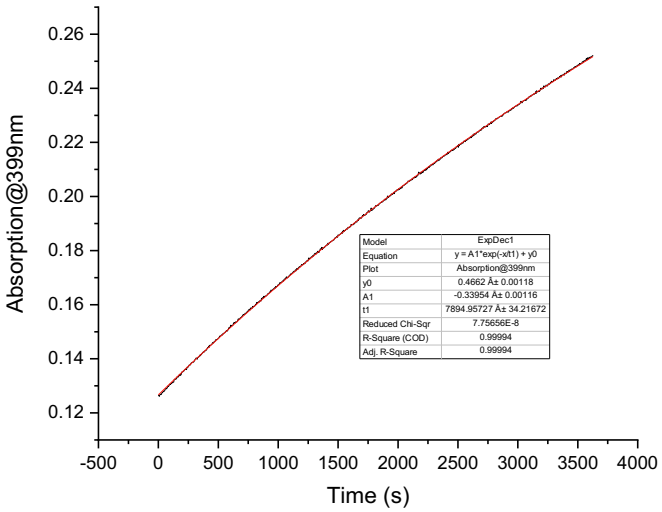

Figure PA4, Related to Figure 1. Absorption of a mixture of cis and trans of compound **8** as a function of time. The black line shows the raw data and the red line show a fit to an exponential decay function, giving the rate constant of the thermal backconversion.

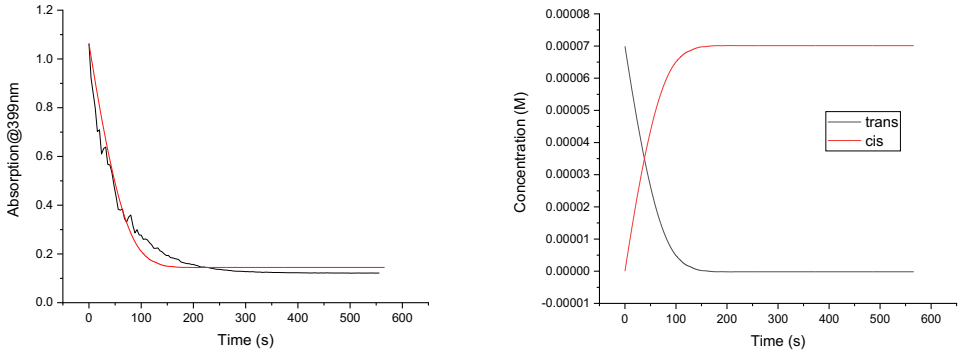

Figure PA5, Related to Figure 1. Left: Absorption of a mixture of *cis* and *trans* of compound **8** as a function of time when simultaneously irradiating the solution and a fit to equation 6, giving the quantum yield of photoisomerization. Right: Concentration of the *trans* and *cis* isomers of compound 8 during the photoisomerization event.

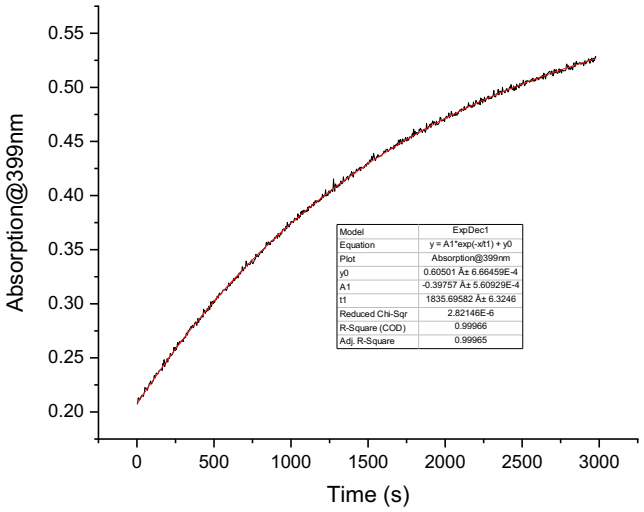

Figure PA6, Related to Figure 1. Absorption of a mixture of *cis* and *trans* of AQ as a function of time. The black line shows the raw data and the red line show a fit to an exponential decay function, giving the rate constant of the thermal backconversion.

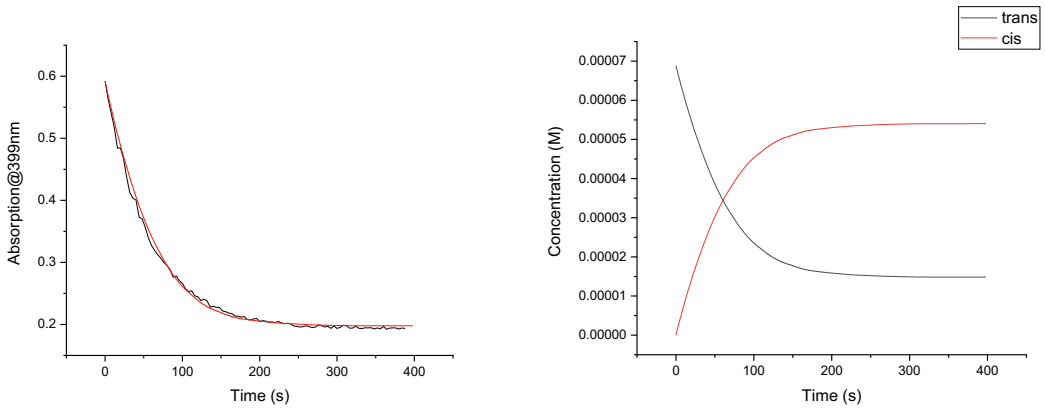

Figure PA7, Related to Figure 6. Left: Absorption of a mixture of *cis* and *trans* of AQ as a function of time when simultaneously irradiating the solution and a fit to equation 6, giving the quantum yield of photoisomerization. Right: Concentration of the *trans* and *cis* isomers of AQ during the photoisomerization event.

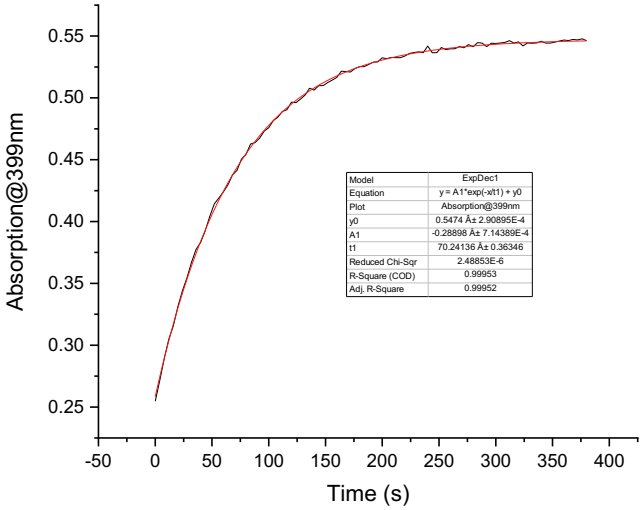

Figure PA8, Related to Figure 6. Absorption of a mixture of cis and trans of AQ_{400} as a function of time. The black line shows the raw data and the red line show a fit to an exponential decay function, giving the rate constant of the thermal backconversion.

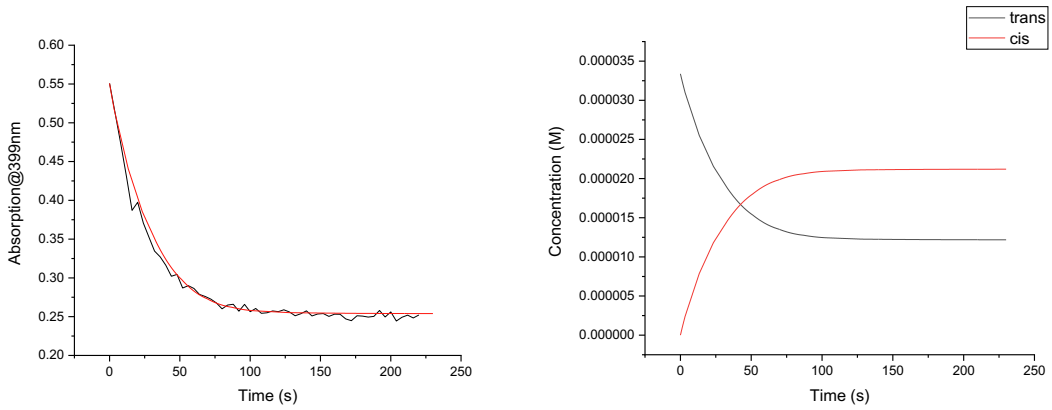

Figure PA9, Related to Figure 6. Left: Absorption of a mixture of *cis* and *trans* of AQ_{400} as a function of time when simultaneously irradiating the solution and a fit to equation 6, giving the quantum yield of photoisomerization. Right: Concentration of the *trans* and *cis* isomers of AQ_{400} during the photoisomerization event.

5. *Supplementary Tables*

Table S1. Summary of photoisomerization characterization. Related to Figure 1 and 6.

Rate of the thermal backconversion ($k_{thermal}$) for the azobenzene derivatives as well as the quantum yield (Φ) of photoisomerization, when irradiating at 399 nm. All photoisomerization quantum yields are averages of two measurements. Columns 7 and 8 show the molecular brightness (Φ * ε) at 399 nm.

Compound	**$\varepsilon_{399\ nm}$ ($M^{-1}cm^{-1}$)**	**Solvent**	**$k_{thermal}$ (s^{-1})**	**$\Phi_{trans\_to\_cis}$**	**$\Phi_{cis\_to\_trans}$**	**$\Phi_{trans\_to\_cis}$ x $\varepsilon_{399\ nm}$ x 10^{-3}**	**$\Phi_{cis\_to\_trans}$ x $\varepsilon_{399\ nm}$ x 10^{-3}**
1	*trans* = 4,606 *cis* = 1,210	DMSO	$7.5 \cdot 10^{-6}$	0.33	0.01	1.52	0.012
8	*trans* = 15,170 *cis* = 1,430	DMSO	$1.3 \cdot 10^{-4}$	0.27	0.11	4.10	0.157
AQ	*trans* = 7,295 *cis* = 1,328	PBS	$5.5 \cdot 10^{-4}$	0.32	0.33	2.33	0.438
AQ_{400}	*trans* = 16,197 *cis* = 1,431	PBS	$1.4 \cdot 10^{-2}$	0.26	0.52	4.21	0.744